Diss. 2005 - 07
July

High-resolution measurements of light nuclides produced in 1 A GeV ^{238}U-induced reactions in hydrogen and in titanium

Maria Valentina Ricciardi

Gesellschaft für Schwerionenforschung mbH
Planckstraße 1 · D-64291 Darmstadt · Germany
Postfach 11 05 52 · D-64220 Darmstadt · Germany

Universidad de Santiago de Compostela

Facultad de Física

Departamento de Física de Partículas

High-resolution measurements of light nuclides produced in 1A GeV ^{238}U-induced reactions in hydrogen and in titanium

Maria Valentina Ricciardi

Santiago de Compostela, 25 Febrero 2005

KARL-HEINZ SCHMIDT, investigador senior del Gesellschaft für Schwerionenforschung (GSI), en Darmstadt, Alemania,

y

JOSE F. BENLLIURE ANAYA, Profesor Titular del Departamento de Física de Partículas de la Universidad de Santiago de Compostela,

CERTIFICAN

que la presente memoria, con titulo ***"High-resolution measurements of light nuclides produced in 1 A GeV ^{238}U-induced reactions in hydrogen and in titanium"***, realizada por **Maria Valentina Ricciardi** en la Universidad de Santiago de Compostela, constituye el trabajo de Tesis Doctoral que presenta para optar el Grado de Doctor en Física.

Santiago, Noviembre 2004

The examination board was composed by:
Dr. Philippe Chomaz, GANIL, Caen, France
Prof. José Díaz Medina, Universidad de Valencia, Spain
Prof. Ignacio Durán Escribano, Universidad de Santiago de Compostela, Spain
Prof. Joaquín Sánchez Guillén, Universidad de Santiago de Compostela, Spain
Prof. Reinhard Stock, Joahann Wolfgang Goethe Universität, Frankfurt, Germany

This Thesis was refereed also by:
Dr. Graziano Fortuna, LNL, Legnaro, Italy
Dr. Maria José García Borge, CSIC, Madrid, Spain
Prof. Joaquín Gómez Camacho, Universidad de Sevilla, Spain
Dr. Berta Rubio Barroso, CSIC, Universidad de Valencia, Spain
Prof. Carolina Torrón Casal, Universidad de Santiago de Compostela, Spain

Contents

Introduction

Just like normal matter, nuclear matter exists in different states. Normal nuclei appear to be in the liquid phase, but there are sites in the universe where nuclear matter exhibits different phases depending on the local temperature and density.

Changes of pressure, temperature and density can lead to transitions of phase of the nuclear matter. The equation of state (EOS) of nuclear matter rules the response of nuclear pressure to temperature and density. The precision of our description of the EOS reflects our basic comprehension of the nuclear matter. It is also of extreme importance for the understanding of many fundamental astrophysical issues. The EOS has to be tested at temperatures and densities as well as in neutron-to-proton compositions far from the conditions in our environment. A possibility is offered by the observation of neutron stars and of supernova explosions, but in both cases the information is limited by the unfavourable detection conditions and by the scarcity of events. A successful experimental access to the study of nuclear-matter properties is offered by the heavy-ion collisions at high energy, where extreme conditions of temperature and density can be created for a very short time.

In nucleus-nucleus collisions at relativistic energies, two types of products are of experimental interest. The first ones are the fragments originating from the disassembly of the *spectator nuclei*, which are constituted by the nucleons that – for geometrical reasons – do not interact during the collision. The second ones are those arising from the *firestreak*, the ensemble of hadrons formed in the interaction of those nucleons that – for geometrical reasons – violently crash during the collision. As the impact parameter decreases, the size of the spectator nuclei decreases in favour of the firestreak size, which is maximum in case of central collision. In the traditional experimental approach, the two groups of products are investigated with different aims. The first group of products is used for the study of the liquid-gas phase transition. Among all the products, the experimental observables mostly exploited are in this case the light fragments (typically with mass number smaller than 30). The second group of products is used normally for the study of the EOS, e.g. its incompressibility. The interesting experimental observables are the production of hadrons (mostly kaons) and the flow characteristics of the expanding firestreak.

Both these investigations rely on the use of full-acceptance (or 4π) detection systems; the first one to get the multiplicity of the fragments produced in one event, the second one to get the angular distribution of the particles. The most important advantage of the 4π set-ups is the possibility of exclusive measurements. The disadvantage is the lack of resolution, which introduces some severe restrictions. For instance, the limited mass resolution reduces the possibility to study the influence of the neutron-to-proton compositions on the behaviour of nuclear matter. In addition, the kinematical properties of the spectator residues cannot be studied with the desired precision.

In this context we propose to use a high-resolution magnetic spectrometer, which can provide extremely accurate results, where different observables are disentangled, limited however by the inclusivity of the measurement. Thus, it provides complementary information to that achievable with 4π detection systems.

To do this, we profit from the experimental infrastructure available at the GSI laboratory (Darmstadt, Germany), where a heavy-ion synchrotron is coupled with a high-resolution magnetic spectrometer, the FRagment Separator (FRS). The aim of the present work is to investigate which features of the nuclear matter are deducible from the light fragments – fully resolved in charge, mass and velocity with a high-resolution magnetic spectrometer – produced in the reactions ^{238}U on ^{1}H and ^{238}U on Ti at 1 *A* GeV. These two reactions belong to a campaign of measurements performed in the frame of a project devoted to obtaining nuclear data for waste-transmutation and radioactive-ion-beam facilities. Although the physics aim of the project is far from that one proposed here, the investigation of these two reactions offered the chance, on the base of the available experimental possibilities, to test the perspectives to use high-resolution magnetic spectrometers for the study of the properties of nuclear matter, eventually leading to the birth of a devoted experimental campaign.

The analysis of the light fragments produced in the two reactions offers the possibility to study the disassembly of the ^{238}U nucleus under very different initial conditions.

It was shown [ReiR97] that the spectators constitute an obstacle for the free expansion of the firestreak, resulting in a *shadowing effect* in the angular pattern of the firestreak flux. If the presence of the spectators affects the features of the firestreak, it is reasonable to expect that the presence of the firestreak affects the features of the spectators. More specifically, the impact of the firestreak expansion should be reflected on the kinematical properties of the remnants of the surviving heavy spectators. The light fragments produced in the reaction ^{238}U on Ti at 1 *A* GeV originate from the projectile spectator. Any small change in the fragments velocity, accurately measurable thanks to the high-resolution spectrometer, would reflect the change of the spectator velocity. In contrast to the flow pattern of the expanding firestreak, this is an early signature, which is established well before the freeze-out of the firestreak. Recent transport calculations [Shi01] predict that the longitudinal momenta of the fragments are almost exclusively sensitive to the momentum-dependent properties of the nuclear mean field, and thus give direct access to the nonlocal features of the nuclear EOS. In the present work we will explore whether the relevant experimental information can be obtained with the necessary precision.

The simultaneous full nuclide identification of all residues, achievable thanks to the excellent resolving power of the FRS, is another rich information. In a previous experiment, a specific method, named the *thermometer for peripheral nuclear collisions*, was applied [Sch93] to determine the excitation energy induced in the heaviest elements produced in very peripheral collisions. This method relates the loss of neutron excess observed in the isotopic distributions of the produced elements with the excitation energy at the beginning of the evaporation cascade. In the present work we want to test the applicability of this method to the light fragments observed in the reaction ^{238}U on Ti, produced in less peripheral collisions, where a phase transition could be observable. This would give us the possibility to determine the freeze-out temperature.

Furthermore, the full nuclide identification of all residues is a powerful tool for the study of structural effects in highly excited nuclear matter, when cooling down in the evaporation process. In the present work we want to investigate how the heated nuclear matter condensates, and if structural effects can appear as a manifestation of the passage from the liquid phase to the superfluid phase. This has interesting consequences on the evaluation of the nuclear temperature using isotopes ratios [Alb85], and also in astrophysics, for instance for the cooling rate of the neutron stars, where the presence of neutron superfluidity in the crust seems to be well established [Mon04].

Concerning the system ^{238}U on ^{1}H at 1 *A* GeV, also analysed in this work, this reaction provides about 40 times less energy than the previous one. Despite this, it could also contain interesting information on the behaviour of nuclear matter. Light products from the proton-induced reaction of gold, silver and nickel at 1 GeV were investigated in previous experiments [Kot95, Bar86]. The authors concluded that the onset of the multifragmentation regime is deducible from the observables they had. On the other hand, it was found that in the proton-induced spallation of ^{238}U medium-mass residues result from fission reactions [Ber03]. According to the conditional saddle-point model, fission is expected to produce very light fragments, too [Mor88]. This would imply that the statistical sequential decay from a compound nucleus could reproduce the features of the light fragments observed here. In the present work we will discuss whether the light residues that we observed are consistent with one or the other picture, making use of the two observables in our posses: the velocities and the production cross sections of the residues.

The work will be organised as follows. The experimental set-up and the data analysis will be described in Chapter 1 and in Chapter 2, respectively. In Chapter 3, we will present the experimental results for the two systems, ^{238}U + ^{1}H and ^{238}U + Ti at 1 *A* GeV, and – when possible – we will compare them with other data available in literature. In Chapter 4, we will discuss about the results of the system ^{238}U + ^{1}H. Specifically, we will discuss the possible reaction mechanism behind the production of the observed fragments. In Chapter 5, the mean *N*-over-*Z* of the residual elements formed in the fragmentation of uranium in the reaction ^{238}U + Ti at 1 *A* GeV will be used as key-information to deduce the freeze-out temperature of the system. The trend of the mean value of the longitudinal velocity of the fragments resulting from the system ^{238}U + Ti at 1 *A* GeV is examined in Chapter 6. The result is related to the blast of particles that takes place after the nuclear collision. We will discuss how the longitudinal momentum of the fragments is sensitive to the momentum-dependence of the nuclear mean field. Finally, in Chapter 7 we will work out how the yields of the light residual nuclei produced in the uranium fragmentation reveal important information on the structural properties of nuclei.

Chapter 1
The experiment

1.1 The inverse kinematics at relativistic energies

The present work concerns two experiments aimed to investigate the reactions ^{238}U on protons and ^{238}U on titanium at the kinetic energy of 1 GeV per nucleon. The experiments were performed in inverse kinematics, by using uranium projectiles and a hydrogen and a titanium target. The liquid-hydrogen target was contained in a vessel with titanium windows. The data from the experiment with the titanium target were used to rectify the results of the liquid-hydrogen target from the presence of titanium. The uranium beam speed was about 26 cm/ns, i.e. 87% of the speed of light. We were, thus, in the relativistic regime.

When compared to the direct kinematics, the inverse-kinematics technique at relativistic energies has several advantages for the systematic measurement of production cross sections. Firstly, all nuclear fragments that originate from the projectile escape from the target, thanks to their high momentum. Thus, the outgoing fragments can easily be registered in-flight by suitable detectors placed behind the target. Secondly, the measurement is independent of the chemical properties and of the beta decay of the fragments, which prevented detecting most nuclides by the radiochemical or activation methods used in many previous experiments. Thirdly, a measurement of their velocities and angles, which are characteristic for the reaction mechanism, is possible for any value of the momentum induced, while experiments in normal kinematics suffer from a lower threshold below which the fragments do not leave the target or cannot be detected.

The GSI synchrotron and the FRagment Separator (FRS) [Gei92] are best suited for this kind of experiment. Firstly, the synchrotron accelerates heavy ions, such as ^{238}U, up to the required energy of 1 GeV per nucleon. Secondly, the FRS is able to separate, to fully identify and to measure the velocities of the produced residues.

In the following sections, we will describe the experimental devices in more detail.

1.2 The experimental set-up

The experiment was performed at GSI in Darmstadt, using the *SIS* heavy-ion synchrotron and the *FRagment Separator* (FRS) spectrometer. A scheme of the experimental set-up is shown in figure 1.1. The FRS is a two-stage, achromatic magnetic spectrometer with a dispersive intermediate image plane. In addition to the four dipoles shown, a number of quadrupoles and sextupoles serve for focussing and for correcting the chromatic aberration, respectively. In the present application, the two stages have different main tasks. In the first stage, formed by the first two dipole sections and the first scintillation detector, the magnetic rigidity of the reaction products leaving the target is determined. In the second stage, formed by the two other dipole sections and an additional scintillation detector, the products are identified in A/Z by their magnetic rigidities and their velocities determined by time-of-flight measurement. From the energy loss, measured with the ionisation chambers at the exit of the FRS, their atomic number Z is deduced. Once the reaction residues are identified, i.e. A and Z are exact integer numbers with no error associated, the measurement of the magnetic rigidity in the first half of the FRS gives precise information on the velocity of the fragments. Thus, a full identification of mass and atomic number and a precise momentum determination of the reaction products are provided.

The ^{238}U beam, accelerated by the synchrotron up to the energy of 1 GeV per nucleon, was monitored after its extraction before it impinged on the target. The produced fragments escaped the target in forward direction, and those with an angle within the FRS angular acceptance entered the fragment separator. Depending on the magnetic fields of the first two dipoles of the FRS, only the fragments with an appropriate combination of mass, A, charge, Z, and velocity, υ, were transmitted. All the others, including the projectiles, hit the walls of the vacuum tube and were stopped either in the iron of the magnets or in dedicated slits. When the fragments passed through the first scintillation detector, they were slowed down and reduced their velocity. Depending on the magnetic fields of the 3rd and 4th dipole, only a group of fragments was transmitted. At the exit of the FRS the fragments passed through the first ionisation chamber, the second scintillator, and the second ionisation chamber. The two scintillators were used to determine the horizontal position of the fragments at the intermediate and final image planes and to measure their time-of-flight. The energy loss and the drift-time in the ionisation chambers were used to measure respectively the charge and the x-position. The latter was used to correct the flight path from the dependence on the angle. Some multiwire detectors, placed along the beam line, were used for the beam monitoring and calibration. During the data acquisition they were not in line, because they could reduce the energy of the fragments and cause secondary reactions.

In the following sections, the experimental apparatus will be described in more detail.

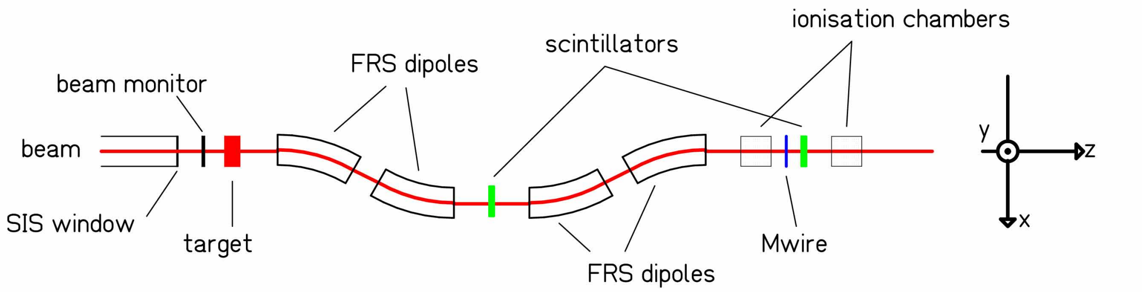

Figure 1.1: Schematic view of the horizontal section of the experimental set-up. The reference axes are conventionally set as shown (y-axis perpendicular to the sheet).

1.3 The production of the beam and its monitoring system

A picture of the GSI facility is shown in figure 1.2. The GSI accelerator system, consisting of the linear accelerator UNILAC and the heavy-ion synchrotron SIS, can deliver any ion beam among all the stable nuclei from hydrogen till uranium, up to an energy that varies from 1 to 4.5 GeV per nucleon, depending on the ion. The beam intensity, at the exit of the SIS, varies nowadays from a maximum of 10^{10} particles per second for neon, to a maximum of 10^{9} particles per second for gold or uranium. The final beam quality is very high, with excellent energy resolution (the momentum spread, $\delta p=\Delta p/p$, is always below 10^{-3}) and small emittance (about 2.5 mm·mrad) [Ste92].

Our experiment was performed with a $^{238}_{92}$U beam, at the energy of 1·A GeV. The ionic charge of the beam at the exit of the SIS was q = +73. SIS was operated in slow-extraction mode. The beam cycle was about 13 seconds long, the beam was extracted with a spill length of 7 seconds. The intensity varied, according to our needs, between 10^{6} and 10^{7} ions/s. The latter value corresponded to the maximum intensity for uranium that the SIS could provide at the time when the experiment was made.

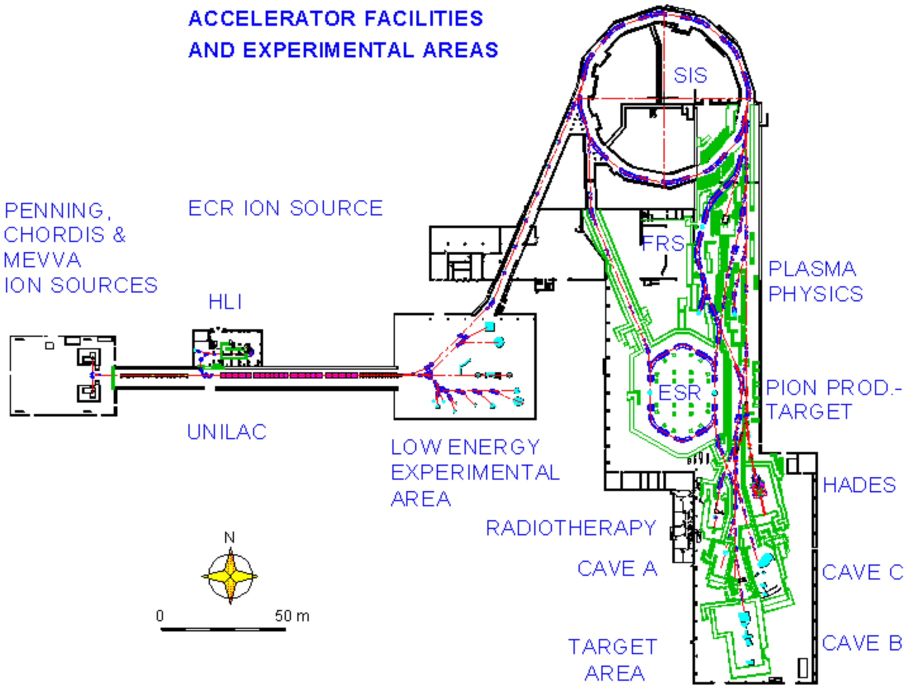

Figure 1.2: Schematic drawing of the GSI facility, which is based on a linear accelerator (UNILAC), followed by a synchrotron (SIS). In the present experiment the ^{238}U ions are extracted from the SIS with a final energy of 1·A GeV and then driven towards the FRS.

Before the beam encountered the target, it had to pass a beam monitor. The monitoring of the beam was necessary in order to have a measurement of the beam flux and of the extraction profile. For this purpose, a specific apparatus, named SEETRAM (Secondary

Electron TRAnsmission Monitor), capable to correctly monitor the intensity of heavy-ion beams with high intensities, was developed at GSI [Zie92]. The SEETRAM consists of three thin metallic foils placed in vacuum parallel to each other and orthogonal to the direction of the beam. The outer foils are connected to a positive voltage (+80 V) and the inner one to the ground via a current integrator. When an ion passes through the SEETRAM, some electrons close to the surface of the inner foil may leave the foil, in such a way generating a positive current in the central layer. The current is then transformed into a voltage. Since the current can have very different intensities (from 10^{-4} to 10^{-10} A), seven levels of sensitivity can be selected through a resistance that can be varied from 10^4 to 10^{10} Ω in order to have an output signal always of the order of some volts. The voltage signals are then filtered, digitised and recorded by a digital counter. The status of this counter is periodically written on tape and accumulated in a spectrum as a function of time.

The thickness of the SEETRAM (8.90 mg/cm^2) is such that less than 0.1% of the beam particles perform a nuclear reaction with the nuclei of the metallic foils.

The SEETRAM counts had to be converted into the number of beam ions with the help of a calibration, which is necessary for each beam type and energy. This calibration was performed at low beam intensity with an ionisation chamber [Jun96, Jur01]. This was done in two steps, first by relating the number of particles to the ionisation current of the ionisation chamber for intensities below 10^4/s, where individual particles can be counted reliably, and secondly by relating the ionisation current of the ionisation chamber to the secondary-electron current of the SEETRAM for intensities below 10^5/s, where recombination effects in the ionisation chamber are still small. The behaviour of the SEETRAM at high intensity was extrapolated from that one obtained for low intensity, since no saturation effects were observed [Jur01].

1.4 The liquid-hydrogen target

To investigate the nuclear reactions occurring in the interaction of protons with uranium in inverse kinematics, a hydrogen target is needed. It was not possible to provide a pure hydrogen target. The choice of a plastic target, like polyethylene ($(CH_2)_n$), is not the best one, especially if the production of light residual nuclei has to be investigated. It was proved [Bin87] that the formation of nuclei with $Z<70$ is mostly due to the interaction with the carbon nuclei. In that case, the error introduced to discharge the contribution of the interactions with the carbon nuclei turns to be extremely high, since carbon makes up a fraction of 1/3 of the target nuclei.

In our experiment, the choice of a liquid-hydrogen target, whose density was high enough to assure a good interaction probability, was done. The target was built at the laboratory Saturne in Saclay, France [Che96]. It is a cylinder with a diameter of 3 cm and a length of 1 cm.

The hydrogen was cooled down to about 20 K and stored in a cryogenic titanium vessel at the pressure of 1.036 atm. The vessel is inside another titanium container, and some foils of mylar and aluminium are inserted between the two in order to ensure thermal insulation. The encapsulation of the vessel is also required to have a safe interface between the target and the beam-line vacuum in case of a possible leakage.

The pressure difference between the vacuum and the hydrogen induces a tiny deformation of the target shape. The hydrogen thickness in the centre was determined from an energy-loss measurement to 87.3±2.2 mg/cm^2 [Mus99]. The total thickness, including the titanium windows and the other layers of the container, corresponds to about 3% of the projectile range, and the probability for nuclear interactions of the projectiles amounts to about 10%. That means that the probability for secondary interactions in the target amounts to about 0.5%. With a total thickness of 36 mg/cm^2, titanium makes up only a fraction of less than one percent of the target nuclei. The choice of the hydrogen thickness represents the best compromise between a large production − large relatively to the production occurring in the titanium windows − and a low secondary-reaction rate.

1.5 The ionic charge of the fragments

After the beam has passed through the target, the beam and the fragments enter the FRS. In order to select and to transmit a given fragment and to discharge all the others, the exact knowledge of the ionic charge state of the ion is needed. Devoted experiments were performed at the GSI to investigate the charge states of high-energy heavy ions in detail [Sch98]. They proved that at the energy of 1·A GeV ions with Z<40 have more than 99.9% chances to be completely stripped behind the target and all along the FRS. Therefore, in the present experiment, it can safely be assumed that all ions passing the FRS are completely stripped.

1.6 The fragment separator

The FRS is a forward, two-stage, magnetic spectrometer. It can be schematised as in figure 1.3. The four dipoles act as dispersive elements. From the ion-optical point of view, the layer of matter in the intermediate image plane, in our case the scintillation detector, acts as a velocity degrader. Altogether 20 quadrupoles form eight lenses, grouped in doublets and triplets. For the operation mode used in the present work, the subdivision of each of the two stages (called section “A” and section “B” in figure 1.3) in two sub-sections with one dipole is not important. It is sufficient to discuss the global properties of the two stages.

To obtain a quantitative formulation of the relations exploited in the present work, we consider the motion of the ion inside a magnetic field, which is ruled by the Lorentz force. Since the magnetic fields inside the dipoles are uniform and perpendicular to the velocity of the ion, the fundamental equation which describes the dynamics of an ion (with ionic charge q and momentum p) inside the FRS is the following:

$$B\rho = \frac{p}{q} = \frac{m \cdot \upsilon}{q} = \frac{m_0 \gamma \cdot \beta \mathrm{c}}{q} = \frac{\mathrm{u}}{\mathrm{e}} \frac{A}{Z} \beta\gamma\mathrm{c} \tag{1.1}$$

where B is the magnetic field inside the magnet, ρ is the radius of the trajectory, υ is the velocity of the ion, $m = \gamma \cdot m_0$ (m_0 = rest mass of the ion), $m_0 = A \cdot \mathrm{u}$ (u = atomic mass unit, A = mass number) , $\gamma = \sqrt{\left(1-\beta^2\right)^{-1}}$, $\beta = \upsilon/\mathrm{c}$ (with c velocity of the light), $q = Z \cdot \mathrm{e}$ (Z = atomic number, -e = electron charge). In equation 1.1 the ion is assumed completely stripped. The magnets bend the ions in circular trajectories. The ratio p/q ($=B\rho$) is called *magnetic rigidity* and is a characteristic of a particle with a certain mass, charge and velocity. If two ions with the same magnetic rigidity would enter into a magnet at the same position but with different angles, they would exit at different positions. In order to avoid this dependence on the angle, two sets of quadrupoles are used as “lenses”, one before and the other after each dipole magnet.

The central image plane of the FRS is *dispersive*, namely two ions that enter the first magnet with different magnetic rigidities, will land on different positions of the plane. Their displacement, Δx, is proportional to their relative difference in magnetic rigidity, $\Delta B\rho/B\rho$, through a constant called *dispersion*:

$$D = \frac{\Delta x}{\Delta B\rho / B\rho} \tag{1.2}$$

The FRS can be operated for magnetic rigidities from 5 to 18 Tm, corresponding to the central trajectory. In the operation mode of the present experiment, the total dispersion is zero, that means it works in the achromatic mode. At the dispersive intermediate plane, the nominal value of the dispersion in momentum is –6.81 cm/%, i.e. 1% of relative difference in magnetic rigidity will produce a shift in position of 6.81 cm. It has an excellent resolution: $\Delta B\rho/B\rho \cong 10^{-4}$-$10^{-3}$. The nominal magnification in the first stage is M = 0.79. The central trajectory is 74 m long, and the flight-path between the two scintillator detectors mounted at the centre and at the exit amounts to about half of it. For a $1{\cdot}A$ GeV ion the typical time-of-flight from the intermediate plane to the final image plane is about 140 ns.

In our experiment, the A/Z of the fragments was measured in the second section of the FRS by measuring the velocity, from the flight path and the time-of-flight, and the $B\rho$, from the measurements of the magnetic fields of the dipoles and the horizontal positions in the intermediate and final image planes. These measurements were performed by two plastic scintillators placed at the two image planes. The values of the dispersions were known from calibration measurements from the primary beam. The value of the charge Z was obtained by an ionisation chamber placed at the exit of the FRS. A detailed description of the equations that lie behind these measurements will be presented in the next chapter. Due to geometrical constraints, the FRS has a longitudinal-momentum acceptance $\Delta p/p \cong 3\%$ and an angular acceptance $\Delta\theta \cong 15$ mrad around the central trajectory. The limited acceptance in momentum has the consequence that many measurements at different magnetic rigidities were needed to have a full picture of the production yields. The limited acceptance in angle restricted the outcome to only inclusive measurements results.

At the intermediate image plane the fragments pass through a layer of matter (a scintillator, in our case) and lose some energy according to the Bethe-Bloch equation:

$$\frac{dE}{dx} \approx f(\upsilon, I, Z_M) \cdot Z^2 \tag{1.3}$$

where Z and υ are the charge and the velocity of the fragment, while I and Z_M are the ionisation potential and the atomic number of the medium. Every fragment will reduce its velocity and consequently its magnetic rigidity according to its nuclear charge. Again, since the FRS allows the transmission only of a limited range of magnetic rigidities, only a limited number of ions, with certain atomic numbers, will have the adequate velocity to be transmitted along the second section of the FRS. The selection in Z turned out to be very useful for the measurement of light residual masses. Their production cross sections are low compared to those of residues with higher mass and similar rigidity. In order not to overload the detectors, the intensity of the beam would have been limited by the high counting rate of the heavier fragments, and consequently the low counting rate of low-mass residues would have caused a large statistical error.

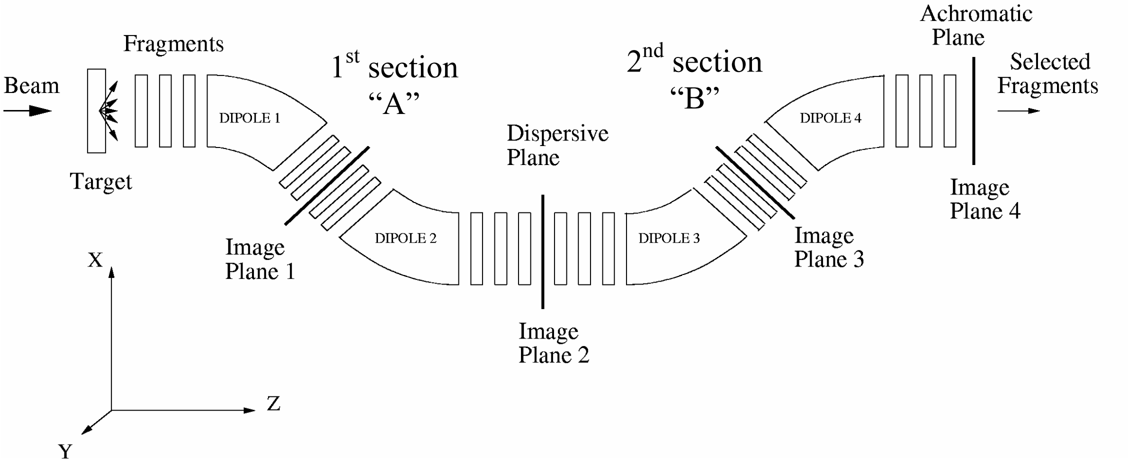

Figure 1.3: Schematic drawing of the FRS according to its ion-optic characteristics. Quadrupoles are placed before and after each dipole to define the ion-optic conditions at each image plane.

The FRS is actually much more complicated than what is described above. The constructors resorted to many expedients in order to make it work correctly. For instance the dependence of the bending power of the quadrupoles on the energy of the fragment (*chromatic aberration*) is corrected by introducing sextupoles behind the quadrupoles. The large number of quadrupoles inserted between the dipoles allows controlling the emittance in x and in y of the beam and other ion-optical parameters, like the dispersion and the magnification. The FRS can operate in different working modes; above we have described only one. Detailed descriptions of the ion-optical characteristics of the FRS can be found in ref. [Gei92].

1.7 The detectors

1.7.1 The Hall probes

Hall probes are used to measure the magnetic fields inside the dipoles with a relative uncertainty of $\sim 10^{-4}$. Their calibration and their stability were checked by repeatedly passing the primary beam on the central trajectory. The voltages of the Hall probes were recorded whenever the dipole fields were changed. Although the response of the Hall probes was found to be stable within the experiment, their response shows a long-term drift due to radiation damages. Therefore, they have to be calibrated for each experiment. The calibration was done with a set of multiwire proportional chambers (see section 1.7.4) by centring the primary beam (whose magnetic rigidity was known) along the FRS.

1.7.2 The scintillators

The two scintillation detectors, SCI2 and SCI4, were used to determine the horizontal positions (x_2 and x_4) of the fragment by the time difference of the signals arriving at the two photo-multipliers (PM), mounted at the left-hand and at the right-hand side.

The signals coming from the photo-multipliers were treated with a constant-fraction-discriminator (CFD) and then used as the start and stop of a time-to-amplitude-converter (TAC). Walk effects, i.e. systematic variations of the time-difference signals on the pulse height, were found to be negligible. The CFD had a threshold of about 10 mV. With the chosen amplification, this limit imposed also a lower limit on the nuclear charge of the ions to be measured from the far end of the detector of about Z = 7. Therefore the identification of fragments was limited to $Z \geq 7$. The analog output of the TAC was then read by an analog-to-digital-converter (ADC).

The same signals were also used to measure the time-of-flight of the fragment, according to the scheme illustrated in figure 1.4. The time-of-flight is the difference of the times at which the ion passes through SCI4 (at the time T_4) and through SCI2 (at the time T_2). The delay, T_0, was chosen in such a way that $T_2 + T_0 > T_4$. The influence of the light propagation inside the scintillator plates was eliminated by averaging the time differences between the left and the right signals. Thus, the measured time-of-flight, ToF^*, was taken from the average of the right and left signals, ToF_R^* and ToF_L^*, opportunely transformed from channel to seconds through the calibration factors α_R and α_L, obtained with a pulse generator:

$$ToF^* = \frac{ToF_L^* \cdot \alpha_L + ToF_R^* \cdot \alpha_R}{2} = T_2 + T_0 - T_4 \qquad (1.4)$$

The *real* time of flight, *ToF*, is:

$$ToF = \frac{s_0}{\upsilon} = T_4 - T_2 \tag{1.5}$$

with s_0, flight-path, and υ, velocity, of the ion. Therefore, the time-of-flight is:

$$ToF = T_0 - ToF^* = T_0 - \frac{ToF_L^* \cdot \alpha_L + ToF_R^* \cdot \alpha_R}{2} \tag{1.6}$$

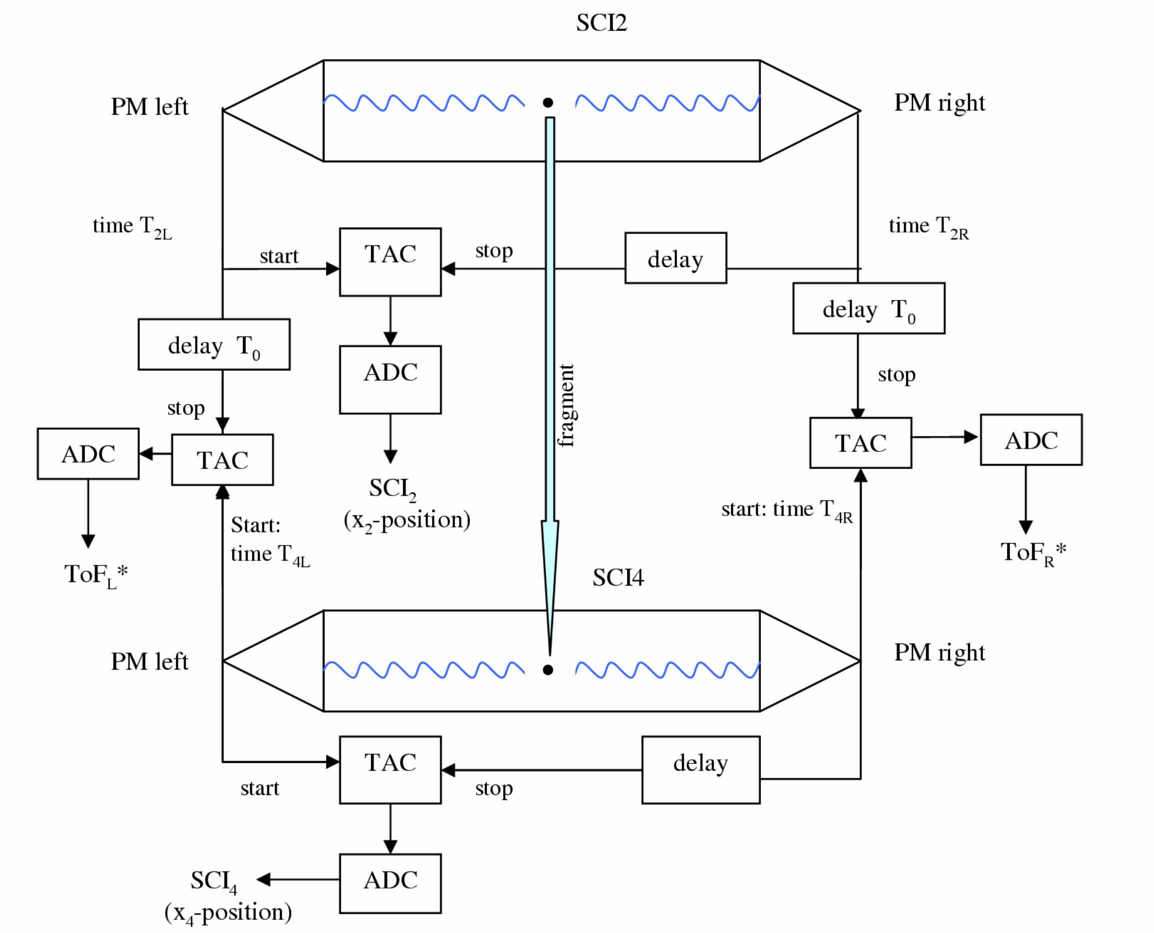

Figure 1.4: Schematic diagram of the usage of the two scintillators for the measurements of the x-positions at S2 and at S4 and of the time-of-flight of the fragment. All photomultipliers (PM) signals pass by constant-fraction discriminators to impose a lower

threshold and to eliminate the pulse-height dependence of the timing signal. They are not shown in this figure. The four ADC signals are recorded.

So the time-of-flight was given by the measure of ToF_R^* and ToF_L^*, and by the delay T_0.

SCI2 and SCI4 are made of a fast plastic scintillator (Bicron BC420), characterised by a high efficiency in the production of light and by a time-response of ~ 1.5 ns. The sensitive area is 218 mm × 80 mm for SCI2 and 200 mm × 80 mm for SCI4. Their thickness is 5 mm. The light signals were read by fast photomultipliers (Hamamatsu HM2431). The effective speed of light inside the scintillator is about c_{scint} = 20 cm/ns. Thus, a shift of Δx = 4 mm – which corresponds to the position resolution (FWHM) of these detectors measured for heavy ions (one can deduce the position resolution from the smoothing of the borders in the position spectrum of x_2) – is equivalent to a time resolution of Δt = 40 ps (FWHM) [Vos95] [Schw98] (please note that $\Delta t = 2 \cdot \Delta x / c_{scint}$). Thus, the time resolution of these detectors is extremely good.

The calibration of positions and of time-of-flight signals will be discussed in the next chapter.

1.7.3 The ionisation chambers

Two identical ionisation chambers were placed at the final image plane, one after the other to measure the electric charge and the drift time of the ionisation signals. These were used to identify the atomic number of the fragments, and to determine their angle in the horizontal plane.

The ionisation chambers used in the experiment are multi-sampling, that is they have four active anodes, as depicted in figure 1.5 [Pfu94]. When a fragment crosses the chamber, it excites and ionises some atoms of the gas and generates in such a way a cloud of electrons and ions. The electrons migrate to the anodes much faster (~ 5 cm/μs) than the ions to the cathode (~ 5 cm/ms), and induce a signal, whose amplitude is roughly proportional to the energy loss and thus (see equation 1.3) to the square of the charge of the fragment. In order to make the induced signal of the electrons independent of the presence of the positive ions and on the distance of the ion trajectory from the anodes, a metallic grid (Frisch grid) is placed close to the anodes, so that the latter feel the presence of the electrons only when the electrons have passed the grid. The drift-times of the electrons (< 5 μs) were measured as the time delay of the different anode signals with respect to the left signal of the plastic scintillator SCI4. The drift-time of the electrons towards the anodes tracks the path of the fragment in the horizontal plane and was used to reconstruct the effective flight-path of the fragment. With two measurements at two anodes on a distance of 80 cm in beam direction and a resolution of a few hundred μm, the horizontal angle was determined with a resolution of about 1 mrad. The vertical angle was not measured, since its influence on the flight path is much weaker and thus its influence on the mass resolution is not crucial.

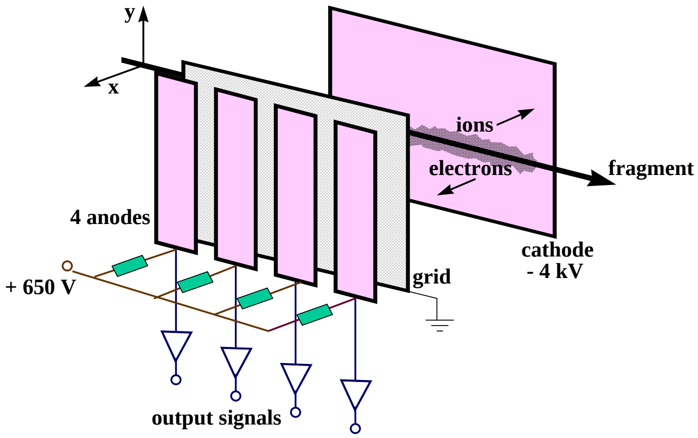

Figure 1.5: Schematic drawing of the MUlti-Sampling Ionisation Chamber, MUSIC, used in the experiment.

The sensitive part of the ionisation chamber is 400 mm in *z* direction and 276×150 mm^2 in *x* and *y* directions. The windows are made of kapton (25 μm), covered by aluminium (40 $\mu g/cm^2$). The chamber is filled with P10 gas (90% argon and 10% methane) at atmospheric pressure and room temperature. The electric field inside the chamber is generated by the voltages applied at the electrodes. Two supplementary anodes, placed at the edges (not represented in the figure) are used to avoid border effects. The output signals are connected to amplifiers and then to an ADC to get the Z from the amplitude, and, after passage of a constant-fraction discriminator, to a TDC to record the value of the drift-time.

1.7.4 The multiwire proportional chambers

A set of multiwire proportional chambers was used to centre the primary beam along the FRS. This measurement served to calibrate the Hall probes with the known magnetic rigidity of the beam. This calibration was indispensable in order to ensure well defined ion-optical conditions during the experiment. The multiwire chambers were placed along the beam line, in the image planes between dipoles. During the measurements of the reaction products, the multiwires along the beam line were not inserted, in order not to spoil the energy and mass resolution. Only the multiwire detectors at the end of the beam line were permanently operating. In spite of their limited detection probability, their stable position information, obtained with a resolution of about 1 mm [Ste91, Stel91], was used to correct the position information of the scintillator and the MUSIC for some long-term instabilities e.g. due to the sensitivity of those detectors to temperature fluctuations.

The multiwire detectors are equipped with four sets of wires in parallel planes. The first plane (cathode) is connected to a negative voltage (up to -4kV). The other three planes are far from the cathode and close to each other. The central plane (anode) is at 0V. The x plane has vertical parallel wires, the y plane has horizontal parallel wires. The cathode and anode wires are mounted in diagonal direction. The distance among the wires is 2 mm for anode and cathode, and 1 mm for the x and y planes. The diameter of the wires is 20 μm for anode and cathode, and 50 μm for the x and y planes. In the x plane (and as well in the y plane), the ends of the wires are connected among each other through 20 ns delay lines. The last wires at both ends are connected to amplifiers and read out. These two signals are called x_{right} and x_{left} (in the y plane: y_{up} and y_{down}). The whole collection is housed in a container filled with a counting gas (90 %Ar, 10% CO_2, and a small mixture of alcohol) at atmospheric pressure. The anode is connected to the start of a TDC and x_{right}, x_{left}, y_{up} and y_{down} to four stops of the TDC.

A fragment passing through the MW leaves a trail of ionised gas particles behind. Under the influence of the electric field, the electrons start to drift towards the closest wire of the anode. Due to the gas amplification in the cylindrical electric field around the anode, a signal is induced on the closest wires of the x plane and the y plane. Due to the delay-line read out, the stop signals of the TDC are delayed with respect to the anode signal. The sum of the delays of the right (up) and left (down) signals is expected to be constant, and it is used to discriminate good events from multi-hit events. The difference of these time delays give the x or y position of the fragment.

Chapter 2
The data analysis

2.1 The method

The data analysis can be described schematically as follows:

1) Identification of the fragments
   One by one, the data of every setting[1] were independently analysed and the nuclides were identified in mass, *A*, and atomic number, *Z*, on the basis of magnetic rigidity, time-of-flight and energy loss, measured in the second stage of the fragment separator.
2) Derivation of the velocity from magnetic rigidity
   The data of every setting were analysed again. Thanks to the previous identification, the mass, *A*, and atomic number, *Z*, of the fragments were known. Their values were fixed to integer numbers, and the velocity distribution of every nuclide was determined on the basis of the magnetic rigidity, measured in the first stage of the fragment separator. Actually, only "pieces" of the whole velocity distribution of a given nuclide are obtained since only a limited range in magnetic rigidity can be observed in one setting.
3) Normalisation of the yields
   Setting by setting, the velocity distributions of every nuclide were normalised to the beam intensity and corrected for dead-time losses of the data acquisition.
4) Reconstruction of the velocity distributions
   All the settings were combined, and the experimental velocity distribution of every nuclide was constructed. The settings with the hydrogen target covered the magnetic-rigidity range almost completely. Only every second of these settings were repeated with the titanium target, thus there were gaps between the pieces coming from the different measurements. To reconstruct the whole velocity distributions, the different components due to the different reaction mechanisms were identified, represented by analytical functions, and fitted. The result of the fit gave the completed velocity distribution for every nuclide. In the case of the hydrogen target, the contribution of the titanium windows was subtracted.
5) Evaluation of the formation cross sections
   From the result of the fit, the production cross-sections of the fragments were evaluated. Corrections for the angular transmission of the FRS and for losses in layers of matter along the beam line were performed.

In the following sections, we will go carefully through the above-mentioned procedure and describe the methods used in the data analysis.

2.2 The identification of the fragments

To identify the residual fragments means to determine their atomic number *Z* and their mass number *A*. The most important measured quantities to accomplish this goal are the time-of-flight

---

[1] With the word "setting" we mean a measurement performed setting certain values of the magnetic fields in the dipoles, in order to select the acceptance of fragments in a certain range of magnetic rigidities.

between the intermediate and the final image planes of the fragment separator, the horizontal positions at these two image planes as well as the energy loss of the fragments in the ionisation chambers. The following sections list the basic relations and document in detail, how these quantities were exploited to achieve the nuclide identification. In addition, several corrections are described which were applied to obtain optimum resolution.

2.2.1 The determination of the A/Z ratio

Since the ions passing through the FRS were completely stripped (see section 1.5), according to equation (1.1) one can formulate:

$$\frac{A}{Z} = \frac{\mathrm{e}}{\mathrm{u}} \frac{B\rho}{\beta_{TOF}\gamma_{TOF}\,\mathrm{c}} \qquad (2.1)$$

where A is the mass number, Z is the atomic number, B is the magnetic field inside the magnet, ρ is the radius of the trajectory, u is the atomic mass unit, -e is the electron charge, $\gamma_{TOF} = 1\big/\sqrt{1-\beta_{TOF}^2}$ with $\beta_{TOF} = \upsilon_{TOF}/\mathrm{c}$, where υ_{TOF} is the velocity of the ion and c is the velocity of the light.

To get the *A/Z*-ratio of a fragment, it is then enough to measure its magnetic rigidity, $B\rho$, and its velocity, υ_{TOF}. Since the velocity was measured in the second half of the spectrometer, also the magnetic rigidity should be measured in the same section.

The magnetic rigidity of the fragment along the FRS can be obtained from the measurements of the magnetic fields and of the radii of the ion trajectory in the dipoles, deduced from the horizontal position at the image planes. For an ion moving on the central trajectory, the magnetic rigidity $(B\rho)_0$ is simply given by the value of the magnetic field, measured with the Hall probes, multiplied by the value of the radius of the dipoles. The magnetic rigidity of fragments moving on other trajectories differs from $(B\rho)_0$ by a quantity that is proportional to the deviation of the x position from the centre. According to equation 1.2, at the intermediate image plane we have[1]:

$$\Delta(B\rho)_A = (B\rho)_A - (B\rho)_{A0} \qquad \Delta x_2 = x_2 - x_{20} \quad \text{with} \quad x_{20} = 0 \qquad D_2 = \frac{\Delta x_2}{\Delta(B\rho)_A/(B\rho)_{A0}}$$

$$\Rightarrow \quad \frac{\Delta(B\rho)_A}{(B\rho)_{A0}} = \frac{x_2}{D_2} \qquad \Rightarrow \qquad (B\rho)_A = (B\rho)_{A0}\cdot\left(1+\frac{x_2}{D_2}\right) \qquad (2.2)$$

where D_2 is the dispersion of the first section of the FRS. The magnetic rigidity of the fragment in the second section of the FRS, $(B\rho)_B$, differs form $(B\rho)_A$ by the quantity $\Delta(B\rho)_{AB}$ that depends on the loss of energy in the scintillator:

$$\Delta(B\rho)_{AB} = (B\rho)_A - (B\rho)_B \qquad \Rightarrow \qquad (B\rho)_B = (B\rho)_{A0}\cdot\left(1+\frac{x_2}{D_2}\right) - \Delta(B\rho)_{AB} \qquad (2.3)$$

With the program AMADEUS [AMA] it was possible to calculate the reduction in magnetic rigidity $\Delta(B\rho)_{AB}$. In table 2.1 some results are reported as an example. The results show that the change in magnetic rigidity of the fragments is very small. The relative error that we would make by neglecting the contribute of $\Delta(B\rho)_{AB}$ is of the order of a few per mille. Such an error does not affect at all the mass identification. Therefore, we decided to set $\Delta(B\rho)_{AB} = 0$ in equation 2.3.

---

[1] Label "0" refers to central trajectory, label "A" to the 1st section of the FRS, label "B" to the 2nd section of the FRS, labels "1", "2", "3" and "4", to the 1st, 2nd, 3rd and 4th dipoles and to the 1st, 2nd, 3rd and 4th image planes – named S1, S2, S3 and S4 – respectively, as defined in figure 2.3.

Z	A	$(B\rho)_A$ (Tm)	$(B\rho)_B$ (Tm)	$\Delta(B\rho)_{AB}$ (Tm)	$\Delta(B\rho)_{AB}/(B\rho)_B$
35	79	12.6620	12.5174	0.1446	0.011
25	55	12.3666	12.2653	0.1013	0.008
15	31	11.6329	11.5734	0.0595	0.005
5	10	11.2805	11.2611	0.0194	0.002

Table 2.1: Reduction of the magnetic rigidity due to the energy loss in the scintillator SCI2.

The signal SCI_2, deduced from the scintillator placed at S2, was transformed into position values by a linear calibration:

$$x_2(mm) = b_2 - a_2 \cdot SCI_2(channel) \qquad (2.4)$$

So, according to equations 2.3 and 2.4, the magnetic rigidity entering into equation 2.1 is given by the measured quantities B_1, B_2 and SCI_2, once the parameters ρ_1, ρ_2, a_2, b_2 are determined with the calibrations. D_2 was obtained with an ion-optical calculation.

$\beta_{TOF}\gamma_{TOF}c$ was obtained by measuring the velocity of the fragment in the second half of the FRS. The velocity is the ratio of the flight-path s to the time-of-flight ToF:

$$\upsilon_{TOF} = \frac{s}{ToF} = \frac{s_0 \cdot (1 + c_\alpha \alpha_x) + \Delta s}{T_0 - ToF^*} \quad \text{with} \quad \begin{cases} \Delta s = d_1 x_2 + d_2 x_2^2 \\ ToF^* = \dfrac{ToF_L^* \cdot \alpha_L + ToF_R^* \cdot \alpha_R}{2} \end{cases} \qquad (2.5)$$

where ToF is the time-of-flight, as defined in section 2.6.2, and s is the flight path.

s_0 is the distance between the two scintillation detectors along the central trajectory. The flight path s can differ from s_0 for two reasons. One is that the fragments acquire a transversal momentum in the nuclear reaction in the target or due to angular straggling inside the scintillator at S2, and consequently they enter the second section of the FRS with different angles. The other is that fragments with different magnetic rigidities enter the second section at different x_2-positions and trace different paths along the FRS. Although the real path inside the FRS depends on the detailed ion-optic properties of the spectrometer, its dependence on the horizontal angle at the exit of the FRS, α_x, can be considered linear in good approximation. In equation 2.5, the nominal flight path s_0 was corrected for the dependence on the angle α_x, which was measured from two drift-time signals of the two MUSICs. The dependence on $B\rho$, is equivalent to a dependence on the x_2 position. This correction introduces a linear and a quadratic term in x_2. A more detailed explanation of these corrections can be found in Appendix A.

The ToF, measured with the scintillator responses, ToF_R^* and ToF_L^*, was calculated according to equation 1.6.

Once the values of the calibration parameters $s_0, c_\alpha, d_1, d_2, T_0, \alpha_L, \alpha_R$, were known and x_2, α_x, ToF_R^*, ToF_L^* were measured, the velocity was determined. Please note that the value of the velocity obtained in this way is used only in equation 2.1 with the purpose of mass identification. Absolute and more precise values of the velocity were obtained afterwards by the measurement of the fragment magnetic rigidity with a method which will be described in section 2.3.

A correct identification of the fragments relies on the correct determination of the calibration parameters ρ_1, ρ_2, a_2, b_2, s_0, c_α, d_1, d_2, T_0, α_L, α_R. These parameters were determined either with dedicated measurements with a pulse generator or with the primary beam, or exploiting the totality of the recorded data that, due to integer numbers of the mass, *A*, and charge, *Z*, of the fragments, form a characteristic pattern. The latter method, described in appendix A, is a very sensitive tool to determine the parameters in an accurate way.

2.2.2 The determination of the atomic charge Z

The determination of the atomic number, *Z*, of the fragments is done in two steps: First, the influence of velocity and position of the ions on the ΔE signal, measured with the MUSIC ionisation chamber, is eliminated; secondly, the biunique correspondence between the peaks in ΔE and the charge *Z* is established.

According to the Bethe theory, the energy loss of the fragment in the gas of the ionisation chamber is proportional to its charge squared and inversely proportional to its velocity squared[1]:

$$\Delta E_{theory} = f(Z,\upsilon) \propto \frac{Z^2}{\upsilon^2} \mathrm{L}(\upsilon, Z) \cong \frac{Z^2}{f(\upsilon)} \tag{2.6}$$

In practice, the measured pulse height of the MUSIC signals depended on additional factors, such as the distance of the ions from the anode, i.e. the x_4 position, due to a recombination effect, leading to a loss of free electrons in the gas, and the density of the gas in the IC, which was observed to vary with the time at which ΔE was measured:

$$\Delta E_{measured} = f(Z,\upsilon,x_4,t) \propto Z^2 \cdot \frac{p(t)\cdot g(x_4)}{f(\upsilon)} \tag{2.7}$$

From the previous relation we get:

$$Z^2 \propto \Delta E_{correct} = \Delta E_{measured} \cdot \frac{f(\upsilon)}{p(t)\cdot g(x_4)} \tag{2.8}$$

So, to determine the charge, the dependence on the velocity ($f(\upsilon)$), the dependence on the position at S4 ($g(x_4)$) and the dependence on the density of the gas ($p(t)$) had to be removed.

The function $f(\upsilon)$ was built up by means of a theoretical calculation. The energy loss of a sample of ions in 63.22 mg/cm² of argon (the quantity of gas in the ionisation chamber) was calculated with the program AMADEUS [AMA], and the function $f(\upsilon) \propto \Delta E_{theory}^{300MeV} / \Delta E_{theory}$ constructed. The energy loss of the selected ions at 300 MeV, $\Delta E_{theory}^{300MeV}$, was used arbitrarily as a reference. In this way, the function $f(\upsilon)$ does not depend on the ion. The velocity was deduced from the time-of-flight (equation 2.5). Although the variation of the energy loss due to its velocity dependence for the ions passing in one setting is only about 1.3 %, and thus this correction does not improve the *Z* resolution very much, it is important to obtain a consistent Z

---

[1] In the function *L* (called *stopping number*) the dependence on υ is perceptible while that one on *Z* can be neglected. The numerical calculations performed in this work are based on ref. [S. P. Ahlen, Rev. Mod. Phys. 52 (1980) 121] which includes among others also relativistic effects.

calibration of the data from different settings, in particular for the light ions studied in this work with their broad velocity distributions.

The recombination of the electrons in the gas of the ionisation chamber causes an exponential dependence on the distance of the fragment from the anodes, i.e. on x_4. By analysing the raw ΔE data for a given element as a function of x_4, the value of the attenuation coefficient $\lambda = 5 \cdot 10^{-4}$ mm^{-1} was obtained. This corresponds to a variation of the raw data by about 10% over 200 mm. Thus, this correction considerably improves the Z resolution.

Finally, the variation of the position of the ΔE peaks with the time of measurement was determined. Since the shift of the peaks from one measurement to the next was small compared to the distance of the ΔE peaks, the corresponding peaks in the ΔE spectra of the different measurements, after correction for velocity and position dependence, could easily be identified, and the time-dependent variation in amplitude was determined. The amplitude of this variation was found to be in the order of a few percent, consistent with the expected variations of atmospheric pressure and temperature in the experimental cave. The final resolution in ΔE after these corrections can be seen from figure 2.1, where the ΔE spectra of all the settings were summed up.

The next step was to associate a charge number Z to every peak of figure 2.1. As we saw, the measurement of the A/Z ratio is essentially independent from the measurement of the charge Z. An absolute Z calibration by means of the A/Z ratio could be obtained exploiting the two-dimensional spectrum A/Z vs. $\sqrt{\Delta E}$ (see figure 2.2, left). The calibration of the ΔE should provide the A/Z-path plotted in figure 2.2 (right). The inverse of the length of the generic horizontal line of figure 2.2 (right), which represents the distance between two close isotopes, is represented by the following variable:

$$P = \frac{1}{((A+1)/Z) - (A/Z)} = Z \tag{2.9}$$

which directly gives the atomic number Z. Figure 2.3 shows the calculated variable P, obtained by the difference between isotopes with $N=Z+1$ and $N=Z$ (left) and with $N=Z+2$ and $N=Z+1$ (right). The figure shows that the first peak corresponds to charge $Z=5$, i.e. Z = *peak-number* + *4*.

A parabolic fit of the peak positions in figure 2.1, now identified in atomic number Z, gives the following calibration as a function of peak number x and atomic number Z, respectively:

$$\Delta E = a_0 + a_1 \cdot x + a_2 \cdot x^2 \quad \Rightarrow \quad Z = \frac{-a_1 \pm \sqrt{a_1^2 - 4a_2(a_0 - \Delta E)}}{2a_2} + 4 \tag{2.10}$$

In the figures 2.4 and 2.5, the calibrated Z spectrum and the two-dimensional presentation of Z versus A/Z, respectively, are presented[1]. A Z resolution of ΔZ=0.4 (FWHM) was obtained. The identification in A was then possible thanks to the pattern of nuclei with N=Z, which fall on a vertical line with constant A/Z = 2 (see figure 2.2). The next curved pattern on the left corresponds to the nuclei with $N=Z+1$, and so on.

---

[1] The Z spectrum does not represent a charge distribution because the settings were summed up without a previous normalisation and without a correction for the transmission.

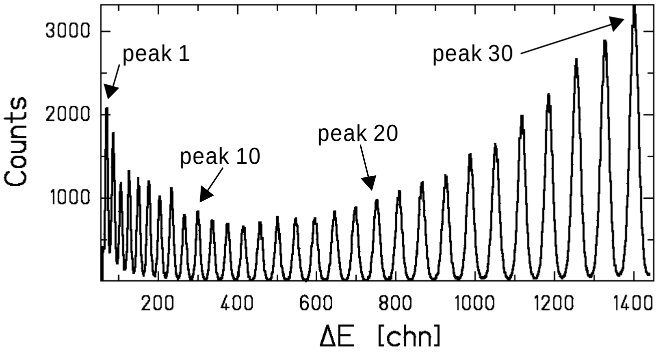

Figure 2.1: Sum of all the ΔE spectra of every setting. With all the corrections applied, individual elements are resolved. The peak numbers denote the peaks above the experimental threshold. At this stage of the analysis, the corresponding Z values are not yet known.

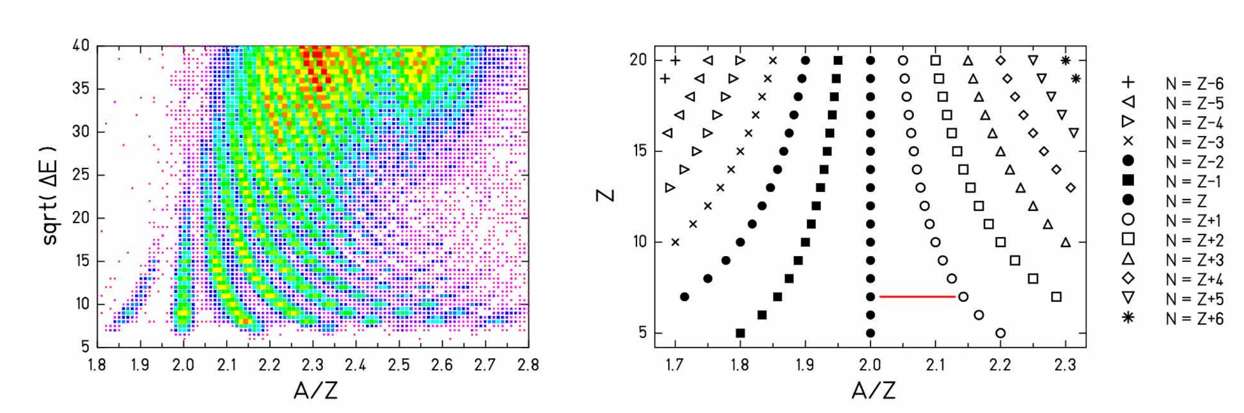

Figure 2.2: Left: experimental two-dimensional spectrum $\sqrt{\Delta E}$ versus A/Z. Right: Exact path Z versus A/Z. The difference in A/Z of neighbouring isotopes is 1/Z. As an example, the length of the line gives the difference in A/Z of two neighbouring isotopes of Z = 7.

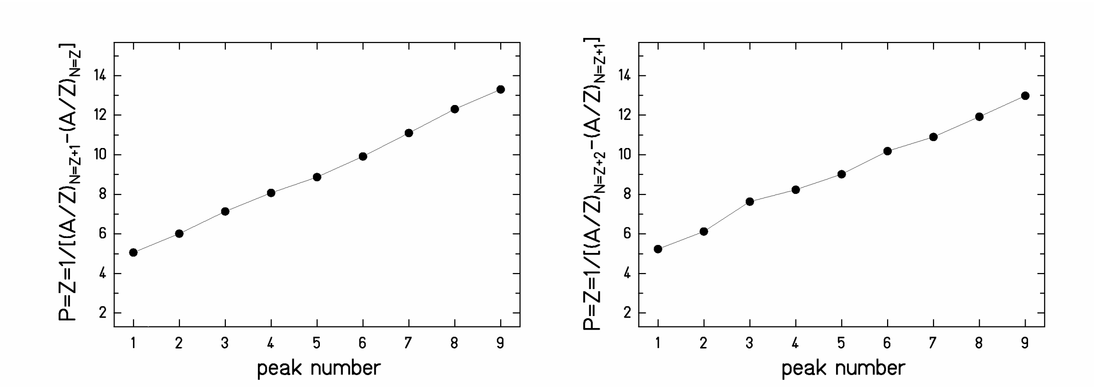

Figure 2.3: Plots of the variable P (see equation 2.9) vs. peak number. P was determined from the difference of the A/Z of isotopes with N=Z+1 and N=Z (left) and isotopes with N=Z+2 and N=Z+1 (right). Both results show that the first peak corresponds to P = Z = 5.

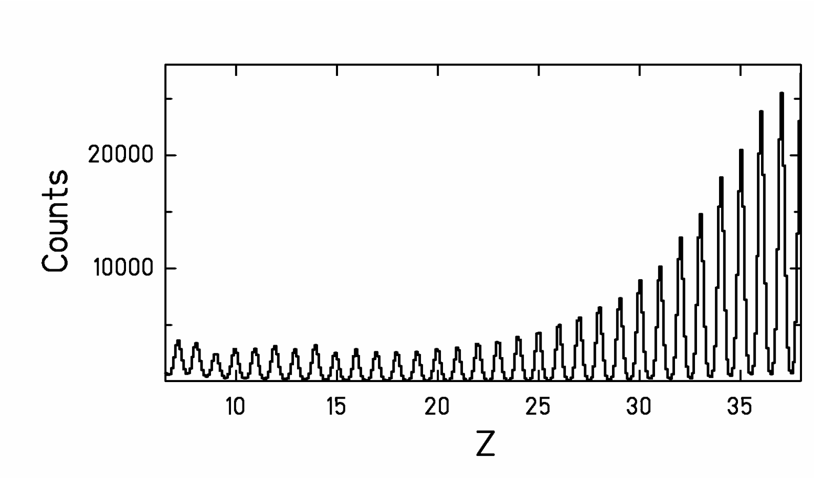

Figure 2.4: Sum of all the Z spectra of every setting. The resolution ΔZ≅ 0.4 (FWHM) is approximately constant along all the spectrum.

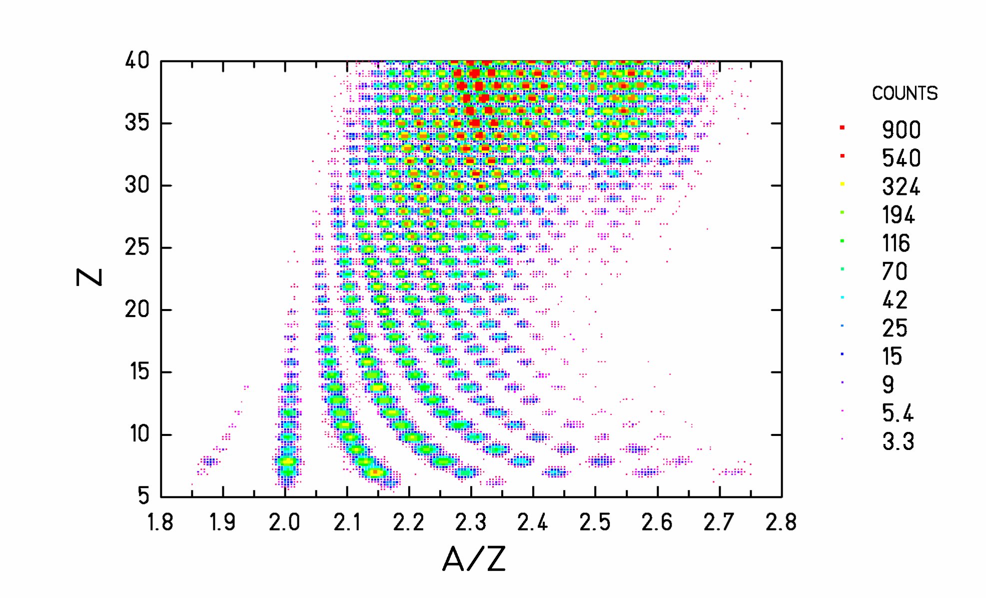

Figure 2.5: Cluster plot of Z vs. A/Z, containing all the data of all the settings. In contrast to the left part of figure 2.2, the ordinate is now calibrated in atomic number Z according to equation (2.10).

2.3 Derivation of velocities from magnetic rigidities

Having identified the produced nuclides, it was possible to select the events belonging to a certain fragment, and to associate them to the corresponding *A* and *Z* numbers of the fragment. In this way equation 1.1 could be exploited to calculate the velocity:

$$\beta\gamma = \frac{\mathrm{e}}{\mathrm{uc}} \frac{(B\rho)_A}{A/Z} \quad \Rightarrow \quad \beta\gamma = \frac{\mathrm{e}}{\mathrm{uc}} \frac{(B\rho)_{A0} \cdot \left(1 + \frac{x_2}{D_2}\right)}{A/Z} \qquad (2.11)$$

In these equations, A and Z are exact numbers[1]. Only $(B\rho)_A$ introduces an error on the velocity. The values of $(B\rho)_{A0}$ of the ions on the central trajectory for the different settings were obtained by scaling the magnetic rigidity of the primary beam with the field strengths of the dipoles, measured with the Hall probes with a precision of about 10^{-4}. The relative uncertainty on the values of $\beta\gamma$ corresponds to that one on the magnetic rigidity $(B\rho)_A$, which is about $6\cdot10^{-4}$, corresponding to a position resolution of 4 mm for single ions. The delicate point is thus the determination of the values of the parameters a_2, b_2 (see eq. 2.4) and D_2. The value of D_2 was established by a calibration measurement using the beam[2], which is consistent with an ion-optical calculation to be 6.8 cm/%. The parameters a_2 and b_2 were determined with the x-position calibration of the scintillator. The calibration was performed by relating the cut-off in the counting rate in the position spectrum (see figure 2.6) to the borders of the detector, which are situated at ±10.9 cm. Supposing that the position response is linear [Vos95], these two points were sufficient to establish a position calibration, according to equation 2.4. The position calibration can be affected by the radiation damage of the scintillator, which reduces the effective speed of light inside the scintillation material [Böc98]. But we had no indication for such an effect in the present experiment. The whole spectrum was found to be slightly shifted from setting to setting, probably due to the sensitivity of the photomultipliers to the temperature in the cave. For this reason, the calibration was performed for every setting individually. It is important to point out that a wrong position calibration leads to wrong values of the magnetic rigidity $(B\rho)_A$. These could lead first to a wrong identification and afterwards to a wrong evaluation of the velocity distributions and of the cross sections. A correct position calibration is thus of extreme importance. But also a wrong value of the dispersion D_2 has similar effects for non-central trajectories. However, the method, described in appendix A, based on the characteristic pattern formed by the mass and charge of the totality of the observed fragments, assures the x_2/D_2-ratio, and thus the velocity, to be correct within the indicated uncertainties.

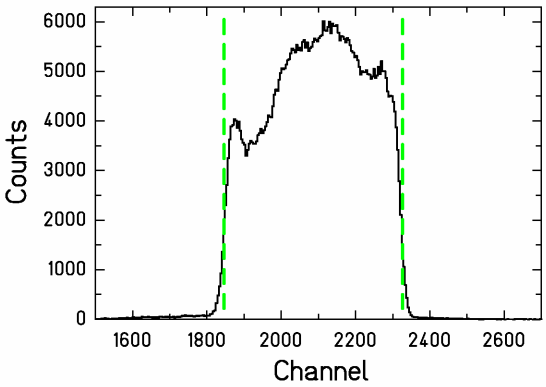

Figure 2.6: Raw data from the scintillator responses used for the position calibration. The channels of the borders of the distribution correspond to extremes of the sensitive range of the scintillator, i.e. to -109 mm and to +109 mm.

---

[1] Equation 2.1 was calculated considering the mass of the fragment equal to Au, where A is the mass number and u is the average rest mass of a nucleon. This approximation on the mass value is acceptable when the formula is used for the identification of the fragments. In the case of the evaluation of the velocity, a more accurate calculation of the mass, which includes the binding energy, is applied.

[2] A devoted measurement showed that for a given energy the dispersion is constant with the x-positions at the intermediate image plane.

A ^{238}U ion exits from the synchrotron with an energy per nucleon of 1 GeV, corresponding to a velocity $\upsilon_{beam-init}$ = 26.2625 cm/ns. The energy in the synchrotron, measured by determining the revolution frequency, is taken as a reference in this work. The velocity of the reaction products, deduced from the measured $(B\rho)_A$ value differs from the beam velocity due to three contributions:

- The energy loss of the beam. Before the nuclear reaction occurs, it transverses some layers and part of the target and reduces its energy because of Coulomb interactions with the electrons of these materials. So at the moment of the reaction the velocity of the beam is $\upsilon_{beam-react} < \upsilon_{beam-init}$.
- The nuclear reaction itself reduces or increases[1] the velocity of the fragment originated from the uranium breaking off: $\upsilon_{frag-react} \neq \upsilon_{beam-react}$
- After its creation, the fragment has to transverse part of the target, depositing in it some energy and reducing consequently its velocity: $\upsilon_{frag-final} < \upsilon_{frag-react}$

The velocity of the fragment in the beam reference frame (where $\upsilon_{beam-react} = 0$) was given by the difference between the velocity of the beam at the moment of the reaction and the measured velocity of the fragment, increased by the contribution due to its energy loss in the target (see figure 2.7): $\upsilon_{frag} = \upsilon_{beam-react} - \upsilon_{frag-react}$

It is assumed that the reaction occurs *on the average* in the middle of the target. This approximation is justified by the fact that the reaction cross section does not vary appreciably with the small variation of energy that the beam can experience. Also the small effect of the attenuation of the beam in the target was neglected.

The target thickness or, equivalently, the energy loss of the beam due to the layers of matter and to the target, was obtained by a previous calibration performed by measuring the reduced magnetic rigidity of the beam. With this method, we got that, as far as the energy loss is concerned, the thickness (in aluminium-equivalent units) is:

Full target (H_2 + titanium windows): 271 mg/cm^2
Titanium dummy target: 42 mg/cm^2
SEETRAM (beam monitor): 8.9 mg/cm^2

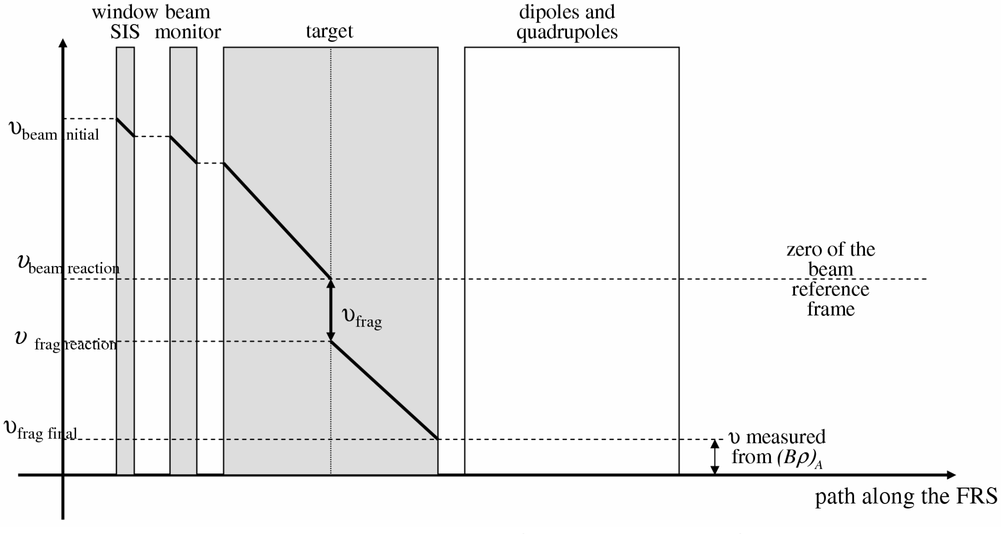

Figure 2.7: Schematic diagram (not to scale) of the variation of the beam velocity (before the reaction) and of the fragment velocity (after the reaction) as a function of their path along the layers of the FRS. The variables are defined in the text. As an example, the reaction is assumed to take place in the center of the target.

---

[1] What is actually observed is the longitudinal component of the velocity of residues produced at about zero degrees. So the decrease, or increase, refers to the component of the velocity along the beam axis.

Considering the uncertainties in the x_2 calibration (about $\Delta x_2 \cong 0.2$ cm) and in the thicknesses of layers in front of the FRS, the relative uncertainty of the deduced mean change of $\beta\gamma$ in the nuclear reaction amounts to $3 \cdot 10^{-4}$. Finally, the Lorentz transformation was applied in order to determine the velocity of the fragments in the reference frame of the beam in the centre of the target, denoted by υ_{frag} in figure 2.7. In the following, if not explicitly said, we will present the results concerning the velocity of the fragments in the beam reference frame (where $\upsilon_{238U} = 0$) .

2.4 Normalisation of the yields

In order to compare the spectra of different settings, the data had to be normalised to the number of beam-monitor counts and corrected for dead-time losses of the data acquisition.

In every setting, the number of beam projectiles, given by the beam monitor, N_P, the counting rate, N, and the efficiency of the data acquisition system due to dead-time losses, ε_τ were recorded. To obtain the production rate, R, the counting rate had to be normalised to N_P and corrected for the reduction due to the dead time:

$$R = \frac{N}{N_P \cdot \varepsilon_\tau} \tag{2.12}$$

In the normalization factor, $N_P \cdot \varepsilon_\tau$, the parameter N_P includes the conversion of the beam monitor (SEETRAM) counts into the number of ^{238}U ions. Since the SEETRAM current is proportional to the intensity of the beam, the conversion is represented by a multiplicative factor. The calibration, performed with an ionisation chamber, gave a calibration factor of 304 ^{238}U projectiles per second, for a monitor current of 10^{-14} A. Due to instabilities in the extraction of the beam from the synchrotron, which lead to saturation effects of the particle counting during the calibration of the SEETRAM, we estimated the uncertainty on the calibration to 7%.

2.5 Construction of the velocity distributions

In addition to the normalisation, all velocity spectra were corrected for the *variation* of the transmission with respect to the central trajectory, resulting from ion-optical calculations [Ben02]. This correction accounts for the variation of the effective angular acceptance of the fragment separator FRS as a function of the magnetic rigidity, as will be clarified in section 2.6.3.

Once all this was done, it was possible to merge together the data resulting from the different settings. In figure 2.8 the two-dimensional cluster plots of the velocity as a function of neutron number are presented for every second element. It can be noticed that in the case of the hydrogen target[1] the velocity spectra are almost continuously covered, while in the case of the titanium target gaps appear between the regions covered by the different settings[2]. In both targets, the setting corresponding to the magnetic rigidity of the primary beam could not be measured. Its position is marked by an inclined line in the cluster plots. Figures 2.9 and 2.10 give a closer look on the velocity distributions of the iron isotopes as one-dimensional spectra obtained with both targets. One can notice that the experimental velocity distributions of individual isotopes do not

---

[1] We recall that the hydrogen target is constituted by liquid hydrogen housed in a container with titanium windows.

[2] Each setting corresponds to a measurement, which – depending on the nuclide selected and on the beam intensity – can last between 15 minutes and 2 hours to have the required number of events. The limited number of settings was a constraint imposed by the limited beam-time available. Strategically, it was decided to reduce the settings of the system ^{238}U+Ti, because that was only a background experiment.

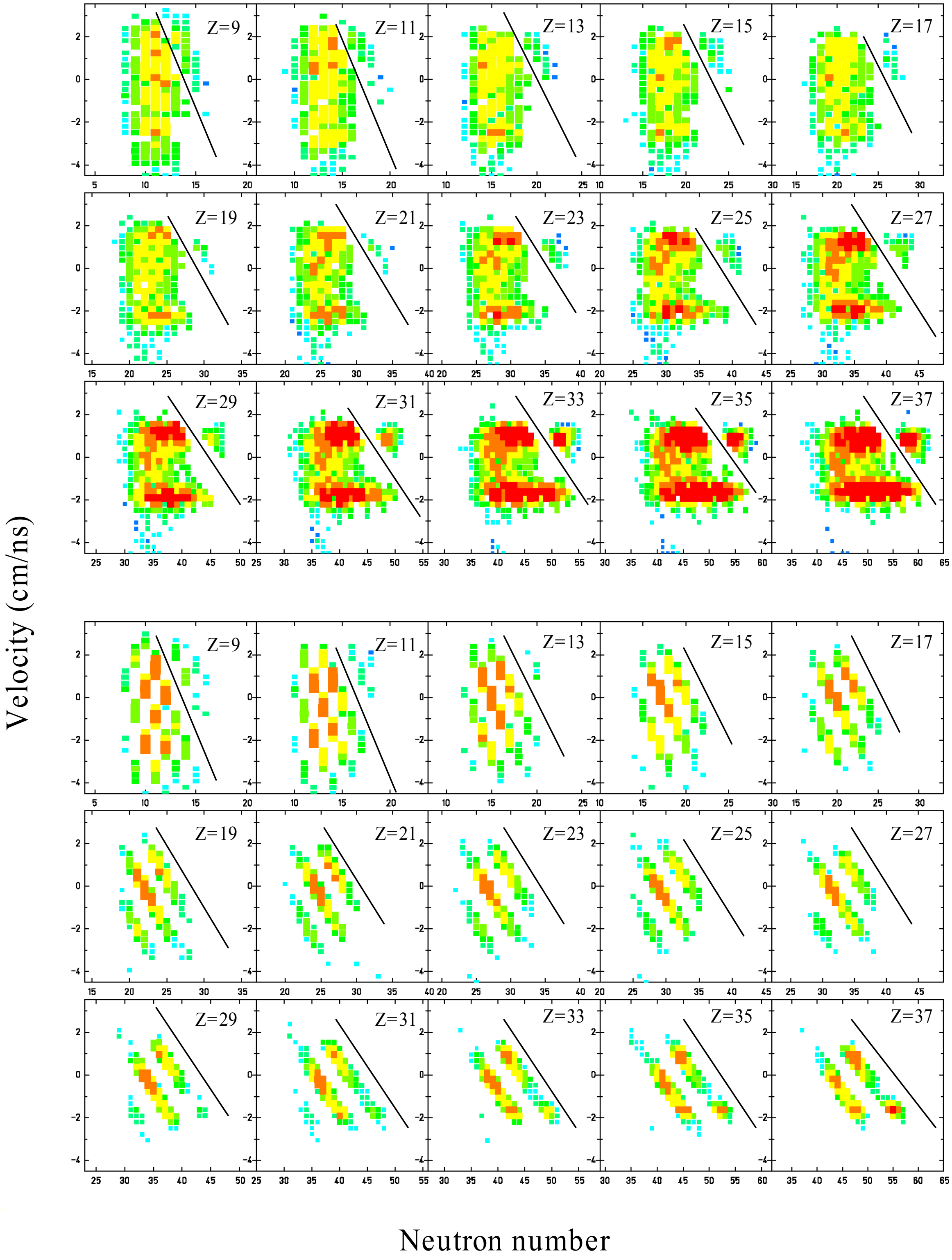

Figure 2.8: Two-dimensional cluster plots of the velocity distributions as a function of the neutron number for every second element produced in the interaction of the uranium beam with H_2 *+ Ti (up) and Ti alone (down). The velocity is presented in the beam frame (*$\upsilon_{238U} = 0$ *cm/ns). The full lines indicate the location of the setting that corresponds to the magnetic rigidity of the beam.*

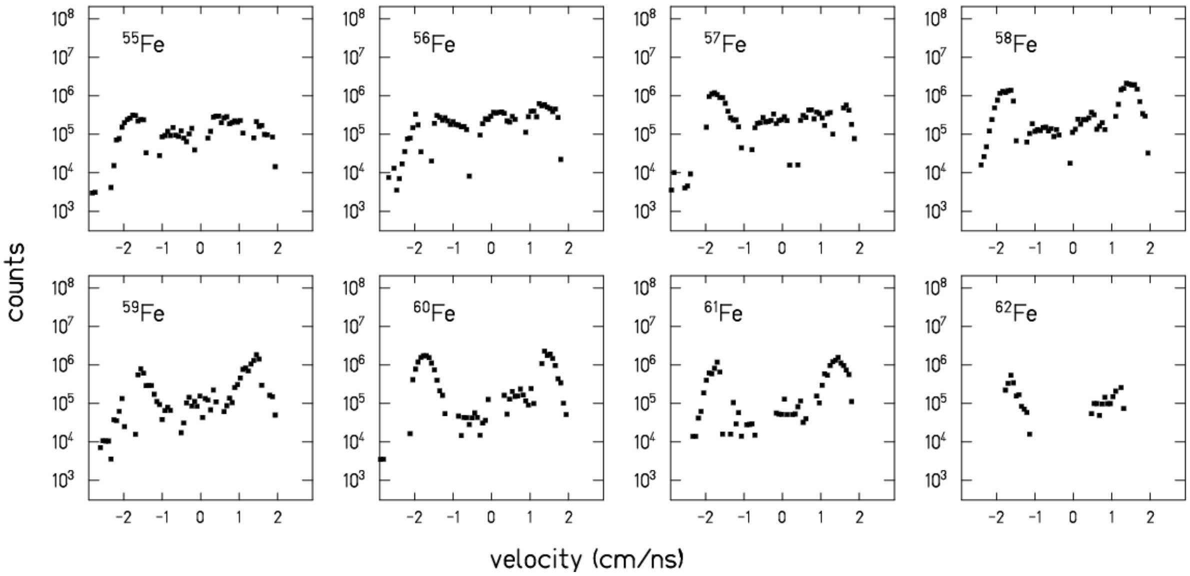

Figure 2.9: Experimental data of the velocity distributions of eight iron isotopes. The velocity is given in the frame of the beam. These isotopes were produced in the interaction of 1 GeV ^{238}U projectiles in the hydrogen target, including the titanium windows.

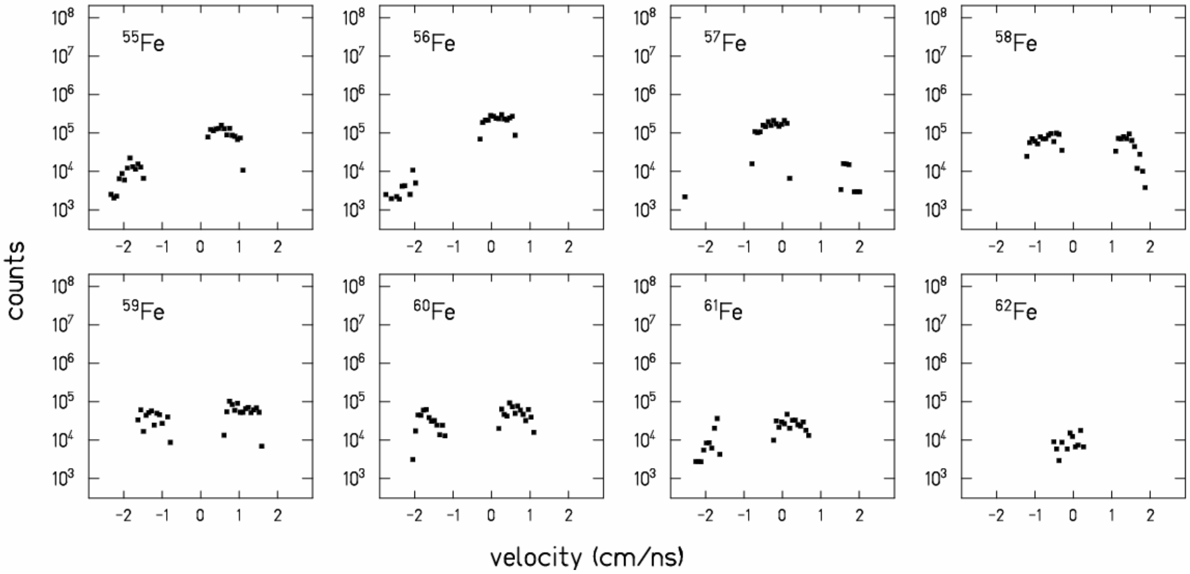

Figure 2.10: Experimental data of the velocity distributions of eight iron isotopes. The velocity is given in the frame of the beam. These isotopes were produced in the titanium target, representing the windows of the liquid-hydrogen target.

depict a full, continuous curve, but suffer of “holes”. The lack of data is not so severe in the case of the liquid hydrogen target (figure 2.9), while it can be noticed clearly in the case of the titanium target (figure 2.10).

As pointed out at the beginning of this chapter, it is from the velocity distributions that we obtain qualitative and quantitative knowledge both on the velocity of the fragments and on their production cross section. To extract this information from the data we proceeded in two steps:

1) we combined all the data of similar nature to extract the *global characteristics and tendencies*

2) we developed a dedicated fit procedure to extract *information on individual nuclides*.

In the following sub-sections we will go carefully through these two points.

2.5.1 Global characteristics and tendencies

Velocity patterns of the reaction mechanisms

Figures 2.8, 2.9 and 2.10 depict the longitudinal component of the velocity vectors of the different reaction products at about zero degree. To interpret these figures, it is necessary to point out how the kinematics of the reaction affects the velocity distributions and how this distribution is cut by the acceptance of the FRS. The discussion in this section is based on the ideas developed in ref. [Enq99] for the system ^{238}U + Pb and applied later also in other systems [Ben01, Enq01, Rej01, Ber03, Cas03, Tai03].

In figure 2.11-up a scheme of the velocities of a certain isotope produced via fragmentation and fission is presented in the beam frame. The velocity distribution of the fragmentation residues is represented in the beam frame by a three-dimensional Gaussian [Hüf85]. A Gaussian-like shape is the result of the statistical superposition of several momentum contributions in space, attributed to the momenta of abraded nucleons [Gol74] and to the recoil of evaporated particles. Also multifragmentation with some subsequent evaporation would produce a similar distribution. Due to the abrasion, the longitudinal mean value is expected to be negative with respect to the beam velocity [Abu76, Mor89]. When the fragment is produced in a fission event, the kinetic energy that it acquires is more or less fixed, assuming that the fissioning nuclei contributing to its production are situated in a quite limited range in *Z*, so the possible values of its velocity cover only the external shell of a large sphere [Wil76]. The centre of the sphere represents the mean velocity of the fissioning nucleus. In the beam frame it is slightly negative, because of the preceding abrasion process. The radius of this sphere results from the Coulomb repulsion between the fission fragments, and thus it is a measure of the charge of the complementary fragment. Please note that a similar pattern in velocity space would also result from any kind of reaction with one heavy remnant, as for instance evaporation of light charged particles or binary break-up reactions. Keeping this remark in mind, in the following, for simplicity, we will call the reaction products showing this kind of kinematical pattern “fission fragments”, but we will come back to a more general discussion in Chapter 4.

Now, because of the limited angular acceptance of the FRS (15 mrad around 0º), represented by a cone in the laboratory frame, only the part of the production inside the cone is transmitted through the FRS and can actually be observed. Projecting the transmitted events on the longitudinal axis (figure 2.11-down), we obtain the triple-humped distributions observed in figure 2.9. The limited angular acceptance of the FRS turns to be a useful tool to disentangle the different reaction mechanisms. The three humps of the velocity distributions of figure 2.9 can be interpreted as **fission** events going in **backward** direction (left peak), **fragmentation** events (central peak) and **fission** events going in **forward** direction (right peak). This interpretation is consistent also with the characteristics of the isotopic distributions that could be extrapolated from figure 2.8 (see for instance the distribution for Z=37): the two external humps (fission) are shifted to the right with respect to the central hump (fragmentation). This agrees with the theoretical expectations: in fission processes fragments with a high value of the A/Z-ratio are produced, while fragmentation generally produces isotopes on the neutron-deficient side of the beta-stability valley.

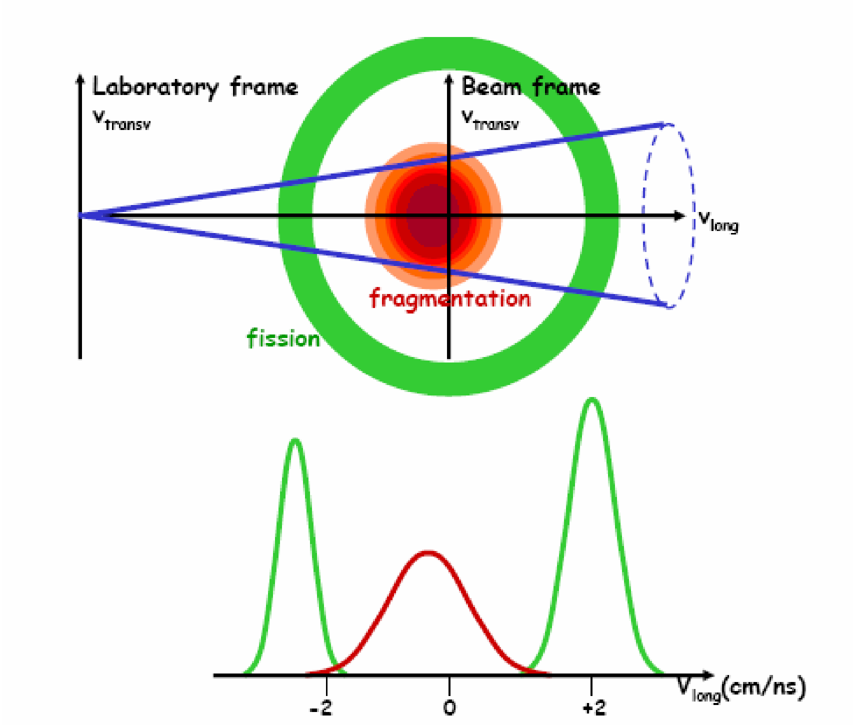

Figure 2.11: Up: schematic representation of the velocity distributions of fragmentation and fission residues, together with the FRS angular acceptance. Down: projection of the accepted events on the longitudinal axis.

The triple-humped spectrum schematically drawn in figure 2.11 is expected to be found for the velocity distributions of intermediate-mass products. Is it reasonable to expect that the same figure holds also for rather light products, as we have in this work? In a recent work [Nap04], Napolitani et al. analysed in detail the shape of the velocity distributions for the products of ^{56}Fe and ^{136}Xe, interacting at 1 GeV per nucleon with protons and with titanium. The experimental results for the all these reactions indicate that the longitudinal velocity distributions, inside the angular acceptance of the FRS, show the same profile as the drawing of figure 2.11, even for extremely light residues (down to Z=3). Napolitani showed that the longitudinal velocity spectra (inside the angular acceptance of the FRS) are always the superposition of two components: a central large hump, attributed to fragmentation, and two external peaks, attributed to fission or fast break-up decay with one heavy remnant, depending on the excitation energy introduced[1]. The position and width of the two external components can vary (in some cases they can even merge together) but the main characteristics remain unchanged. We conclude that it is reasonable to expect the picture presented in figure 2.11 remains valid also for very light products of the reaction ^{238}U+Ti at 1 *A* GeV. In the following, we will denote the process populating the external components of the longitudinal velocity spectra as “fission” also for the case of the light products of the reaction ^{238}U+Ti, well aware that the kinematical pattern only proves the formation of a heavy remnant together with the observed fragment, typical for very asymmetric fission, but also present in specific fast break-up processes [Nap04].

---

[1] For both the reactions 1A GeV ^{56}Fe on H and on Ti, Napolitani deduced that a fast break-up process is responsible for the two symmetric humps.

The reaction mechanisms in the two targets

The reaction ^{238}U + Ti, although incompletely covered, seems to fully account for the central hump in the distributions presented in figures 2.8-up and 2.9, representing the reaction of uranium in the hydrogen target including the titanium windows. In order to prove this, a more careful analysis was done. Here we present, as an example, the analysis done for Z=17. In figure 2.12-up we plot again the two-dimensional cluster-plots of the velocity distributions as a function of the neutron number. The dashed closed lines, named S1, S2 and S3, enclose all the events produced during three specific measurements (“settings”). In each measurement the magnetic fields were set to select fragments with a certain magnetic rigidity. The three settings were done once with the H+Ti target and once with the Ti dummy target. The velocity distributions obtained in the three measurements (i.e. the events falling inside S1, S2 and S3) with the Ti dummy target are compared with those obtained with the H+Ti target (figure 2.12-down). The 4th picture of figure 2.12-down is constructed by determining the maximum of the three spectra S1, S2, and S3 for each velocity bin (it is like to overlap the three figures and draw the skyline). Please note that the distributions of figure 2.12-down do not resemble the triple humped distribution of figure 2.11, expected for one isotope. This is because inside one setting several isotopes contribute to the velocity spectrum, but each isotope has a different production rate (or cross section) and therefore contributes with a different weight. However, the purpose of the comparison was to show that the contributions of the different targets to the different regions of the velocity distribution can clearly be determined. One concludes that the fragmentation products in the central velocity range are exclusively produced in the titanium target. No additional production from the interaction of the ^{238}U projectiles with hydrogen can be found inside the uncertainties of the analysis. Fission residues, appearing in the regions around –2.2 cm/ns and +1.8 cm/ns, are predominantly produced in hydrogen, but the production in the titanium target also extends into these regions. This is not surprising, while fission occurs also in the system ^{238}U+Ti. Their cross section seems to be low because fragmentation, filling the central part of the spectrum, is dominating.

The same analysis, as done for Z=17, was done for every Z. We concluded that the only production mechanism of light fragments for the reaction ^{238}U + ^{1}H at 1 A GeV is fission, or some other process in which the velocities of the fragments are strongly influenced by the Coulomb repulsion of one other heavy fragment. The measured velocity distributions concentrate on two peaks with strongly positive and strongly negative velocities. Also the titanium windows contribute to these velocity regions as demonstrated in figure 2.12. Therefore, at first, a careful study of the residue production in the reaction ^{238}U + Ti is needed, before the production of light residues in the spallation of uranium by 1 GeV protons can be determined.

Shape of the distributions

As it will become clear in the next section, the determination of the approximate shape of the velocity distributions is a pre-requisite for the analysis performed in this work. Since the measurements were incomplete, a method had to be developed to reconstruct the parts which were not covered. The key for this method is the observation that the velocity distributions develop smoothly as a function of neutron and proton number of the residues as suggested by the plots of figure 2.8 and demonstrated in several investigations [Enq99, Ben01, Enq01, Rej01, Ber03, Cas03, Tai03].

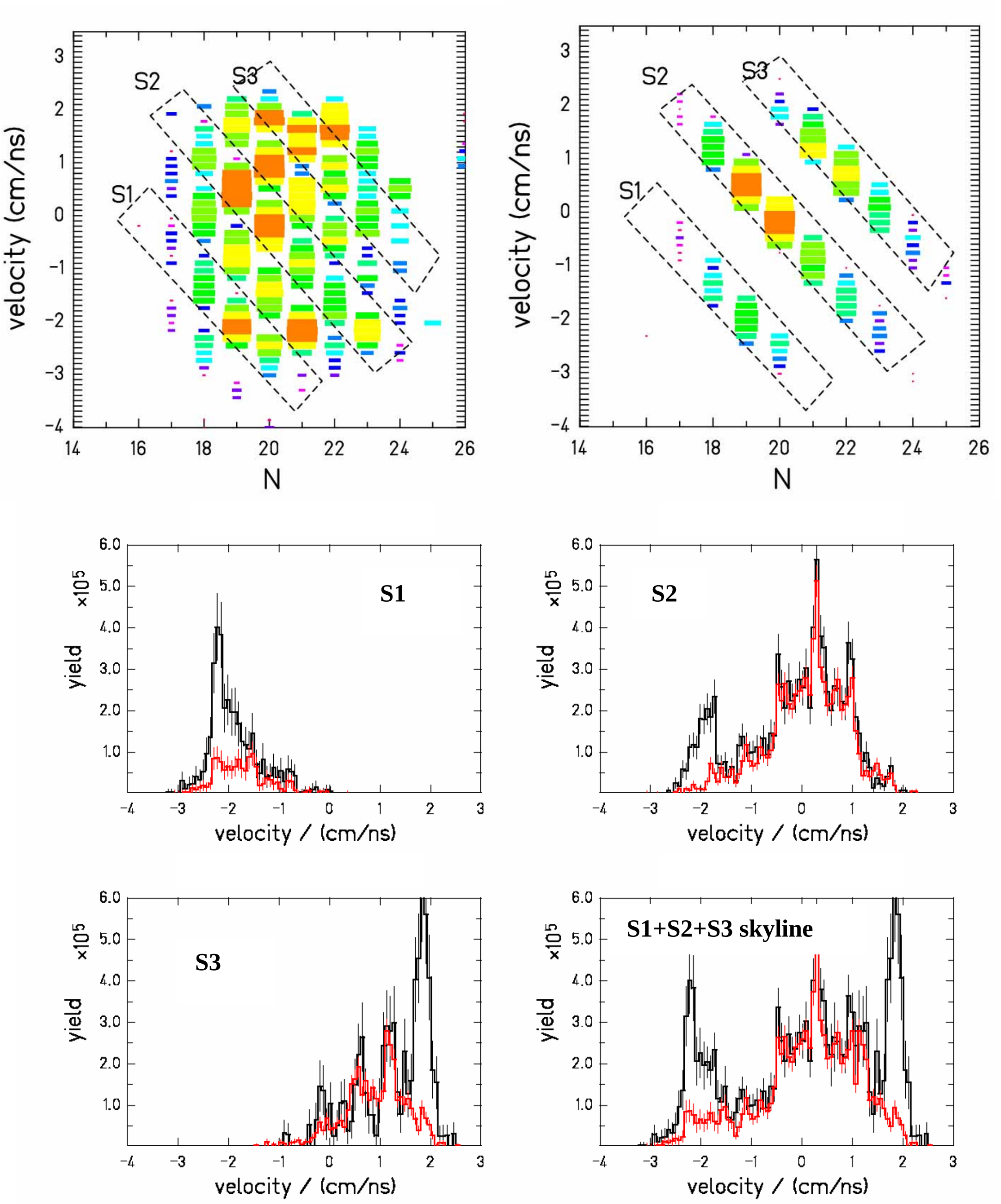

Figure 2.12: Up: Two-dimensional cluster-plots of the velocity distributions of the chlorine (Z=17) isotopes as a function of the neutron number obtained in three settings, in the H+ Ti target (left) and in the Ti target (right). The velocity is presented in the beam frame (υ_{238U} = 0 cm/ns). Down: Velocity spectra of fragments produced in the interaction of the uranium beam with the H+Ti target (black) and with the titanium dummy target (red) for the three setting S1, S2 and S3. The last figure depicts the combined distributions of three settings.

The approximate shape of the velocity distributions was reconstructed directly by overlapping all the velocity distributions of the isotopes of one element. The overlapping was done comparing channel by channel all the velocity distributions of the isotopes and taking the maximum value. This corresponds to overlap the distributions of all the isotopes and draw the skyline. In this way, to the velocity distribution of every element contribute its most-produced fragmentation isotope and its most-produced isotope by fission processes. Since in many cases (especially for the titanium dummy target), due to the missing settings, the most produced fragmentation (or fission) isotope alone cannot cover all the fragmentation (or fission) distribution, part of the distribution is covered by a close isotope. This is for instance the case of the spectrum of chlorine produced in the titanium dummy target, where the part between -0.05 cm/ns and 0.015 cm/ns is covered by N=20, and the part between 0015 cm/ns and 0.1 cm/ns is covered by N=19 (see figure 2.12-up). Considering that the integral of the velocity spectra of close isotopes changes appreciably (although continuously), accordingly to the change in the production cross-sections, the resulting distribution is staggering (see figure 2.12-down). To minimize this problem, we combined the distributions of three close elements, again with the method of the maximum value for every channel. This combination is justified by the fact that the velocity distributions of close elements vary smoothly with the charge number. Although it is difficult to estimate the precision of this method, it is best suited for the heavier elements, because one finds several nuclei with similar cross sections and similar shapes of the velocity distribution, contributing to establish a rather complete velocity distribution.

For the systems ^{238}U + Ti, the result obtained with this method is shown in figure 2.13 for every third element. It reveals the basic characteristics of the velocity distributions and their evolution with atomic number of the residues. The heaviest nuclei ($Z \geq 22$) are composed of three Gaussian-like components, similar to the system ^{238}U + Pb investigated previously [Enq99]. The positions and the widths of the components develop in a regular way. The widths of the fragmentation component and the difference in velocity of the forward and backward fission component increase with decreasing nuclear charge. The heights of the components show some fluctuations, because the nuclides with the highest yields were not measured in some cases. This is visible in the variation of the ratio of the yields of forward and backward fission, which should be about 1.1 due to the higher transmission in forward direction. Nevertheless, one can deduce some global trends: The fragmentation yield slightly increases and the fission yield strongly decreases with decreasing mass. As a result, for $<Z> = 23$ the forward fission component is almost completely covered by the broad and intense fragmentation peak. For $Z < 22$, the position, the width and the yield of the fragmentation component develop continuously with decreasing mass, the backward fission component is increasing in width and intensity and the forward fission component is not visible anymore because it merges with the fragmentation peak.

With the same method, also the shape of the velocity distributions for the nuclides produced in the system ^{238}U + (^{1}H+Ti) was obtained. The result is presented in figure 2.14.

Compared to the distributions of single isotopes in figure 2.9 and 2.10, in figures 2.13 and 2.14 the fission and fragmentation components are much better established. As expected from figure 2.11, the fission humps are narrow and positioned at large absolute values of the velocity. The fission forward peak is a bit higher than the backward one because of the geometrical cut of the FRS. Fragmentation generates a wider distribution, approximately centred at zero (υ_{238U} = 0 cm/ns). At first glance, the fragmentation yield, which exclusively originates from reactions with titanium, smoothly increases with decreasing atomic number, while the fission yield, which predominantly originates from reactions with hydrogen, first decreases with decreasing nuclear charge, then remains approximately constant below $Z = 16$ (or even tends to increase again). The global characteristics and tendencies will be now established with more precision.

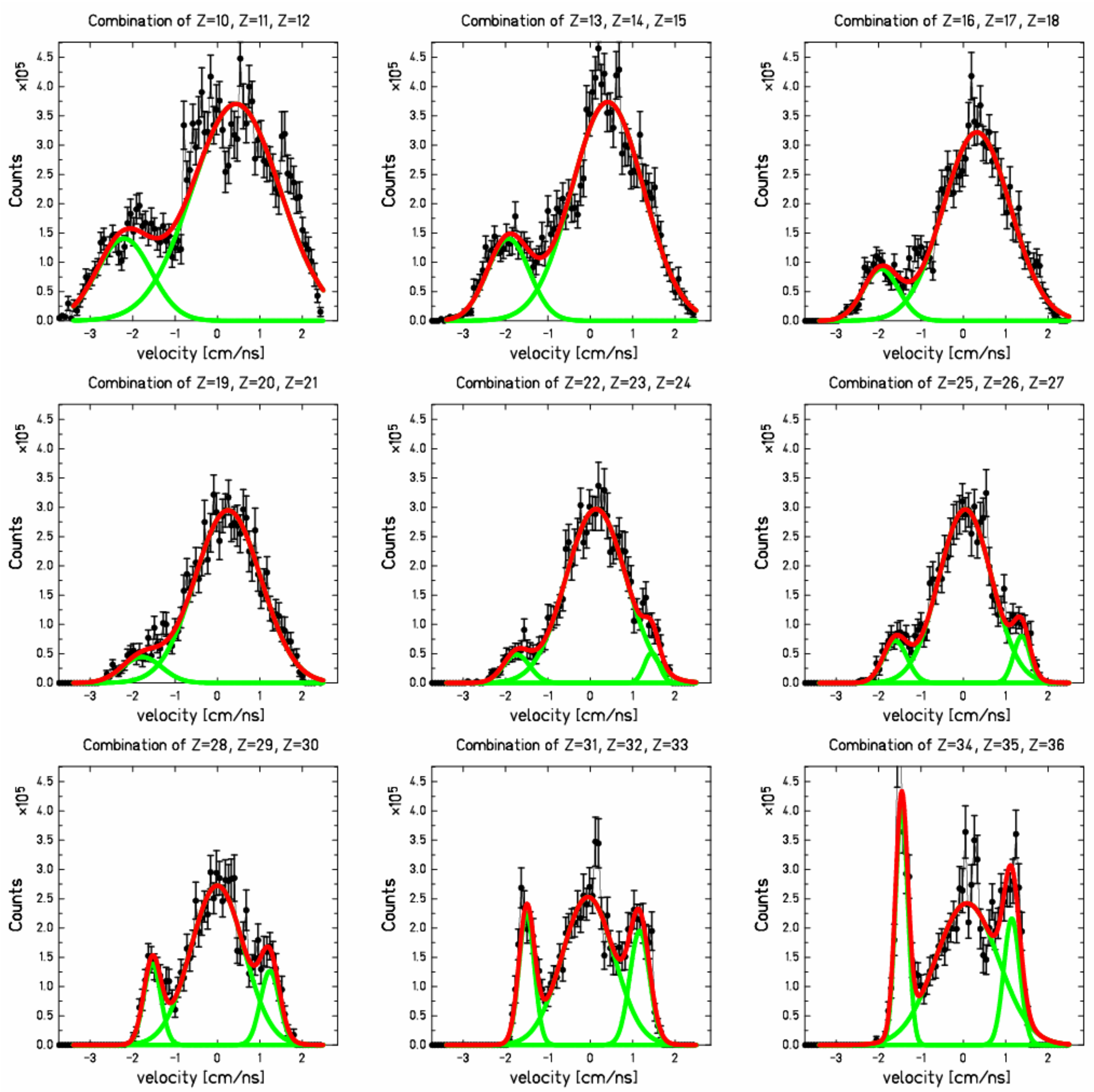

Figure 2.13: Approximate shapes of the velocity distributions of fragments produced in the interaction of the uranium beam with the titanium target. Each figure depicts the combined distributions of three close elements. The lines represent the result of a fit.

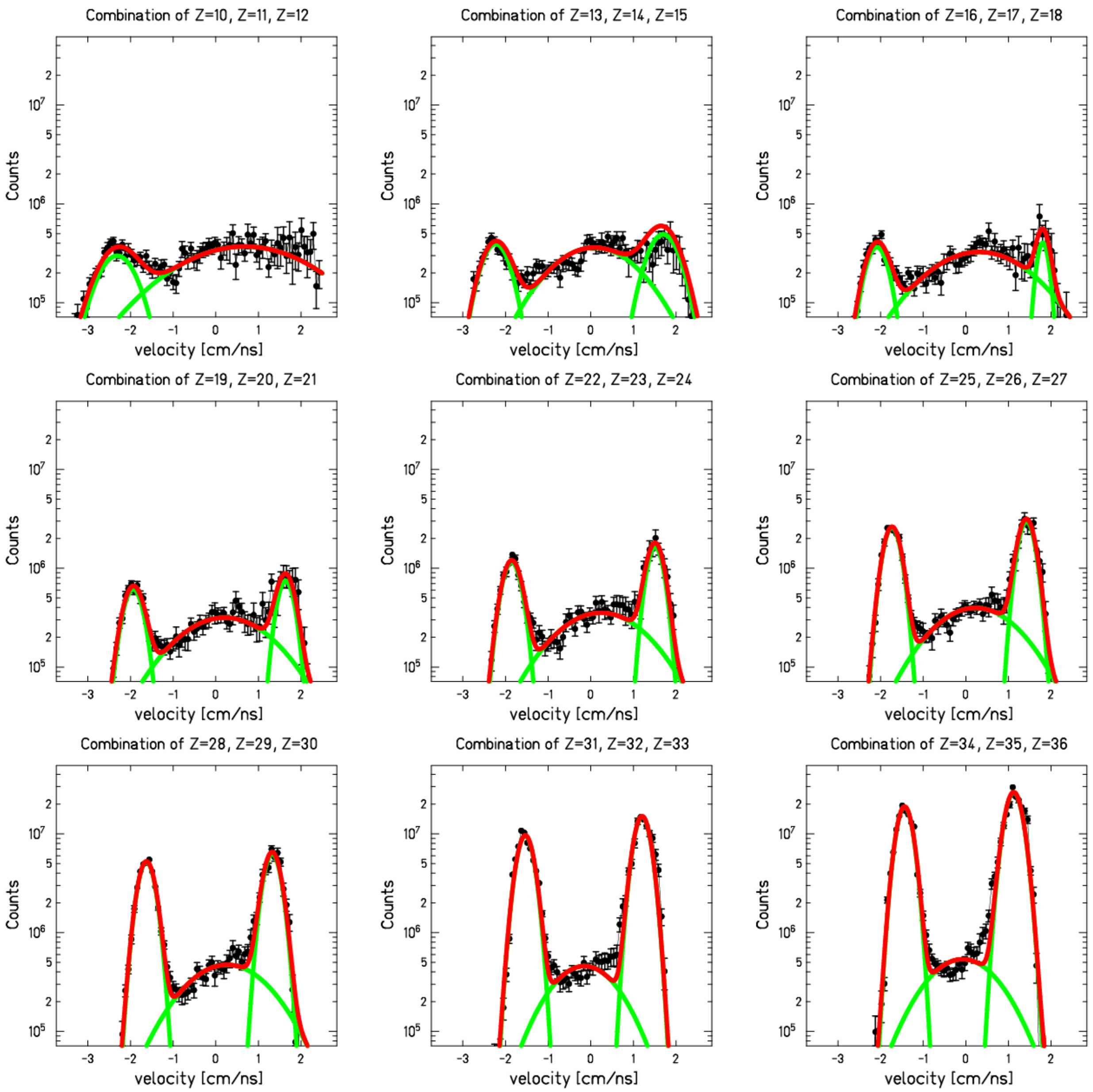

Figure 2.1.4: Approximate shapes of the velocity distributions of fragments produced in the interaction of the uranium beam with the hydrogen including the contribution of the titanium windows. Each figure depicts the combined distributions of three close elements. The lines represent the result of a fit.

Global characteristics and tendencies

Each of the distributions of figures 2.13 and 2.14 was fitted with up to three Gaussian curves. The result gives us important information on the dependence on the atomic number of the mean values, of the standard deviations and of the yields of the different components of the velocity distributions (figures 2.15 and 2.16). This information is needed as input for a fit procedure from which we will extract information on the individual nuclides (see next section). The physical meaning of these results will be widely discussed in chapters 4, 5, 6 and 7. It is important to remind here that the names “fission” and “fragmentation” are used in some extended meaning, as pointed out at the beginning of section 2.5.1.

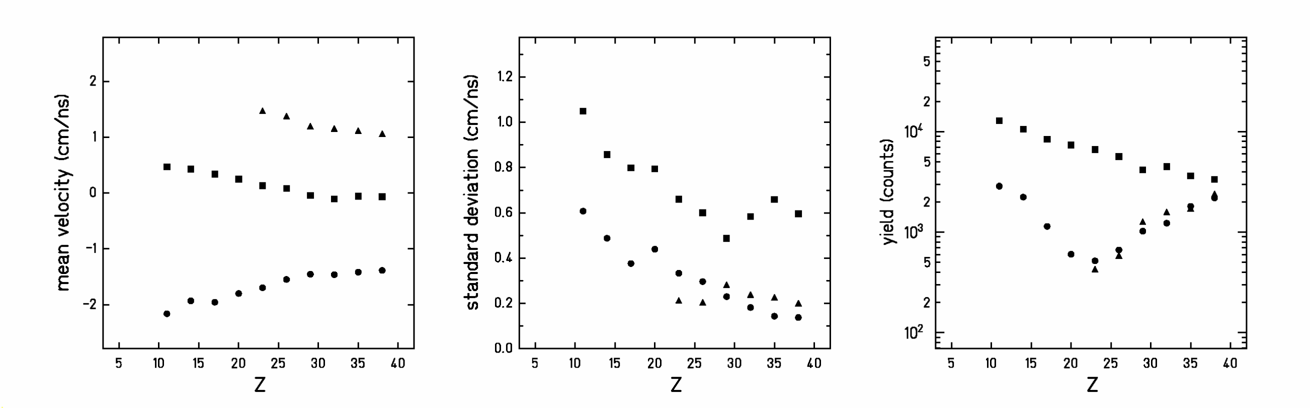

Figure 2.15: Mean values (left), standard deviations (centre) of the velocity distributions and yields (right) of the different components fitted to the spectra shown in figure 2.13 (^{238}U on Ti). The symbols represent: fission backward (λ), fission forward (▲), fragmentation (ν). The plots do not yet represent quantitative results.

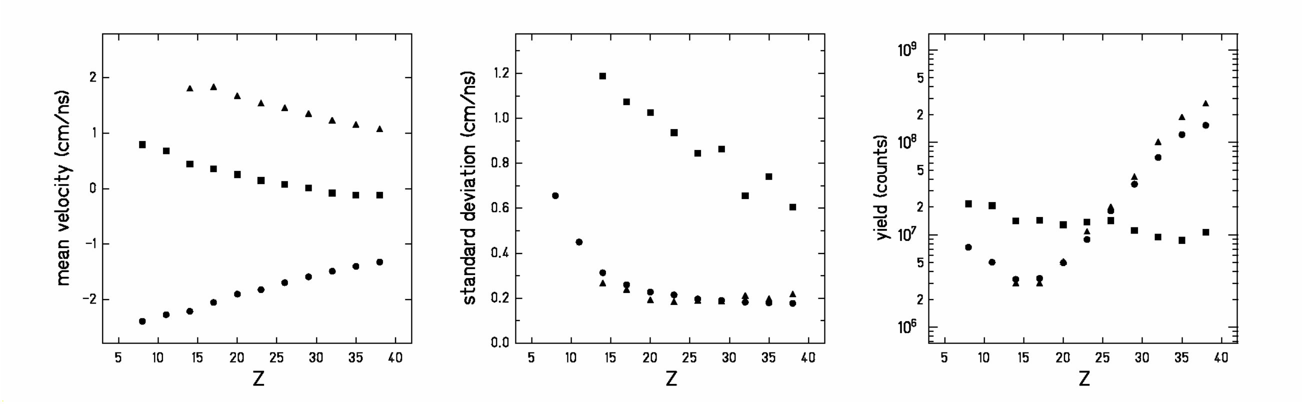

Figure 2.16: Mean values (left), standard deviations (centre) of the velocity distributions and yields (right) of the different components fitted to the spectra shown in figure 2.14 (^{238}U on H+Ti). The symbols represent: fission backward (λ), fission forward (▲), fragmentation (ν). The plots do not yet represent quantitative results.

A good overview on the raw data is given by two-dimensional cluster plots of the velocity distributions as a function of the produced elements for the Ti and the ^{1}H+Ti targets (figure 2.17). The plots were obtained combining the velocity distributions of every element, obtained with the method described before (the maximum value for every channel of the velocity spectra of the isotopes).

The following characteristics are seen, which essentially agree with the observations mentioned above:

1) The velocity distributions of close elements vary smoothly with the charge number

2) Fission occurs in the interaction with both hydrogen and titanium. In the hydrogen target it is much stronger, because the hydrogen target is thicker than the titanium windows.

3) Fragmentation occurs only in the interaction with titanium.

4) Fragmentation in titanium generates residues in all the observed Z range. The fragmentation products have velocity close to zero. As the charge of the fragment decreases, its velocity increases and seems even to overcome the velocity of the beam.

5) The fission events occupy two “wings” at large absolute values of the velocity. Figure 2.16 seems to indicate that in the reaction ^{238}U on ^{1}H fission generates light nuclides. In the case of the system ^{238}U on Ti, the forward fission wing seems to merge with the fragmentation peak.

6) Both in the reaction ^{238}U on ^{1}H and in ^{238}U on Ti, the yields of the two external fission wings decrease with decreasing mass down to a certain value, then they increase again.

We want to comment shortly what is stated in point 5). In the system ^{238}U + Ti the forward fission component is not anymore observable below Z=23, although we expect its existence [Nap04]. The tendency of the data indicates that it is covered by the fragmentation products. In section 2.6.6, we will discuss about this hidden forward fission peak and under which assumptions we can bypass this problem and extract the numerical values of the fragmentation cross sections. At this stage it is enough to remark that below charge 23 the velocity distributions for the system ^{238}U + Ti can be described by just two Gaussians. In the next section, for technical reasons, we will call the component at strongly negative velocities “side-peak” instead of fission backward[1].

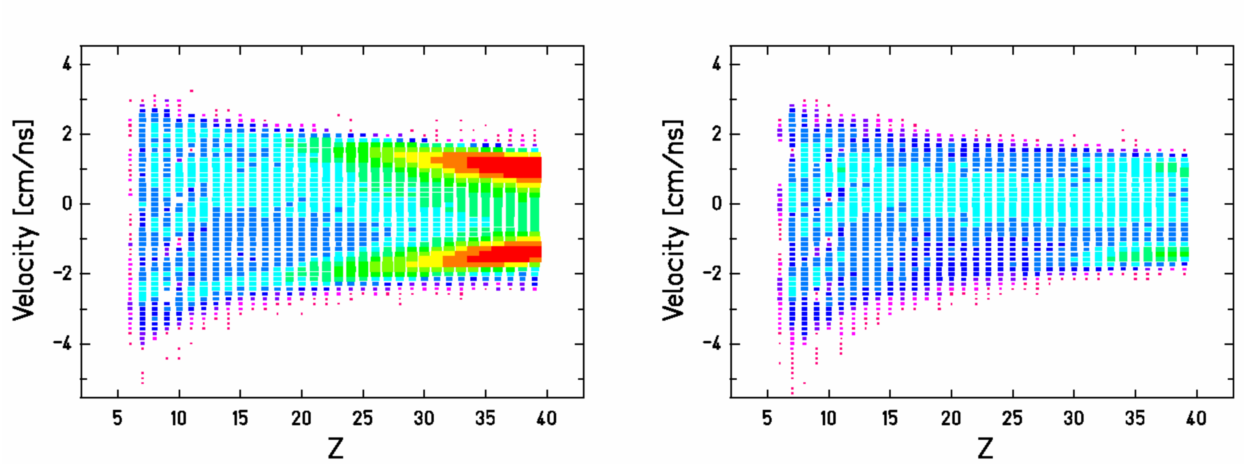

Figure 2.17: Two-dimensional cluster plot of the experimental velocities of fragments produced in the interaction of the uranium beam with the hydrogen-plus-titanium-window (left) and with the titanium-dummy target (right). The velocity is presented in the beam frame (υ_{238U} = 0 cm/ns).

---

[1] From here on, we will use the acronyms: “FB” for fission-backward, “FF” for fission-forward, “FR” for fragmentation, “SP” for side-peak, denoting the backward fission-like peak from U+Ti.

It is worthwhile to remark that all the characteristics, collected in figure 2.15 and 2.16, of the shape velocity distributions were obtained from the raw data. The only assumption done up to this moment to combine the data together is that in the observed systems the velocity distributions develop smoothly as a function neutron number and proton number of the residues. This seems to be proved by figures 2.8 and 2.17 and it is demonstrated to be valid in many other investigations [Enq99, Ben01, Enq01, Rej01, Ber03, Cas03, Tai03] for similar systems.

To conclude, we want to underline that these spectra are intended to provide only the *approximate shape* of the velocity distributions of the produced elements. The precise analysis of the data, the exact shape of the distributions, the quantitative results and the subtraction of the background will be performed with another technique, which requires, however, as input the knowledge of the approximate shape of the velocity distributions.

2.5.2 Precise information on individual nuclides

In order to get quantitative information on the velocity distribution and on the cross section of the single nuclides, a dedicated procedure was developed to fit the spectra of the individual isotopes.

The following three problems had to be solved: first, which functions to use as bases of the fit, secondly, how to perform the fit when too few data points are available, thirdly, how to disentangle the contribution of hydrogen and of titanium in the case of the hydrogen+titanium target.

The first problem was easily solved. In case of fragmentation, it is expected from theory that the momentum distribution of a fragment forms a Gaussian distribution [Gol74, Mor89]. The small cuts at the sides, due to the angular acceptance of the FRS, should not appreciably modify it. In case of fission it was shown in previous similar experiments [Enq99] that the two humps are in good approximation described by Gaussian distributions. The approximation is due to the fact that the two tails of the Gaussian curve are slightly asymmetric. This approximation introduces a negligible error in the evaluation of the cross section[1].

The solution of the second and third problems profited from the smooth behaviour of the distributions as a function of Z. The results of the fit of the combined distributions of three close elements (figures 2.15 and 2.16) provided information on the mean values, $\overline{\upsilon}(Z)$, and on the standard deviations, $\sigma(Z)$, of the Gaussian curves as functions of the atomic number. In principle, these values could be used to fit the data of the velocity distribution of every single isotope. For instance, the distribution of any isotope of iron could be obtained imposing the values of $\overline{\upsilon}_{FB}(Z=26)$, $\overline{\upsilon}_{FR}(Z=26)$, $\overline{\upsilon}_{FF}(Z=26)$, $\sigma_{\upsilon_{FR}}(Z=26)$, $\sigma_{\upsilon_{FF}}(Z=26)$ and fitting the existing data to adjust the height. However, with this method, the mean velocity values and the standard deviations are average values among three elements. As a consequence the result is slightly inaccurate in the description of the single element (or nuclide), because the functions $\overline{\upsilon}(Z)$ and $\sigma_{\upsilon}(Z)$ are not linear and their combination is also affected by the different weights (cross sections) of the element. A fit based on *slightly* wrong values of $\overline{\upsilon}$ and σ_{υ} can result in a *largely* wrong integral. For instance, in the case of ^{59}Fe, a difference of 4% in the mean values of

---

[1] A more detailed analysis in ref. [Enq99] showed that one of the two sides of the Gaussian distribution is better reproduced with an exponential tail. In our case, the improvement obtainable using the combination of these two functions would be anyhow covered by the error bars.

the two external humps produces a difference of 30% in the integral, thus in the final value of the cross section (see figure 2.18). For this reason, a more precise method was developed.

The new method is divided in two steps. In the first, a global fit that takes into account all the available experimental data is performed, i.e. all the isotopes of all the elements are fitted at once. In the second, the fit is performed on the data of the individual isotopes, having fixed the values $\overline{\upsilon}(Z)$ and $\sigma_{\upsilon}(Z)$ obtained with the global fit. Thus it adapts better to the characteristics of the velocity distributions.

The information contained in the two-dimensional plots, like that ones of figure 2.8, can be represented by seven basic functions, as schematically shown in figure 2.19. To take into account the results presented in section 2.5.1, we assumed that the velocity distribution is the composition of four Gaussian curves. The two distributions for fission, forward and backward, are not the

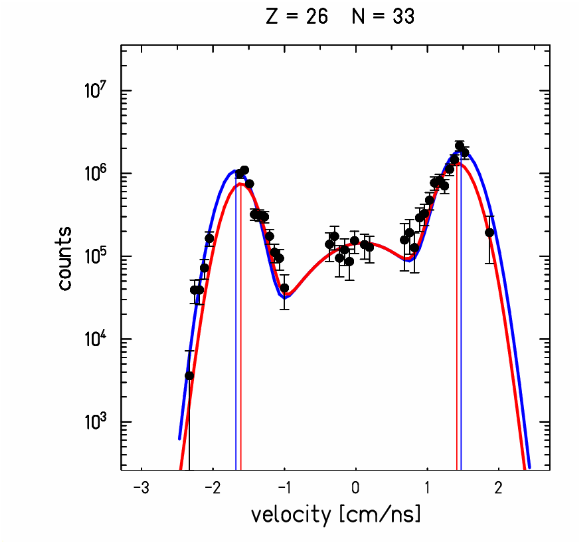

Figure 2.18: Two possible fits for ^{59}Fe, imposing different mean values of the fission Gaussian distributions. The data refers to the system ^{238}U + (H+Ti).

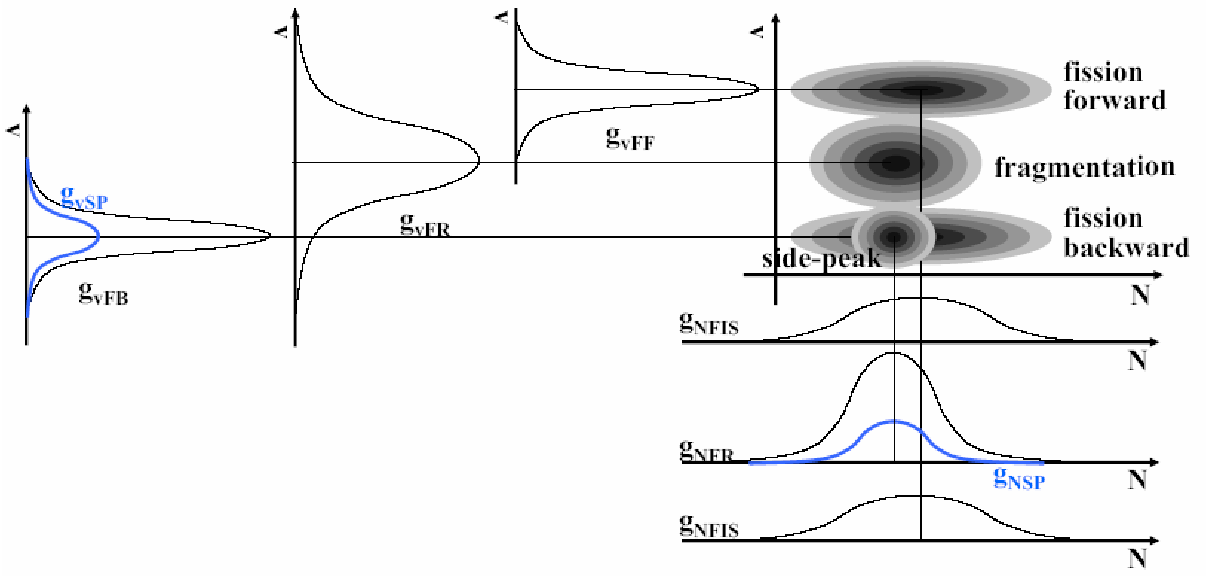

Figure 2.19: Scheme of the three-dimensional plot neutron number vs. velocity, for a given element Z. It is assumed that the velocity distribution is the composition of four Gaussian curves, and the isotopic distribution of four, two of which are equal.

same because the cone of figure 2.11 cuts different amounts of the fission shell. We assumed that the isotopic distribution is given by the combination of three Gaussian curves, one for the fission residues (for the isotopic distribution there is no difference between backward and forward fission events), one for the fragmentation residues and a third one for the backward fission peak produced in titanium, namely the side-peak. In reality, the isotopic distributions are reproduced by a Gaussian only partially, since the neutron-rich tail of the distributions deviates from it, as can be seen in the results presented in literature [Enq99, Enq01, Enq02]. We will see at the end of this sub-section that this approximation has no consequences for the final result.

To reconstruct the three-dimensional plots like that ones of figure 2.8, it is necessary to know for every element Z the mean values and the widths of the distributions, i.e. the fourteen values $\bar{\upsilon}_{FB}$, $\bar{\upsilon}_{SP}$, $\bar{\upsilon}_{FR}$, $\bar{\upsilon}_{FF}$, $\sigma_{\upsilon_{FB}}$, $\sigma_{\upsilon_{SP}}$, $\sigma_{\upsilon_{FR}}$, $\sigma_{\upsilon_{FF}}$, $\bar{N}_{FIS}$, $\bar{N}_{FR}$, $\bar{N}_{SP}$, $\sigma_{N_{FIS}}$, $\sigma_{N_{FR}}$, $\sigma_{N_{SP}}$ which enter in the seven Gaussians (normalised to 1):

$$g(\upsilon) = \frac{1}{\sqrt{2\pi}\cdot\sigma_{\upsilon}}\cdot e^{-\frac{(\bar{\upsilon}-\upsilon)^2}{2\sigma_{\upsilon}^2}} \qquad g(N) = \frac{1}{\sqrt{2\pi}\cdot\sigma_{N}}\cdot e^{-\frac{(\bar{N}-N)^2}{2\sigma_{N}^2}} \tag{2.14}$$

and also the values of the areas of the curves: Y_{FB}, Y_{FR}, Y_{FF}, Y_{SP}, in such a way that for every point (N, υ) it is possible to calculate the corresponding yield:

$$\begin{aligned} Y_Z(N,\upsilon) = {} & g_{FB}(\upsilon)\cdot g_{FIS}(N)\cdot Y_{FB} + g_{SP}(\upsilon)\cdot g_{SP}(N)\cdot Y_{SP} + \\ & g_{FR}(\upsilon)\cdot g_{FR}(N)\cdot Y_{FR} + g_{FF}(\upsilon)\cdot g_{FIS}(N)\cdot Y_{FF} \end{aligned} \tag{2.15}$$

The Gaussians $g(\upsilon)$ give the shape of the velocity distribution, the Gaussians $g(N)$ give the relative weight of each isotope of one element, the areas Y, give the height of the three humps in the three-dimensional plot of figure 2.8 (or figure 2.11).

The functions describing the dependence on Z of the areas of the curves, Y_{FB}, Y_{FR}, Y_{FF}, Y_{SP}, of the mean values of the velocity distributions, $\bar{\upsilon}_{FB}$, $\bar{\upsilon}_{SP}$, $\bar{\upsilon}_{FR}$, $\bar{\upsilon}_{FF}$, and of the standard deviations of the velocity distributions, $\sigma_{\upsilon_{FB}}$, $\sigma_{\upsilon_{SP}}$, $\sigma_{\upsilon_{FR}}$, $\sigma_{\upsilon_{FF}}$, were deduced from the functions depicted in figures 2.15 and 2.16:

$$\begin{aligned}
Y_{FB}(Z) &= e^{(p_1+p_2 Z+p_3 Z^2)} & \bar{\upsilon}_{FB}(Z) &= p_{13}+p_{14}\cdot Z+p_{15}\cdot Z^2 & \sigma_{FB}(Z) &= p_{25}+p_{26}\cdot Z+p_{27}\cdot Z^2 \\
Y_{FF}(Z) &= e^{(p_4+p_5 Z+p_6 Z^2)} & \bar{\upsilon}_{FF}(Z) &= p_{16}+p_{17}\cdot Z+p_{18}\cdot Z^2 & \sigma_{FF}(Z) &= p_{28}+p_{29}\cdot Z+p_{30}\cdot Z^2 \\
Y_{FR}(Z) &= e^{(p_7+p_8 Z+p_9 Z^2)} & \bar{\upsilon}_{FR}(Z) &= p_{19}+p_{20}\cdot Z+p_{21}\cdot Z^2 & \sigma_{FR}(Z) &= p_{31}+p_{32}\cdot Z+p_{33}\cdot Z^2 \\
Y_{SP}(Z) &= e^{(p_{10}+p_{11} Z+p_{12} Z^2)} & \bar{\upsilon}_{SP}(Z) &= p_{22}+p_{23}\cdot Z+p_{24}\cdot Z^2 & \sigma_{SP}(Z) &= p_{34}+p_{35}\cdot Z+p_{36}\cdot Z^2
\end{aligned} \tag{2.16}$$

To get the functions $\bar{N}(Z)$ and $\sigma_N(Z)$, we projected on the x-axis the combined three-dimensional plot neutron number vs. velocity (as that one of figure 2.8) of three close elements. The projection was done two times, once selecting with a graphical window the fragmentation events and once selecting the fission events. The so-obtained values of $\bar{N}$ and for σ_N every group of three elements were plotted as a function of the charge Z and fitted. We obtained that both the mean value and the standard deviation are described by second-order polynomials:

$$\begin{aligned}
\bar{N}_{FIS}(Z) &= p_{37}+p_{38}\cdot Z+p_{39}\cdot Z^2 & \sigma_{N_{FIS}}(Z) &= p_{40}+p_{41}\cdot Z+p_{42}\cdot Z^2 \\
\bar{N}_{FR}(Z) &= p_{43}+p_{44}\cdot Z+p_{45}\cdot Z^2 & \sigma_{N_{FR}}(Z) &= p_{46}+p_{47}\cdot Z+p_{48}\cdot Z^2 \\
\bar{N}_{SP}(Z) &= p_{49}+p_{50}\cdot Z+p_{51}\cdot Z^2 & \sigma_{N_{SP}}(Z) &= p_{52}+p_{53}\cdot Z+p_{54}\cdot Z^2
\end{aligned} \tag{2.17}$$

The parameterisation of $\overline{\upsilon}(Z), \sigma_{\upsilon}(Z), Y_{\upsilon}(Z), \overline{N}(Z), \sigma_N(Z)$ required 54 parameters p_i. The fits in figures 2.13 and 2.14 provided approximate values of 36 parameters p_i and the fit of the functions $\overline{N}(Z)$ and $\sigma_N(Z)$ provided the other 18 parameters p_i. These values of p_i were used as starting values for a global fit, in which all the isotopes of all the elements were fitted at once. The generic data-point of the fit represents the measured counts, Y_{exp}, as a function of the measured velocity (in the beam frame), of the charge number and of the neutron number. The global fit has to find the best parameters, p_i, for which the function Y_{fit} coincides with Y_{exp}:

$$\begin{gathered} Y_{\exp} = counts = f(\upsilon, Z, N) \\ Y_Z^{fit}(N,\upsilon) = g_{FB}(\upsilon)\cdot g_{FIS}(N)\cdot Y_{FB} + g_{SP}(\upsilon)\cdot g_{SP}(N)\cdot Y_{SP} + \\ g_{FR}(\upsilon)\cdot g_{FR}(N)\cdot Y_{FR} + g_{FF}(\upsilon)\cdot g_{FIS}(N)\cdot Y_{FF} \\ Y_{\exp}(\upsilon, Z, N) = Y_Z^{fit}(N,\upsilon) \end{gathered} \tag{2.18}$$

Although 54 parameters seem to be a large number, about 60000 experimental data points were used for the fit. The fit package of SATAN [SAT] was used to perform the fit, with a previous implementation of our own fit function, described in equation 2.15. The SATAN fit-program is based on the function χ^2, given by the weighted sum of squares of the differences between the data and the corresponding calculated values divided by the errors squared (method of least squares). The program searches for the local minimum of the χ^2 as function of the parameters. This is to say that, if Y_{exp_i} is the experimental data in correspondence of the abscissa x_{exp_i}, and $Y_{fit_i}(p_j)$ is the fit function that depends on the parameters p_j, χ^2 is:

$$\chi^2(p_1, p_2, \ldots, p_{54}) = \frac{\sum_i \left(Y_{exp_i} - Y_{fit_i}(p_j)\right)^2}{err_i^2} \tag{2.19}$$

The best values of the parameters are obtained by finding the minimum of $\chi^2(p_j)$ for all the p_j.

The errors, err_i, are the absolute experimental uncertainties associated with every data-point. They derive from the experimental relative uncertainties, deduced from the raw measured counts in every point. The latter correspond to the inverse of square root of them, according to the Poisson statistic.

An example of the result of the global fit procedure is given in figure 2.20, for some germanium isotopes (Z=32). The figure shows that the result of the global fit gives a good description of the shape of the velocity distributions, although the height can be rather off for some isotopes.

The determination of the yields of individual isotopes was obtained by a specific fit, nuclide by nuclide by keeping the parameters of the velocity distributions fixed. The specific fit for every nuclide was performed by fixing the values of the parameters, p_i, obtained with the global fit for $\overline{\upsilon}$, σ_{υ}, $\overline{N}$, σ_N, and letting the parameters that determine Y_{FB}, Y_{FR}, Y_{FF}, Y_{SP} free to vary. In order to discharge the events occurred in the windows of the titanium container of the hydrogen target, it was necessary at first to perform the full analysis (first the global fit, and then the fit of the single nuclide) of the production in the titanium target. The result of the individual fit for the single nuclide for the titanium target was used as a fixed "background" for the fitting procedure in the hydrogen target. In this way, the fission Gaussian distributions determined by the fit of the data of the hydrogen target contain the net counts, without the contribution of the titanium windows. The final result of the fitting procedure is presented in figure 2.21 for four nuclides. The fit procedure also gives the statistical uncertainties on the fit parameters, based on the statistical uncertainties of the individual experimental points. From the uncertainties of the fit parameters the statistical error were deduced, as will be explained in section 2.6.5.

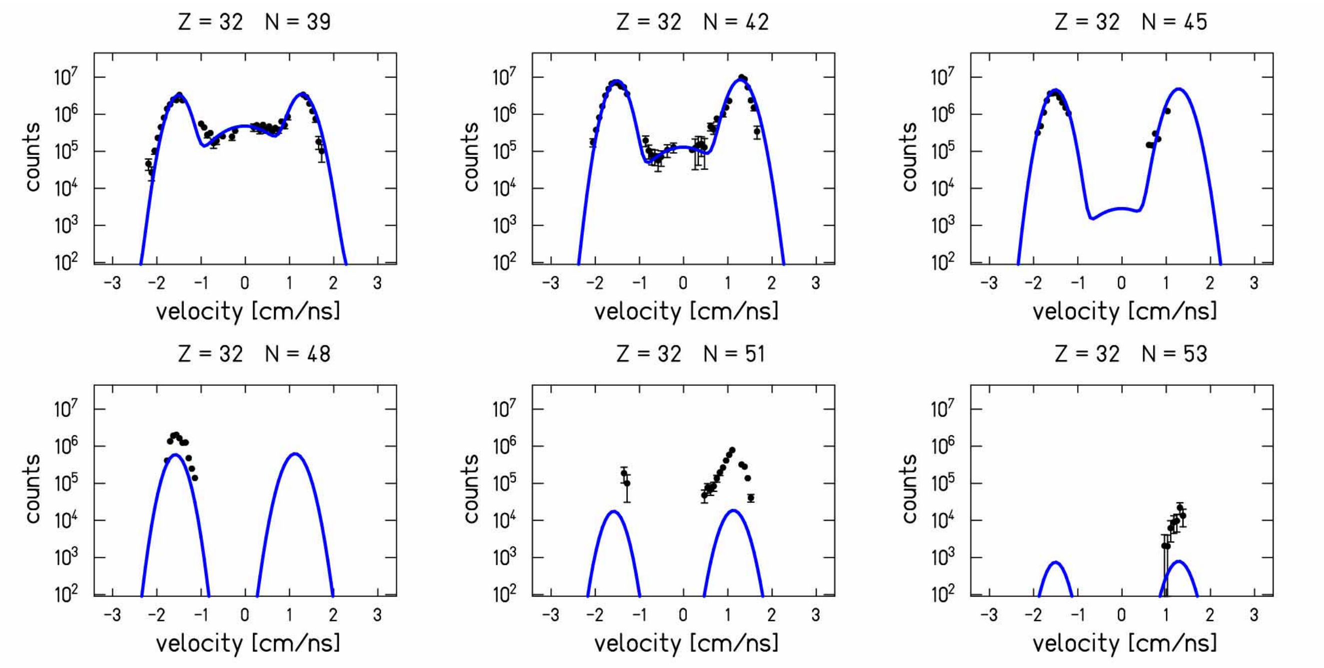

Figure 2.20: Results of the global fit for some isotopes of germanium (Z=32) produced in the interaction of the uranium beam with the H+Ti target. For the most neutron rich isotopes, the fragmentation component in the central velocity range falls below the detection limit of the experiment. The fit curves are established on the basis of the global fit, simultaneously adapted to the totality of the experimental data of all the nuclides produced. The shapes of the curves are already established, but their height has still to be determined on the basis of the individual fit.

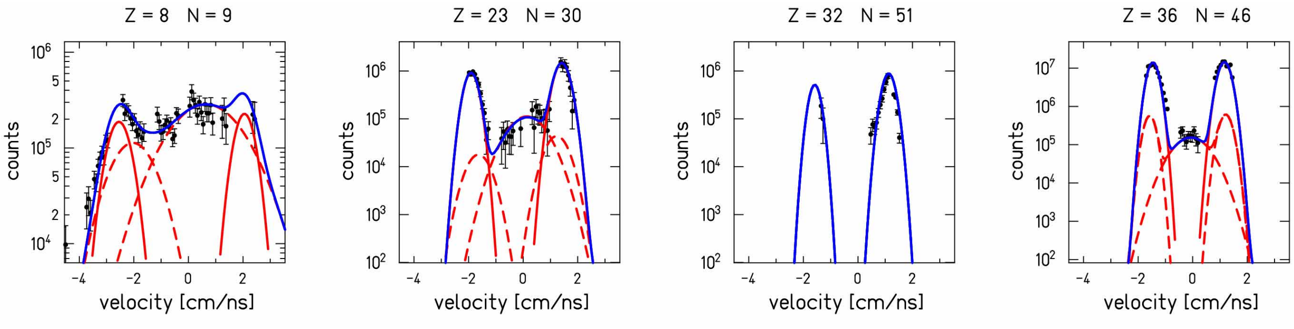

Figure 2.21: Results of the individual fit for four nuclides produced in the interaction of the uranium beam with the H+Ti target (blue solid curves) and with the Ti dummy target (red dashed curves), which constitutes the background. The fission components in hydrogen (red solid curves, which in the last three cases are hidden behind the blue solid curves), give the fission reaction rates for the reaction ^{238}U+H. The fission and fragmentation components in the titanium target are represented by the red dashed curves.

2.6 Evaluation of the formation cross sections and of the mean velocity of the fragments

2.6.1 Evaluation of the formation cross sections

The integral of the different components (fission and fragmentation) of the individual fit of the velocity distribution of every nuclide provided the total production rates per incident projectile for the formation of that nuclide via the different reaction mechanisms: *R(Z, N).* The production cross section of a specific nuclide is:

$$\sigma(Z,N) = \frac{R(Z,N)}{\eta \cdot \varepsilon(Z,N)} = \frac{R_{real}(Z,N)}{\eta} \quad \text{with} \quad R_{real}(Z,N) = \frac{R(Z,N)}{\varepsilon_{SR}(Z,N) \cdot T(Z,N)} \tag{2.20}$$

where η is the number of target nuclei per unit area, and ε is the efficiency, connected to the secondary reactions occurring in the target, ε_{SR}, and to the losses due to the angular transmission of the FRS, T. The corrections due to the secondary reactions and to the angular transmission of the FRS will be explained below.

For the evaluation of the fission cross sections for the hydrogen-induced reactions the almost completely covered velocity distribution provided a good basis. The fragmentation cross sections for the titanium-induced reactions could also reliably be determined, in spite of the incomplete coverage, since the velocity distributions are very broad, and thus for every nuclide several sections of the velocity distribution were available from the experiment.

Since below Z=22 the forward fission-like peak is not explicitly seen, the fragmentation cross sections for nuclei with Z<22 produced in the reaction ^{238}U+Ti could not be evaluated with the method presented in section 2.5.2. A different method, which will be explained in section 2.6.6, was used. Since this method is based on some assumptions, the experimental data will be presented in the following way:

- integrated differential production cross sections, in the range from 0 to 15 mrad, are given for the system ^{238}U+Ti for the production below Z=22. This very basic experimental information does not oblige to disentangle the possible reaction mechanism, neither requires any assumption on the isotropy of the process,
- fragmentation cross sections for the system ^{238}U+Ti are given for production above Z=21. Above Z=21 the backward and forward and fission peaks are still recognizable and separable from the fragmentation hump, and the yields follow a smooth trend (as shown in figure 2.15). The cross sections are obtained using the transmission values calculated assuming an isotropic fragmentation process,
- fragmentation cross sections for the system ^{238}U+Ti for nuclei with Z≤21, obtained with the method that will be explained in section 2.6.6, are also given but in a separate table, underling under which assumptions the result is valid.
- fission cross sections for the system ^{238}U+H are given for the entire Z range. The contribution of the titanium target could be discharged safely thanks to the method presented before. The knowledge of the reaction mechanisms which delineate the velocity spectra of isotopes produced in the titanium-induced reactions is not a condition necessary for that purpose. Please note that the subtraction of the background is done before the calculation of the cross sections, with equation 2.20. Once the background is subtracted, the cross sections are obtained using the transmission values calculated assuming an isotropic fission (or binary decay) process.

In the following two sections we will present how the efficiency coefficients, ε_{SR} and T, used to calculate the fission and fragmentation cross section, are obtained.

2.6.2 The correction for secondary reactions

Both projectiles and reaction products may interact with the target nuclei. Since the target is not thin, this reaction probability is not very small, and its effect cannot be neglected. Beam reactions reduce the effective primary-beam intensities. The amount of this reduction was calculated with the program AMADEUS [AMA], which calculates the total nuclear reaction cross sections according to the model of ref. [Ben89]. The result for the hydrogen target gives a reduction of 5.7% on the average. So the effective beam intensity is 5.7% smaller than the intensity monitored with the SEETRAM. For the titanium target this attenuation is negligible.

Reaction products may undergo consecutive nuclear reactions, with the net effect that the production of the heavy residues is decreased, and the production of the light ones is increased. This effect is more important in the hydrogen target, due to the larger thickness. Therefore, formation cross-sections of nuclides produced in the hydrogen target have to be corrected.

The method to correct the cross sections for this effect is described in the appendix of ref. [Enq01] and in ref. [Nap03]. For any nuclear species, characterised by the atomic number Z_f and the mass number A_f, the evolution of the intensity along the target is described by a differential equation:

$$\frac{d\dot{n}(Z_f,A_f)}{\dot{n}(Z_f,A_f)\cdot dl}=\frac{dn_t}{dV}\cdot\left[\sum_{Z_i,A_i}\{\sigma(Z_i,A_i\to Z_f,A_f)\}-\sum_{Z_{ff},A_{ff}}\{\sigma(Z_f,A_f\to Z_{ff},A_{ff})\}\right] \tag{2.21}$$

l denotes the coordinate in beam direction, and $\frac{dn_t}{dV}$ is the number of target atoms per volume, if the consideration is limited to one-step and two-steps reactions. Formulating this equation for every nucleus gives a complete system of differential equations. The exact consideration of multiple reactions requires the knowledge of all reaction cross sections $\sigma(Z_i,A_i\to Z_f,A_f)$ for the production of any nucleus with atomic number Z_f and mass number A_f from any projectile with atomic number Z_i and mass number A_i. The boundary conditions are defined by the primary-beam intensity ($\dot{n}(Z_p,A_p)$ for $l = 0$) and by the requirement that the intensities of all other nuclei are zero at the entrance of the target.

At the moment, there is no code capable to predict these formation cross sections accurately enough. Consequently an accurate correction for this effect could not be performed. However the possible contribution was estimated in order to consider an additional systematic uncertainty on the affected nuclides. This estimate was done by P. Napolitani, who treated explicitly the case of 1 *A* GeV ^{238}U on ^{1}H in ref. [Nap03]. He found that light fission fragments are mostly not affected. In reality, the predictive power of the code he used is limited to fragments above Z ≅ 20, but in any case there are theoretical reasons to expect that secondary reactions do not play an important role in the range of products below Z=20. In the case of the heavier fission products, the secondary reactions affect the isotopes of one element with different weights. Neutron-rich isotopes are overestimated by few percent. Isotopes at the middle of the isotopic distribution are practically not affected. The most exotic isotopes on the neutron-deficient side could be underestimated by even 50%. This uncertainty does not affect the global results, which are mostly determined by the central part of the isotopic distributions. However, in the results of the formation cross section for the individual isotopes the error bars were increased according to the estimation reported in ref. [Nap03]. In most cases, this error is negligible with respect to the other systematic uncertainties.

2.6.3 The FRS angular transmission

The angular transmission of the FRS was intensively investigated in case of fission and fragmentation processes. Devoted studies and computational tools have been carried out in order to accurately estimate the value of the FRS angular transmission. The analytical formulae that quantify these effects were determined in a previous work [Ben02] and are shortly reported here.

The angular transmission of fragmentation products is given by:

$$T_{frag} = 1 - exp\left(-\frac{\alpha_{eff}^2}{2\sigma_\theta^2} \right) \tag{2.22}$$

where α_{eff} is the angular acceptance of the FRS ($\alpha_{eff} \approx 0.015\ rad$) and σ_θ is the standard deviation of the Gaussian describing the angular spread in the laboratory frame, which is correlated to the standard deviation of the observed velocity distribution by the equation:

$$\sigma_\theta = \frac{\sigma_{\upsilon\, frag}}{\upsilon_{beam}} \cdot \sqrt{1 - \beta_{beam}^2} \tag{2.23}$$

where $\beta_{beam} = \upsilon_{beam}/c$. The transmission of every fragmentation residue can be evaluated from the width of its measured velocity distribution. With $\sigma_{\upsilon\, frag} = \sigma_{meas}$, the real production rate is given by:

$$R_{real}^{frag} = \frac{R^{frag}}{T_{frag}(\sigma_{meas})} \tag{2.24}$$

For the fragmentation products presented in this work, the transmission varies from 20% for Z = 7 to 60% for Z = 30.

The angular transmission of the fission fragments is determined by the caps of the shell of the sphere in velocity space which lie inside the FRS angular acceptance (see figure 2.11). The caps can be described by the corresponding angle φ with the vertex at the centre of the sphere in the velocity space. When isotropic emission in the centre-of-mass system is assumed, the transmission T for forward (φ < 90º) or backward (φ > 90º) fission is given by the area of the cap of the distribution divided by the area of the full sphere:

$$T_{forward} = \frac{1 - cos\,\varphi}{2} \qquad T_{backward} = \frac{1 + cos\,\varphi}{2} \tag{2.25}$$

The angle can be calculated knowing the radius, $R = \upsilon_\perp$, of the sphere, which varies with the charge of the observed fission fragment, and the longitudinal velocity of the fissioning nucleus, i.e. the position of the centre of the sphere, $\overline{\upsilon}$. These two quantities can be determined experimentally, as we will show in the next sub-section. The real production rate is:

$$R_{real}^{fiss} = \frac{R^{fiss}}{T_{fiss}(\upsilon_\perp, \overline{\upsilon})} \tag{2.26}$$

In the Z range of the nuclides presented in this work, only 3% for Z = 7 to 10% for Z = 30 of the produced fission residues are transmitted.

The angular acceptance of the FRS depends on the magnetic rigidities of the fragments along the spectrometer. For fragments passing close to borders of the dipoles, the angular acceptance is reduced. This geometrical reduction of the transmission depends on the x-positions of the ions at the intermediate and final focal planes. This effect was corrected by assigning a certain weight to the events, in such a way that the counts were increased depending on the x_2 and x_4 positions of the ion, before the spectra were accumulated. The amount of this increase was determined with accurate ion-optical calculations [Ben02]. It is different for fission and fragmentation products. Finally, the deduced reaction rates were corrected for the transmission for residues following the central trajectory ($x_2 = 0$, $x_4 = 0$).

2.6.4 Evaluation of the mean velocity of the fragments

The mean velocity of the fission and fragmentation products is not directly the value obtained with the fit procedure because of the limited FRS angular acceptance.

In the case of fission the fit procedure gives the mean value of the backward and forward Gaussian distributions, $\overline{\upsilon}_{FB}$ and $\overline{\upsilon}_{FF}$. In first approximation we assumed that the centre of the velocity sphere is $\overline{\upsilon} = \left(\overline{\upsilon}_{FB} + \overline{\upsilon}_{FF}\right):2$ and the radius is $\upsilon_{\perp} = \left(\overline{\upsilon}_{FF} - \overline{\upsilon}_{FB}\right):2$. With these values we calculated a first approximate value of the transmission $T^{(0)}_{fiss}(\upsilon_{\perp}, \overline{\upsilon})$. This value is in turn used to calculate more accurate values of the centre and the radius: $\overline{\upsilon}^{(1)} = \overline{\upsilon} \cdot \left(1 + T^{(0)}_{fiss}\right)$ and $\upsilon^{(1)}_{\perp} = \upsilon_{\perp} \cdot \left(1 + T^{(0)}_{fiss}\right)$. These values of $\overline{\upsilon}^{(1)}$ and $\upsilon^{(1)}_{\perp}$ are used to calculate again the transmission. This procedure was found to converge after the first iteration.

In the case of fragmentation, the angular cut enhances the transmission of fragments in forward direction, with the net result that the mean value of the observed fragmentation distribution is shifted towards positive velocities. In order to correct for this effect, a Monte Carlo program was written. In the program, a three-dimensional Gaussian distribution in the velocity space is generated, centred in the centre-of-mass frame. According to the supposed isotropy of the fragmentation reaction, the width was the same in the three directions. Event by event, the velocity was randomly sampled from this distribution and transformed into the laboratory frame. If the angle that the vector formed with the beam axis was less the 15 mrad, corresponding to the angular acceptance of the FRS, the event was considered as transmitted. The projection on the beam axis of the velocity vectors of the transmitted events generates a distribution whose mean value is shifted with respect to zero, i.e. with respect to the centre of the original distribution. This shift represents the correction that had to be applied to the experimental data. In the Monte-Carlo calculation, the widths of the initial distributions were chosen in such a way that the final widths coincided with the experimental widths of the fragmentation velocity distributions (see figure 2.15). Thus, the correction to apply to the measured mean values of the velocity distribution was determined as a function of Z. The result is presented in figure 2.22.

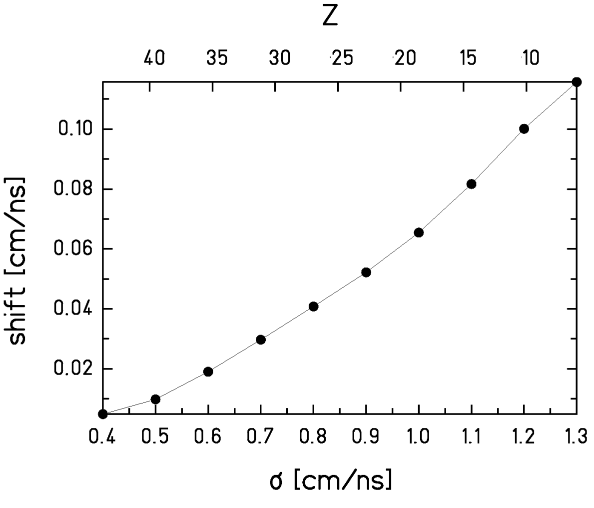

Figure 2.22: Shift of the mean value of the fragmentation velocity distribution of transmitted ions with respect to the mean value of all events as a function of the width of the distribution (standard deviation, σ) and of the charge Z. The correlation between σ and Z was taken from fig. 2.15.

2.6.5 Uncertainty of the results

The uncertainty of the cross sections was determined by the statistical uncertainty and by five systematic uncertainties. All the uncertainties contribute independently to the final uncertainty, so the relative uncertainties were summed up quadratically.

The statistical uncertainty was determined by the error associated to the fitted parameter in the individual fit of the velocity distribution of every nuclide. In turn, the latter reflects the statistical uncertainties associated to the single data points forming the velocity distribution. The relative uncertainties on the experimental points were determined by the inverse of the square root of the number of counts, according to the Poisson statistics. Since the fit function (Gaussian) not always corresponded to the correct function, the statistical uncertainty was increased until the square root of the χ^2 divided by the degrees of freedom was approximately 1. Due to the asymmetry of the Poisson distribution, a confidence interval of 68% is not symmetric around the most probable value. This fact results in not symmetric error bars. This asymmetry is important for low counting and tends to disappear in case of a large number of events. In our data, a difference of a few percent between the relative upper and lower error bars is reflecting this asymmetry. Larger differences are connected to the different influence of the systematic uncertainties.

The five systematic uncertainties are due to: 1) the uncertainty on the width and mean value of the velocity distributions, 2) the calibration factor that converts the beam-monitor counts into ^{238}U projectiles, 3) the evaluation of the angular transmission, 4) the thickness of the target, 5) the secondary reactions.

The first uncertainty is the largest one. Due to the incompleteness of data, the fit of the velocity distribution for the single isotope was done providing the mean values and the standard deviations. In figure 2.18 we presented a case in which a change of the mean value of 4% resulted in a variation of 30% in the cross section. Small variations in the deduced velocity are expected due to fluctuations in the position calibration of x_2. For this reason the mean value was let free to vary, within a relative limitation of 2% from its nominal value (obtained with the global fit). This assures that, whenever the peak of a distribution was well defined, the result was correct. We estimated that this procedure introduced a relative uncertainty of 15%. For the same reason, whenever there were no data covering the peak of a distribution, the result was discharged. The result was discharged also for those isotopes whose velocity was such that the magnetic rigidity coincided with the magnetic rigidity of the most produced low-energy fission residues. The cross section of the latter can be 10000 times higher than that one of the observed fragments. In this case, the high load of the first scintillator introduces a systematic error on the measured counts. The production rate of light fission fragments produced in the hydrogen target was comparable with that one of the fragmentation events in the titanium vessel. For these nuclides an additional uncertainty due to the propagation of the uncertainty on the fragmentation cross sections was considered.

The beam-monitor calibration introduced a relative uncertainty of 7%, as said in section 2.4.

The formulas to evaluate the angular transmission are well established, but the values $\upsilon_{\perp}$, $\overline{\upsilon}$, $\sigma_{\upsilon\, frag}$, used in the calculation, suffer from experimental uncertainties. We estimated that they introduce a relative uncertainty of 6%.

The thickness of the target was established with an uncertainty of 3% by a dedicated measurement. In addition to this, another uncertainty arises from the fact that the thickness varies with the vertical position. The value we used in the evaluation of the cross section is 87.3±2.2

mg/cm^2 which corresponds to the maximum thickness of the target. The target was positioned near its maximum thickness, but an uncertainty on its vertical position of 6 mm was considered. This gives a total uncertainty of 6%.

Finally, the secondary reactions, as we said, bring an uncertainty that varies from isotope to isotope.

The final results on the mean values and on the standard deviations of the velocity distributions are given only for the combined spectrum of three close elements. The velocity distributions for the single isotopes did not show any substantial deviation from these values. The statistical uncertainty was calculated from error propagation. Also for the velocity parameters, the statistical uncertainty was increased until the square root of the χ^2 divided by the degrees of freedom was approximately 1. The only systematic uncertainty that contributes to the uncertainty of the velocity parameters is the one on the transmission. In the case of fragmentation the systematic uncertainty on the mean velocity is around 0.025 cm/ns. In the case of fission the uncertainty is negligible.

2.6.6 Evaluation of the fragmentation cross sections and mean velocities for the nuclei with Z<22

As explained in section 2.5.1 there are evidences [Nap04] that the longitudinal velocity distributions (inside the angular acceptance of the FRS) of light nuclei should show the triple humped spectra as found for the heavier nuclei analysed in this work. Napolitani showed that with respect to the system Fe+H the fission-like humps of the system Fe+Ti are less separated and much broader, and that the mean position of the two peaks is more shifted to the negative velocities. We expect that the same situation has to be found also in the system U+Ti with respect to the system U+H. This would explain the differences in the fission spectra of the two systems (U+Ti and U+H) that can be seen in figures 2.13 and 2.14. So, we expect that for the system U+Ti the forward fission-like[1] component is shifted to the left with respect to the system U+H. This effect combines with the trend of the fragmentation hump to move towards positive velocities as the nuclear charge of the fragment decreases (see chapter 6 for a wider discussion). The net effect is that the forward fission-like peak is not visible anymore.

In order to evaluate the fragmentation cross sections for the light products, we made the following assumptions:

- the fragmentation process is isotropic,
- the forward fission-like hump exists and it is completely covered by the fragmentation hump,
- the size (area) of the forward fission-like hump can be calculated form the backward fission-like hump, corrected for the backward-to-forward ratio of the fission transmissions.

Under these assumptions, the fragmentation cross sections were obtained from the yield of the fragmentation hump, obtained from the difference of the integral of the central hump and the integral of the estimated forward hump. Once the yield of the light fragmentation residue is known, the cross sections can be determined by taking into account the transmission coefficient, with the same method used for the heavier nuclei, as explained in section 2.6.1 and thereafter.

In order to have an idea of the contribution of the forward component to the central hump, we present in figure 2.23 a comparison of the yields of the central and backward humps. The following features can be found from the analysis of the isotopic distributions of figure 2.23:

---

[1] Here we use the expression “fission-like” to stress again the fact that it is due to a process with fission-like kinematical pattern (which could be fission or any kind of decay with one heavy remnant).

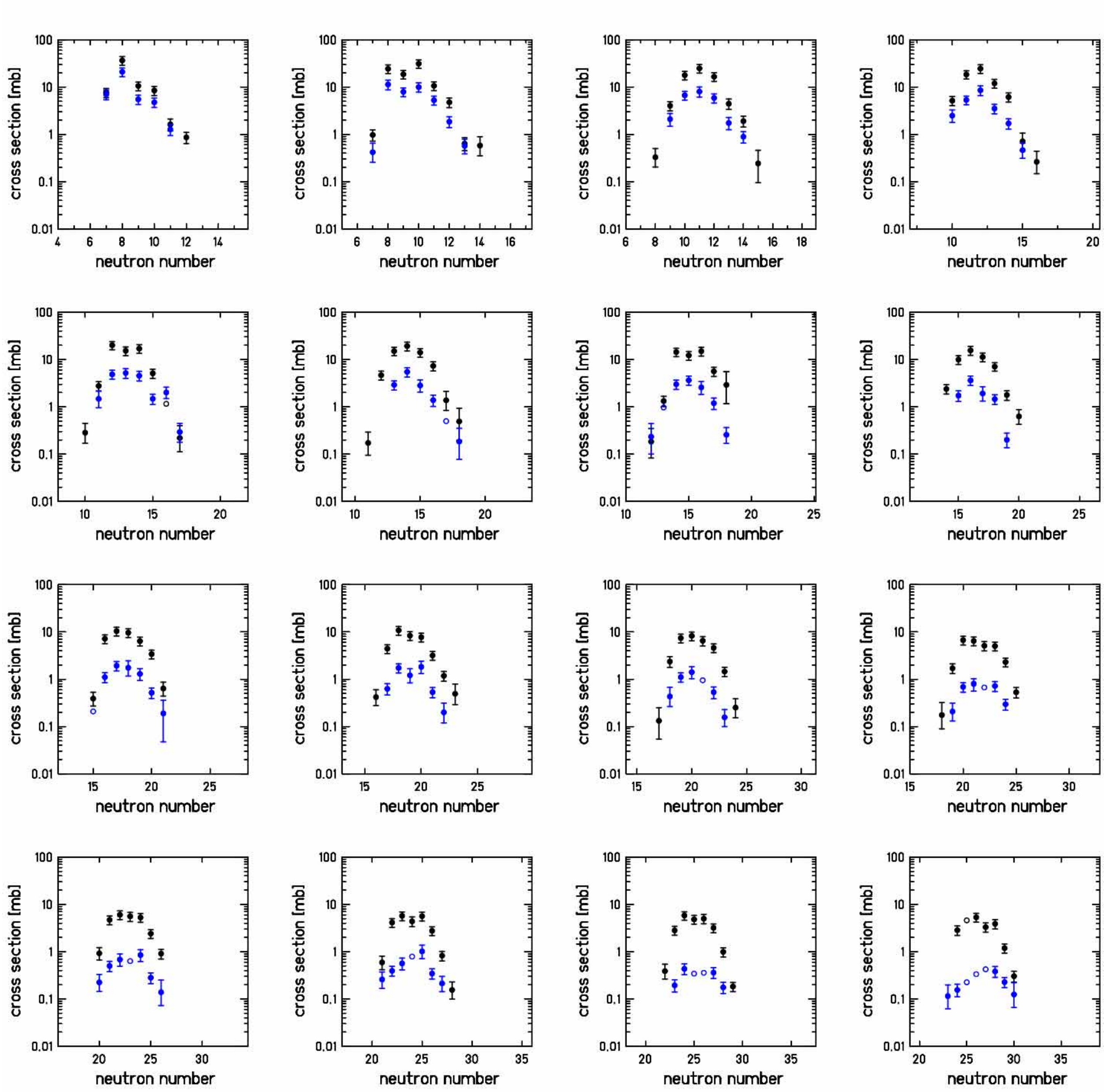

Figure 2.23: Isotopic distributions from Z=7 to Z=22 (from left to right). Comparison of the yields corresponding to the central hump (black) and to the hidden forward hump (blue). The yields of the forward hump were corrected from the presence of a hidden forward hump, whose intensity was deduced from the backward hump (see text for details).

- the yield of the central hump is much higher than the yield of the backward hump. This means that, even if the assumptions listed above were false, the production cross sections of the central hump, attributed to fragmentation, are slightly affected. The error bars were determined to cover this uncertainty,

- the isotopic distributions for the two types of contributions (backward hump and central hump) show the same structure. This has an important consequence: the subtraction of the yields does not lead to any modification of the shape of the isotopic distributions, obtained from the integral of the fragmentation Gaussian components given by the fits. In particular the mean value

($<N>/Z$) and the staggering structure (appearing as an even-odd effect) are not affected by the subtraction of the backward component. These two features, the mean value $<N>/Z$ and the even-odd effect, will be widely discussed in chapters 5 and 7, respectively.

One may be surprised by the fact that the isotopic distributions of the backward hump, attributed to a fission-like process, and of the central hump, attributed to fragmentation, present the same $<N>/Z$. This is probably due to the fact that for the case of light products the phase space available for the decaying nucleus is limited, since the valley of stability is very narrow. The same effect is found for the isotopic distribution of the fission products of the system ^{238}U+H, as will be shown in chapter 4. Also the appearance of the same even-odd structure in the two components could be surprising; the reason for this will be given in chapter 7.

An interesting question is how the subtraction of the backward hump affects the mean position of the central hump. In chapter 6 we will see that the shift of the mean positions of the central hump towards positive velocities has an important physical significance. Here we want to discuss how to determine the lower limit of the mean velocity of the fragmentation light products.

To do this, we fitted again the first four spectra of figure 2.13, this time using three Gaussian functions instead of two. The position, width and area of the third Gaussian, corresponding to the forward hump, were defined a priori, and were not let free to vary during the fit. The area was calculated from the area of the backward peak, increased by the backward-to-forward ratio of the fission transmissions. The width was assumed to be the same of that one of the backward peak. The value of the mean position was chosen as the most extreme value to the right such that the Gaussian forward hump remains completely covered by the central hump. This extreme position to the right of the forward hump was determined controlling that the value of the χ^2 of the fit did not suddenly increase by a slight shift of the forward Gaussian to the right. In correspondence to these values, we obtained the results presented in figure 2.24. The mean values of the central Gaussian obtained with these fits are smaller than those presented in the left picture of figure 2.15. Each of the spectra of figure 2.24 is a combination of all the isotopes of three elements. Since the fragmentation cross sections differ slightly for three close elements, we estimated the atomic number making the average of the three nuclear charges, weighted with the respective cross sections. Analogously, we estimated the atomic number also for the spectra of the nuclei with $Z>21$, presented in figure 2.13. All data are collected in table 2.2. All the results in table 2.2 include the correction for the limited angular acceptance, discussed in section 2.6.4 and presented in figure 2.22.

It is clear that the mean position of the forward hump should vary smoothly with the fragment nuclear charge, as shown in the left pictures of figures 2.15 and 2.16. This means that the position of the forward Gaussian curve depicted in the last picture of figure 2.24 (combination of $Z=19,20,21$) is rather reasonable. For the lower nuclear charge, it is difficult to imagine how far from the real value the lower limit determined with the above-described method could be. But as will become clear in chapter 6, for the physical significance of this effect, the most interesting point is to establish the lower values of the mean velocity.

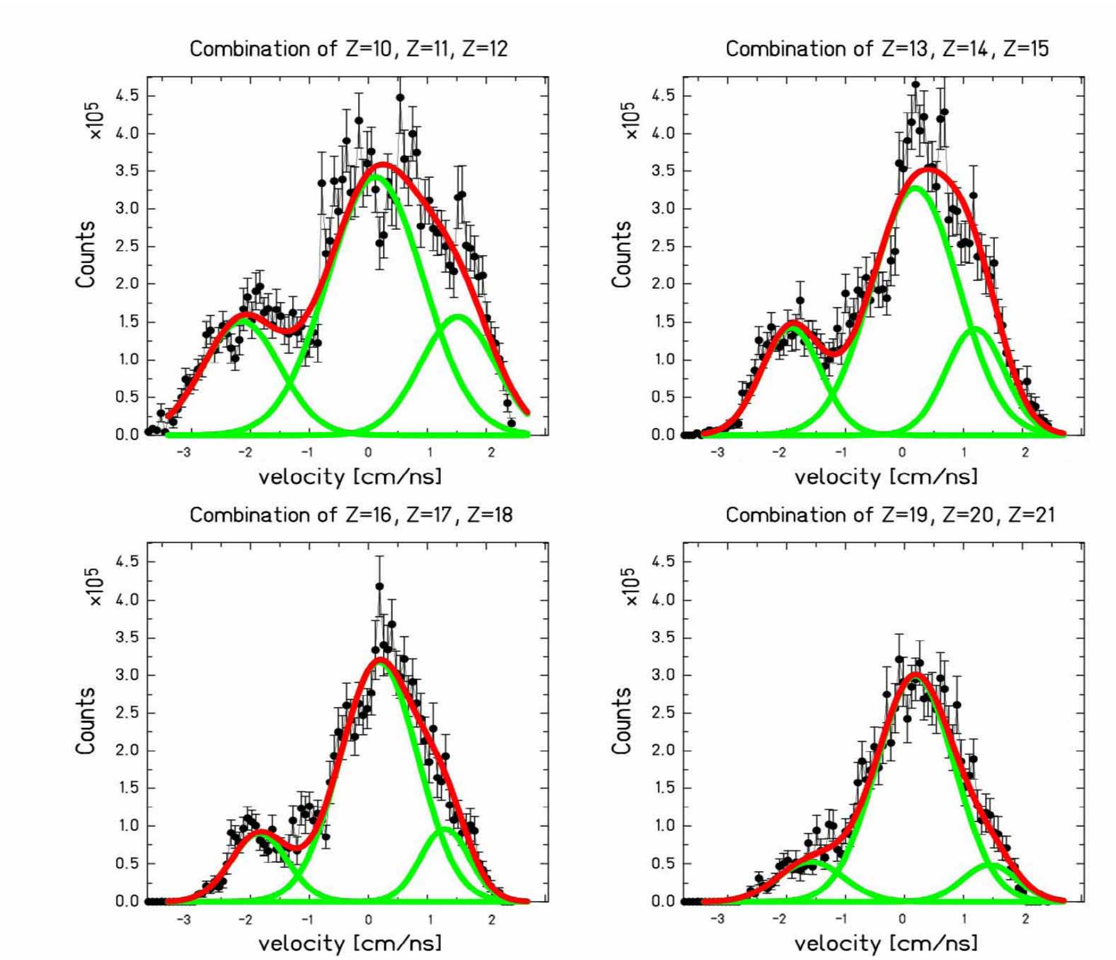

Figure 2.24: Fit of the velocity spectra for the products of the reaction 1·A GeV ^{238}U with titanium. The fit was obtained imposing the values of the area, of the width and of the mean position of the forward peak.

Table 2.2: Mean values of the fragmentation products for the system $^{238}U+Ti$. For Z<22 only lower limits are given (see text for details).

atomic number	mean velocity (cm/ns)	mean position of central peak(*) (cm/ns)
10.96±0.04	> 0.19±0.03	0.39±0.03
13.90±0.06	> 0.18±0.02	0.38±0.02
16.91±0.06	> 0.18±0.02	0.30±0.02
19.96±0.08	> 0.18±0.03	0.21±0.03
22.95±0.09	0.11±0.02	
25.99±0.10	0.06±0.02	
29.02±0.12	-0.05±0.03	
31.98±0.13	-0.12±0.03	
35.04±0.14	-0.08±0.05	
38(**)	-0.08±0.04	

(*) Here, the mean position of the central peak of figure 2.13 was corrected for the effects of the limited angular acceptance of the fragment separator. For Z>22, this value coincides with the mean velocity of the fragment.

(**) The combination of Z=37, 38, and 39 could not be weighted for the cross sections, because for technical reasons we could get fragmentation cross sections only below Z=37.

Chapter 3
Results

3.1 Experimental results for the reaction ^{238}U on ^{1}H at 1 *A* GeV

In this section, the measured cross sections and velocity distributions of the isotopes of the elements between *Z*=7 and *Z*=37 produced in the interaction of ^{238}U with hydrogen at 1 GeV per nucleon are presented.

As shown in Chapter 2, the velocity pattern of these fragments indicates a strong Coulomb repulsion in the decay of a rather heavy system, which might be fission, evaporation or any kind of break-up reaction with one heavy remnant. It is reasonable to expect that fission is the dominant production mechanism of the binary products with larger atomic number (Z=37 and close below). M. Bernas et al. [Ber03] showed that all the characteristics of the nuclides formed in this same reaction (^{238}U + ^{1}H at 1 *A* GeV) in the range $28 \leq Z \leq 64$ are consistent with a fission production mechanism. However, it is not straightforward to assume that fission remains the dominant reaction mechanism also for the production of the lighter fragments. In Chapter 4 we will discuss the role of fission and the possible contribution of other decay channels. Here, for simplicity, we will always refer to these light products as "fission fragments".

3.1.1 Measured production cross sections

In figure 3.1, the isotopic distributions of oxygen, sulphur and chromium are shown as examples. The complete presentation of the cross sections in form of isotopic distributions is reported in figure B.1 of appendix B. The numerical results are collected in table B.1 of appendix B. The experimental results were obtained from the analysis described in section 2.5.2. The production cross sections of some isotopes are missing, because the magnetic-field settings for those isotopes were not performed. In addition, some data had to be discharged for technical reasons (see section 2.6.5 for details). The data points are connected with a dashed line. When a data point is missing the dashed lines have to be taken just as guidelines for the eye. They do not represent the real physical content, since generally the data do not follow a continuous behaviour. The reason for this will become clear in Chapter 7; the specific case of fission will be treated in section 7.3.

The lengths of the isotopic chains and their positions with respect to the stable nuclides vary significantly among the elements that were observed. This can be noticed in figure 3.1, and even more in figure 3.2, where the totality of the nuclide cross sections from the system ^{238}U + ^{1}H at 1 *A* GeV, analysed in this work, is presented on the chart of the nuclides.

The data on light-nuclide production in the reaction 1·*A* GeV ^{238}U on hydrogen analysed in the present work belong to a systematic study of nuclide production in proton-induced reactions needed for the design of the accelerator-driven system. Three other works proceeded in parallel to analyse the data: in the fission region (28≤Z≤64, [Ber03], and 65≤Z≤73, [Ber04]), and in the fragmentation region (74≤Z≤92, [Tai03]). In this systematic study, the present work covers the part of the lightest nuclei (below Z=37). The entire compilation of the data is available in [DATA]. The complete overview on residual-nuclide production cross sections was presented in ref. [Arm04] and it is shown in figure 3.3 as a cluster plot on the chart of the nuclides. These data represent the most complete residual-nuclide distribution of a proton-induced spallation reaction on uranium ever obtained.

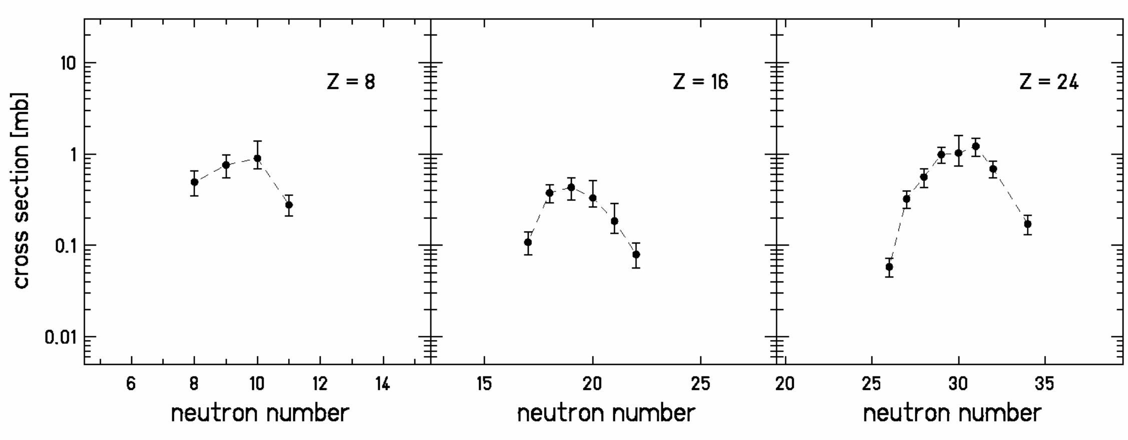

Figure 3.1: Isotopic cross sections for oxygen, sulphur and chromium from the reaction ^{238}U on hydrogen at 1 GeV per nucleon. The dashed lines are set to guide the eye.

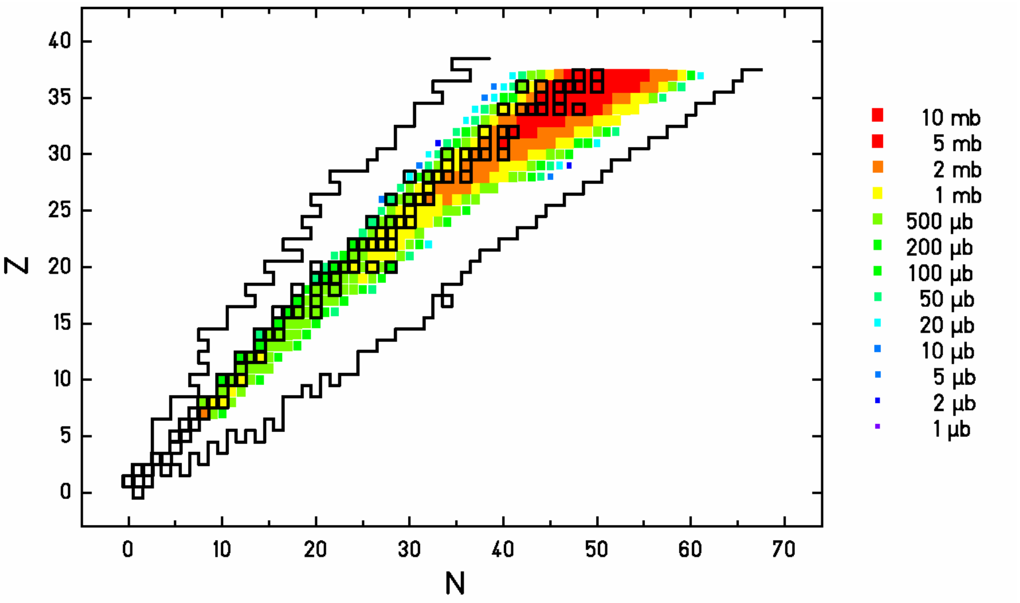

Figure 3.2: Two-dimensional cluster plot of the nuclide production cross sections in the reaction $^{238}U + {}^{1}H$ at 1 A GeV, measured in this work, on a chart of the nuclides. The numerical values of the measured data are collected in Table B.1. For those nuclides which could not be measured, the cross sections were extrapolated from the existing data by smoothing the isotopic distributions. The open black squares correspond to stable nuclides. The lines indicate the limit of the known nuclides.

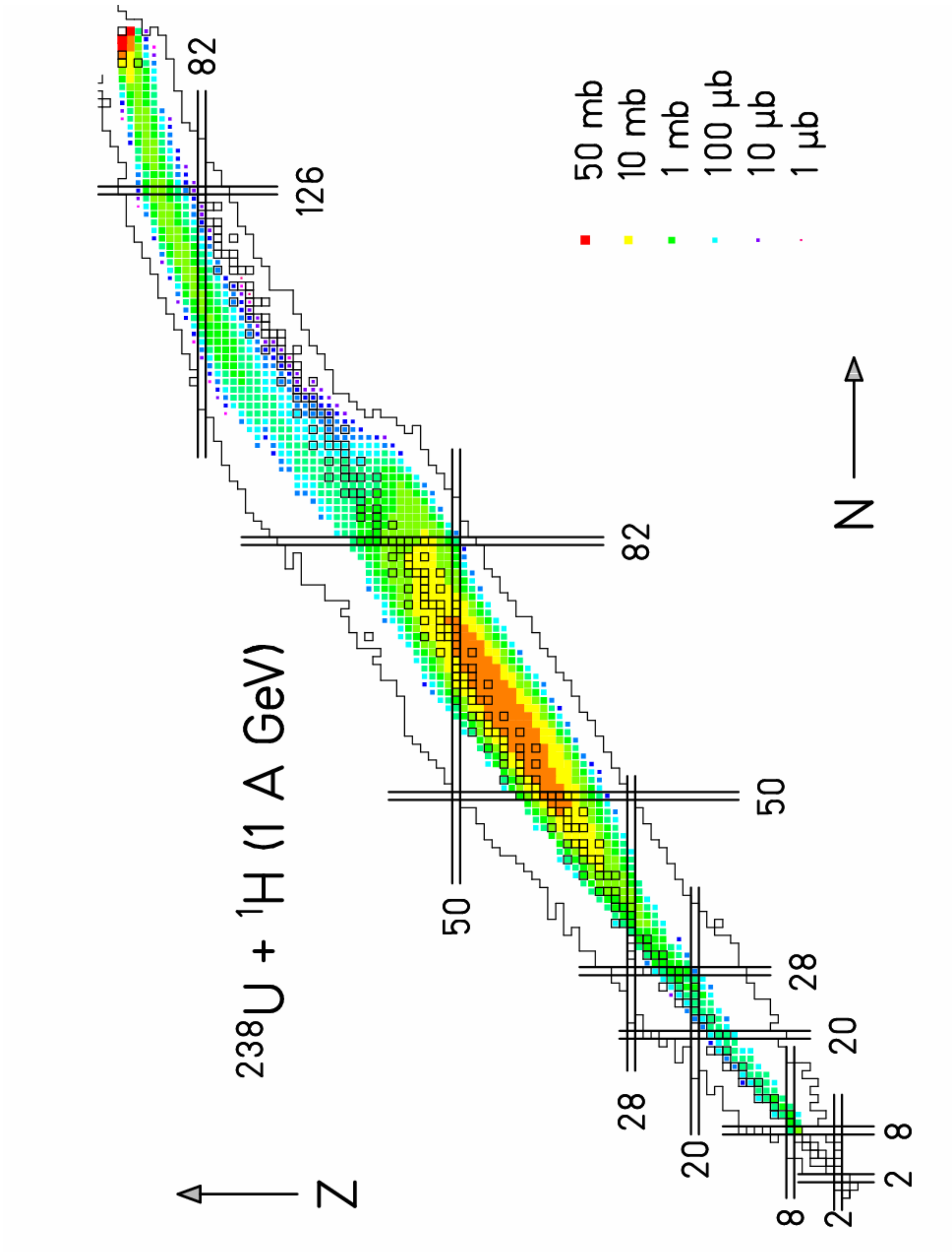

Figure 3.3: Nuclide cross-sections of the reaction ^{238}U + ^{1}H at 1 A GeV measured at the FRS at GSI, presented on the chart of the nuclides. The data presented here are taken from: this work (below Z=37), ref. [Ber03] (for 38≤Z≤64), ref. [Ber04] (for 65≤Z≤73), ref. [Tai03] (above Z=73). The open black squares correspond to stable nuclides. The lines indicate the limit of the known nuclides. Nuclides with Z≤6 were not measured.

Regarding the region of light masses, three interesting aspects can be noticed from figure 3.1 and from the overview of figures 3.2 and 3.3. The isotopic distributions are long and shifted towards the neutron-rich side for heavy fragments; they shorten and move towards stability as the mass decreases. A second interesting effect is the fact that the production extends down to very light fragments. Our measurement was technically limited to $Z \geq 7$, but the production seems to extend even farther down. A third feature is the height of the cross sections. As expected, the cross sections are very high in the main fission region (around $Z=44$) and decrease rapidly from $Z=30$ to $Z=20$. But then they stay constant and finally increase again below $Z=10$, as will be clearly shown in figure 3.9. All these aspects will be discussed in Chapter 4.

3.1.2 Velocity distributions

In addition to the production cross-sections, the velocity distributions of the fragments were measured. All fragments from the reaction $^{238}U + ^{1}H$ at 1 *A* GeV analysed in this work appear in two velocity peaks, one clearly lower, the other clearly higher than the beam velocity. This observation is compatible with the scenario of a binary decay of a heavy emitting source with an isotropic angular distribution. The two peaks represent the fraction of the fragments emitted predominantly in forward and backward direction, which fall into the angular acceptance of the FRS (see figure 2.11). The mean velocities and the standard deviations of these two peaks were evaluated for every element. They were obtained from the common fit to the velocity distributions of all nuclides with the method described in section 2.5.1. The variations of the mean velocities and of the standard deviations in the isotopic chain of one element were found to be small.

In figure 3.4-a, the mean velocities of the fragments emitted in forward and backward directions, deduced from the forward and backward peaks of the velocity distributions, are presented in the beam frame. The velocities were corrected for the mean energy loss of the projectiles in the first half of the target and for the mean energy loss of the reaction products in the second half of the target as described in section 2.3. In addition, the average of these two values is shown, which corresponds to the mean recoil velocity of the mean mother nucleus in the beam frame. In figure 3.4-a, the absolute values are slightly larger than those presented in figure 2.16 because the influence of the finite angular acceptance of the spectrometer has been corrected, as explained in section 2.6.4. Data stop at Z=17 because the forward peak was not clearly disentangled below Z=16 (see section 2.5.1). The characteristics of the velocity distribution for could be determined also for Z=38 and Z=39 (although the production cross sections for the isotopes of these two elements were not deducible because these elements fall at the border of the last dipole and part of their yield could be cut by the dipole walls). The mean velocity of the fragments, presented in the frame of the mother nucleus, is shown in figure 3.4-b. A magnification of the mean recoil velocity of the mother nucleus in the beam frame as a function of the atomic number of the fragment is shown in figure 3.4-c. Figures 3.4-b and 3.4-c include also the data obtained in a parallel analysis ([Ber03]). In all three figures the error bars which are not visible are inside the data points. Numerical values are collected in table B2 of Appendix B.

To conclude this section, we present in figure 3.5 the standard deviations of the velocity distributions of the fragments observed in forward and backward directions for $Z \geq 17$. The widths of the velocity distributions of the lighter nuclei with $Z<17$ could not be determined with good precision, mostly due to the relatively large correction for the production in the titanium windows. The result of the global fit described in chapter 3 is shown by the lines in figure 3.5. The widths of the velocity distributions are presented as a function of the atomic number of the nuclides because inside the error bars no variation was observed among isotopes of the same element (see for instance figure 2.8).

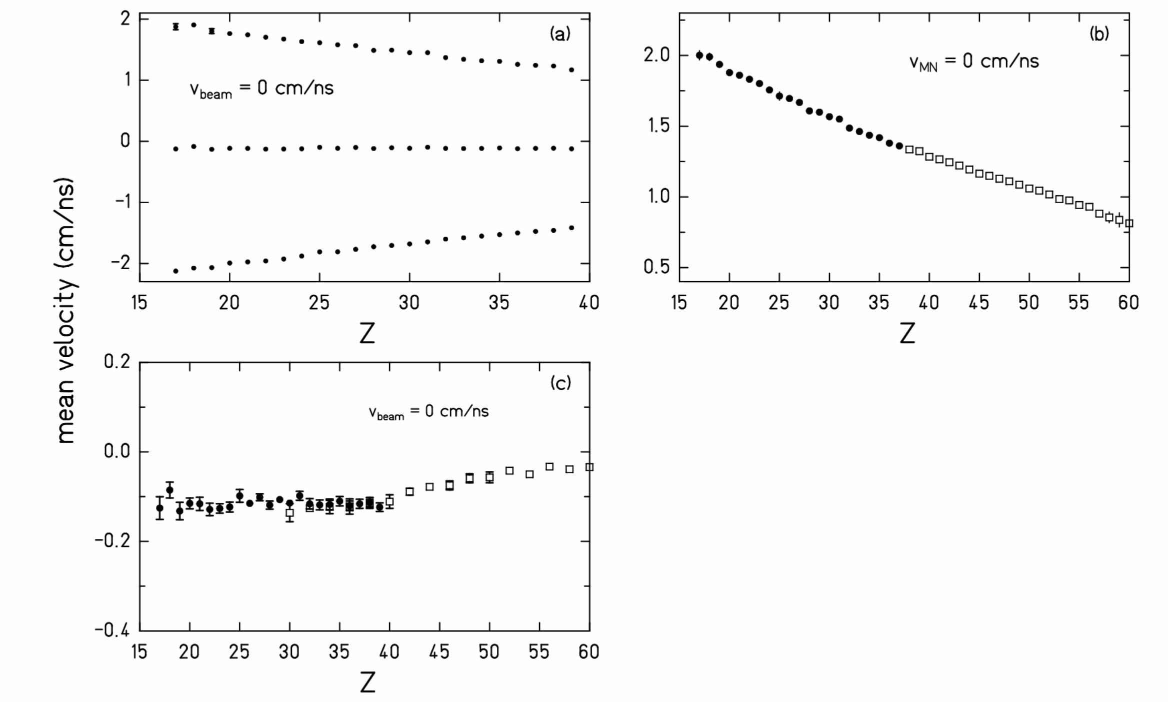

Figure 3.4: a): Mean velocities of the fragments emitted in backward and forward direction and mean velocity of the mean mother nuclei, presented in the beam frame (υ_{beam}=0 cm/ns); b): Mean values of the velocities of the fragments in the frame of the mother nuclei: this work (full dots), ref. [Ber03] (empty squares); c); Mean recoil velocities of the mother nuclei presented in the beam frame: this work (full dots), ref. [Ber03] (empty squares). All values are drawn as a function of the atomic number of the fragment.

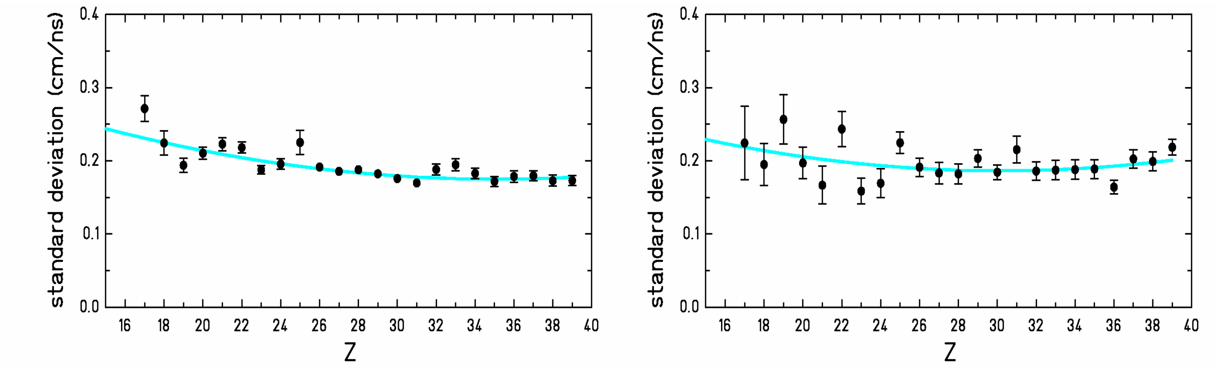

Figure 3.5: Left: Standard deviations of the velocities of fragments observed in backward (left) and forward (right) acceptance range, produced in the reaction ^{238}U + ^{1}H at 1 A GeV. The light lines are the result of the global fit described in chapter 2. The data are affected by the FRS angular transmission and by the location straggling in the target.

These curves do not give direct information on the physics of the reaction, since the widths of these distributions are affected by two main disturbing contributions. One is the finite angular range accepted by the FRS, which introduces an increase in width in the longitudinal momentum (see figure 2.11), that is larger for larger nuclear charges [Sch98], which are more transmitted than the light ones. The difference in energy loss of projectile and fragments in the target before and after the reaction introduces another energy broadening of the residues, named “location straggling” by Dufour [Duf86], which slightly decreases with increasing nuclear charge. Both effects depend mostly on the atomic number, Z. In table 3.1, the measured widths of the backward velocity humps have been corrected for these two contributions for two nuclei, Ar and Sr (in the calculation two isotopes were used). The energy loss was calculated with the program AMADEUS [AMA] and the effect of transmission by means of the equations presented in section 2.6. For a specific nuclide, the relative width in velocity induced in the reaction ($\sigma_{\upsilon}^{\mathrm{react}}/\upsilon$) results to about 9 %, approximately constant over the whole range of Z. This corresponds to a relative width in kinetic energy of the fragments of about 18 %.

Table 3.1: Contributions to the measured width $\sigma_{\upsilon}^{\mathrm{meas}}$ *of the backward peak of the velocity distribution of two fragments: due to location straggling (*$\sigma_{\upsilon}^{\Delta\mathrm{E}}$*) and due to the variation of the Z component of velocity in the transmitted angular range (*$\sigma_{\upsilon}^{\mathrm{T}}$*). The velocity width caused by the reaction* $\sigma_{\upsilon}^{\mathrm{reac}}$ *is deduced.*

Nuclide	σ_{υ}^{meas}	$\sigma_{\upsilon}^{\Delta\mathrm{E}}$	$\sigma_{\upsilon}^{\mathrm{T}}$	$\sigma_{\upsilon}^{\mathrm{reac}}$
^{40}Ar (Z=18)	0.21 cm/ns	0.087 cm/ns	0.092 cm/ns	0.17 cm/ns
^{90}Sr (Z=38)	0.19 cm/ns	0.064 cm/ns	0.118 cm/ns	0.13 cm/ns

3.1.3 Comparison with other data

Nuclide production

The existing knowledge on nuclide production in proton-induced reactions at this energy was indeed quite scarce. Before the use of inverse kinematics, the measurement of the formation cross-sections of individual nuclides mostly relied on their radiochemical properties and on the online mass-separator technique. In most counter experiments only mass distributions are obtained. In a recent experiment with secondary beams a large number of element distributions has been determined [Sch00], however no mass identification could be given. Only a few experiments on thermal-neutron-induced fission, performed at ILL, Grenoble, have given a rather comprehensive overview on the nuclide production in the light fission-fragment group for a few even-even systems [Gön91], however not extending below $Z \approx 26$ [Ber93]. Data of excellent quality on nuclide production from higher excitation energies only exist for fission induced by relativistic ^{238}U projectiles in various targets, e.g. [Enq99, Sch98], but they did not extend to very light elements. One of the few experiment with full isotopic distribution of products is that one of rubidium (Z=37), measured by Belyaev et al. [Bel80] in 1980. The comparison with the new data is presented in figure 3.6. The two sets of data essentially agree within their error bars. The figure shows a very long isotopic chain, extending over about 20 isotopes, from the very neutron-rich to the stable ones.

Yields of very light nuclides produced in interactions of 600 MeV protons with ^{238}U were already observed in direct kinematics [Klu86]. As an example, in figure 3.7 the potassium isotopic distribution obtained in our experiment is compared to the yields obtained at ISOLDE from 600 MeV protons in a thick uranium-carbide target [Klu86]. The yields from the ISOLDE experiment (scale on the right) were normalised to our cross sections (scale on the left). The difference in energy is not expected to produce a significant difference in the cross sections [Pro01]. The isotopic distribution is quite neutron rich with respect to the beta-stability valley. Since the ISOL method provides high efficiencies for a limited number of elements only, there was no knowledge on the overall nuclide production in the target from these measurements. Figure 3.3 can be considered a sort of "map" of the potentially available radioactive beams by proton-induced reactions using a ^{238}U target. In addition, the systematic results offered by our measurements can be exploited for the determination of the efficiency of the ISOLDE technique.

The data of ref. [Bel80] and [Klu86] were measured in direct kinematics. The experiments could not supply any information on the velocities, thus there was no knowledge on the reaction process that produced them. The velocity characteristics of the data measured in our experiment indicate that the rubidium and potassium nuclides formed in proton-induced spallation of ^{238}U at 1 *A* GeV originate from the binary-decay of a heavy nucleus. We can deduce that also the data of ref. [Bel80] and [Klu86] have the same kinematical characteristics.

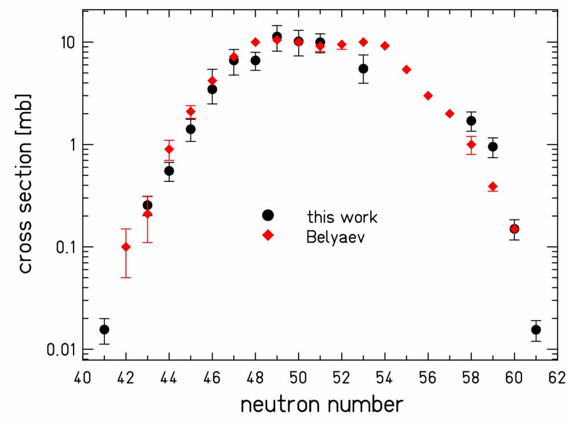

Figure 3.6: Comparison of the fission cross sections of the isotopes of rubidium (Z=37) from the interaction of 1 GeV protons with ^{238}U measured in direct kinematics (♦), ref. [Bel80], and in inverse kinematics (●), this work.

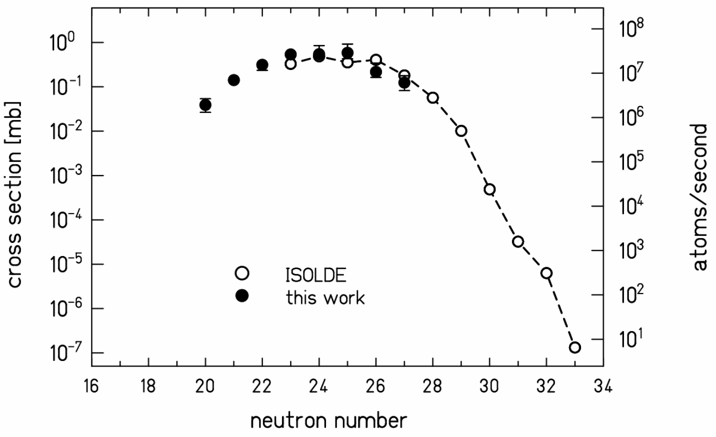

Figure 3.7: Measured cross-sections of potassium isotopes from 1 A GeV ^{238}U in hydrogen of this work (open dots) are compared with the yields of potassium isotopes from the reaction of 600 MeV protons in a thick uranium-carbide target (closed dots), measured at ISOLDE [Klu86]. The yields from the ISOLDE experiment (right scale) were normalised to the cross sections of this work (left scale).

In 1958 the production of ^{24}Na from proton-induced reactions on several targets at several energies was investigated [Car58]. The result for 1 GeV protons on ^{238}U can be compared with our data. The two measurements give: (0.63±0.16) mb [Car58] and (0.53±0.12) mb [this work]. The results agree within the error bars.

Mass and charge distributions

A few additional rather dispersed data are available for yields of nuclides from reactions of protons with heavy nuclei. Most of them were measured with radiochemical detection methods in experiments performed in direct kinematics [Wol56, Gro62, Kat68, Eng74, Kau80, And86]. Only in few cases, as for instance for 340 MeV protons on tantalum [Ner55], the mass distribution, deduced from the experimental data, extended with continuity from tantalum to very light fragments, forming an W-shaped distribution (see figure 3.8-left). In an experiment performed at LEAR (Low Energy Antiproton Ring) at CERN [Hof94], the mass distribution of fragments produced in the antiproton-induced fission of ^{238}U nuclei at 5.9 MeV was obtained. Due to the proton-antiproton annihilation, this beam kinetic energy is expected to introduce similar excitation energy as a 1 GeV proton beam. The fission products could be selected by their kinetic energy and by a coincidence condition. The mass spectrum shows a minimum between A~20 and A~40 (see figure 3.8-center). A similar behaviour was observed also in nucleus-induced reactions on a heavy nucleus, such in 8.4·A MeV ^{232}Th + ^{12}C [Sar89] (see figure 3.8-right).

The mass and charge distributions of the binary-decay products observed in this work also present a similar shape, as can be seen in figure 3.9, where the data of this work are presented together with the data analysed by M. Bernas [Ber03]. These results will be discussed in section 4.2.

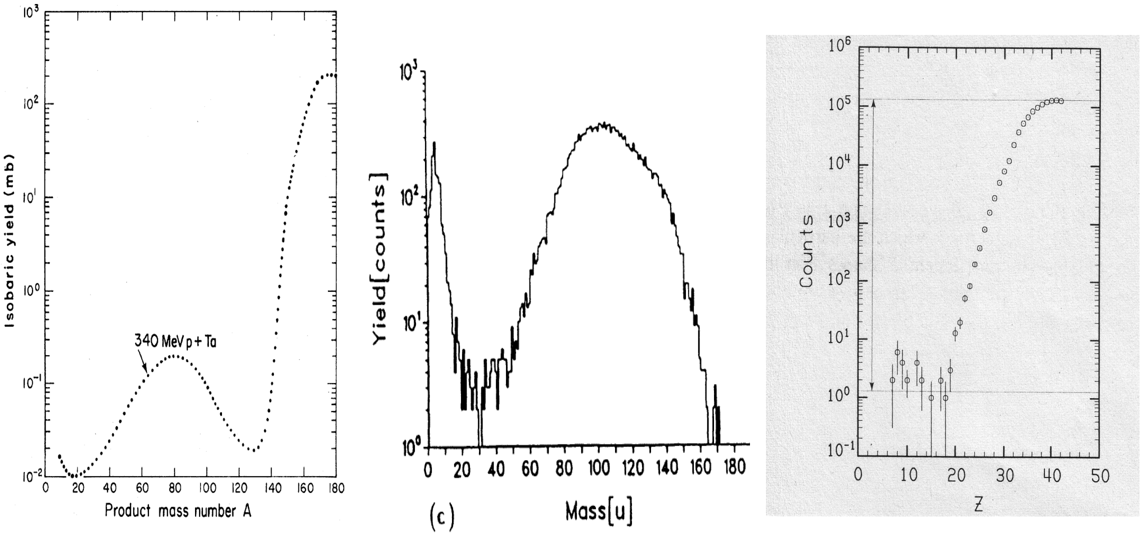

Figure 3.8: Left: Estimated isobaric cross-sections obtained from measured nuclides produced from 340 MeV protons on tantalum [Ner55]; Centre: Coincident-mass spectrum for binary product from the U($\overline{p}$,X) reaction, measured at LEAR [Hof94]. Right: Relative yields of the binary events as a function of the Z-value, measured in the reaction 8.4·A MeV ^{232}Th + ^{12}C [Sar89].

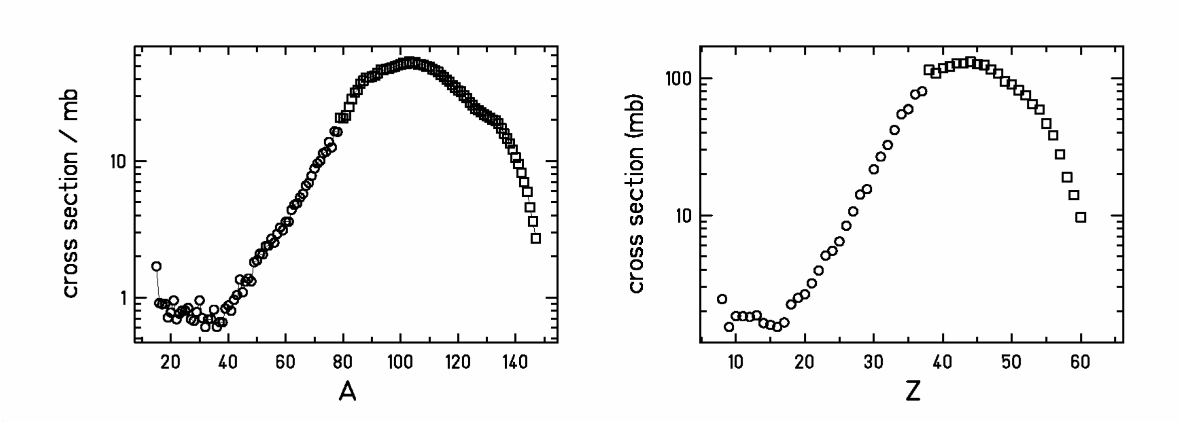

Figure 3.9: Mass and charge distributions of binary-decay products measured in the reaction of ^{238}U+p at 1 GeV. Dots: this work; squares: ref. [Ber03].

<u>*Velocities*</u>

In the review "Fission of highly excited nucleï", Andronenko et al. [And87] collected a large amount of experimental data for reactions induced by 1 GeV protons. Among other results, the review summarizes data on angular distributions, mean longitudinal momenta and kinetic energies. Besides the review of Andronenko such kind of data are reported and discussed in several publications, e.g. [Ale63], [Zol74], [Wes78], and [Bar86]. However, we could not find any measured data directly comparable with the light fragments produced in ^{238}U + ^{1}H at 1 *A* GeV, analysed in this work.

3.2 Experimental results for the reaction ^{238}U on Ti at 1 A GeV

In Chapter 2, we showed that the velocity pattern of the products of the reaction ^{238}U on Ti at 1 *A* GeV indicates the superposition of two kinematically different components: a large central hump, attributed to fragmentation, and two external peaks, attributed to fission. In the present work, only the analysis of the central component was carried out completely, in order to determine the production cross sections and mean velocities of the residual fragments. The analysis of the two external fission peaks was hindered by technical reasons[1].

In this section, the measured cross sections and velocity distributions of the nuclides produced by the fragmentation of ^{238}U with titanium at 1 GeV per nucleon are presented.

In literature, there are several evidences that residual nuclei with mass close to the mass of the mother nucleus can be successfully described by an abrasion-evaporation ("fragmentation") model, which implies the development of the surviving nucleus after the

---

[1] The absence of the forward peak for light fission fragments and the missing data in the forward peak of those heavy fragments whose magnetic rigidity coincided with the magnetic rigidity of the beam did not allow reconstructing in an accurate way the velocity spectrum of the fission fragments. Without this precise knowledge, the determination of the production cross section becomes unreliable.

abrasion into a compound nucleus. On the other hand, there are also evidences that the production of extremely light residues requires the simultaneous formation of a number of intermediate-mass fragments (a "multifragmentation" process). The masses of the fragments studied in this work occupy somehow an intermediate position, and it is not clear a priori if one or the other mechanisms is responsible for their production. Their velocity pattern is represented in the beam frame by a three-dimensional Gaussian. In fragmentation, the Gaussian-like shape is attributed to the momenta of abraded nucleons [Gol74] and to the recoil of evaporated particles. However, also multifragmentation with some subsequent evaporation would produce a similar velocity distribution.

At this stage, we cannot clearly deduce the production mechanisms of the residues formed in the reaction ^{238}U + Ti at 1 *A* GeV. In this chapter we will call the light residues from the reaction ^{238}U+Ti at 1 *A* GeV "fragmentation residues", although we will conclude (Chapter 5 and 6) that a break-up picture would be probably more appropriate. Actually, in this chapter we will only present the experimental results. The discussion and interpretation of the results will be divided in three separate subjects, treated in Chapters 5, 6 and 7.

3.2.1 Measured production cross sections

In this section the measured isotopic production cross sections for elements from nitrogen to rubidium, produced in fragmentation reactions of ^{238}U in titanium, are presented.

For $Z \geq 22$, the data were obtained from the fit of the main peak in the velocity spectra (see figure 2.11), attributed to fragmentation, as explained in section 2.5.2. By means of equation 2.20, the fragmentation cross sections were obtained using the angular-transmission values calculated assuming angular isotropy. A compilation of the data is presented in table B.5 of Appendix B.

In the velocity spectra of products with $Z<22$, the forward fission-like hump was hidden below the central hump, attributed to fragmentation. A devoted technique had to be used to extract the value of the fragmentation cross sections (see section 2.6.6). The so obtained data are presented in table B.4 of Appendix B. Since that technique was based on same specific assumptions, differential production cross-sections integrated between 0 and 15 mrad are given for $Z<22$ in table B.3 of Appendix B. These latter results were obtained directly from the experimental data without any assumption about the contributing reaction processes.

Concerning the interaction target, we must keep in mind that the uranium projectiles did not only interact with the titanium target nuclei but also with the nuclei of the beam monitor, placed in front of the target. The number of nuclei per area in the monitor (8.9 mg/cm^2 of aluminium, equivalent to $0.33 \cdot 10^{-3} \cdot N_A$ atoms/cm^2) amounts to less than half the value in the titanium target (36.3 mg/cm^2 of titanium, equivalent to $0.76 \cdot 10^{-3} \cdot N_A$ atoms/cm^2). Since the distances of the beam monitor and of the titanium target from the entrance of the FRS are different, the angular cut seen by the fragments produced in the two sources is also different. The cross sections are normalized to the number of target nuclei, corrected for the two different angular transmissions. For the lightest elements, the transmission of the fragments produced in the SEETRAM is about 25% of the transmission of the fragments produced in the titanium target. This means that more than 90% of the observed events originate from the titanium target. Since the characteristics of the nuclide production cross sections are expected to be very similar [Süm00], the small contamination from reactions in aluminium are not crucial.

In figure 3.10, the measured isotopic distributions of oxygen, sulphur and chromium are depicted as examples. A complete presentation of the cross sections in form of isotopic distributions is shown in figure B.2 of appendix B. Please note that the zigzagging structure in the cross sections, which will be discussed in chapter 7, is not due to experimental inaccuracy.

Figure 3.11 summarises the totality of the fragmentation production cross sections analysed in this work, on the chart of the nuclides. With this overview it is possible to mark two general tendencies. The first one is that the intensity increases with decreasing mass. This feature is expected for fragmentation in the low-mass region. The second general tendency is that the more the mass decreases the more the production shifts towards the neutron-rich side of the valley of stability. This result, completely unexpected in the traditional picture of fragmentation reactions, will be discussed and interpreted in the Chapter 5.

In figure 3.12, the mass and charge distributions for the fragmentation of 1·A GeV ^{238}U on titanium are presented. Numerous fragmentation cross sections have been measured under different conditions (targets, projectiles, beam energies). The available experimental data indicate that the production cross sections decrease with decreasing mass of the fragment, reach a minimum (or even stay flat) and then increase steeply for very light fragments, forming characteristic mass and charge distributions which look like a "U" [Hüf85]. The distributions of figure 3.12 are consistent with the previous results, reproducing the expected rising of the cross sections with the decreasing mass and charge of the fragments. The shape of the "U-distributions" can vary noteworthy from one case to the other, depending on the reacting system and on the total energy. For this reason, it will not be possible to compare quantitatively our data with the data of another system. It is interesting to note that the charge distribution shows an evident even-odd effect in the yield of the lighter fragments. Chapter 7 will be devoted to a detailed discussion of this result.

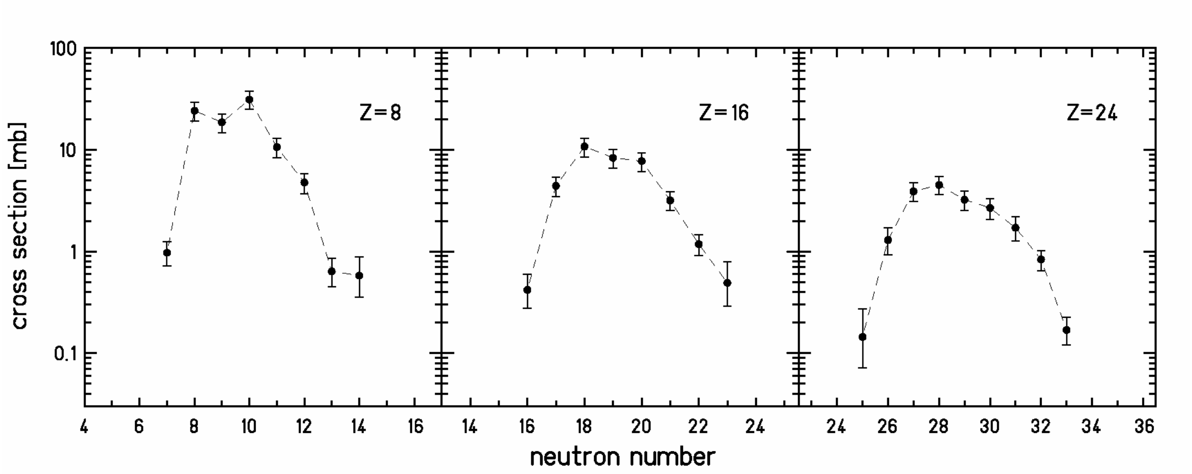

Figure 3.10: Isotopic distributions for oxygen, sulphur and chromium originated from the fragmentation of 1·A GeV ^{238}U in titanium.

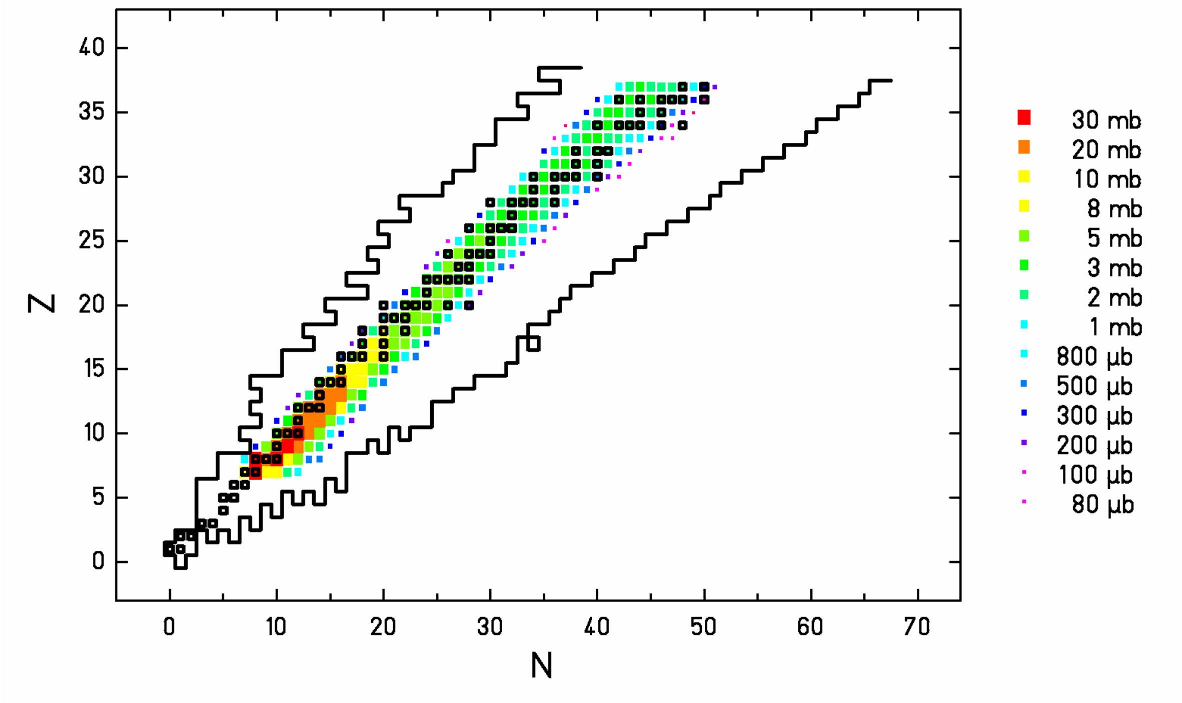

Figure 3.11: Two-dimensional cluster plots of the fragmentation cross-sections for the reaction 1·A GeV ^{238}U with titanium, obtained in this experiment, shown on a chart of the nuclides. The numerical values of the measured data are collected in tables B.4 and B.5. For those nuclides which could not be measured, the cross sections were extrapolated from the existing data by smoothing the isotopic distributions. Open black squares correspond to stable nuclides. The border line signs the limit of the known nuclides.

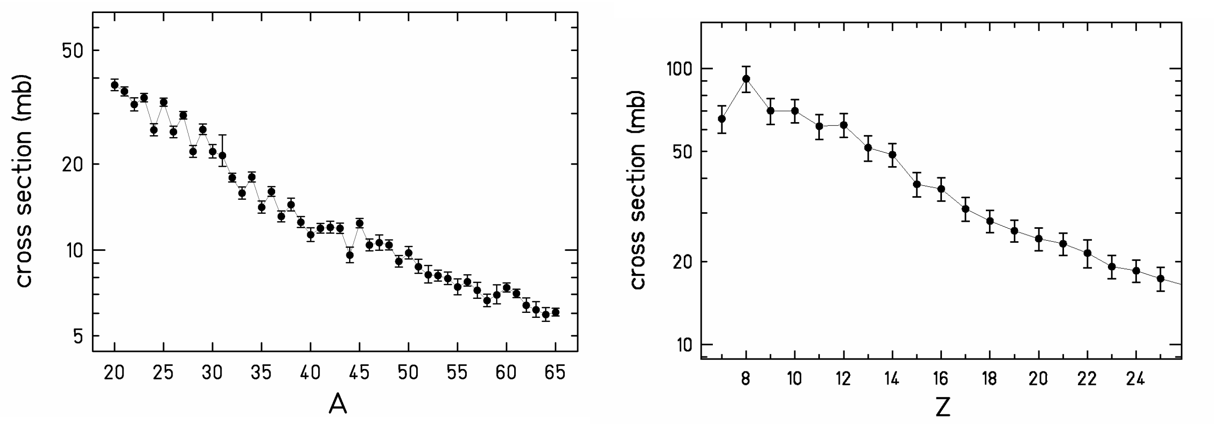

Figure 3.12: Mass and charge distributions for the lightest uranium fragmentation residues observed in this experiment, produced in the reaction 1·A GeV ^{238}U on titanium.

3.2.2 Velocity distributions

In this section, we will present the results on the velocity distributions of the produced nuclides. No distinction could be done among the characteristics of the velocity distributions of the isotopes of the same element.

Here, we present two types of results: the result of the global fit, described in section 2.5.2, with which the general tendencies of the velocity distributions were found, presented as a continuous curve, and the result derived from the fit made on the distributions of figure 2.13, presented as data points. The data points are given every third element because the velocity distributions of figure 2.13 result from the combination of all the isotopes of three close elements. The determination of the mean velocities of the fragmentation products from the fit of the spectra of figure 2.13 was explained in sections 2.5.2 (for Z≥22) and 2.6.6 (for Z<22).

In figure 3.13 the experimental results for the fragmentation of ^{238}U on titanium are presented in the beam frame ($\upsilon_{beam} = 0$) as a function of the charge of the fragment. The numerical values of the data points were listed in table 2.2. For Z≥22 the data points are derived from the mean position of the central hump of the velocity spectra, but with respect to the results of figure 2.15 here the correction for the angular cut of the FRS is taken into account. The curve gives the result of the global fit. The curve does not include the correction for the angular cut of the FRS. For Z<22 the open points gives the lower possible value of the mean velocity determined as described in section 2.6.6; the full dots indicate the mean position of the main hump of the velocity distributions of figure 2.13, corrected for the angular cut of the FRS.

The tendency of the mean velocity is evident: the velocity increases with decreasing mass. As we will show in section 6.2, this result is not understandable in the light of the traditional picture of fragmentation reactions. The results on the mean velocity of the light fragments will be discussed and interpreted in Chapter 6.

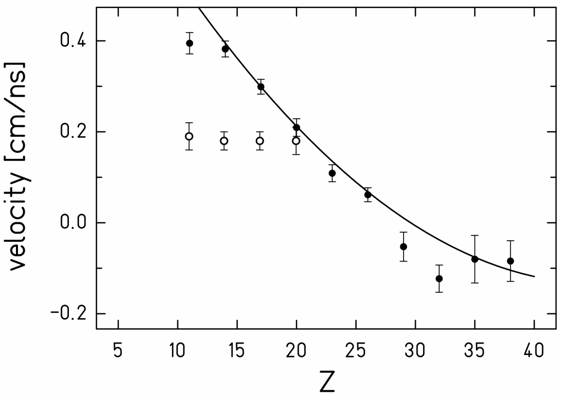

Figure 3.13: For Z≥22: Mean values of the velocity distributions for the projectile fragmentation of ^{238}U on titanium at 1 A GeV. For Z<22: The full dots represent the mean position of the central peak of the velocity distributions obtained by fitting the spectra of figure 2.13, corrected for the angular transmission of the FRS. The empty circles give the lower possible values of the mean velocities of the fragmentation products, estimated as explained in section 2.6.6. The curve gives the result of the global fit.

In figure 3.14 the standard deviations of the velocity distributions of the fragments is presented. The result of the global fit described in Chapter 2 is shown by the line. We observe a drastic increase in the width of the velocity distributions of the lightest elements.

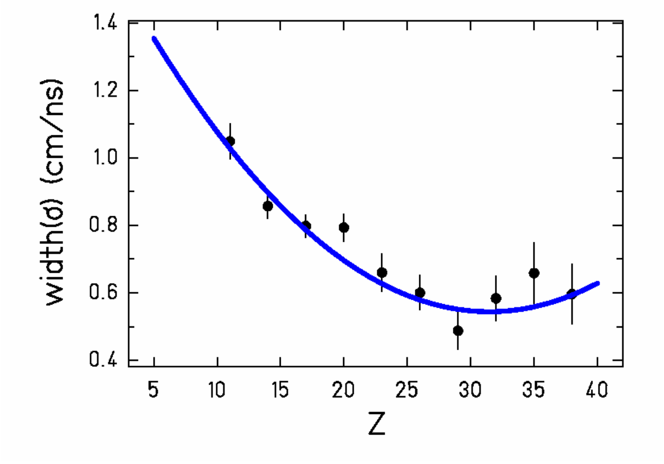

Figure 3.14: Standard deviation of the velocity distributions for the projectile fragmentation of ^{238}*U on titanium at 1 A GeV. The full dots represent the results obtained by fitting the spectra of figure 2.13. The empty circles are extrapolated data. The curve gives the result of the global fit.*

Chapter 4
The binary decay of 1·*A* GeV ^{238}U on hydrogen

4.1 Possible mechanisms for the production of the light-nuclides

In this chapter, the reaction mechanisms behind the production of light nuclides in reaction ^{238}U on hydrogen at 1 GeV per nucleon, analysed in the present work, will be discussed. These light products are characterised by the production cross sections depicted in figure B.1 of Appendix B, and summarised in the chart of the nuclides in figure 3.2, and by the kinematical properties depicted in figure 3.4.

In this context, it is useful to have an overview of the whole production for the reaction ^{238}U on ^{1}H at 1 *A* GeV, presented on the chart of the nuclides in figure 3.3.

The proton-rich heavy evaporation residues, filling the upper part of the chart of the nuclides, are kinematically characterised by narrow, Gaussian velocity distributions, with mean values close to the velocity of the projectile. In the past, it was assumed [Kös01] that the light fragments produced in proton-induced reactions of ^{238}U originate from the spallation-evaporation of uranium. Selecting kinematically the evaporation residues, Taïeb et al. [Tai00] proved that the spallation-evaporation corridor dies out rather soon (around Z=70). The length of the evaporation corridor is determined by the excitation energy introduced in the system, which is rather low for ^{238}U+hydrogen (typically a few hundred MeV).

Around Z=70, the spallation-evaporation residues encounter another class of products, filling the neutron-rich side of the chart of the nuclides: the fission fragments. The fission data were measured in the present experiment and analysed by M. Bernas [Ber03, Ber04]. As explained in section 2.5.1, due to the angular cut of the FRS, the fission fragments are characterised by a double-humped distribution of the longitudinal velocity. The shorter is the distance between the two humps the smaller is the velocity of the fragment. At Z>63, the two humps start to merge and form a single hump. Up to the last element investigated (Z=74) the width of this hump is too large to be interpreted as the velocity spectra of just an evaporation residue. Thus the large width of the hump indicates the presence of a fission fragment and, at the same time, the existence a complementary light fission partner with large velocity. Bernas showed that the velocity increases as the mass of the fragment decreases. The data analysed by Bernas merge perfectly with the light fragments analysed in this work (see figure 3.4-b).

So, in a consistent way with what observed by Bernas, the present experiment proves by the velocity distributions that the light nuclides in the spallation of ^{238}U by 1 *A* GeV protons are produced together with a complementary heavy residue. The Coulomb repulsion from the complementary heavy residue explains the large velocity in the beam frame. These velocities follow on with continuity the pattern indicated by the fission fragments (figure 3.4-b). Also the charge and mass distributions of figure 3.9 do not present any discontinuity. All the experimental evidences indicate that the light residues observed in this work are fission fragments. As will be discussed in the next section, it is even expected from theoretical considerations and proven by several experiments that mass distributions in fission show increased production yields for very asymmetric mass splits. These very asymmetric splits have been interpreted as a natural transition to evaporation.

The fission-evaporation mechanism contributes for sure to the production of light fragments. However, one may question whether this is the *dominant* production process. In the past, it was discussed [Bar86] if the production of the light nuclides could be due mostly to a fast decay occurring from the break-up of the nucleus right after the intra-nuclear cascade phase. Such a process would release residual nuclei having similar characteristics as the fragments observed in the present work: large velocities – increasing as the mass decreases – and rapidly increasing cross sections below Z=10.

In view of these considerations, we will discuss at first the role of fission-evaporation in the production of the light residues (section 4.2). At the end of the chapter, the contribution of a possible break-up channel will be discussed (section 4.3).

4.2 Fission

4.2.1 Transition from fission to evaporation

According to the transition-state model, the decay rate for fission depends on the properties of the fissioning nucleus in the "transition state", i.e. on the phase space available at the saddle-point configuration. The saddle point represents a kind of bottleneck through which the nucleus is forced to pass on the way to fission [Boh39]. At the saddle point the potential energy, U, associated with the shape (deformation, ε) of the nucleus, $U(\varepsilon)$, has reached a maximum. The height in energy of this maximum with respect to the ground state of the nucleus is the fission barrier, B_{fiss}. The potential energy as a function of the nucleus deformation depends on mass-asymmetric deformations, which lead to the formation of two fragments of different size. The relation between mass-asymmetry deformation at saddle and mass split at scission is assumed to be essentially strict and undisturbed by fluctuations due to the dynamics of the system between saddle and scission [Mor88]. If A_1 and A_2 are the masses of the two fragments, the mass-asymmetric deformation can be expressed in terms of the "mass asymmetry parameter", $\eta=A_1/(A_1+A_2)$. Consequently, also the fission barrier can be calculated for every mass asymmetry: $B_{fiss}(\eta)$. The potential energy forms a ridge line along the mass-asymmetry coordinate whose points are called "conditional saddle points", because of the constraint of a fixed mass asymmetry [Mor88]. The energy of the conditional saddle points as a function of the mass asymmetry is illustratively presented in figure 4.1 for some nuclear systems. A description of the correlation of the variation of the height of the conditional saddle with mass asymmetry with the final mass distribution can be found in ref. [Itk98].

In the statistical model of fission [Mor75] for a given excitation energy, E^*, the yield of a certain fission fragment is calculated by the statistical weight of the transition states above the conditional potential barrier. This weight is in turn correlated to the density of nuclear levels. In the thermodynamic Fermi-gas picture, i.e. assuming the nucleus as a system of non-interacting fermionic particles, the density of states is in good approximation:

$$\rho(E^*) \propto e^{2\sqrt{aE^*}} \quad \text{with} \quad E^* = E^{ags} - B_{fiss}(\eta) \quad \text{and} \quad a \cong A/10 \ \ MeV^{-1} \tag{4.1}$$

where E^* is the energy above the saddle point and E^{ags} is the energy above the ground state. The yields as a function of mass asymmetry are then given by:

$$Y(\eta, E^*) \propto e^{2\sqrt{a\left(E^{ags} - B_{fiss}(\eta)\right)}} \tag{4.2}$$

The result, for a heavy fissile nucleus at high excitation energies, is approximately a "W-shaped" distribution (see figure 4.1), whose maximum is at the symmetric split.

The central part of the M-shaped potential can in first approximation be described by a parabola, whose stiffness, C_η, affects the width of the central part of the mass distribution, which becomes a Gaussian function, whose variance is given by:

$$\sigma^2(\eta, E^*_{\eta=1/2}) = \frac{1}{2}\sqrt{\frac{E^*}{a}} \cdot \frac{1}{C_\eta} = \frac{1}{2}\frac{T}{C_\eta} \quad \text{being} \quad T = \sqrt{\frac{E^*}{a}} \tag{4.3}$$

The excitation energy introduced in the system and the stiffness of the potential affect the width of the mass distribution. Therefore, in a heavy system, the difference in intensity from the top of the yield at symmetry (for x=0.5 in figure 4.1-right), to down where the stiffness changes sign (for $A_1/A_1+A_2=0.08$ in figure 4.1-right), is very large at low excitation energies. The consequence of this fact is that in most of the experimental observations available in literature, limited to some tens of nanobarns, fission seems to die out at about Z≈25. This is one of the reasons why the very light products (from A=1 to A~20) have been always called "evaporation fragments", as well as the heavy residues "evaporation residues". For a long time fission and evaporation were treated as separated

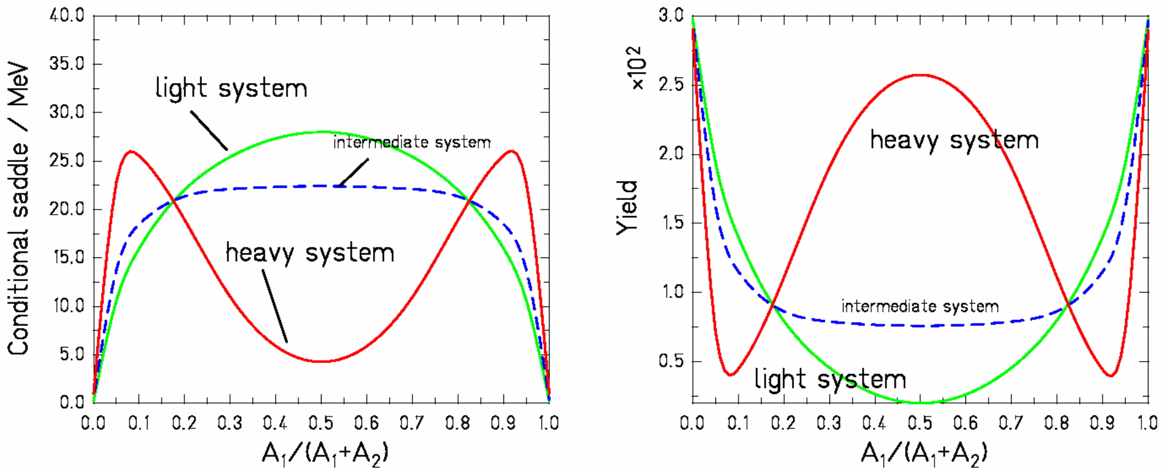

Figure 4.1: Left: Schematic presentation of the fission-barrier height for a given mass split for a light, an intermediate and a heavy system. Right: corresponding yields (arbitrary units).

processes. Moretto [Mor75] pointed out and discussed the inconsistency of the two separate pictures and proposed that evaporation and fission should be treated as two manifestation of the same kind of binary decay with a continuous transition to be considered fission in a generalised sense [Sto88].

In the review "Fission of highly excited nuclei" published by Andronenko et al. [And87] the mass distributions show the characteristics expected from the general properties of fission barriers as a function of mass asymmetry [Bus57] illustrated by figure 4.1: While for heavy fissioning systems symmetric fission distributions are observed, characterized by Gaussian distributions which are centred around half the mass of the mother nuclei, lighter systems show flat or even U-shaped distributions. Thus, these findings are compatible with a generalised fission process, according to the proposition of Moretto. The mass distributions of figures 3.8-centre [Hof94] and 3.8-right [Sar89] were attributed to high-energy fission, extending to very large mass asymmetry. While in these two cases it was possible to verify the binary nature of the decay, for the mass distribution of figures 3.8-left [Ner55] no information on the kinematics was possible. However, we believe that the left tail of the distribution reflects the transition from fission to evaporation, because the total available excitation energy is rather lower than that one of the other two cases.

To conclude, in the decay of any excited fissile compound nucleus, the full mass range is expected to be populated by binary decay, understood as a generalisation of evaporation and fission. Therefore, this process for sure contributes to the production of light residues in the spallation reaction analysed in this work. Whether it is the dominant production mechanisms or not will be discussed in section 4.3.

4.2.2 The scission configuration

The mean velocity of fission fragments can be estimated by the following empirical liquid-drop description of the total kinetic energy:

$$TKE = \frac{Z_1 Z_2 e^2}{D} \qquad \text{with} \qquad D = r_0 A_1^{1/3}\left(1+\frac{2\beta_1}{3}\right) + r_0 A_2^{1/3}\left(1+\frac{2\beta_2}{3}\right) + d \tag{4.4}$$

where A_1, A_2, Z_1, Z_2 denote the mass and charge numbers of a pair of fission fragments prior to neutron evaporation. D repesents the distance between the two charges and is given by the fragment radii ($r_0A^{1/3}$), corrected for the deformation (β), plus the neck (d). The parameters (r_0=1.16 fm, d=2.0 fm, β_1=β_2=0.625) were deduced from experimental data in ref. [Böc97] and are consistent with values previously found in the analysis of ref. [Wil76]. The formula (4.4) is valid for sufficiently excited nuclei, where shell effects are negligible. When the momentum conservation is imposed to the reaction, the velocities of the two fission fragments are determined.

We have estimated the mean velocities of the fission fragments for two compound nuclei: ${}^{238}_{92}\mathrm{U}$ and ${}^{185}_{79}\mathrm{Au}$. They are compared with our data in figure 4.2. While for the heavier fragments, the experimental data fall in between these two estimates, for fragments below Z = 25, the mean velocity tends to be higher than the estimation for the ${}^{238}\mathrm{U}$ compound nucleus. This is probably due to the fact that the experimental parameters of equation 4.4 that were obtained in symmetric fission are not applicable to very asymmetric mass splits.

In very asymmetric fission, both the neck (parameter d) and the deformation (parameter β) might be smaller, with a consequent increase of the kinetic energy.

To verify the validity of this assumption, we have performed a calculation of the mean velocity in case of asymmetric binary decay from undeformed nuclei. We assumed that the binary decay can be described as the inverse process of fusion. The shape of the potential is given in terms of the nuclear, Coulomb and centrifugal contributions:

$$V_{eff} = -V_N + \frac{Z_1 \cdot Z_2 \cdot e^2}{r} + \frac{l(l+1)\cdot \hbar^2}{2\mu r^2} \tag{4.5}$$

where Z_i are the charges, r is the distance between the centers of the nuclei, μ is the reduced mass, and l is the quantum number for the angular momentum. In our calculations, the empirical nuclear potential of R.Bass [Bas79] is used:

$$V_N(r) = -\left(\frac{C_1 \cdot C_2}{C_1 + C_2} \cdot 1\Big/\left(0.033\,exp\left(\frac{r - C_1 - C_2}{3.5\,fm}\right) + 0.007\,exp\left(\frac{r - C_1 - C_2}{0.65\,fm}\right)\right)\right)\frac{MeV}{fm} \tag{4.6}$$

where:
$$C_i = \left(R_i - \frac{0.9984^2}{R_i^2}\right)fm \quad R_i = \left(1.28A_i^{1/3} - 0.76 + \frac{0.8}{A_i^{1/3}}\right)fm \tag{4.7}$$

R_i represent the values of the radii, A_i the masses, and C_i the position at which the nuclear force is maximum. The total kinetic energy of the two nuclei is assumed to be equal to the height of the potential barrier. Imposing momentum conservation, the velocity of the two fragments was determined. The result of this calculation for the compound nuclei ${}^{238}_{92}\mathrm{U}$ and ${}^{185}_{79}\mathrm{Au}$ is represented in figure 4.2 by the dashed lines. The experimental data fall in between the cases of a split into highly deformed nuclei and undeformed nuclei.

This result gives an indication that the lightest fragments are produced in configurations which are more compact than predicted by the systematics (4.4) that is based on more symmetric fission.

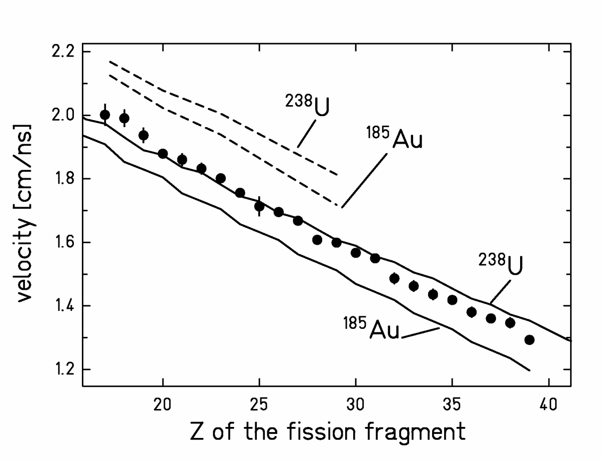

Figure 4.2: Measured mean values of the velocities of fission fragments in the frame of the fissioning nucleus (●). The lines represent expected values of the velocity of fragments originated in the compound nuclei ${}^{238}U$ and ${}^{185}Au$. The solid lines represent the expected velocities for the scission-point model (deformed nuclei) and the dashed lines the values obtained by the nucleus-nucleus fusion approach (undeformed nuclei).

4.2.3 Comparison with the ABRABLA code

Mass distribution

From the integral of the isotopic distributions we obtained the production cross section of every element. The result of this analysis is presented in form of a charge distribution in figure 4.3. The data show a clear deviation from the Gaussian at about Z ≈ 20.

In the proton-induced fission reaction of ^{238}U this feature is unambiguously identified with the present experiment. The observed change of slope of the charge distribution can be related to the underlying M-shaped potential energy as a function of mass asymmetry (see figure 4.1). The present experiment provides the full isotopic distributions for these elements for the first time. This is an extremely important information, not only for the physics content, but also for the technical applications. Most of the codes used to predict formation cross section in fission reactions for technical applications are based on empirical systematics (e.g. [Atc80]). Others, based on the conditional-saddle point model, represent the potential energy at saddle by a parabola (with some additional structures in order to take into account the effect of the shells at low excitation energies, e.g. [Ben98]). This approximation was considered sufficient since fission was expected to die rapidly below Z~25. Our results show that this is not the case. The correct shape of the potential has to be introduced to improve the predictive power of the codes. In figure 4.3 the dashed line represents the prediction obtained with ABRABLA [Gai91]. ABRABLA is a statistical model where, after the proton-nucleus interaction, the pre-fragment at every step of its evolution has two possible decay channels: evaporation and fission. Evaporation is treated as described in ref. [Jun98] and fission as described in ref. [Ben98]. In the fission model of ABRABLA the barrier as a function of mass asymmetry is defined by three components. The first is the symmetric component defined by the liquid-drop potential by means of a parabolic function with a curvature obtained from experimental data [Mul98]. This parabola is modulated by two neutron shells, represented by Gaussian functions. Shells are supposed to wash out with excitation energy [Ign79]. The heights and the widths of the

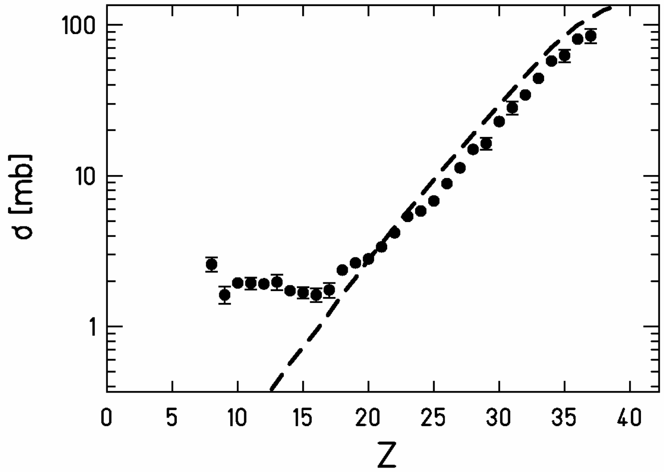

Figure 4.3: Fission cross sections for elements produced in ^{238}U (1·A GeV) + p. The dashed line represent the prediction of ABRABLA.

Gaussians representing the shell effects and additional fluctuations in mass asymmetry acquired from saddle to scission are derived from experimental data [Ben98]. The prediction is good where the charge distribution is determined by the parabolic behaviour of the potential, but then it deviates drastically. In figure 4.4, five isotopic distributions are compared with the calculation. The calculation underestimates the cross sections appreciably, because the conditional saddle is overestimated, with the consequent reduction of the fission decay width. The shape of the isotopic distributions however, which reflects the charge polarisation [Arm70] in the fission process and the evaporation of neutrons, seems to be well reproduced.

Mean value and width of the isotopic distributions

Other results of the isotopic distributions of every element are presented in figure 4.5. There the N/Z-ratio and the standard deviations of the distributions are shown as a function of the proton number. The solid black line represents the stable isotopes. The dark grey light lines are the result of the ABRABLA prediction.

In the fission model inside the ABRABLA code, the population of the fission channels is assumed to be basically determined by the statistical weight of transition states above the potential-energy landscape at the fission barrier, as described in the previous section. Several properties, however, are finally determined at scission, among them the mean value and the fluctuations in the neutron-to-proton ratio, which are responsible for the so-called "charge polarisation". The fluctuations in the neutron-to-proton ratio are considered by describing the potential in this degree of freedom by a parabolic function. Assuming that the equilibration in this variable is fast compared to the saddle-to-scission time, the curvature of this potential was calculated in a touching-sphere configuration. Consequently, two fission pre-fragments are obtained and their excitation energies are calculated from the excitation and deformation energy of the fissioning system at the scission point. A full description of the model is given in ref. [Ben98].

It can be noticed that the ABRABLA calculation reproduces correctly the mean values (the $\langle N \rangle / Z$-ratio) of the isotopic distributions. Also the qualitative trend of the widths is well described, although the standard deviations are slightly overestimated. This is an indication that both the charge polarisation in the fission process and the competition with the evaporation of nucleons in the statistical model are well described in the code.

The products are neutron rich, as expected to be in fission. Compared to electromagnetic-induced fission (see for instance ref. [Don98, Arm96, Enq99]), where the mean N/Z is close to the one of ^{238}U, here the neutron abundance is less deceptive, demonstrating that the process occurred at higher excitation energies. The neutron enrichment decreases slightly with the decreasing mass, as well as the width of the distribution. The latter effect is more evident. The reason for these tendencies is connected to the fact that the valley of stability becomes quickly narrow and the large fluctuations in N/Z become more and more unlikely.

To conclude this section, we like to point out that the result of the ABRABLA code is remarkable, because the theoretical model behind it could never be compared before with experimental results on fully identified nuclide distributions in the region of light fission fragments from proton-induced fission. Data on the production of nuclides, fully identified in Z and A, by nuclear fission are scarces. In most experiments only mass distributions are obtained [Gön91], in a recent experiment with secondary beams a large number of element distributions has been determined [Sch00], however no mass identification could be given. Only a few experiments performed at ILL, Grenoble, on thermal-neutron-induced fission have given a rather comprehensive overview on the nuclide production in the light fission-fragment group for a few systems [Gön91], however not extending below $Z \approx 30$. Since ^{238}U does not fission after capture of thermal neutrons, no data of that kind are available for this nucleus. Data of excellent quality on nuclide production from higher excitation energies only exist for fission induced by relativistic ^{238}U projectiles in various targets, e.g. [Arm96, Don98, Sch98, Enq99], but they did not extend to very light masses. In our experiment, full isotopic distributions of light elements from the fission of ^{238}U were measured for the first time.

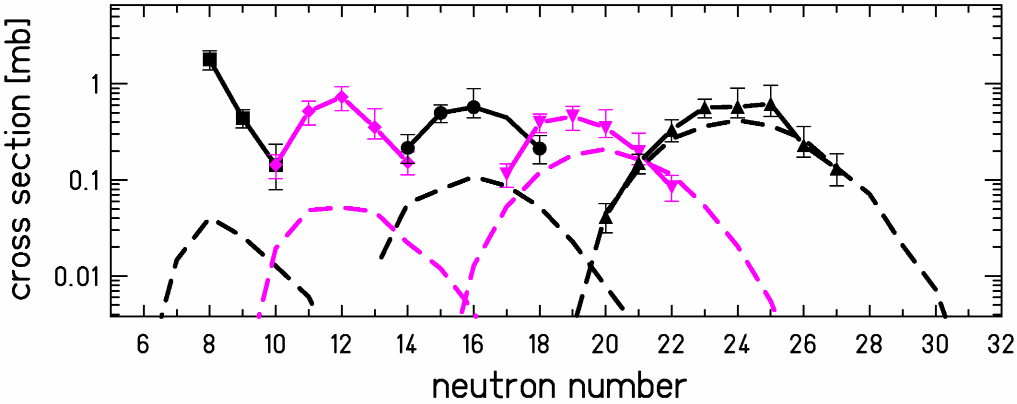

Figure 4.4: Cross sections for the isotopes of the elements $_7$N, $_{10}$Ne, $_{13}$Al, $_{16}$S, $_{19}$K produced in the reaction ^{238}U (1·A GeV) + p. The dashed lines represent the prediction of ABRABLA.

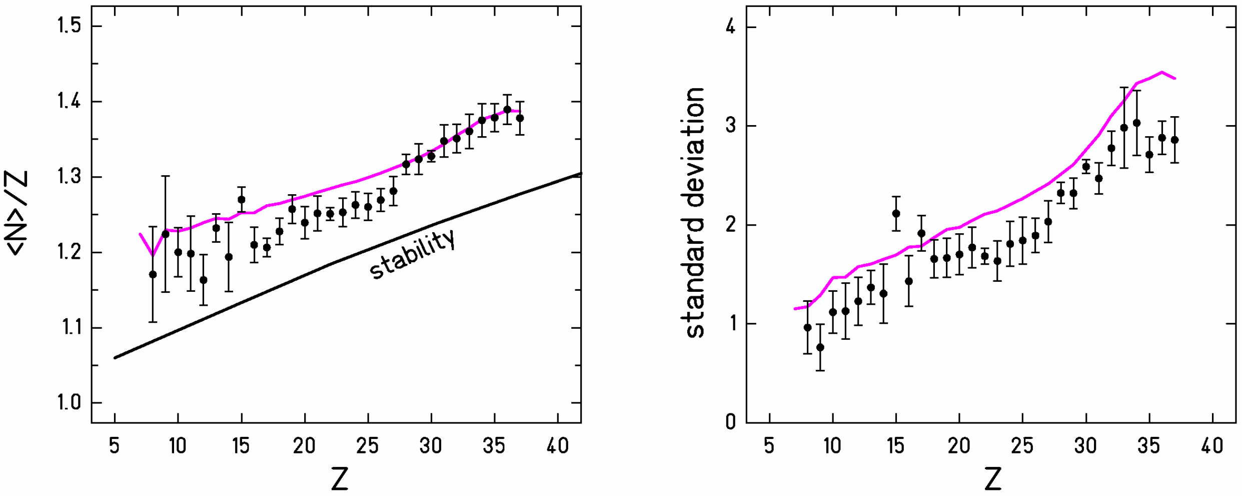

Figure 4.5: Left: Mean neutron-to-proton ratio of isotopic distributions as a function of the atomic number, compared with the stability line (black line). Right: Standard deviations of the distributions. The grey lines represent the prediction of the ABRABLA code.

4. 3 Fast binary decay

In the preceding sections we have investigated the contribution of fission, which for sure is present. Here we want to discuss the possible contribution of a fast break-up process. With fast break-up we mean a multifragmentation-like reaction mechanism. The dynamical picture thought to be behind it is that of a *fast* thermal expansion right after the intra-nuclear cascade phase, with the formation of two clusters, successively driven apart by the Coulomb repulsion. In contrast to this fast process, the fission-evaporation picture assumes the *slow* formation of a fully equilibrated compound nucleus. Observables that could hint at one or the other process are the time scale of the process, the multiplicity distribution of the products, the excitation energy of the decaying system, its momentum transfer, and the mean velocity of the fragments. In the following, we will analyse all these signatures. We will also critically investigate the justification of previously drawn conclusions in some other works that found indications for fast break-up processes in similar systems.

Time scale

A recent theoretical work [Wag99] investigates the compatibility of the measured properties of light fragmentation products with a binary sequential decay model. They find that the experimental charge and energy distributions of the fragments produced in the spallation of gold by 8.1 GeV protons are well reproduced. Only the time scale, deduced from angular correlations of IMFs, is off by about a factor of three. Unfortunately, the method of angular correlations of light fragments is not applicable for the appreciably lower projectile energy of 1 GeV used in the present work, since the probability for the emission of more than one light fragment is very low [Sch96]. Eventual evidence on the compatibility with a fission process in the generalized sense might only be drawn from the other observables.

Multiplicity

In our experiment, no direct measurement of the multiplicity was possible. Very light fragments from lithium to argon were also investigated in 1 GeV proton-induced spallation of gold and some lighter nuclei [Kot95]. They observe that the probability for multiple IMF production ($Z \geq 3$) with a multiplicity ≥ 3 in the reaction Au + ^{1}H at 1 GeV is only 0.4 %. One may expect that in the system ^{238}U + ^{1}H at 1 GeV the percentage will comparable, since the energy in the centre of mass for the two systems is rather similar.

Excitation energy

In the reaction Au + ^{1}H at 1 GeV investigated in ref. [Kot95], along with the multiplicity equal to 2, the velocity spectra of the emitted light fragments indicate that they are produced by the binary decay of a heavy nucleus. Thus, the production of light fragments in this reaction is predominantly a binary process, forming one heavy and one light fragment. In order to deduce the excitation energy of the decaying system, the energy spectra were fitted with a Maxwellian distribution, assuming isotropic emission. The deduced slope parameter gave an apparent temperature of about 8.4 MeV for all light fragments between Z = 7 and Z = 18. If interpreted as a temperature value, this would correspond to an excitation energy of about $E = a T^2 = A/10\ T^2 = 197/10 \cdot 8.4^2$ MeV ≈ 1400 MeV in a fully thermalised system, which is even higher than the centre-of-mass energy, available in the reaction. However, the slope parameter cannot be interpreted as the temperature of the emitting source, because it is strongly influenced by several additional effects. One is the Fermi motion of the nucleons in a nucleus which is breaking up. This effect has been described by Goldhaber in [Gol74]. Its relevance for the interpretation of the kinetic properties of nuclear decay products has been underlined by Westfall et al. [Wes78] and recently discussed in [Ode00]. That means that the slope parameter of the energy spectra of the light fragments observed by [Kot95] mostly relflect the velocity distribution of the decaying system and thus cannot be attributed to the characteristics of the decay process. There is also another effect, which has an important influence on the interpretation of the energy spectra. It relates to the fact that the light fragments may be produced by the decay of a variety of mother nuclei with different mass and atomic number. Also this fact was not considered in [Kot95]. This effect alone causes an important fluctuation on the kinetic energy of the emitted fragments. The two effects discussed, the Fermi motion and the variety of emitting sources, make it rather difficult to find a straight-forward quantitative interpretation of the slope parameter in the energy spectra of the IMFs produced in a 1 GeV proton-induced spallation reaction. We conclude that the large value of the slope parameter cannot be taken as a proof for a fast binary decay, occurring before the formation of a thermalised compound nucleus.

Momentum transfer

Barz et al. [Bar86] reported folding-angle distributions of binary-decay products from the spallation of uranium, samarium and silver by 1 GeV protons. While for uranium the momentum transfer and its fluctuation are small, both quantities increase when going to samarium. Fragments produced in the spallation of silver reveal a very large spread in momentum transfer but no further increase of the momentum transfer. These findings were interpreted as an indication for the onset of multifragmentation in the lighter systems. As for the excitation energy, also the very large spread in momentum transfer in the spallation of silver [Bar86] can be related to the fact that the light fragments may be produced by the fission of a variety of mother nuclei with different mass and atomic number, without the need of introducing a multifragmentation process. The same arguments might also explain the rather broad relative energy width (around 18 % standard deviation) found in the present work if compared to the energy width known from low-energy fission of uranium isotopes (about 5%, see ref. [Lan80]).

Mean velocities of the fragments

The mean velocity of the fragments with respect to the emitting source was the key information from which the binary nature of the decay was deduced. In figure 4.2 the comparison of the data with the results of calculations performed assuming a fission-evaporation scenario seems to reproduce satisfactorily the data. Under the hypothesis of a fast binary break-up, the expansion stage would result in a larger distance between the two clusters, with the consequence of a reduction of the Coulomb repulsion and eventually of the mean velocity. The possible presence of a third small cluster would sort out the same effect. In the end, we conclude that the mean velocities represent a rather strong evidence that the reaction mechanism is a generalised fission process.

Other observables

Other observables, like the mean N/Z of the fragments, the width of the isotopic distributions, the global trend of the cross sections, do not shed any light on the question, since in both processes these signatures would be similar. In particular, the neutron enrichment of the intermediate-mass fission fragments is not expected to be found here because the structural effects limit the fluctuations in N/Z, as explained in the previous section.

A similar investigation, as presented above, was performed already in 1984 by Andronenko [And84]. He analysed all the signatures (among which angular correlations, mass and energy distributions) of the binary products from several proton-induced reactions at 1 GeV. The interaction of a proton with nuclei followed by fission, described applying a cascade-evaporation model, could reproduce all the observed signatures, and he excluded the contribution of other decay modes.

We conclude that the results from several experiments, including the present work, give unanimous indications that light fragments in the reaction ^{238}U + ^{1}H at 1 GeV are produced in a binary decay. Although the nature of this decay could not be identified without doubt, clear indications for a fast break-up process in this reaction seem to be absent. On the contrary, it may be concluded that, at the current stage of knowledge, the experimental signatures in the reaction ^{238}U + ^{1}H at 1 GeV are consistent with the binary decay of a fully equilibrated compound nucleus. As discussed in [Sto85], this includes fission and evaporation with a natural transition in-between, and it might be called fission in a generalized sense [Mor88]. Thus, very asymmetric fission of the system ^{238}U + ^{1}H at 1 A GeV seems to reach down to rather light nuclei, extending below $Z = 18$.

Chapter 5

The mean neutron excess of the fragmentation residues of 1·*A* GeV ^{238}U on titanium

The investigation presented in this chapter arises from the observation that the light fragmentation products of the reaction 1 *A* GeV ^{238}U+Ti are surprisingly neutron rich, as can be observed in figure 3.11. In the following, we will make use mostly of one observable: the mean *N*-over-*Z* ratio of the fragmentation residues, obtained from the isotopic distributions presented in Appendix B. At first, we are going to recall some concepts, which are important for the discussion later.

5.1 Abrasion and sequential evaporation

Fragmentation reactions at relativistic energies are often described by means of a two-step process: the collision itself, where part of the mass is removed from projectile and target and excitation energy is introduced in the surviving nuclei, and a successive sequential decay, where the excitation energy is consumed to evaporate, one after the other, nucleons and light nuclei (figure 5.1).

In nucleus-nucleus collisions at relativistic energies, the first step is often called "abrasion" [Hüf75]. At relativistic energies the bombarding energy is well above the Fermi energy. Under this condition, the interaction can be considered a sequence of quasi-free nucleon-nucleon collisions. It is assumed that the trajectories of the interacting nucleons are straight lines and the nucleons participating to the interactions are those which belong to that part of the projectile nucleus which geometrically overlap with the target nucleus. Therefore, the masses of the remaining nuclei (both projectile and target spectator) are determined by the geometrical overlap as a function of the impact parameter. The mean N/Z-ratio of the removed nucleons (and thus of the remaining nucleus) is determined just

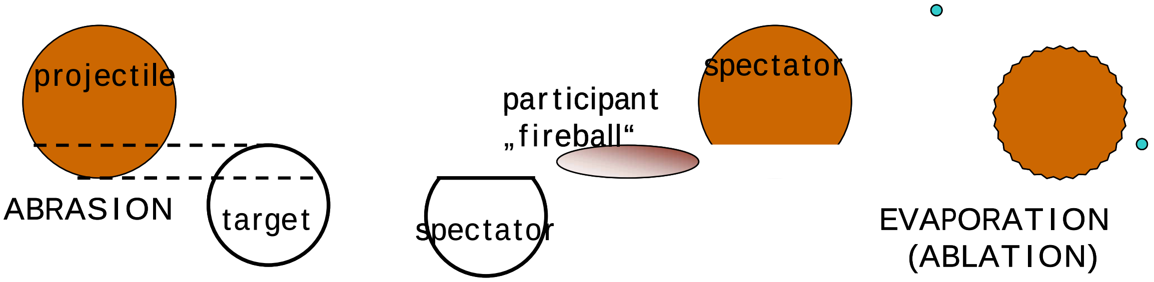

Figure 5.1: Schematic drawing of the abrasion-evaporation process, used to describe peripheral nucleus-nucleus collisions at relativistic energies.

by statistical consideration. The distribution of the N/Z-ratio after the collision can be calculated by hypergeometrical distribution (take ΔZ out of Z protons and ΔN out of N neutrons at random for fixed ΔA=ΔZ+ΔN):

$$P(\Delta Z) = \frac{C\left(\frac{Z}{\Delta Z}\right) \cdot C\left(\frac{N}{\Delta N}\right)}{C\left(\frac{A}{\Delta A}\right)} \qquad C\left(\frac{Z}{\Delta Z}\right) = \frac{Z \cdot (Z-1) \cdot \ldots \cdot (Z-\Delta Z)}{\Delta Z \cdot (\Delta Z - 1) \cdot \ldots \cdot (1)} \tag{5.1}$$

For the above consideration, after the abrasion stage the remaining nucleus for a given mass is left with a mean N/Z-ratio equal to its original N/Z-value, although with large statistical fluctuations, which lead to large variations in the N-over-Z ratio of the reaction products.

The nucleons occupying the overlapping volume of the two nuclei are distributed at random in momentum space inside the Fermi spheres of projectile and target in the Fermi-gas model. As they are removed they leave a "hole" to which is associated a certain energy. It is assumed that this internal energy of the single nucleons is redistributed among all the degrees of freedom of the remaining nucleus, which thermalises and forms a compound nucleus. The total excitation energy induced in the remaining nucleus is given by the sum of the hole-excitations. Again, for statistical considerations, the excitation energy is proportional to the number of nucleons removed, i.e. to the abraded mass ΔA. However, also the energy induced in the collision is subject to a large fluctuation and extends to rather high values. Therefore, the consecutive evaporation cascade has an important influence on the nuclear composition of the fragmentation products observed.

In the second step, the compound nucleus de-excites by means of the sequential evaporation of nucleons and light nuclei. In each step the nucleus (mother nucleus) decays into another nucleus (daughter nucleus) by emitting a particle. The probability of evaporating one particle or the other depends on the decay widths of the particles. The decay width, Γ, can be calculated (e.g. ref. [Wei37]) and depends on several quantities, like the excitation energy, the density of energy levels of the mother nucleus and of the daughter nucleus, the separation energy of the emitted particle, the capture cross section of the particle. Since all the above quantities change at every step, also the probability of evaporating one particle or the other changes after every step. In figure 5.2 it is shown how the decay width changes for different position of the mother nucleus on the chart of the nuclides. A neutron-rich nucleus will evaporate most probably neutrons, because of the high Coulomb barrier in the potential that protons experience. In analogy, a proton-rich nucleus will evaporate mostly protons. An excited nucleus on the beta-stability line will also tend to evaporate neutrons, because the Coulomb barrier still hinders the escape of protons. There is a corridor, between the stability and the proton drip line, where neutrons and protons face the same barrier inside the potential. In this case the decay widths for proton and neutron evaporation are approximately the same. This condition is what characterises the "evaporation corridor".

In the light of the above picture, the evaporation stage of an excited nucleus can be considered as a diffusion process on the chart of the nuclides, which tends to enter into the universal evaporation corridor [Duf82], where the evaporation of essentially protons and neutrons is in equilibrium. This idea was introduced by Campi and Hüfner [Cam81] and later refined by Gaimard and Schmidt [Gai91]. Afterwards, the evaporation corridor was also denoted as evaporation “attractor line” [Cha98], because in whatever position the initial nucleus starts its decay, if it has got enough excitation energy it tend to approach the evaporation corridor. If the excitation energy at the beginning of the evaporation cascade is not sufficiently high, the residues keep some memory of the *N*-over-*Z* ratio of the initial excited nucleus, but with every evaporation step, this memory is more and more lost. The universal behaviour of the *N*-over-*Z* ratio of evaporation residues is the prerequisite for semi-empirical parameterisations of the cross sections of heavy residues from fragmentation reactions like EPAX [Süm00]. EPAX is a semi-empirical code based on the idea that fragmentation products result from long, sequential evaporation chains, at the end of which the evaporation attractor line is reached. In this scenario, which represents one of the characteristics of the *limiting fragmentation*, it is expected that the fragmentation products generated with such a mechanism eventually land on a universal and rather narrow corridor on the chart of the nuclides. In this parameterisation, it is assumed that the lighter fragments are formed in more violent collisions, leading to longer evaporation chains, where the limiting-fragmentation regime is for sure achieved. This means that, from a certain mass loss on, the shape of the isobaric distributions is universal. It neither depends on the projectile nor on the target nucleus. This assumption seems to be confirmed by a great variety of data.

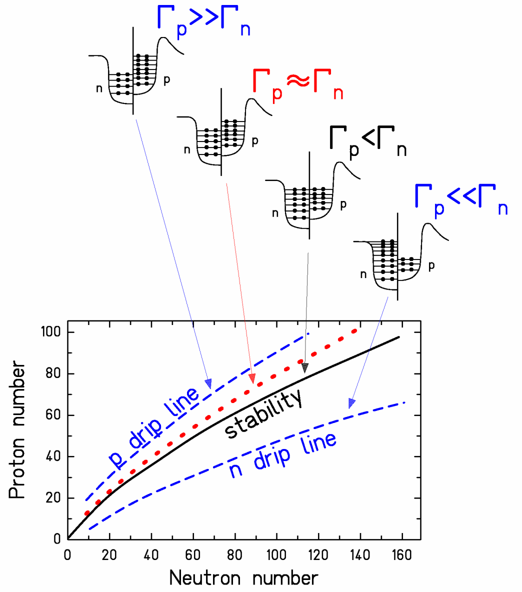

Figure 5.2: Decay widths for the evaporation of protons and neutrons of mother nuclei occupying different positions on the chart of the nuclides. The position of the universal evaporation corridor is between the stability line and the proton drip line.

5.2 The mean N/Z of the fragments

From the isotopic distributions presented in figure B2 of Appendix B we could calculate the mean neutron-to-proton ratio of the observed elements. In figure 5.3, the so-obtained values of the mean *N*/*Z* ratio of the fragmentation products are presented as a function of the nuclear charge, *Z*. Along with our data the results for other projectile-fragmentation reactions are depicted (see figure caption for the details). All the presented experimental data were measured with high-resolution magnetic spectrometers. Fission events are never included. The experimental results are compared with two “reference” lines. The solid line represents the stability valley; it was calculated using the formula taken from ref. [Mar69]. The dashed line is the result of a calculation for ^{197}Au on hydrogen performed with EPAX [Süm00]. For the reactions ^{197}Au on hydrogen at 800·*A* MeV and ^{56}Fe on hydrogen at 414·*A* MeV the accordance with EPAX is excellent, and the sequential evaporation picture seems to be the valid one. Since the higher the excitation energy of the pre-fragment is, the more valid the hypothesis of limiting fragmentation should be, we would expect to find an even more perfect overlap between the mean *N*-over-*Z* ratio of the fragmentation products for ^{238}U on titanium and the EPAX prediction. Surprisingly enough, the experimental data show larger mean values, and products with nuclear charge below ≈ 22 even cross the stability line. The mean neutron number in the large element range $10<Z<60$ shows a significant deviation of about 2 neutrons towards more neutron rich nuclei, and in the whole range never reaches the EPAX line. We looked for other evidences of this effect by the analysis of other data in literature. We found that the data of 1·A GeV ^{238}U on lead [Enq99], 1·A GeV ^{208}Pb on titanium and on deuterium [Enq02] show the same surprising result. In particular, the data of 1·A GeV ^{238}U on lead, presented in figure 5.3, merge perfectly with our data and release a more extensive picture. For the data of ref. [Enq99, Enq01, Enq02] the *N*-over-*Z* ratio was not investigated by the authors, therefore the deviation from EPAX was not noticed. Indications for deviations of the neutron-to-proton ratio of fragmentation products from EPAX were already reported – but not commented –

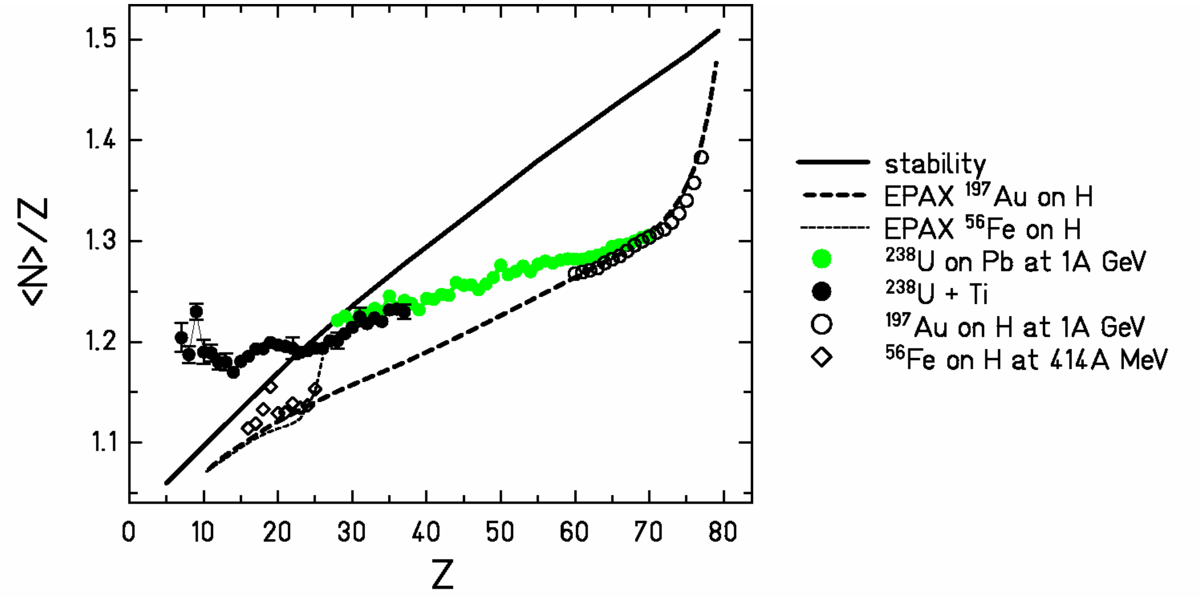

Figure 5.3: Mean neutron-to-proton ratio found in the isotopic distributions of ^{238}U in titanium at 1·A GeV. The results are compared with those obtained in the fragmentation of ^{238}U in lead at 1·A GeV [Enq99], with the beta-stability line [Mar69] and the prediction of EPAX [Süm00] for the fragmentation of ^{197}Au and for the fragmentation of ^{56}Fe. The measured mean values from the fragmentation of ^{197}Au in hydrogen at 800·A MeV [Rej01] and of ^{56}Fe in hydrogen at 414·A MeV [Web98] are shown in addition. Fission events are excluded

by Lindenstruth [Lin93] for the light products (Z<10) of the reactions ^{197}Au on copper and on aluminium, measured at ALADIN [Tra97]. The question remains then unsolved: why do some data agree with the EPAX prediction and some others deviate? Lighter residues from the fragmentation of uranium obviously experienced an evaporation cascade that was too short to reach the evaporation corridor. *More violent collisions seem to introduce lower excitation energies.* This is a quite surprising finding that demands for a careful analysis.

5.3 A possible picture

In this section we want to test the hypothesis that the lack of apparent excitation energy found in the fragmentation products of ^{238}U is related to a break-up stage before the evaporation cascade. A simultaneous break-up has two essential characteristics: Firstly, the excitation energy acquired in the collision is partially converted into nuclear surface energy, while the remaining part is shared among the clusters. Secondly, the *N*-over-*Z* ratio of these clusters is expected to be close to the one of the total decaying system [Bot01].

To test our hypothesis we will not use elaborate break-up models, at first. In the following, we will make use of a simple reasoning based on two assumptions. The first assumption is that the break-up produces clusters of different size, with the N/Z-ratio on average equal to that one of the mother nucleus. The second assumption is that the excitation energy acquired by the spectator nucleus is partially consumed for the formation of clusters. At the end of the break-up stage all the clusters are in a heat bath, i.e. they are all formed with the same freeze-out temperature.

Here below, with the help of figure 5.4, we want to illustrate the basic idea of our hypothesis. In these considerations we neglect the influence of fission in all aspects. Several additional approximations are made in this section in order to work out the basic concept in the clearest way. For a quantitative analysis, we refer to the calculations with a more elaborate model, presented in section 5.5.

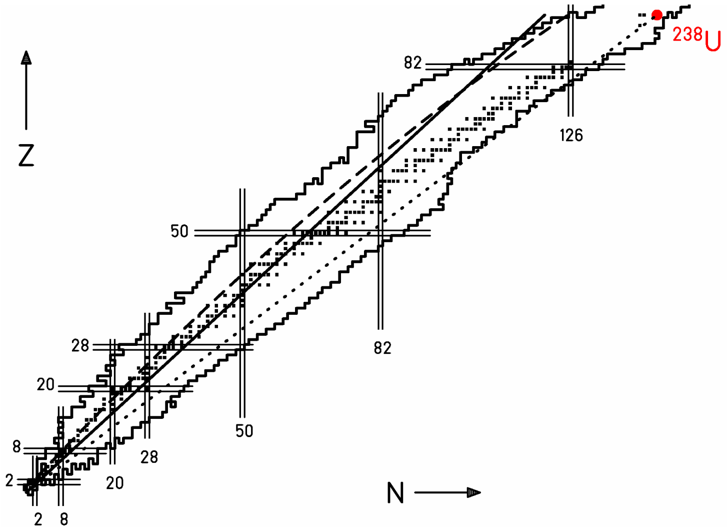

Figure 5.4: Schematic illustration of the application of our reaction picture. Dotted line: Mean N/Z of the primary clusters after break-up. Dashed line: Evaporation-residue corridor. Solid line: Position of the final clusters after the evaporation cascade if only neutron evaporation is considered. A freeze-out temperature of 4 MeV is assumed. Full squares mark the primordial nuclides. The full surrounding lines indicate the limits of known nuclides. See text for more details.

The break-up produces clusters of different sizes that are formed with the *N*-over-*Z* ratio of the ^{238}U projectile. They all lie on the dotted line of figure 5.4. Their excitation energy leads to an evaporation cascade. Since the primary clusters are very neutron-rich, neutron evaporation dominates, and depending on the initial excitation energy, the products lose part of their neutron excess. If the excitation energy is sufficiently high, they enter into the evaporation corridor, where the competition between neutron and proton evaporation comes into equilibrium. The evaporation-residue corridor, as predicted by EPAX, is indicated by the dashed line.

All clusters are formed with the same freeze-out temperature. This leads to excitation energies of:

$$E_{freeze\text{-}out} = a\ T_{freeze\text{-}out}^{2} \tag{5.2}$$

With the level-density parameter set to $a = A/10$, and assuming a guess value of $T_{freeze\text{-}out} = 4$ MeV, we get $E_{freze\text{-}out} = 1.6 \cdot A$ MeV. We can reasonably assume that from the beginning of the evaporation process only neutrons are evaporated, until the evaporation of neutrons and protons comes into equilibrium. We further assume that 15 MeV are needed to evaporate one neutron. This value results from estimating the expression $S_n + 2T$ (neutron separation energy plus kinetic energy of the neutron which amounts on the average to two times the nuclear temperature). At the beginning of the cascade, the binding energy of the neutron is low, the average kinetic energy it acquires is high. At the end of the cascade, the situation is reversed, with the net result that the sum of the binding and kinetic energies is approximately constant and equal to 15 MeV. Under these conditions, all end-products have the same *N*-over-*Z* ratio of:

$$N_{final} \,/\, Z_{final} = (N_{initial} - 1.6\ A_{initial} \,/15) \,/\, Z_{initial} \approx 1.3, \tag{5.3}$$

corresponding to the solid line in figure 5.4. It is clear that the restriction to neutron evaporation is unrealistic for elements above $Z \approx 70$ where the final fragments according to the solid line would be more neutron deficient than the evaporation-residue corridor. In this range, the *N*-over-*Z* ratio is expected to saturate at the evaporation corridor. Only for $Z < 70$ the excitation energy of the primary clusters is not sufficient to reach the evaporation-residue corridor at the end of the evaporation cascade. They preserve part of the large neutron excess of the ^{238}U nucleus.

The solid line marks nuclei that are more neutron-rich than the evaporation-residue corridor below $Z \approx 70$, and even more neutron-rich than the beta-stability line below $Z \approx 30$. These characteristics are in remarkable qualitative agreement with the findings reported in figure 5.3. Thus, it seems that the hypothesis of a simultaneous break-up process that precedes the statistical evaporation is compatible with the behaviour of the mean neutron-to-proton ratio of the fragmentation observed.

Such a break-up stage is known to occur at high excitation energy, leading to multifragmentation, i.e. the formation of intermediate-mass and light fragments. The neutron excess of the heavy fragmentation products might indicate another manifestation of nuclear instabilities, similar to multifragmentation at relatively small excitation energies. The basic process behind could be the nuclear liquid-gas phase transition.

5.4 Basic idea to determine the freeze-out temperature

In the previous example, the mean N/Z of the final fragments was determined, assuming a certain temperature at freeze-out. In this section, we want to apply the same idea for the reverse purpose: assuming that the average N/Z-ratio of the cluster is that one of ^{238}U, we want to deduce the temperature at the beginning of the evaporation decay – the *freeze-out temperature* – by tracing back the evaporation. This idea is at the base of the "thermometer for peripheral nuclear collisions" [Sch93], a method to deduce the temperature of nuclear systems from the isotopic distributions of the residues at the end of the evaporation cascade. The method consists of applying an evaporation code with the quite well known ingredients of the statistical model in order to deduce the temperature at the beginning of the evaporation cascade. It has been applied in ref. [Sch93] to deduce the mean excitation energy induced in peripheral relativistic heavy-ion collisions as a function of mass loss. In this way, a value of 27 MeV per abraded nucleon was deduced.

For a correct application of the method to our case, not only the evaporation cascade but also the system of clusters at the freeze-out has to be correctly reproduced. Of course the simplified calculation performed in the previous section is too poor for a quantitative analysis. A more adequate model is needed.

5.5 Results of statistical models

5.5.1 Comparison with a three-stage-model calculation

We have used a three-stage model with an abrasion stage [Gai91], a break-up stage (modelled as explained below) and an evaporation stage [Jun98] for a more detailed interpretation of the available data.

The characteristics of the first stage, the abrasion process, are rather well established. In the present context, the mass loss and the excitation energy induced as a function of impact parameter are the most important ones. They are given by geometrical considerations [Hüf75] and experimental information [Sch93], respectively. It is further assumed that the mean neutron-to-proton ratio is preserved in the abrasion stage [Hüf75]. In the abrasion stage the projectile spectator acquires an excitation energy of 27 MeV per nucleon removed [Sch93].

If this energy leads to temperatures above the freeze-out temperature, we assume that the system undergoes a break-up stage. At this stage, part of the initial energy is removed through the loss of mass in form of nucleons or light clusters, which is not specified explicitly. The energy consumed to lose one mass unit varies from 8 MeV for an initial temperature of 5.5 MeV to 4 MeV for an initial temperature of 10 MeV; the higher the temperature, the smaller the consumed energy per unit mass loss is. At first glance, this tendency is opposite to the expectation that the particles should be emitted with higher kinetic energies when the temperature of the source increases. The explanation is that the average size of the clusters emitted increases with increasing temperature, since the remaining binding energies of the clusters would tend to reduce the energy release in the break-up process. Please note that the value of this energy reduction only enters into the absolute cross sections, not into the shape of the final isotopic distributions. Note also that the multiplicity of the emitted clusters does not affect the evaluation of the cross section of large residual fragments, since the probability that two of them are generated in the same (non-fission) event is zero if the mass of the break-up product exceeds half the mass of the projectile and it is still negligible for fragments with Z>25, according to references [Lin93, Tra97, Sch96]. On the other hand, we should expect that for lighter fragments the three-stage model predicts reliably only the shape of the isotopic distributions, while the absolute values of the cross section will be reduced. In the model, we assume that in the break-up stage the *N*-over-*Z* ratio is conserved, so the break-up product has the same *N*-over-*Z* ratio as the projectile spectator after abrasion.

Finally, a standard evaporation [Jun98] follows for every pre-fragment.

If the temperature of the system after the abrasion is lower than the freeze-out temperature, the spectator is considered to be the only pre-fragment and the evaporation starts immediately. Under these conditions, the reduction of the neutron excess by the evaporation cascade can directly be used to determine the excitation energy (and thus the temperature) of the compound nucleus at the starting point of the evaporation process, i.e. at freeze-out after the break-up phase. Figure 5.5 compares the data of the fragmentation of ^{238}U from with the result of the three-stage model. The freeze-out temperature was varied between 2 and 7 MeV. The lines are not equidistant. The smaller distance of the high-temperature curves is caused by the smaller sensitivity of the neutron and proton decay rates to the separation energies at high excitation energies, i.e. in the first part of the deexcitation process (see the discussion in ref. [Cha02]). A remarkable agreement with the data is found, if a value of 5 to 6 MeV is used for the freeze-out temperature in all cases.

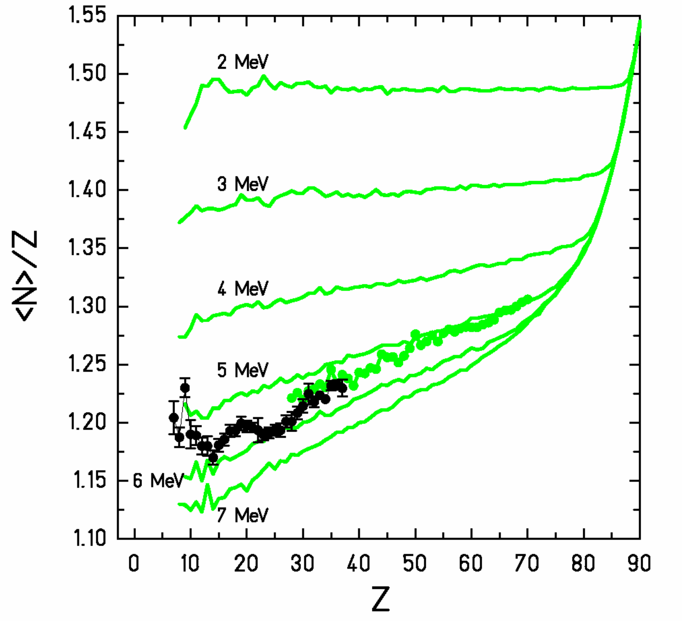

Figure 5.5: Experimental data on mean neutron-over-proton ratios of heavy fragmentation-evaporation residues produced in the fragmentation of ^{238}U + Ti (●) and of ^{238}U + Pb (●) [Enq99] at 1·A GeV, in comparison with the results of a three-step nuclear-reaction model. It considers abrasion, break up and sequential decay (see text), using different values of the freeze-out temperature of the break-up stage.

5.5.2 Comparison with SMM calculations

The method applied in the preceding section to back-trace the conditions at the beginning of the evaporation cascade from the mean values of the observed isotopic distributions was based on the assumption that all products of the break-up stage have the same N-over-Z ratio. This assumption is not made in the statistical multifragmentation model [Bot85, Bot87, Bot90]. Within this model, a microcanonical ensemble of all break-up channels composed of nucleons and excited fragments of different masses is considered. It is assumed that an excited nucleus expands to a certain volume and then breaks up into nucleons and hot fragments. All the possible break-up channels are considered. It is also assumed that at the break-up time the nucleus is in thermal equilibrium characterised by the channel temperature T. The probability of a certain decay channel is proportional to its statistical weight, which depends on the entropy of the system in a state corresponding to that decay channel, which in turn depends on excitation energy E^* and other parameters of the system. The fragments with mass number $A_f > 4$ are treated as heated nuclear liquid drops. Each fragment contributes the bulk-, surface-, Coulomb- and translational terms to the free energy and to the entropy of the system. The light fragments with $A_f \leq 4$ are considered as elementary particles having only translational degrees of freedom. The Coulomb interaction between all fragments and gas particles is taken into account via the Wigner-Seitz approximation [Wig33].

The break-up channels are simulated by the Monte-Carlo method according to their statistical weights. In the present calculations it was assumed that the break-up occurs at a density of one sixth of the normal nuclear density. After break-up of the system, the fragments propagate independently in their mutual Coulomb fields and undergo secondary decays. The de-excitation of large fragments ($A_f > 16$) is described by the evaporation-fission model, and for smaller fragments by the Fermi break-up model [Bot87].

Since the intermediate and heavy residues observed in the experiment indicate that rather peripheral collisions are involved, the approximation is made that the initial system at break-up still contains all nucleons of the projectile. The excitation energy at break-up was taken as a parameter of the calculations. This also defines the temperature of the system.

The mean N-over-Z ratio of the isotopic distributions that results from these calculations is compared to the experimental values of the reactions ^{238}U on titanium and ^{238}U on lead at 1 A GeV [Enq99] in figure 5.6. The excitation energies of 1, 1.5, 2, 2.5 and 8 MeV/u correspond to temperatures of 3.1, 3.9, 4.4, 4.9 and 7 MeV, respectively. With increasing temperature, the mean neutron excess approaches the evaporation-residue corridor, marked by the EPAX prediction. In the beginning, this trend is fast, then it slows down until the temperature saturates in the region of the phase transition at the level of 5 to 6 MeV, and then it increases again in the gas phase. The corridor is finally reached at very high excitation energies.

For fragments with Z>22, there is a remarkable agreement found with the data when an energy around 2.5 MeV per nucleon is assumed. This corresponds to a freeze-out temperature of 5 MeV. It is interesting that the freeze-out temperature is independent of the mass of the residue with Z>22. The experiment does not sort the observations according to impact parameter (however, there is a good experimental information on the correlation of the largest Z produced in one event and the impact parameter [Sch96]). Therefore, the observed fragments of a given size emerge from different initial conditions. Nevertheless, it is a remarkable finding that collisions, which predominantly produce relatively light clusters, proceed by the same freeze-out temperature as those which predominantly produce very heavy clusters. This seems to be an indication that the freeze-out temperature is rather independent of the initial conditions. For fragments with Z<22 (figure 5.6, right), the SMM calculation with the initial temperature of 4.9 MeV reproduces very well the structure of the data, although the numerical values are not correct. The data are reproduced by calculations with initial values of the temperature fluctuating not always with continuity from one Z to the next one from 4.5 to 5 MeV. This is a region where a correct modelling of structural effects in the nuclear level density is of great importance for a correct prediction. We suppose that the discrepancy is due to the fact that the model suffers of this problem, although the global structure, in particular the isolated large value for Z=9, is well reproduced. Looking carefully at figure 5.6-right one may note that odd nuclei are systematically more neutron-rich than the even ones. This is probably connected with the strongly enhanced production of even-*Z* nuclei with N=Z, that will be discussed in Chapter 7. These nuclei are at the left borders of the isotopic distributions (see figure 3.10) and pull the mean value toward the neutron-deficient side for even elements.

We investigated, to which extent the input conditions of the SMM calculation affect the validity of this result. In the previous calculations a value of the density 6 times smaller than the normal nuclear density was chosen. When the calculations are performed with a density 3 times smaller than the normal nuclear density, the results agree with the data with

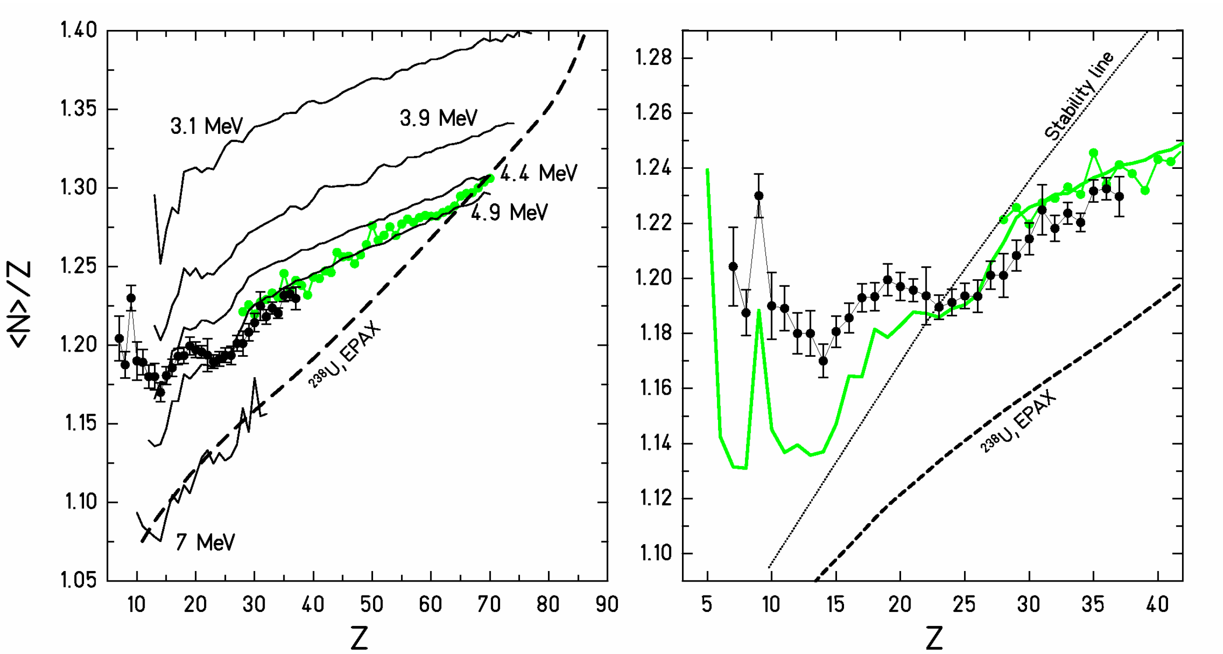

Figure 5.6: Mean neutron excess of the isotopic distributions of heavy residues obtained with the SMM model with different values of the temperature in comparison with the experimental values of the reactions ^{238}U on titanium (●) [this work] and ^{238}U on lead (●) [Enq99] at 1·A GeV. For clarity the calculations are not presented below Z=10. The right picture is just a magnification of the left one. There the data below Z=40 are compared with a full calculation of SMM with a value of T=4.9 MeV and with the EPAX prediction and the stability line.

a mean value of the freeze-out temperature of 5.1 MeV instead of 4.9 MeV. Also a variation of the mass of the system at break-up is not expected to have an essential influence on the *N*-over-*Z* ratio of the heavy residues in the calculation, as long as the *N*-over-*Z* ratio of the initial system is not changed. For this reason, we consider the value of 5 MeV substantially correct.

5.6 Comparison of the calculations with the isotopic distributions

The previous section showed that both models released substantially the same fundamental result. In this section we want to compare the width of the experimental isotopic distributions with those predicted by the two models. A general good agreement is obtained also in the evaluation of the cross sections, as shown in figure 5.7, where the results of the three-stage model, of SMM and of EPAX are compared with the experimental data.

The widths of the isotopic distributions predicted by the three-stage model are basically consistent with the experimental ones; they seem to be even a bit overestimated by the calculations. As expected, the absolute value of the cross section is underestimate for lighter elements. Note that the calculations were performed assuming a sharp value of the freeze-out temperature. This fact lets little room for introducing a fluctuation of the freeze-out temperature in the calculation, because this would even increase the width of the isotopic distributions. Fluctuations in the *N*/*Z*-ratio of the prefragments after abrasion and in the kinetic energies of the evaporated particles seem to be sufficient to explain the observed width of the distributions.

In figure 5.7, the SMM isotopic distributions were normalised to the experimental data. In fact, the SMM calculation was performed starting always with a fixed charge and mass of the system (Z=92, A=238). That means that the mass loss in the abrasion phase is neglected. In this way, the calculation is representative for very peripheral collisions only. However, the calculation is intended to yield the shape of the isotopic distributions, not to give a quantitative prediction of the cross sections. The SMM calculation reproduces the shape of the isotopic distributions rather well, although they tend to be too narrow for the heavier elements. This could be explained by the fact that the SMM calculation did not consider any fluctuation in the N-over-Z ratio of the prefragments. It is known that fluctuations of the temperature tend to broaden the isotopic distributions, too. The fact that the measured widths are relatively small give us confidence that there are no important fluctuations of the freeze-out temperature, i.e. the freeze-out temperature cannot deviate too much from 5 MeV. Changes in the values of the nuclear density in the input of the SMM calculation affect only the height of the cross sections.

5.7 Application of the method to other experimental data

In the previous sections we have seen that the results offered by the reactions 1·A GeV ^{238}U on titanium (this work) and 1·A GeV ^{238}U on lead [Enq99] can be explained assuming a break-up stage in-between the abrasion and the evaporation stages, where the clusters are formed with the same average neutron-to-proton ratio of the projectile, and in a heat bath at a certain temperature. This is the temperature at the freeze-out, i.e. at the stage in which the pre-fragments start to cool down by means of a sequential evaporation cascade of nucleons and light clusters. The simulations showed that T_{FO}≈5 MeV in a large number of events, specifically in all those events which will lead to the formation of residues with Z>22. This means that in the comparision of the N/Z-ratio of residual fragments with Z>22, a fixed value of T_{FO}≈5 MeV can be assumed. In this section we want to apply this method to other experimental data found in literature to check whether our picture is still valid.

From the considerations presented in section 5.3 it becomes clear that the method applied in this thesis to determine the freeze-out temperature works best in the fragmentation of a very neutron-rich nucleus like ^{238}U. Assuming an unchanged freeze-out temperature value of 5 MeV, the fragmentation of lighter, less neutron-rich nuclei would also produce less neutron-rich primary clusters. Consequently, the evaporation process would lead to final fragments closer to or eventually even on the evaporation-residue corridor, where any memory of the initial stage is lost. Therefore, ^{238}U was the best choice as a projectile, although the strong fission competition introduces some complications. However, this was not a severe problem, since fission products could be suppressed due to the high-resolution detection device.

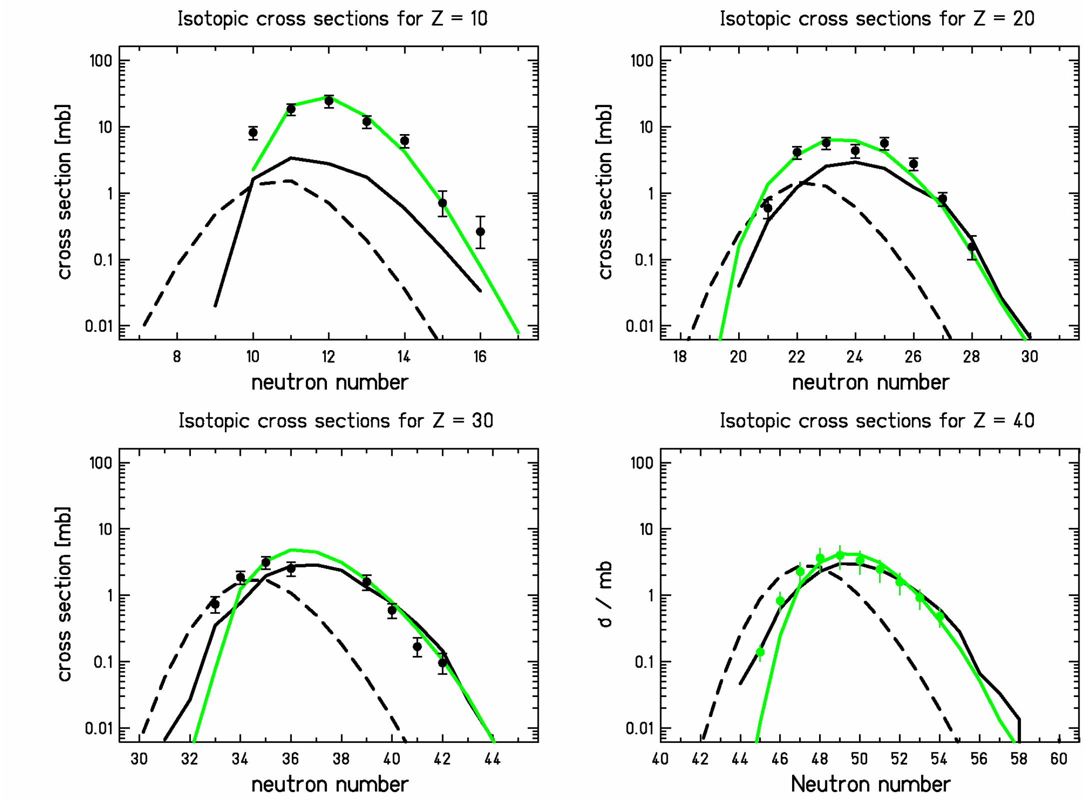

Figure 5.7: Measured cross sections of neon (Z=10), calcium (Z=20), zinc (Z=30), and zirconium (Z=40), isotopes produced by fragmentation in the reactions ^{238}U + Ti at 1·A GeV (●) and ^{238}U + Pb at 1·A GeV (●) compared to the prediction of the three-stage code (black line), to the prediction of the SMM code (green line) and to the prediction of EPAX (dashed line). The SMM results were normalised to the sum of the measured cross sections of each element.

Therefore, this method requires very neutron-rich primary nuclei, high-resolution detection systems to get full isotopic distributions, and the possibility to disentangle fission, if it occurs. Apart from ^{238}U on lead [Enq99], the only data found in literature that comply with these requests concern the reactions ^{208}Pb on titanium and on deuterium at 1·A GeV [Enq02]. In figure 5.8 the mean N/Z-ratio obtained from the isotopic distributions of the elements produced in these reactions is presented as a function of the charge of the element. There is a remarkably good agreement with the SMM calculation, when a value of 5 MeV is used for the initial temperature. In the experimental data, separated and observed with the FRS, the contribution of fission had to be discharged. This is probably the reason for the uncertainty of the data in the region between Z=35 and Z=50.

It is interesting to note that, as already noticed in the case of 1·A GeV ^{238}U on titanium and on lead, the target has no influence on the mean value of the isotopic distributions. On the contrary, it has influence on the mass distribution of the fragments, as demonstrated by the data of ^{208}Pb on deuterium, which stop at Z=50. According to our picture, when the abrasion leads the system to a temperature above 5 MeV, the system undergoes a break-up stage. Since the total excitation energy that the reaction can put into the surviving spectator increases with the target mass, and since the larger the initial energy, the larger the probability to form more – and lighter – clusters is, this signature is a confirmation of the validity of our picture.

To close this section, we can conclude that the comparison with the ^{208}Pb residues offered three interesting results. First, the freeze-out temperature seems to be established at 5 MeV, regardless of the projectile mass, for all peripheral collisions that lead to the formation of fragments with Z>22. Second, the higher excitation energy introduced in more violent collisions seem to generate a larger number of (lighter) clusters instead of inducing longer evaporation chains. Third, the *N*-over-*Z* ratio of fragmentation-evaporation residues,

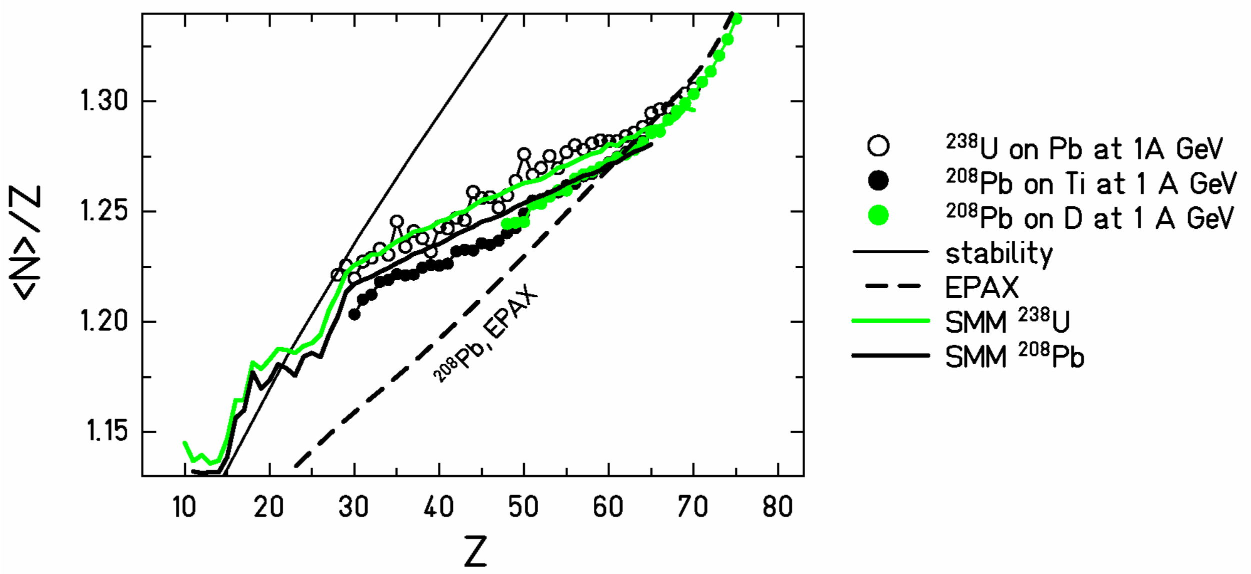

Figure 5.8: Mean neutron excess of the isotopic distributions of heavy residues obtained with the SMM model with an initial temperature of 5 MeV in comparison with the experimental values of the reactions ^{208}Pb on titanium (●) and on deuterium (●) [Enq02] at 1·A GeV.

even for masses appreciably lighter than the projectile, is not universal. Due to the limited freeze-out temperature, they are influenced by the *N*-over-*Z* ratio of the initial nucleus that is fragmented. That means that the concept of limiting fragmentation, which is behind some semi-empirical parameterisation of residue cross sections (e.g. EPAX), should be considered with caution.

5.8 The transition from fragmentation to multifragmentation

When combining the conclusions drawn from the application of our method to deduce the freeze-out temperature with other experimental information available, we come to some general conclusions on heavy-residue production in relativistic heavy-ion collisions. Figure 5.9 shows a schematic summary of the results. The mean excitation energy at the beginning of the evaporation cascade is shown as a function of the atomic number of the pre-fragment, entering into the evaporation cascade. Since neutron evaporation dominates, the picture would not look much different, if drawn as a function of the atomic number of the *final* fragment.

When starting from very peripheral collisions, few nucleons are removed from the projectile, leaving an excited heavy spectator nucleus. According to the results obtained in the fragmentation of ^{197}Au in an aluminium target [Sch93], the average excitation energy amounts to about 27 MeV per abraded nucleon. We assume that the result of the fragmentation of gold in aluminium can directly be applied to the fragmentation of uranium

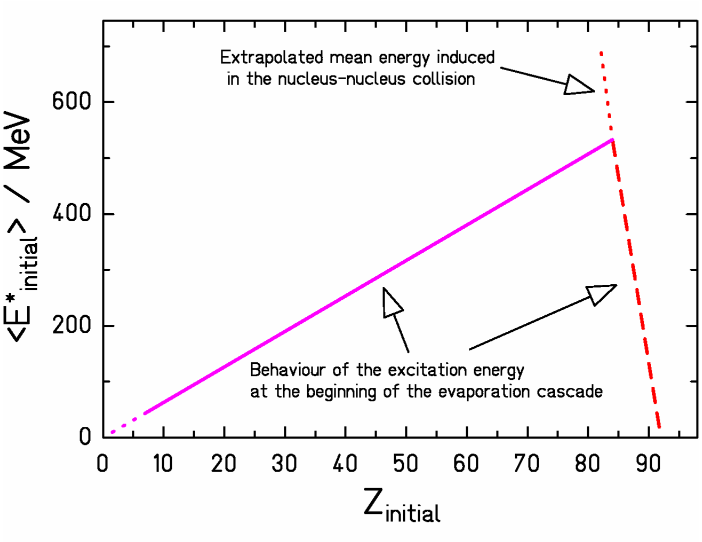

Figure 5.9: Schematic presentation of the initial energy induced in the abrasion stage and of the mean excitation energy at the beginning of the evaporation cascade after fragmentation of ^{238}*U in a titanium or lead target. Close to the projectile, the excitation energy induced increases linearly with the loss of protons, determined in ref. [Sch93] (dashed line). At Z = 84, the temperature of 5 MeV is reached in the abrasion, and the break-up sets in. The energy introduced into the evaporation cascade linearly decreases with decreasing mass number, corresponding to the constant value of 5 MeV of the freeze-out temperature deduced previously (solid line).*

in titanium and in lead. This seems to be justified from the different experimental results on several systems, which have been accumulated in several experiments [DeJ98, Jun98]. The difference in binding energy of protons and neutrons should not have any influence on the abrasion phase. Therefore, protons and neutrons are expected to be abraded according to their abundance in the projectile. That means that one proton is accompanied by 1.59 neutrons on the average in the fragmentation of ^{238}U. This leads to an average excitation energy of about $\Delta Z \cdot 70$ MeV introduced per ΔA nucleons abraded (with $\Delta A = \Delta N + \Delta Z$).

Near $Z = 84$, the excitation energy induced corresponds to a temperature of 5 MeV. It is to be expected that the excitation energy induced in the nuclear collision increases further for an increasing number of protons abraded, but the high values of the extrapolated dotted curve are not found in the evaporation cascade of the final fragments, because the system rather looses part of its energy first by break up. The evidence for the real nature of these reactions has to come from a combined analysis, including the information from kinematically more complete measurements. However, on the base of this simple picture our analysis seems to indicate that there is a limiting temperature of about 5 MeV of any equilibrated system when it enters into the statistical de-excitation cascade. The experimental signature from the data of our work and of ref. [Enq99, Enq02] directly relates to the range between $Z = 8$ and $Z = 70$. That means that great part of the full line in figure 5.9 is directly deduced from experimental data.

From the statistical multifragmentation model, no direct conclusion on the dynamical evolution of the system before forming a thermalised nuclear system can be made. Together with the rich information gathered on multifragmentation from the observation of light clusters, however, one may speculate that the nucleus expands after the abrasion process due to thermal pressure. As a result of density fluctuations during the expansion, light and intermediate-mass fragments are produced firstly. In this way, the nucleus looses its excessive energy, and the formed big residue keeps only the temperature of around 5 MeV. For peripheral collisions the energy introduced in the spectator is enough to form only one large prefragment. As the energy increases, the size of the largest cluster becomes smaller and eventually is accompanied by the formation of more clusters. Therefore, a possible interpretation of our experimental result leads to a picture where the transition from the "mono" fragmentation to the "multi" fragmentation is not sharp but gradual. While, in accordance with the abrasion model, there is a simple geometrical relationship expected between the atomic number of the heaviest fragment and the impact parameter above $Z = 84$, this relationship is less direct below $Z = 84$. Here, the charge found in the heaviest initial cluster after the break-up does not comprise all protons of the heated spectator nucleus. Part is rather lost by the simultaneous formation of light clusters and single protons during break-up. There is still a correlation between the impact parameter and the charge of the heaviest fragment, as has been discussed in previous work of the ALADIN group [Sch96]. But the simple correspondence deduced from the abrasion model is not preserved after break-up.

5.9 Some ALADIN results

In the previous sections the interpretation of our data indicated that the transition between "mono" fragmentation and multifragmentation is not sharp but gradual. This can also be noticed observing the products of the reaction 1·A GeV ^{238}U on copper, detected with the large acceptance spectrometer ALADIN [Tra97], displayed in figure 5.10. The data were taken from ref. [ALA]. In figure 5.10-left a two-dimensional cluster plot maps the number of events in correspondence of which the two heaviest fragments, reported in the x- and y-axis, were produced. The upper corner represents the fission events, which produces fragments of intermediate mass. The events are naturally caught inside the region delimited by the lines $y=x$ and $y=92-x$. The events on the flat distribution are probably generated via "standard" fragmentation, with the production of a big fragment and the evaporation of few light clusters. On the left corner there are the "standard" multifragmentation products. In between there is a corridor, in the range of products observed in this thesis.

Figure 5.10-right collects the number of events with a certain multiplicity as a function of the heaviest fragments produced in the event. The multiplicity does not include protons and neutrons. In the latter figure fission events were excluded. As the charge of the heaviest fragment decreases, the multiplicity increases and forms a bent corridor. At the other side, for the lightest elements the multiplicity increases steeply with the charge of the heaviest fragment. In the region between $10<Z_{max}<30$ the two distributions merge. Again, this is the range of products observed in this thesis.

In conclusion, all the collected data seem to indicate that there are several clear evidences of a transition between fragmentation (with one dominant large fragment) and multifragmentation (forming more than one IMFs with similar size). These signatures seem to indicate that the transition from a purely two-step fragmentation model to a multifragmentation picture is not sharp but continuous.

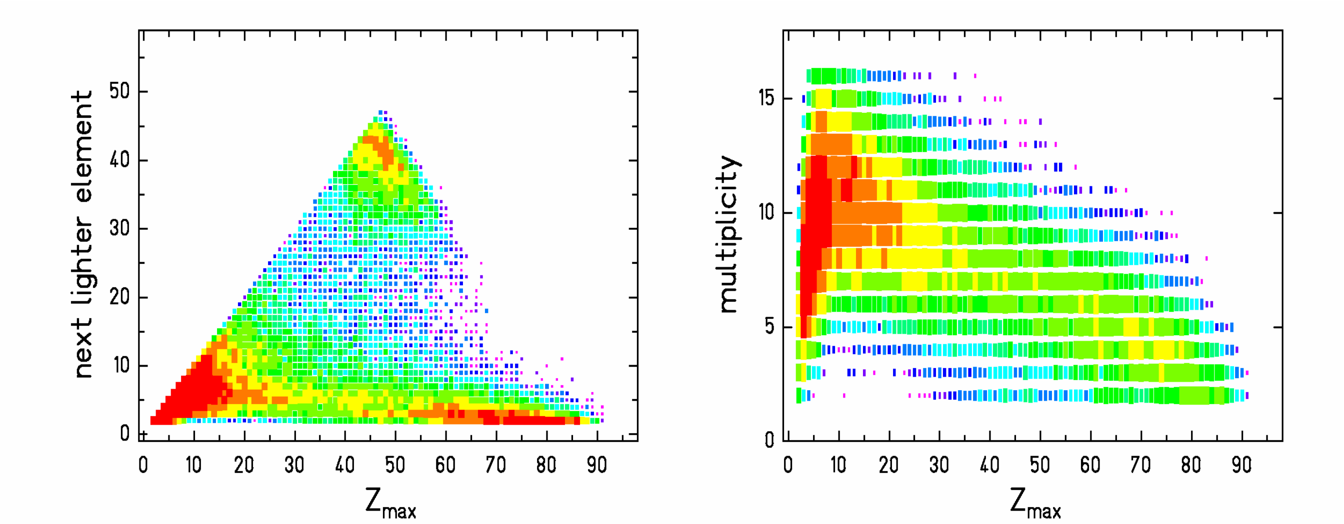

Figure 5.10: ALADIN data for the products from the reaction 1·A GeV ^{238}U on copper (data taken from ref. [ALA]). Left: two-dimensional cluster plot of the 1st and 2nd heaviest produced fragments. The upper corner represents fission events. Right: two-dimensional cluster plot of the multiplicity of fragments with $Z \geq 2$ for events with a certain heaviest fragment. Fission events are not reported in the plot.

5.10 Discussion

To conclude this chapter, we would like to underline two aspects. The first one is the question on the physical interpretation of the neutron-to-proton ratio of heavy fragmentation residues. The second one is the common understanding of the results from IMF production and from the heavy residues.

In this chapter, the neutron-to-proton ratio of heavy fragmentation residues was interpreted applying the method presented in ref. [Sch93], and recently named "isospin[1] thermometer" in ref. [Sch02], where the temperature of a thermalised system was deduced tracing back the evaporation cascade. The quantitative result of this method relies on the separation of the fragmentation process into three stages, and in the modelling of the isospin degree of freedom in the first two stages and on the treatment of the sequential decay in the evaporation code. The separation of the three reaction stages seems justified, because they can roughly be attributed to different time scales, the abrasion to the contact time, the break-up to the nuclear radius divided by the Fermi velocity, the evaporation to the compound-nucleus life-time.

The first essential assumption that the projectile spectator keeps the neutron-to-proton ratio of the projectile seems to be well justified, since the abrasion process directly probes the neutron and proton density distributions.

It was also assumed that the break-up products preserve the neutron-to-proton ratio of the projectile. In the light of the vivid discussion on the neutron distillation, this assumption seems to be in question. In fact, the very interesting phenomenon of neutron distillation[2] would reduce the neutron excess of the final residues, since an enhancement of neutrons is expected in the gaseous phase [Mül95, Bao97]. Still, according to the current predictions [Mül95, Bao97], the quantitative effect of the neutron distillation on the isosopin of the heavy residues is not clear, but in any case, the evaporation process will provide the dominant influence on this quantity.

Certainly, the quantitative result of the isospin-thermometer method also depends on some critical parameters used in the evaporation code, like the possible dependence on the excitation-energy of the barriers for charged-particle emission. It is a challenge to carefully consider independent experimental information concerning the evaporation process to best define the parameters of the evaporation code in order to come to most reliable results.

We would like to stress that the nuclide distributions of the heavy residues form an important test ground for any nuclear-reaction model, which complements the information from the properties of the IMFs. Nuclide distributions of heavy residues are particularly sensitive to the value of the freeze-out temperature and to the effect of neutron distillation.

The indications reported here from the properties of heavy residues for a universal freeze-out temperature of 5 MeV remind the interpretation of the caloric curve for a saturation of the temperature of the liquid phase at this very same value. In fact, the characteristics of the IMFs and those of the heavy residues fit to a common picture. They seem to be all formed at a freeze-out temperature of about 5 MeV. Only the experimental signatures exploited in the analysis were different. Heavy residues are formed with rather high excitation energies leading to a long evaporation chain, which strongly masks the conditions after freeze-out.

---

[1] The term "isospin" is used here as a measure for the neutron-to-proton ratio in the nucleus.

[2] The term "distillation" indicates the process that occurs in the phase transition of a mixture of two liquids, where the liquid with smaller binding energy evaporates at first.

However, as it was shown in this chapter, the important reduction of the neutron excess in the evaporation process can be exploited as the prominent signature for the excitation energy consumed in evaporation. Light residues, formed at the same temperature after freeze-out, have so low excitation energies that only very few nucleons can be evaporated. Therefore, the initial population of isotopes or excited states can well be exploited to determine the magnitude of the freeze-out temperature from a thermodynamical approach. This is the more traditional approach exploited in the study of the multifragmentation reactions [Alb85, Poc95, Sou00]. In the interpretation of the production of very light fragments, however, another difficulty arises, because they may also be produced in an evaporation scenario. In some cases, it might be difficult to disentangle these from the break-up products.

To conclude, in this chapter we have explored, and maybe demonstrated, the applicability of the isospin-thermometer method [Sch93] for the determination of the freeze-out temperature. This method permits to investigate the phases of the nuclear matter by studying the reaction products in a mass region wider than that one typically investigated in multifragmentation, and relies on the high-resolution determination of the masses.

Chapter 6
The acceleration of the fragmentation products of 1 *A* GeV ^{238}U on titanium

In this chapter we will discuss the apparent acceleration of the light nuclides produced in the fragmentation of 1 *A* GeV ^{238}U on titanium, observable in the longitudinal momentum of the fragments presented in figure 3.13. In this context, it is interesting to discuss at first the longitudinal momentum of the fragmentation residues of other systems, found in literature.

6.1 The longitudinal velocity of fragmentation products

Many experimental results can be found in literature concerning the mean longitudinal velocity of the fragment. In most experiments, this quantity is not easily accessible.

In target-fragmentation experiments, the mean values of the velocity distribution were often measured with the "thick-target thick-catcher nuclear recoil" method. In these experiments the target is in between two tick foils, where the recoiling fragments are stopped. The target is irradiated for some weeks and then the radioactivity of the two foils is measured. The mean value of the longitudinal velocity is found to be proportional to the forward-to-backward ratio intensity.

In projectile fragmentation, the longitudinal velocity transferred is obtained by time-of-flight measurements or by magnetic-rigidities measurements (as in the present experiment). In this system a reaction that in direct kinematics would give a forward-to-backward ratio larger than 1, would have a longitudinal velocity smaller than the beam velocity.

In 1989 Morrissey collected many experimental results concerning the mean momentum transfer both in direct and inverse kinematics, and tried to establish a systematic behaviour from the data [Mor89]. The variation in velocity was found to be proportional to the mass loss ΔA for numerous experiments, if the mass of the fragment is not much smaller than the mass of the primary nucleus. Morrissey found a mathematical expression for this systematic behaviour, according to which the momentum transfer increases linearly with increasing mass loss, ΔA. However, for larger values of ΔA, the data showed large fluctuations and contradictory behaviours, which invalidate the systematics (see figure 6.1).

Deviations from the systematics were found also more recently in experiments performed in inverse kinematics. In 1993 Lindenstruth [Lin93], analysing the residual nuclei produced in the interaction of gold with several targets, showed that for $\Delta A>70$ (approximately $Z<50$) the momentum transfer stops definitely to increase, levels off and eventually starts slowly to decrease (see figure 6.2).

Also Enqvist [Enq99] found a similar behaviour as Lindenstruth for the fragmentation of ^{238}U in lead at 1 GeV per nucleon. The deviation from the Morrissey systematics observed by Enqvist was even more enhanced: the momentum transfer stops definitely to increase, starts strongly to decrease and even changes its sign.

Our data present the same kind of behaviour found for the fragmentation of ^{238}U in lead at 1 GeV per nucleon. In figure 6.3 our data are compared with the results of ref. [Enq99].

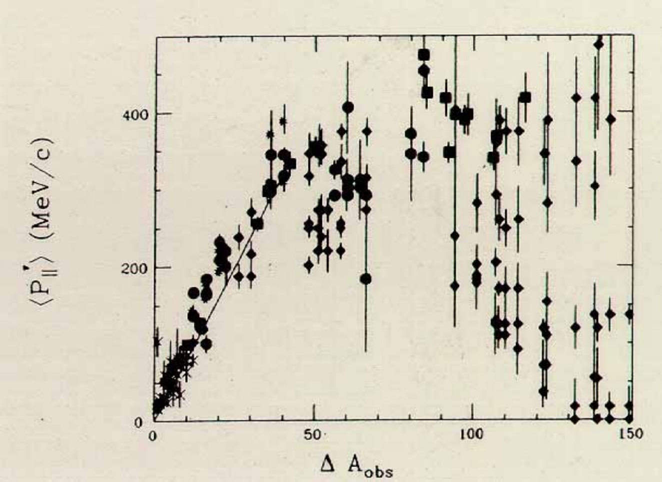

Figure 6.1: The average longitudinal momentum transfer as a function of the observed mass loss for several nucleon-nucleus and nucleus-nucleus reactions at relativistic energies. The figure is taken from ref. [Mor89]. The data are presented in the target frame. According to the Morrissey systematics, in the target frame the momentum transfer has to be always positive.

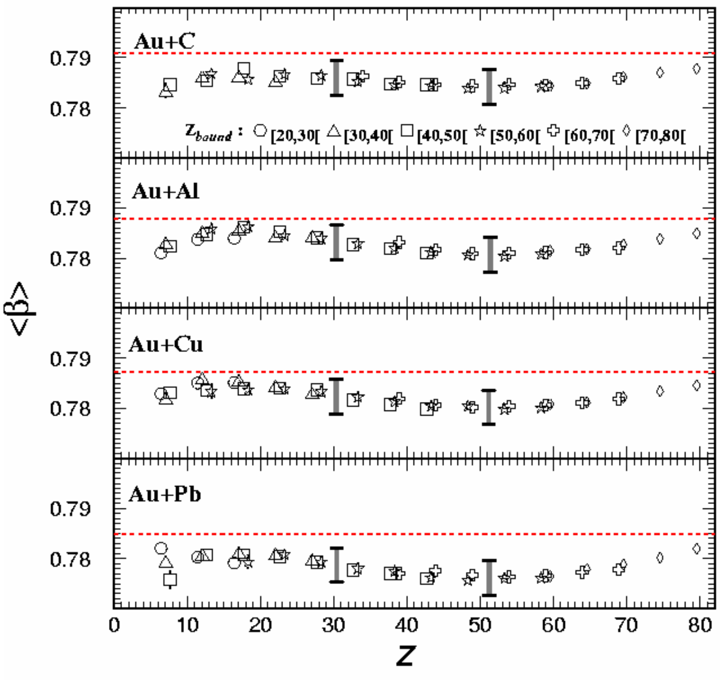

Figure 6.2: Velocity – relative to the light speed – of the heaviest fragments produced in several reactions at 600 A MeV, as a function of the fragment charge. The dashed lines indicate the beam velocity. The figure is taken from ref. [Lin93]. The data are presented in the beam frame. According to the Morrissey systematics, in the beam frame the momentum transfer as to be always negative.

Other isolated data showed the same evident counter-tendency to the Morrissey systematics found by Lindenstruth, Enqvist and us. Using a thick-target thick-catcher technique, target-like fragments around *A*=60, produced in the bombardment of gold by ^{12}C at 25 GeV [Kau80], were found to be produced with mean velocity close to zero in the laboratory frame. An experiment of Loveland *et al.* [Lov88], based on the same technique, revealed a backward emission of ^{24}Na, produced in the reaction oxygen on gold at 232 GeV.

This chaotic landscape of many data with no clear universal tendency composes a puzzle, whose solution is probably hidden behind the mechanism of the fragment formation. The comparison of our data with others existing in literature is not self-evident, and demands for a more careful discussion.

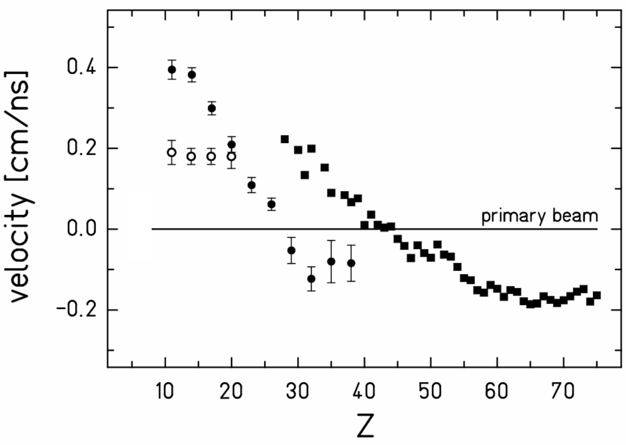

Figure 6.3: Comparison of the average mean values of the velocity distributions, as a function of the fragment charge, induced in two fragmentation reactions: 1 A GeV ^{238}U on lead (squares) [Enq99] and 1 A GeV ^{238}U on titanium (dots) [this work]. In the latter reaction, for Z<22, the full dots represent the mean position of the central peak of the velocity distributions obtained by fitting the spectra of figure 2.13, corrected for the angular transmission of the FRS; the empty circles give the lowest possible values of the mean velocities of the fragmentation products (see section 2.6.6).

6.2 The physical justification of the Morrissey systematics

Numerous experimental data of nucleus-nucleus collision have shown that in the velocity space the distribution of fragmentation residues is represented by an isotropic three-dimensional Gaussian centred on the longitudinal axis, as schematically illustrated in figure 6.4-left. The momentum imparted to the residual nucleus ("momentum transfer") is generally described in terms of "mean longitudinal momentum transfer" (i.e. the average value of the projection of the momentum distribution on the beam axis) and of width of the Gaussian distribution. For peripheral nucleus-nucleus reactions, the above experimental observations were explained in the following way.

As discussed in section 5.1, the interaction of the two nuclei is usually described in terms of "abrasion" of the nucleons that geometrically overlap during the interaction [Oli79]. This "participant" zone is considered geometrically well separated from the "spectator" nucleus (see figure 6.4-centre), from which the residual fragments originate. While the participant nucleons will finally form a hot fireball, or "firestreak", from the point of view of the spectator nucleus, the interaction acts as a sharp cut of the nucleus: the nucleons hit at random go off together as a single piece.

Two effects mainly determine the width of the isotropic three-dimensional Gaussian momentum distribution of the final fragment: the Fermi momentum of the abraded nucleons, and the evaporation cascade from the excited residual spectator. In the frame of the Fermi-gas model, the momenta of the nucleons follow a certain distribution. Their vectorial sum gives the momentum of the nucleus, which is zero in the centre-of-mass frame. Since the momenta of the ejected nucleons are sampled randomly from their distribution (see figure 6.4-right), the sum of the momenta of the ejected nucleons will form a Gaussian distribution. For momentum conservation the surviving spectator will also exhibit a Gaussian momentum distribution. Goldhaber [Gol74] calculated the width of this distribution and found that it is approximately proportional to the square root of the abraded mass. Crespo et al. [Cre70] calculated the random combination of small recoil momenta from the sequential evaporation of nucleons and found that it contributes to the width of the momentum distribution of the residual fragment by a quantity proportional to the square root of the abraded mass. Between the two contributions, the one originating in the abrasion stage is dominant.

Abul-Magd, Hüfner and Schürmann [Abu76] estimated the magnitude of the longitudinal momentum assuming that the fragmentation reaction could be described as a friction phenomenon. Considering a projectile-fragmentation reaction, some nucleons of the projectile are hit by the nucleons of the target and are kicked off. A nucleon of the projectile that receives a "kick", i.e. a momentum transfer $\boldsymbol{q}$, has to spend part of it, $\boldsymbol{P}=\boldsymbol{q}-\boldsymbol{q}'$, for climbing up the potential well and emerging with momentum $\boldsymbol{q}'$. For momentum conservation the projectile-fragment will gain a momentum $\boldsymbol{P}$, equal in module to the momentum loss $\boldsymbol{P}=\boldsymbol{q}-\boldsymbol{q}'$ of the nucleon. The momentum gain $\boldsymbol{P}$ can be described by a friction coefficient f, $\boldsymbol{P}=f\boldsymbol{q}$. The average value of the transversal component of $\boldsymbol{P}$, $\langle P_{\perp}\rangle$, is equal to zero for symmetry reasons (projectile and target interact in each direction of the impact parameter with equal probability). The average value of the longitudinal component of $\boldsymbol{P}$, $\langle P_{//}\rangle$, is proportional to the longitudinal component of the momentum transfer $\boldsymbol{q}$ of the nucleon-nucleon collision, according to the relation $\boldsymbol{P}=f\boldsymbol{q}$. Abul-Magd, Hüfner and Schürmann derived the expression for the friction coefficient, and estimated a value of $f\approx1/3$ for a great variety of reactions. Therefore, the global effect on the longitudinal momentum of the fragment depends on the number of nucleons removed. In other words, they found that the module of the longitudinal momentum is proportional to the abraded mass ΔA_{ABR}.

Later Morrissey [Mor89] compared the momentum distributions of residues produced in several different systems (target/projectile/energy) measured both in inverse and direct kinematics. On the bases of the physical considerations presented above, he derived semi-empirical parameterisations for the longitudinal momentum transfer (proportional to the mass loss, ΔA) and for the width of the Gaussian distribution (proportional to the square root of the mass loss, $\sqrt{\Delta A}$).

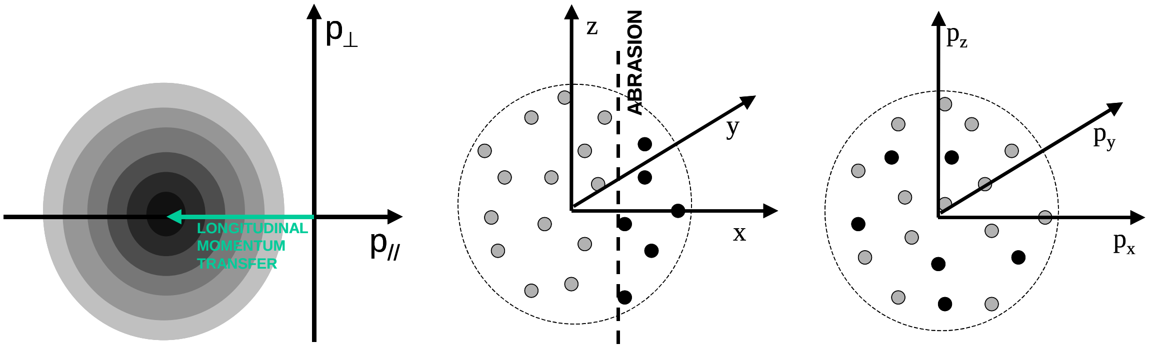

Figure 6.4: Left: three-dimensional Gaussian distribution of fragmentation residues in the frame where the beam is at rest; centre: the abrasion process acts as a sharp cut of the nucleus in the space; right: the expelled nucleons (black ones) can occupy any position in the three-dimensional Gaussian distribution in the momentum space.

6.3 The experimental results for large mass loss

As shown in figure 6.1, many results on the mean velocity are in agreement with the above expectations. The variation in velocity is found to be proportional to the mass loss ΔA for numerous experiments, where the mass of the fragment is not much smaller than the mass of the primary nucleus and the longitudinal mean transfer is anti-parallel to the beam direction (for projectile-fragmentation). Justified by the physical picture presented in the previous section, it seems reasonable to expect that a more violent collision, which will abrade a larger mass, will suffer a larger friction and induce a larger (anti-parallel) momentum transfer. However, for larger values of ΔA, the data show large fluctuations and contradictory behaviours (figure 6.1). The friction occurring in the collision is such a valid argument that there was always the suspicion that all the observed deviations from the Morrissey systematics could be due to failures of the measurement techniques. Loveland [Lov88] defined “unusual” the observed backward emission of light fragments resulting from the fragmentation of gold that, according to the expectations should have gone onward. Lindenstruth [Lin93], in his PhD thesis, admitted that his data deviated for some reason from the Morrissey systematics. Still, the determination of the velocity from time-of-flight measurements with high precision is difficult due to the pulse-height dependences of the time signals. Maybe for this reason, his results were never published.

Coming to our results, one expects the velocity of any pre-fragment[1] to be lower than the velocity of ^{238}U and to decrease more and more with the mass loss ΔA. The pre-fragment will then reach a stable configuration by an evaporation process or by fission. These processes are expected to be isotropic and will not change the mean velocity of the pre-fragment. In case of fission the two fragments will run apart in opposite directions in the frame of the fissioning nucleus: the centre-of-mass velocity of the two nuclei must be equal to the velocity of the compound nucleus from which they originated, thus slightly negative. In case of fragmentation, due to the violence of the abrasion process and the consequent strong friction, it is expected that the velocity of the pre-fragment, which will become a

---

[1] With "pre-fragment" we refer to the projectile spectator just after the abrasion.

certain isotope at the end of the evaporation chain, is much smaller than the velocity of the compound nucleus that will generate the same isotope as a fission fragment. However, figure 6.5 shows clearly that, on the contrary to the expectation that the spectator projectile is slowed down, the lower is the atomic number (i.e. the larger the mass loss) the higher the mean velocity of the fragment is. It even exceeds that one of the beam for fragment charges lower than $Z \approx 28$.

The figure presents also the mean recoil velocity of the fissioning nuclei observed in the interaction of the uranium beam with the hydrogen nuclei as a function of the atomic number of the observed fission fragment. This velocity is approximately -0.1 cm/ns for every pre-fragment going to fission after the interaction with hydrogen. As commented above, we would expect to find the mean velocity of the fragmentation residues much lower than -0.1 cm/ns. But this is not the case, as the experiment clearly shows. Although the method offered by the FRS to measure the absolute velocity of fragments by the magnetic rigidity is very accurate, the comparison with the mean recoil velocity of the fissioning nuclei offers an additional calibration on the basis of the nuclei observed in the same Z range. As deduced from the fission velocities, the fission fragments are emitted from a heavy fissile nucleus only slightly lighter than the projectile (see section 4.2.2). The momentum transfer in the preceding abrasion process, where the heavy fissioning nucleus is formed, is slightly negative ($\langle \upsilon_{//} \rangle \approx -0.1$ cm/ns). This is consistent with the Morrissey systematics. So, the velocity of the light fission fragments reflects the negative recoil of the heavy target-like fissioning nucleus. But this negative velocity is not observed for the fragmentation residues measured at the same time and with the same detectors. Therefore, any systematic error in the measurement that would affect the observed acceleration tendency can be excluded.

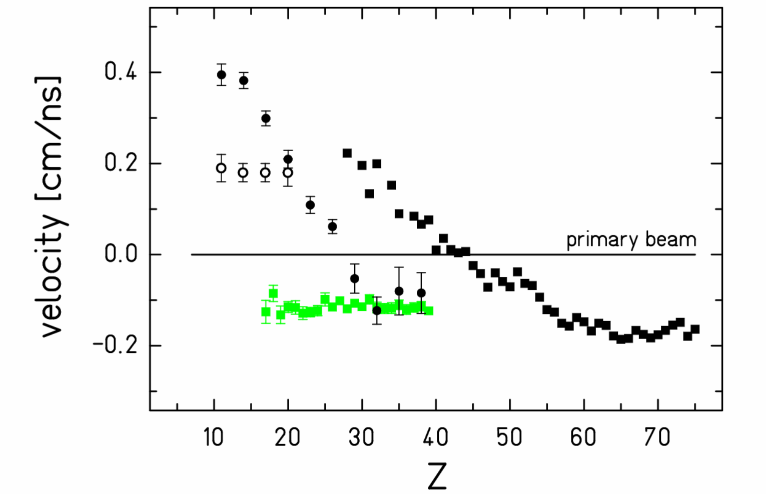

Figure 6.5: Comparison of the average mean values of the velocity distributions induced in two fragmentation reactions: 1 A GeV ^{238}U on titanium (dots) [this work – see figure 3.13 for details] and 1 A GeV ^{238}U on lead (black squares) [Enq99]. The grey squares (🟩) at about -0.1 cm/ns represent the mean recoil velocity of the fissioning nuclei in the reaction 1 A GeV ^{238}U on proton [this work].

The comparison with the recoil of the fissioning nuclei is for sure the clearest proof of the observed acceleration effect. Although the global tendency is clear, we want to spend few more words about the quantitative results. In the following, we will give a list of the magnitude of the different systematic uncertainties and corrections that affect the determination of the velocity of the fragments.

The larger constraint on the quantitative results is related to the expected existence of a hidden forward hump due to the fission component of the velocity spectra. The forward hump evidently affects the mean position of the fragmentation velocity distribution. As showed in figure 2.24, the most extreme position of this hidden hump is well defined, thanks to values assumed by the χ^2 resulting from the fit. So the minimum values of the mean velocity, represented in figure 6.5 by the empty circles with their own error bars, could be established as explained in section 2.6.6.

The limited angular acceptance of the FRS can also affect the quantitative result in a systematic way. Due to the angular cut, fragments emitted in forward direction are more transmitted, and the measured mean value of the longitudinal velocity distribution is shifted towards positive velocities. The correction of the effects of the transmission was performed as explained in section 2.6.4. It goes from 0.1 cm/ns for Z=10 down to 0.01cm/ns for Z=40 (see figure 2.22). The correction is visible only in the difference between the lightest data point (Z=11) of figure 3.13 and the result of the global fit (where the correction for the angular transmission was not considered). For fragments with Z>30, for which the angular transmission is larger than 90%, no correction is needed. This implies, by the way, that the deviation from the Morrissey systematics observed in our data would remain independently of any correction for the limited angular transmission.

Also the position calibration of the scintillator of the intermediate image plane influences the determination of the velocity. The position calibration was done exploiting the geometrical border of the sensitive area of the scintillator, as shown in figure 2.6, assuming linear response of the detector. The method described in Appendix A assures that the calibration parameters were correct inside the estimated uncertainties.

6.4 Dynamics of nuclear collisions at relativistic energies

The physical picture for peripheral nucleus-nucleus collisions developed independently from the study of the dynamics of the reaction for mid-peripheral or central nucleus-nucleus collisions. This subject was always connected to the study of nuclear multifragmentation, because the smaller impact parameter induces a larger excitation energy, which leads to the formation of several intermediate-mass fragments[1] (IMFs), or even to the total disassembly of the nucleus. From the experimental point of view, detectors developed in order to record all the fragments produced in one event (as for instance large-acceptance spectrometers, or the so-called “4π” detectors). As a counterpart of this global view, the experimental conditions limited the mass (and sometimes even charge) resolution of fragments with A<30. The physical signatures and observables for projectile-like fragments and IMFs produced in the same system (as for instance 1 A GeV ^{238}U on Ti) at different impact parameters can be extremely different. For this reason, the two scientific communities (“fragmentation” and “multifragmentation”) developed quite independently.

---

[1] With the term IMFs are in general indicated fragments with mass smaller than A≈30.

In this section we want to shortly describe the dynamic of the nucleus-nucleus collisions at relativistic energies.

Large-acceptance spectrometers and 4π detectors allow the study of the products originating in two different zones of the system: the IMFs generated in the simultaneous break-up of the spectator, and the particles emerging from the fireball. The two classes of products, IMFs and particles from the fireball, are generally investigated independently, because their characteristics are quite different and require different experimental set-ups. However, they are not uncorrelated. Indeed, they are connected by the dynamic of the collision.

All theoretical models agree that the longitudinal kinetic energy transferred from the impinging nucleons to the nucleons of the participant zone is converted into thermal and potential compressional energy. In other words, in the participant zone, the incoming matter both from projectile and target is mixed, heated and compressed. In a successive fast expansion (or blast) of the participant matter, the stored energy is converted again into kinetic energy of the nucleons and subnuclear particles emitted outwards. Initially, when the spectators are still in touch, they block the escape of compressed matter along trajectories in the reaction plane, "squeeze-out" the matter, and force it to flow out of the compressed region in directions perpendicular to the reaction plane ("out-of-plane") (see figure 6.6). Later, after the spectators pass, the nucleons from the compressed central region preferentially escape along trajectories parallel to the reaction plane ("in-plane") that are no longer blocked. The enhancement of this later in-plane emission begins at "the end" of the collision, i.e. when the spectators are "separated" again. Thus, the emission first develops out-of-plane (along the y-axis) and then spreads into all direction of the x-y plane. The later in-plane emission becomes the dominant direction at higher excitation energies (e.g. it was estimated that for Au on Au this happens at 5 GeV/nucleon [Dan00]), where the passage time is considerably less.

In the light of this dynamical process, it can be easily understood how the characteristics of the particle emission from the fireball are affected by the spectators (i.e. by IMFs) and vice versa. The collective flow of particles is strongly influence by the presence of the nearby cold spectators, and suffers of the so-called "shadowing" effect of the spectators, with the result that their angular distribution is not isotropic. On the other hand, the spectators are hit by the particles from the exploding fireball, and their kinematical properties change.

Although this dynamical picture is commonly accepted, the quantitative determination of this or the other effect is still far from having a well-established solution.

Concerning the flow, the directions in which matter expands and flows away from the compressed region depend primarily upon two things: the time-scale for the blockage of the emission in the reaction plane by the spectators, and the time-scale for the expansion of the compressed nuclear matter. The blockage time-scale depends on the radii of the nuclei and on the incident velocity. The expansion time-scale depends on the density of energy stored in the nuclear matter and on the nuclear mean field potential. Different modelling of the mean field potential leads to different behaviour of the flow. More repulsive mean fields lead to higher pressures and to a more rapid expansion when the spectator matter is still present. This causes preferential emission perpendicular to the reaction plane where particles can escape unimpeded. Less repulsive mean fields lead to slower expansion and preferential emission in the reaction plane after the spectators have passed.

The sideways deflection of the spectators depends on the pressure of the compressed region, therefore on the same quantities on which the flow depends. This sideways deflection of the spectators occurs primarily while the spectators are adjacent to the compressed region. In general, larger deflections are expected for more repulsive mean fields, which generate larger pressures, and conversely, smaller deflections are expected for less repulsive ones. However, the change in the momentum that results from a sideways deflection is in all cases not large.

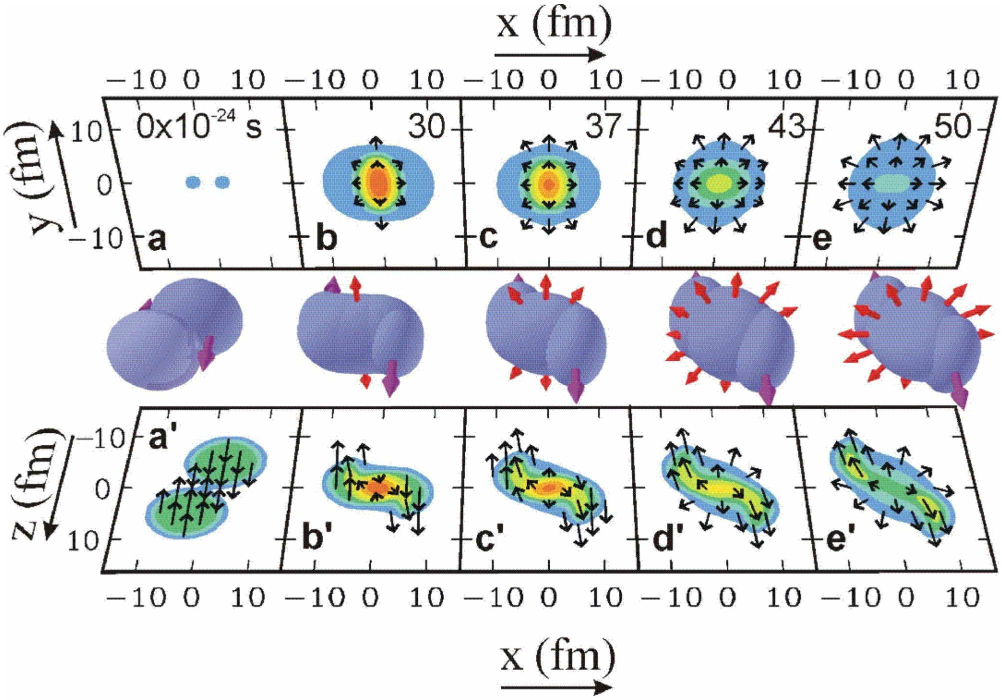

Figure 6.6: Schematic overview of the dynamics of a mid-peripheral nucleus-nucleus collision. The figure is taken from [Dan02].

6.5 Predictions for the deflection of the spectators

As said in the previous section, both the pattern of the elliptic flow and the deflection of the spectators depend on the nuclear mean field (MF). The strength of the nuclear force acting among nucleons determines the nuclear mean field potential, which in turn determines the nuclear compressibility. It is often referred to a “hard” or “soft” equation-of-state to indicate a lower or higher value of the nuclear compressibility.

There is another possible characteristic of the nuclear force that can affect the nuclear mean field: this is the momentum dependence of the nuclear interaction. It is commonly accepted that, in analogy with the electromagnetic interaction, the nuclear interaction should act differently on a hadron in movement. However, the exact quantitative description of the momentum dependency of the mean nuclear field is not yet achieved, because the experimental observables are always mixed up with other parameters, like the hardness (or softness) of the EOS.

All considered, the quantitative determination of the characteristics of the flow and of the deflection of the spectators is a complicated task, because the results of the models are sensitive to both the nuclear-matter incompressibility and to the momentum dependence of the mean field.

To describe the early stage of the reaction, before the thermal equilibration and the successive statistical deexcitation, theoreticians have developed different types of dynamical models where all the above aspects are modelled or parameterised. One type of model is the "intra-nuclear cascade" (INC), where the collision is described following one by one the nucleon-nucleon interactions, but the potential is neglected, and also most of the quantum mechanical aspects. This makes the predictive power of INC models rather limited. An exact description is in principle realized by the "Fermionic-molecular-dynamics" (FMD), where nucleons are treated by their corresponding wave function. Although in principle correct, for technical reasons this model is only applicable to very light nuclei. A more widely used approach are the "hydrodynamical transport models" (like BUU or VUU models) where the matter is treated as a continuum and the characteristics of each "cell" of volume (in space and momentum) are determined applying phase-space laws under the constrains imposed by the acting forces. In this way, effects of the collision as well as the mean field can be considered. These models do not describe the particles as separated entities, but can give anyhow a quite good microscopic insight.

In 1988 Molitoris et al., by means of a transport code, studied the transverse momentum change of all the nucleons in a nucleus-nucleus collisions. They found that as the energy increases the mean field loses the ability to bind the hot expanding nuclear matter and the transverse momentum change from negative to positive. Several other theoretical works studied the effects on the elliptic flow on the transferred transverse momentum. In ref. [Dan00] it is shown that in peripheral heavy-ion collisions the high-momentum elliptic flow is strongly sensitive to the momentum dependence of the mean field. However, the magnitude of the transverse momentum depends both on the nuclear incompressibility and on the momentum dependence of the mean field, with the results that an appropriate combination of soft EOS and momentum-dependency or hard EOS and momentum-independency could produce the same results.

It was only recently that a transport code was applied to investigate the change of properties of the spectators emerging from a nucleus-nucleus collision [Shi00]. Shi, Danielewicz and Lacey [Shi00] investigated the possibility of using the spectators' properties as indicators of the characteristics of hot and dense nuclear matter. In fact, spectators are present at the site of the nuclear explosion, and since they deflect particle emissions toward the reaction plane, their properties may be significantly modified, and carry direct information on the hot and dense region. Among the properties of the spectators that can be affected by the explosion, the kinetic ones carry the most valuable information. Shi, Danielewicz and Lacey studied in detail the change in the centre-of-mass of the net average momentum per nucleon of the spectator, $\Delta|\langle P/A\rangle|$. This change regards not only the transversal but also – and mostly – the longitudinal momentum. According to their BUU transport calculation, the change in the magnitude of the c.m. momentum per nucleon is generally dominated by the change in the longitudinal momentum per nucleon.

According to their calculations, $\Delta|\langle P/A\rangle|$ is strongly sensitive to the momentum dependence of the mean field but insensitive to the softness or hardness of the EOS. This can be clearly seen in figure 6.7, where the change in the average net c.m. momentum per nucleon $\Delta|<P/A>|$ as a function of the impact parameter is presented for four representative EOS: hard momentum-dependent (HM), soft momentum-dependent (SM), hard momentum-independent (H), and soft momentum-independent (S) for the spectators of the system ^{124}Sn+^{124}Sn at 800 A MeV (left) and ^{197}Au+^{197}Au at 1 A GeV (right). But the most interesting result of their work is the acceleration observed for the system Au+Au at low impact parameters (*b* = 6 fm, in figure 6.7-right). Shi, Danielewicz and Lacey [Shi00] support this result giving the following explanation: «The speeding up of the spectator at low *b* in Au+Au may be understood in terms of the explosion of the participant zone. On one hand, the spectator acquires the transverse momentum. On the other hand, in the longitudinal direction the explosion acts more on the rear of the spectator piece than on the front. If the explosion is strong enough, the ordered push may overcome the friction effects, producing a net longitudinal acceleration for a piece. There is no issue of energy conservation since the work is done by the participant on the spectator zone. The difference between Sn+Sn and Au+Au is in the equilibrium time scale relative to the duration of the fireball. Differences in the net final momentum per nucleon between different mean-fields for both systems, with significantly higher net momenta for the momentum-dependent than momentum-independent mean-fields, may be understood in terms of the violence of the explosion that accelerates the spectator.» Note that for very peripheral collisions $\Delta|\langle P/A\rangle|$ is negative even for momentum-dependent calculations. It increases and becomes even positive as the impact parameter decreases. The change in the magnitude of the c.m. momentum per nucleon with *b* indicates that the friction phenomenon dominating at peripheral collisions is overcome by the blast of the exploding particles from the participant zone as the reaction becomes more violent.

Another interesting aspect of their calculation is the dependence of $\Delta|\langle P/A\rangle|$ on the impinging kinetic energy. This can be seen for Sn+Sn in figure 6.8. If one takes the magnitude of $\Delta|\langle P/A\rangle|$ as a measure of the violence of the collision, one notices that the initial kinetic energy plays also a big role. All considered, the mass of the system, the impact parameter, the kinetic energy, they all contribute to the quantitative determination of $\Delta|\langle P/A\rangle|$, once the nuclear compressibility and the EOS are established.

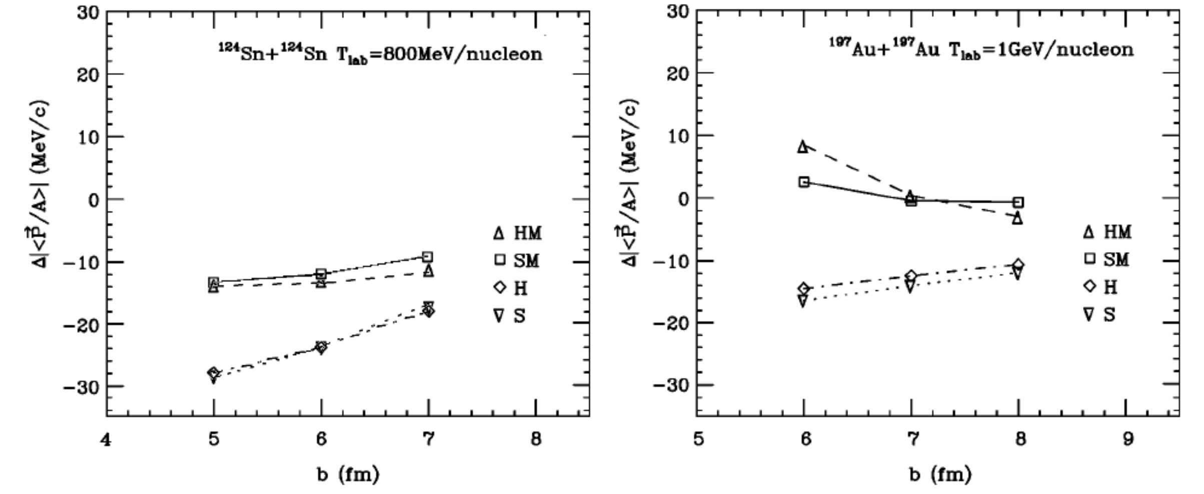

Figure 6.7: Change in the average net c.m. momentum per nucleon $\Delta|<P/A>|$ as a function of the impact parameter for four representative EOS: hard momentum-dependent (HM), soft momentum-dependent (SM), hard momentum-independent (H), and soft momentum-independent (S) for the spectators of the system ^{124}Sn+^{124}Sn at 800 A MeV (left) and ^{197}Au+^{197}Au at 1 A GeV (right). Results of the BUU calculation reprinted from [Shi00].

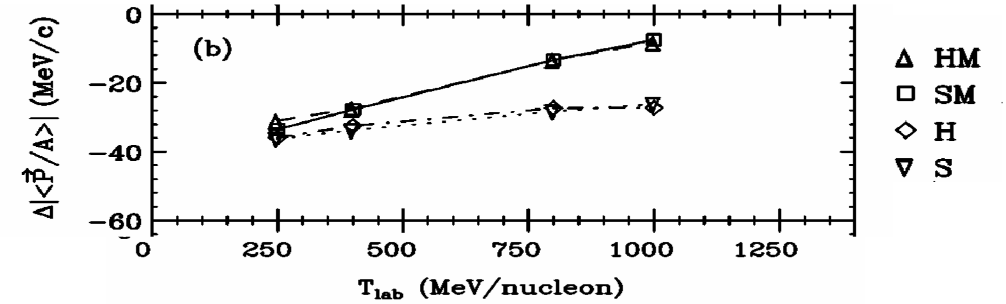

Figure 6.8: Change in the average net c.m. momentum per nucleon Δ|<P/A>| as a function of the beam kinetic energy for the spectators of the system ^{124}*Sn+*^{124}*Sn at 800 A MeV at b=5 fm. See caption of figure 6.7 for the symbols. Results of the BUU calculation reprinted from [Shi00].*

6.6 Interpretation of the results

The high-precision measurement of the velocity distributions of the remnants of the projectile in the reactions ^{238}U + Ti and ^{238}U + Pb at 1 *A* GeV, presented in figure 6.5, revealed that the mean values of the velocities of the fragmentation products do not decrease any more if the mass loss becomes large. They increase and finally they are even faster than the projectiles.

The BUU calculations of Shi, Danielewicz and Lacey [Shi00] offer a natural explanation to this result: the observed re-acceleration of the spectator fragment is due to the participant blast. At large impact parameters, where heavy residues are formed [Hub91], the two nuclei experience some friction, which slows them down. At relatively small impact parameters, leading to the production of light reaction residues [Hub91], the hot and compressed fireball starts to play a role in the dynamics. The explosion of the fireball overcomes the friction phenomenon, and the global effect can result in a net acceleration of the spectators.

One should not be surprised that this effect was not observed so clearly with other experimental techniques. The Δ|<P/A>| is in order of 1% of the initial momentum per nucleon, so an extremely precise determination of the longitudinal momentum is required. The extremely careful time-of-flight calibration performed in the work of Lindenstruth [Lin93] could reveal an unexpected tendency (figure 6.2), but still the error bars were large enough to cast a doubt. With the FRS it was possible to achieve a resolution with a relative uncertainty of $5\cdot10^{-4}$, about 10 times more precise than the typical TOF measurements.

We cannot directly compare our data with the calculations, because the interacting system is different from the ones presented in ref. [Shi00]. However, it is noteworthy that the post-acceleration effect in the calculations amounts to 10 to 20 *A* MeV/c in the center-of-mass system, corresponding to about 0.25 to 0.5 cm/ns in velocity in the projectile frame, if a momentum-dependent mean field is used, compared to calculations with a momentum-independent mean field. This is in the order of magnitude of the positive velocity values observed in the present experiment for the lightest fragments.

This finding sheds a new light on the systematics of previously measured data, in particular on the velocities of residues far from the projectile. According to ref. [Shi00], the velocity of the spectator is modified by the expansion of the fireball, and, as pointed out in the previous section, other parameters like the mass of the target nucleus and the beam energy have a strong influence. This might explain the large spreading in the Morrissey systematics of previous data for light fragments, including those collected by Morrissey himself, presented in figure 6.1.

The predicted acceleration effect is rather sensitive to the size of the system. Therefore, one might be surprised about the relatively small difference in the measured acceleration effects of the two systems, ^{238}U + Pb and ^{238}U + Ti (see figure 6.5). The abrasion model [Oli79] gives a plausible explanation for this finding: If the impact parameters are chosen in a way that the projectile spectators of the two systems have the same mass, e.g. $A \approx 100$, the abrasion model predicts that the size of the fireball in the system ^{238}U + Ti is only about 20% smaller than in the system ^{238}U + Pb. For a more quantitative assessment, dedicated calculations of the systems studied in the present work and in previous experiments performed with different techniques and instruments would be required.

If our interpretation is correct, the measure of the longitudinal momentum, as an observable that carries information on the participant blast, leads to some interesting consequences.

1) According to the model calculations of Shi, Danielewicz and Lacey, the peculiar nature of the longitudinal momentum as an observable is the selective sensitivity to the momentum dependence of the mean field. This property is rather unique compared to most experimental signatures, which are sensitive to both, the hardness of the equation of state and the momentum dependence of the mean field. Therefore, a systematic investigation of the longitudinal momentum for different combinations of systems and energies, cross-checked with the theoretical predictions, could elucidate the question of the momentum dependence of the nuclear mean field, and help to interpret other experimental signature that depend also on the stiffness of the EOS.

2) As shown in ref. [Hub91] and in many other experiments, there is a clear correlation between the mass of the fragment and the impact parameter between the two colliding nuclei. One can then correlate the momentum of the fragment with the impact parameter, i.e. with the energy deposited in the fireball. Thus, the strength of the momentum dependence of the mean field could be correlated with the energy deposited in the fireball.

3) The heat and compression achieved in the fireball depends on the in-medium properties of the nucleons that constitute it. A systematic investigation of the longitudinal momentum for different combination of projectile-target, which would lead to different neutron-to-proton ratio of the participant matter, could provide new information on the isospin dependence of the nuclear mean field.

To conclude, the re-acceleration of the projectile spectator will provide a new tool to investigate the equation of state of nuclear matter. According to these calculations, the longitudinal momentum is selectively sensitive to the momentum dependence of the nuclear force. Further theoretical and experimental studies are needed to establish quantitatively the dynamic of the process.

Chapter 7
The even-odd structure in the yield of the fragmentation products of 1 *A* GeV ^{238}U on titanium

The charge distribution of the fragmentation products of 1 *A* GeV ^{238}U on titanium, analysed in this work, revealed an evident even-odd effect (figure 3.12). In this chapter, we will analyse in detail this result.

Signatures of nuclear structure, manifested as an even-odd staggering, appear also in the isotopic distributions from different types of nuclear reactions at low energies, like low-energy fission or transfer reactions. The characteristics of the even-odd effects, appearing in the yield distributions, were understood in the framework of the statistical model as the manifestation of *pairing correlation* in the nucleus.

Before entering into the analysis of the experimental results, here we want to shortly remind the basic features of the pairing correlation, pointing out some aspects that will be useful for the discussion later.

7.1 Basic features of the pairing correlation in nuclei

Pairing, critical temperature, binding energies

The prominent residual interaction which goes beyond the mean field description of the nucleus is due to the pairing correlation.

The stationary states obtained when the pairing interaction is considered are lower than those determined using a shell-theory potential, which represents the average force of all the other nucleons in the nucleus. In particular, the energy of the ground state is lowered considerably with respect to the one predicted by the liquid-drop and by the shell models by a quantity called “condensation energy”. By coupling the identical nucleons, the nuclear binding energy is increased compared to its value predicted by the shell model.

The difference between the excited states, which are also a bit lower that those obtained with the average potential, vanishes gradually approaching a certain value of the excitation energy (corresponding to a *critical temperature* T_c). This means that after T_c the effect of pairing is not visible anymore, and the nucleus can be described directly using an average potential.

One of the most important aspects of pairing is that in an even-even nucleus the condensation energy is larger than the condensation energy of an even-odd or odd-odd nucleus by Δ or 2Δ, respectively. 2Δ, a quantity called “pairing gap”, is connected – as the name suggests – to pairing, i.e. to the coupling interaction of two identical nucleons outside a closed shell. When there is a pair of identical nucleons outside a closed shell (case of an even-even nucleus), they can profit of all the orbits available, and their coupling will result in the most binding possible interaction. When there is a pair of identical nucleons plus one other nucleon outside a closed shell (case of an odd-even or even-odd nucleus), the pair of identical nucleons will interact, but they cannot profit of all the orbits available, because one is blocked by the spare nucleon, and their coupling will result in a smaller binding interaction. Finally, when there is a pair of identical nucleons plus one proton and one neutron outside a closed shell (case of an odd-odd nucleus), the pair of identical nucleons will interact, but they have even less orbits available, because two are blocked by the spare nucleons, and their coupling will result in the smallest binding interaction. Therefore Δ can be considered as what has to be paid in binding energy to introduce one nucleon and block one level for the correlate motion. With the same principle, in an even-even nucleus the difference in energy between the ground state and the first excited states is 2Δ. The organised motion of all the paired nucleons makes gain 2Δ of binding energy. To bring a nucleon in the 1st excited states means to break one pair and spoil the ordered motion, thus to pay 2Δ of energy.

Δ represents the staggering of the mean value of the condensation energy (and therefore of the binding energies). The condensation energy (as well as the binding energy) varies of Δ or 2Δ among even-even, even-odd (or odd-even) and odd-odd nuclei. The experimental masses include the condensation energy. Often the experimental ground states of odd-odd nuclei are taken to set the ground states for the liquid drop models. Thus liquid-drop models already include the smooth part of the condensation energy. So, while the condensation energy is around 4 MeV, Δ is only around 1 MeV (about 3 MeV are incorporated in the ground state predicted by the liquid-drop).

The binding energies, E_{gs}, can be divided into 3 contributions: a part due to the liquid drop, E_{gs}^{ld}, a part due to shells, E_{gs}^{shell}, and a part due to pairing, $E_{gs}^{pairing}$: $E_{gs} = E_{gs}^{ld} + E_{gs}^{shell} + E_{gs}^{pairing}$.

The term E_{gs}^{ld} is a smooth quantity and does not contribute to the staggering. In absolute value the E_{gs}^{ld} is the largest contribute. In order to magnify the even-odd structure due to pairing, it is convenient to investigate the staggering effects on the reference base ($E_{gs} - E_{gs}^{ld}$). Figure 7.1-left shows how the pattern of the binding energies of nuclei with Z=N looks like if the energies of the ground states are plotted relatively to the energy of the corresponding liquid-drop ground state.

The term $E_{gs}^{pairing}$ introduces the effects of pairing. $E_{gs}^{pairing} = 2\Delta, \Delta, 0$ for even-even, even-odd (or odd-even) and odd-odd nuclei, respectively. Experimentally it is found that the magnitude of the fluctuation depends on the mass of the nucleus: $\Delta \approx 12/\sqrt{A}$ MeV. The magnitude of Δ was extracted avoiding the local fluctuations of the masses due to the presence of shells.

The term E_{gs}^{shell} is the most difficult to be determined. It can be calculated using the other terms: $E_{gs}^{shell} = E_{gs} - E_{gs}^{ld} - E_{gs}^{pairing}$, where E_{gs} is the experimental value of the binding energies.

In figure 7.1-right it is plotted the extracted systematic behaviour of the pairing term, $E_{gs}^{pairing}$, introduced on the reference base of the liquid drop (the zero coincides with the ground state of odd-odd nuclei). For what said above, it coincides with $E_{gs} - E_{gs}^{ld} - E_{gs}^{shell}$ (when other contributions to the binding energy, like the Wigner term, are neglected). This reference base will also be used for explanation sometimes in the next sections.

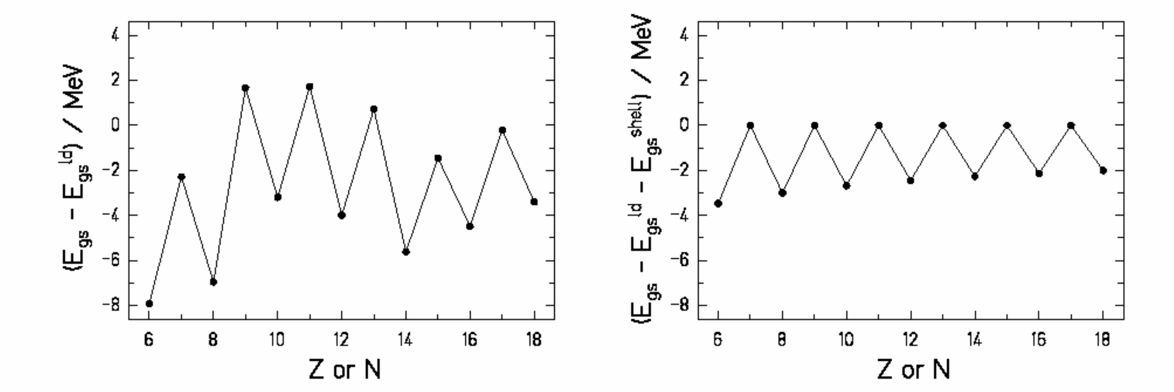

Figure 7.1: Schematic pattern of the binding energies for N=Z nuclei (see text for explanation).

Superfluidity

The ground state corresponds to the most coherent motion of nucleons. There, nucleons are paired as much as they can. The excited states correspond to configurations of the nucleus where a less coherent motion is achieved. It can be imagined as a configuration where the unpaired nucleons block possible orbits for the scattering. The higher is the energy, the more nucleons will occupy (and block) levels. After T_c there is no coherent motion due to pairs anymore, then we enter in the single-particle-excitation picture.

Since pairing interaction represents an ordered motion of pairs of nucleons, it represents a "global" behaviour of the nucleus. It can be well described by means of the BCS theory[1]. The excitations of the system are not given by the single-particle excitations but by the so-called "quasi-particle" excitation. When describing its superfluid properties, the nucleus can be considered composed of two subsystems (proton subsystem and neutron subsystem). The two subsystems can be independently analysed.

Let us consider the proton subsystem. We assume that the neutron subsystem is not excited. In an even-Z nucleus 2Δ of energy are needed to excite the first state. This

---

[1] The BCS theory is the microscopic theory of superconductivity that was created by John Bardeen, Leon Cooper and Robert Schrieffer in 1957. According to this theory, the electrons join up to form pairs, known as Cooper pairs, due to interactions with the crystal lattice at low temperatures (the Coulomb repulsion of the electrons is overcome by the attraction induced by the exchange of phonons between electrons close to the Fermi surface). Electrons in these Cooper pairs have opposite values of momentum, meaning that the pairs themselves generally have zero orbital angular momentum (to maximize the attraction, the Cooper pairs appear in the simplest s-wave channel). The formation of Cooper pairs also leads to the creation of a superconducting energy gap, which means that single electrons cannot occupy states near the Fermi surface. Such energy gaps - which are essentially equal to the energy needed to break up the Cooper pairs - show up clearly an exponential drop in the specific heat and thermal conductivity at what is known as the critical temperature, Tc. Immediately after its creation, BCS theory had a significant impact on many other fields of physics. BCS theory predicts that any system of interacting fermions could undergo a superconducting, or in the case of fermions with no charge, a superfluid transition, provided one had a net fermion attractive interaction in some angular momentum channnel. In 1957 Bhor, Mottelson and others predicted that in nuclear matter the attractive nuclear interactions would lead to neutron superfluidity and proton superconductivity, i.e. the pairing of protons and neutrons in the nuclei also would lead to an ordered phase with an energy gap between paired (even) and odd nuclei. The energy gap for nuclei can be calculated using the Bardeen-Cooper-Schrieffer (BCS) equation.

corresponds to the energy needed to break a pair. Once a pair is broken, the nucleons can occupy higher energy levels, which are separated by much less than 2Δ. In an odd-Z nucleus the unpaired proton can immediately jump on the next levels. This situation is schematically plotted in figure 7.2. The difference of Δ between the two ground states is due to the different binding energies of the two nuclei. The critical temperature and the critical excitation energy are about 0.5 MeV and 10 MeV, respectively, for all nuclei. Above this excitation energy the single-particle excitation levels are a valid description of the possible states of the nucleus. Please note that the levels plotted in figure 7.2 are not to scale. Appropriate quantum-mechanical models can calculate how the quasi-particle excitation levels are spaced in the two cases [Hui72, Ign73].

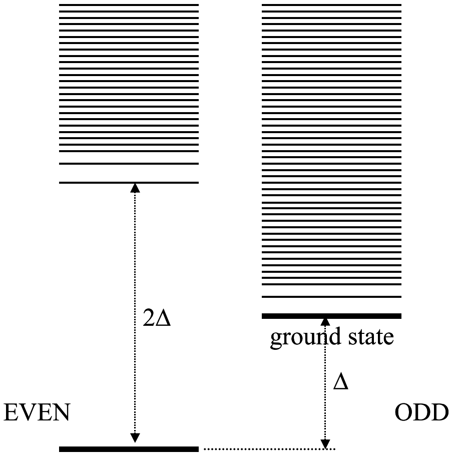

Figure 7.2: Schematic plot of the levels of energies (not to scale) for the proton subsystem for an even-Z nucleus and for a close odd-Z nucleus, when the differences due to the liquid drop and shell effects are neglected.

7.2 Even-odd structure in low-energy reactions: the case of low-energy fission

In this section we want to discuss the reason for the structural effects in some features of low-energy reactions. These structures only appear at low excitation energies, gradually disappearing and giving rise to smooth distributions with increasing excitation energy induced in the reaction. The enhanced production of even elements and the appearance of fission channels in low-energy fission and the production yields in transfer reactions are typical examples of structural effects in low-energy reactions. Here below, we will discuss the case of low-energy fission.

Already from the early radiochemical experiments it has become clear that the production of even elements is enhanced in low-energy fission [Ami75]. The development of methods allowing for in-flight identification of the fission fragments (see e.g. [Lan80]) revealed the dependence of this even-odd structure on the total kinetic energy of the fission fragments. The first systematic overview on even-odd structure in a continuous region of fissioning nuclei [Ste98] was obtained only a few years ago by studying electromagnetic-induced fission from excitation energies around 11 MeV, using secondary beams [Sch00]. Typical examples of these results are depicted in figure 7.3, where the element yields of an even-Z ($^{226}_{90}$Th) and an odd-Z ($^{220}_{89}$Ac) fissioning nucleus are shown.

While the even-Z system ($^{226}_{90}$Th) shows an enhanced production of even elements all over the range with an increase of the local even-odd effect for asymmetric charge splits, the odd-Z system ($^{220}_{89}$Ac) shows a positive even-odd effect in the left wing and a negative even-odd effect in the right wing of the distribution. About 70 systems have been investigated, and all reveal essentially the same features. These results could be interpreted with theoretical considerations based on the statistical model. The local even-odd effect of the odd-Z systems and an essential part of the variation of the even-odd effect of the even-Z system have been attributed to the larger single-particle phase space available for unpaired nucleons in the heavier fragment. Once this effect was considered, the enhanced production of fission fragments with even neutron or even proton number was quantitatively explained by the number of excited states with a completely paired configuration of the proton or the neutron subsystem, respectively, at the effective scission point, see [Rejm00]. It was shown that the subsystem of one kind of nucleons (e.g. protons) may remain in the ground-state configuration with a certain probability, while the energy is stored in quasi-particle excitations of the other kind of nucleons (e.g. neutrons), even if the excitation energy exceeds the pairing gap. The global even-odd effect in proton and neutron number as a function of the excitation energy at scission was calculated by that model. The analysis clearly showed that the observation of this kind of even-odd effect in fission is restricted to excitation energies at scission below the superfluid phase transition, which occurs around 10 MeV [Ign74].

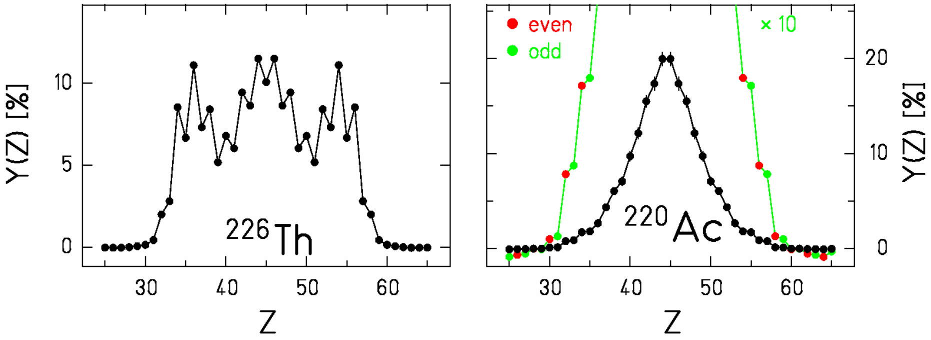

Figure 7.3: Elemental yields of fission fragments produced in electromagnetic-induced fission of ^{226}Th and ^{220}Ac [Ste98].

7.3 The complexity of the even-odd structure in the yield of the fragmentation products of 1 A GeV ^{238}U on titanium

In figure 3.12, the even-odd effect was found in the charge distribution of the uranium-fragmentation products. Looking back to the identification pattern, presented in figure 2.5, the cluster plot reveals that the staggering is rather complex. The vertical line at A/Z=2, collecting the nuclei with N=Z, shows a clear enhanced production of even-Z nuclei. The

7th sequence to the right, corresponding to the nuclei with N=Z+5, shows, on the contrary, an enhanced production of odd-Z nuclei. These observations suggested us to filter the data according to the neutron excess, N-Z. The sequences of nuclei with N-Z=constant correspond to chains of nuclei at 45° in the chart of the nuclides. The production cross sections of the observed fragments, grouped according to this filter, are shown in figure 7.4. The data reveal a complex structure. The nuclide distributions are divided in two different groups: nuclei with even mass (chains: N=Z, N=Z+2, N=Z+4, N=Z+6), and nuclei with odd mass (chains N=Z+1, N=Z+3, N=Z+5). In the first group of fragments, an enhanced production of even-Z nuclei is observed; the strongest effect is observed in the N=Z chain. In the second group, the effect is reversed: the production of odd-Z nuclei is enhanced, and the effect is stronger for the most neutron-rich chains. However, for nuclei with N-Z=1 the reversed even-odd effect vanishes out at about Z=16, and an enhanced production of even-Z nuclei can be observed for $Z > 16$. In other words: the odd-even effects turns into an even-odd effects at Z=16. Finally, all the observed structural effects seem to vanish out as the mass of the fragment increases. Please note that the increase of the reversed even-odd effect in atomic number Z for the neutron-rich odd-A nuclei can also be interpreted as an enhanced production of even-N nuclides, i.e. as a positive even-odd effect in neutron number.

The "strength" of the local even-odd effect can be quantified by the local deviation of the cross sections from a Gaussian-like distribution, according to the formula proposed in ref. [Tra72]:

$$\delta\left(Z+\frac{3}{2}\right)=\frac{1}{8}\cdot\left(-1\right)^{Z+1}\cdot\left[\ln\sigma(Z+3)-\ln\sigma(Z)-3\cdot\left(\ln\sigma(Z+2)-\ln\sigma(Z+1)\right)\right] \qquad (7.1)$$

$\delta(Z)$ is a quantity measured over four consecutive cross sections centred at (Z+3/2). A value equal to 0 means a smooth behaviour, a result approaching 1 indicates an extremely strong fluctuation, tending to total suppression of odd-Z nuclei. The positive sign points out that the production of even-Z nuclei is enhanced, while the negative sign indicates the enhancement of odd- nuclei. The result is presented in figure 7.5, both for even nuclei and

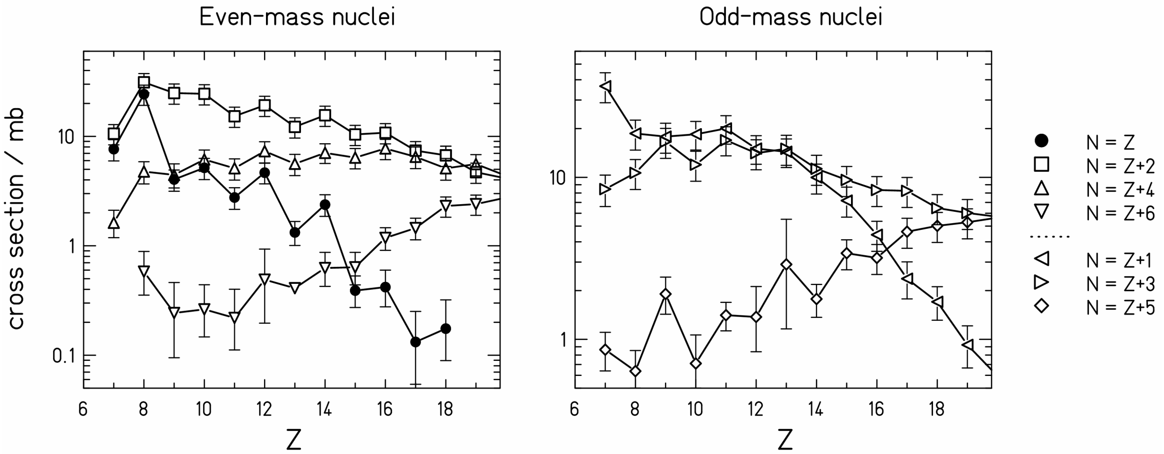

Figure 7.4: Experimental data for the reaction 1·A GeV ^{238}U on titanium. Fragmentation cross sections of residues with even (left part) or odd mass (right part). The two points without error bars

(Z=13, N=19 and Z=11, N=16) do not represent experimental data but extrapolated values from the systematic behaviour of the measured isotopic cross sections.

for odd nuclei. The effect is very strong for nuclei with *N*=*Z* (≈50%): it is even stronger than any even-odd structure observed in low-energy fission [Gön86]. It is still present in the other even-mass nuclei but with strongly reduced strength, about 10% for all the other chains of even-mass nuclei. The enhancement of the odd-*Z* nuclei, corresponding to even-*N* nuclei, is strongest for the most neutron-rich nuclei (*N*=*Z*+5). All the features observed in the experimental data are summarised in table 7.1.

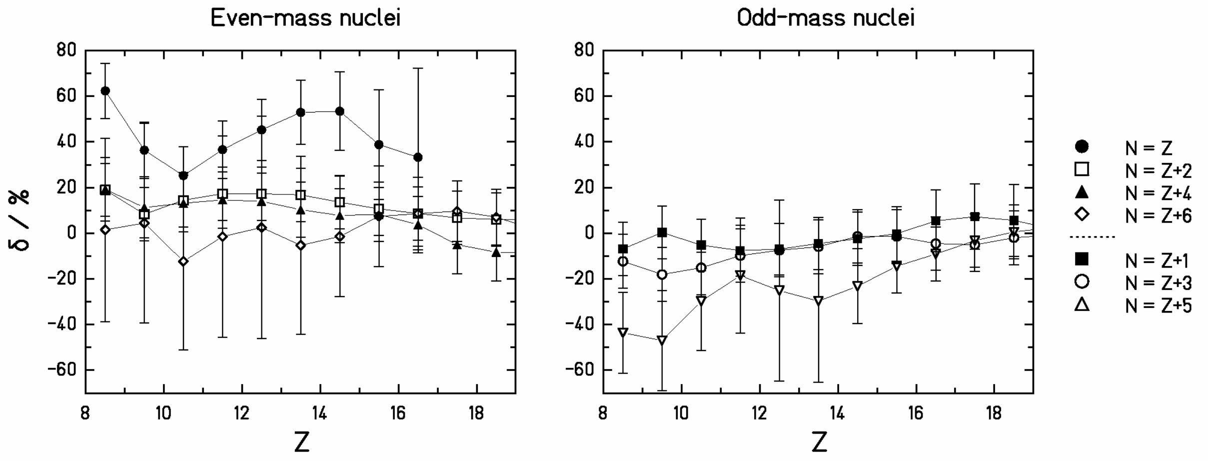

Figure 7.5: Strength of the even-odd effect as a function of Z expressed by δ(Z), defined in equation 7.1. The results show an enhanced production of neutron-deficient even-Z fragments and of neutron-rich odd-Z fragments.

Table 7.1: Summary of the features observed in the experimental data of figure 7.4.

Even-mass nuclei	**Odd-mass nuclei**
Enhanced production of even-*Z* nuclei	Enhanced production of odd-*Z* nuclei
Staggering of same strength (~10%) for *N*=*Z*+2, *N*=*Z* +4, *N*=*Z* +6 chains	The strength of the staggering increases as the neutron excess (*N*-*Z*) increases
Staggering particularly strong (~50%) for the *N*=*Z* chain	In the *N*=*Z* +1 chain the staggering turns from odd-even to even-odd as *Z* increases
Staggering gradually disappears as *Z* increases	

7.4 Even-odd structure in high-energy reactions

In several experiments, in which different rather violent nuclear reactions have been investigated, a fine structure in the nuclide production, manifested as an even-odd effect, has been observed. A (probably incomplete) compilation of these experiments is presented in table 7.2. Most experiments could determine the nuclear charge of the reaction products, only. Consequently, only the enhancement in the production of even-*Z* elements, found in the order of a few tens per cent, could be investigated. Lately, with the use of spectrometers, also the neutron number became accessible: the most remarkable finding of these more recent experiments was a variation of the magnitude of this fine structure with the mean neutron excess of the reaction products [Win01, Bac93]. The results of the present work are in agreement with the results from the experiments reported in table 7.2, but they provide more detailed information.

The complex behaviour observed in the fragmentation yields of the present work can be found also in the nuclide distributions of light fragments produced in the proton-induced high-energy fission of ^{238}U at 1 A GeV, analysed in this work (see Chapter 4). In figure 7.5 the fission cross sections are presented along the chains *N*-*Z*=constant. Four chains could be reconstructed. The results of the analysis of the staggering with the formula of Tracy (equation 7.1) are also presented. In spite of the large error bars, the four chains clearly indicate a similar behaviour of what found for the titanium-induced fragmentation of ^{238}U at 1 A GeV, presented before.

Among the data published in literature, we could only find one set of data where the analysis along the chains *N*-*Z*=constant was possible. They concern the production cross-sections of products in the spallation of ^{238}U at 5.5 GeV [Pos71]. The results are shown in figure 7.6. Due to the scarcity of data, the Tracy analysis was not possible, since it requires more than four consecutive points. Anyhow, by the light of our data, one can recognize the same complex behaviour of the even-odd effect also in the cross sections from 5.5 GeV protons on ^{238}U.

As discussed in section 7.2, the effects of the pairing interaction on the levels of energy, described in terms of superfluidity of the nucleus, can explain the surviving of structural effects in all the products of low-energy reactions. However, the presence of even-odd structure in light residual nuclei produced in high energy reactions does not seem justified by the explanation offered in section 7.2. In fact, structural effects cannot survive above the critical temperature.

In the following sections we will offer our interpretation to these experimental evidences.

Table 7.2: List of fragmentation, spallation and deep-inelastic reactions, reactions occurring at high excitation energies, where an even-odd structure in the charge distribution of produced nuclides was observed.

Reference	Reaction	Beam energy [*A* MeV]
Sl. Cavallaro et al. [Cav98]	^{35}Cl + ^{24}Mg	8
E. M. Winchester et al. [Win01]	^{40}Ca + ^{58}Ni ^{40}Ar + ^{58}Fe	25
Ch. O. Bacri et al. [Bac93]	^{40}Ar + Ni	44
L. B. Yang et al. [Yan99]	^{58}Fe + ^{58}Fe ^{58}Ni + ^{58}Ni	45 to 105
B. Blank et al. [Bla90]	^{40}Ar + ^{12}C	403
C. N. Knott et al. [Kno96]	e.g. ^{32}Si + ^{1}H	e.g. 571
W. R. Webber et al. [Web90]	^{56}Fe + ^{12}C	600
C. Zeitlin et al. [Zei97]	^{56}Fe + div.	1050
A. M. Poskanzer et al. [Pos71]	^{238}U + ^{1}H	5500

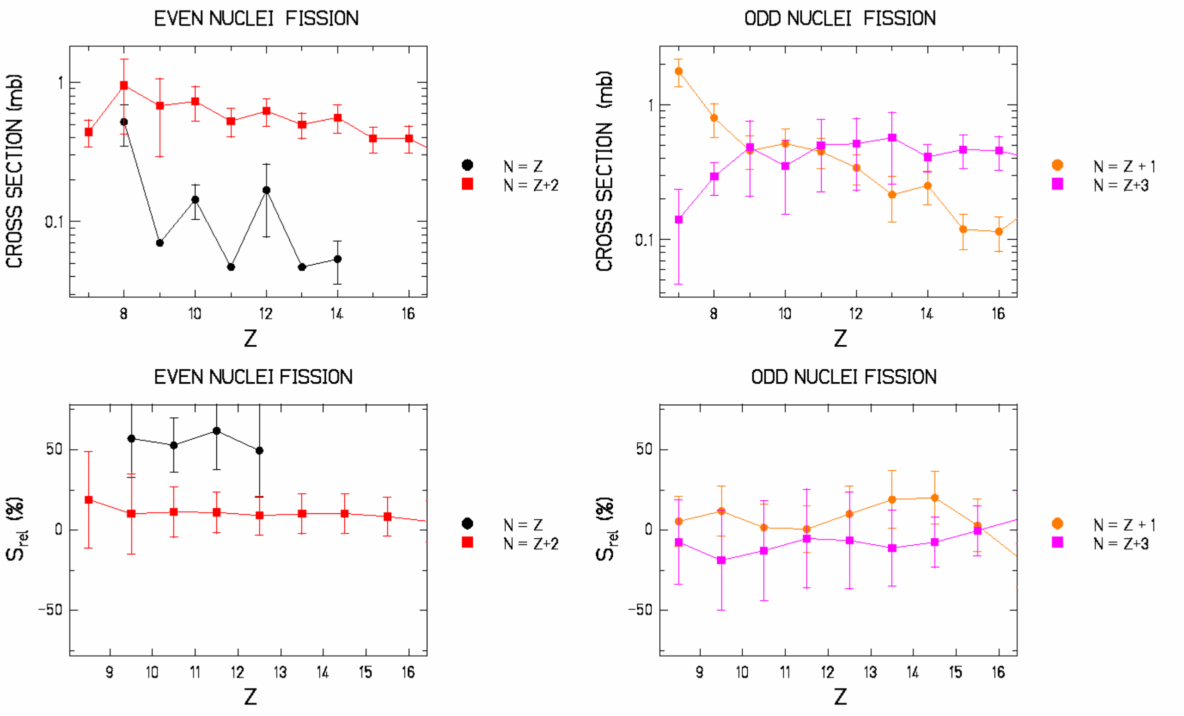

Figure 7.5: Up: production cross-sections of high-energy fission residues with even A (chains N=Z and N=Z+2) and with odd A (chains N=Z+1 and N=Z+3) [this work]. Down: Strength of the even-odd effect as a function of Z expressed by δ(Z), defined in equation 7.1.

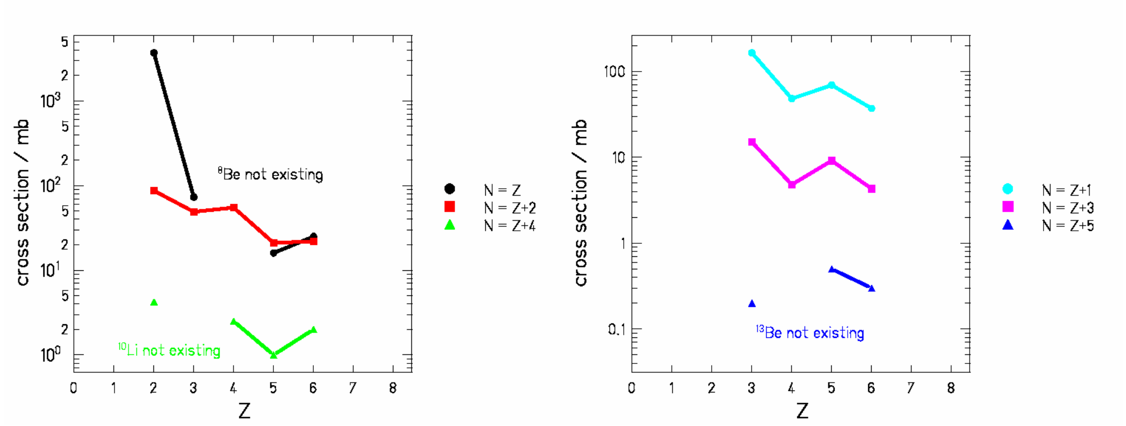

Figure 7.6: Production cross-sections of residues produced in the reaction 5.5 GeV protons on ^{238}U, with even A and with odd A. Data are taken from [Pos71].

7.5 Analysis with a simple statistical model

The experimental evidences of the even-odd staggering in high-energy reactions can be summarised as follows:

1) the charge distributions of the light elements produced in many different high-energy reactions (fragmentation, spallation, deep-inelastic) present an even-odd structure,

2) the production cross sections of light nuclides produced in fragmentation, high-energy fission and spallation reactions at high energies revealed a complex even-odd/odd-even structure.

In a recent study, Balasubramaniam et al. [Bal03] obtained staggering effects in the charge distribution of intermediate mass fragments with the dynamical cluster-decay model (although the qualitative agreement with the data is extremely poor). However, we consider that the large variety of high-energy nuclear reactions where the even-odd effect appears is a strong indication that these fluctuations are not sensitive to the first steps of the reaction, but they are rather produced in the later stage of the deexcitation process. Since for all these reactions the statistical evaporation is the final reaction-stage, it seems logical to assume that structural effects are connected to the evaporation process.

If on one hand all the evidences point at the evaporation process, on the other hand already in 1960 Ericson [Eri60] discussed the effects of the pairing interaction in the evaporation cascade and predicted that "the combined pairing effects in binding energies and level densities cancel in such a way that evaporation cross sections become approximately independent of pairing effects". His conclusion was supported by many experimental data of heavy residues produced as end products of the evaporation cascade, which do not show any staggering. Nevertheless the light residues measured in the last decade show an opposite behaviour.

To overcome the impasse, we will investigate carefully the statistical evaporation. First we will do it following the same approach employed by Ericson. To do this we will use a simple statistical model (this section). Then we will check the estimate of a more elaborate abrasion-evaporation model (next section), in order to test if the structural effects can be restored in the last stage of the evaporation cascade.

Ericson's simple statistical model

Following Ericson's idea, we assumed that the probability to produce a certain residue is proportional to the available phase space offered by this nucleus in the last step of the evaporation cascade. In the statistical model this means that we have to calculate the number of final bound states. The number of final states is determined by the number of states available between the ground state and the threshold, which is determined by the minimum value of the neutron separation energy, S_n, and the proton separation energy, S_p. The Coulomb barrier for proton emission was neglected for these light nuclei.

Ground states and separation energies are given by the nuclear masses. The masses were calculated with the liquid-drop model of Myers and Swiatecki [Mye67] without shell and pairing terms. The effect of pairing was reinserted by modulating the binding energies by an even-odd staggering quantified by $\Delta \approx 12/\sqrt{A}$ MeV, in such a way that nuclei with an even proton (or neutron) number are on average more bound by Δ than nuclei with an odd proton (or neutron) number, as explained in section 7.1.

The density of energy levels, ρ, was calculated with the *shifted level-density* formula of Ericson [Eri60], described by the equation:

$$\rho = \frac{\sqrt{\pi}}{12} \frac{exp(2\sqrt{a(E-\delta)})}{a^{1/4} E^{5/4}} \tag{7.2}$$

where a is the level-density parameter, E is the excitation energy of the nucleus and δ is a parameter connected to the pairing energy. It is equal to 0, Δ or 2Δ, for odd-odd, odd-even or even-odd, and even-even nuclei, respectively. Equation 7.2 indicates that the density of energy levels is approximately the same, providing to shift back the energy of the ground state of 0, Δ, or 2Δ. Despite its simplicity, the level-density formula of equation 7.2, describes satisfactorily the reality. It was inspired by a more accurate calculation of the density of levels done in 1958 by Strutinsky [Str58]. In the frame of the Boltzmann-gas model, Strutinsky derived an analytical formula of the density ρ_n of n-quasiparticle states as a function of excitation energy E. For the simplified case of one kind of nucleons (e.g. protons), he obtained:

$$\rho_n = \frac{g^n \left(E - n\Delta\right)^{n-1}}{\left[(n/2)!\right]^2 (n-1)!} \tag{7.3}$$

Figure 7.7 shows the resulting number of levels below a given energy E for two nuclei with an even and an odd number of nucleons with the same single-particle level density g. The figure reveals an important feature, which is also found in the more complex formulation of the superfluid-nucleus model (e.g. [Ign73]): When the excitation energy is corrected for the even-odd staggering of the ground-state binding energy, the level densities are almost identical. This is the feature considered in the level-density formula 7.2. Please note that the figure refers to the proton subsystem. The same shift of Δ would be found for the neutron subsystem. Therefore the shift between an even-even nucleus and an odd-odd nucleus is 2Δ, because both subsystems are involved.

The effects of the shifted level density can be better understood by means of figure 7.8, where the levels of energy of three close nuclei are schematically presented (not to scale) in the frame based on the liquid-drop + shell prediction (described in figure 7.1). In this base the ground states are staggered for the nuclei of a chain N-Z=even, i.e. an even-even–odd-odd–even-even chain (see figure 7.8-up). Below a certain energy (e.g. below the separation energy) the number of levels is approximately the same. The case for a chain N-Z=odd, i.e. an even-odd – odd-even – even-odd chain is presented in figure 7.8-down. The ground states do not stagger, because both even-odd and odd-even nuclei are shifted by Δ with respect to a liquid-drop prediction. The energy levels start immediately because there is always one unpaired nucleon, and their density is approximately the same for close nuclei.

Please note that in this picture the "absolute" separation energy[1] does not show any staggering for the even-mass nuclei. One may object that if one plots the experimental values of the separation energies, they do show a staggering. But in reality this staggering reflects the staggering on the binding energy: it is not a specific feature of the separation energies, which would have physical relevance. This can be seen clearly in figure 7.9, where the neutron separation energies for the nuclei of the chain N=Z are presented in absolute scale (figure 7.9-left) and relative to the base (E_{gs} - E_{gs}^{ld}) (dashed line of figure 7.9-right). The situation is different for odd-mass nuclei. The neutron separation energy for a even-mass nucleus (Z, N) is defined by the ground state of the nucleus (Z, N-1). The latter nucleus is either odd-odd or even-even. So the dashed line of figure 7.8-down represents

---

[1] With absolute particle separation energy we mean the sum of the ground-state energy E_{gs} and the particle separation energy S_v. It corresponds to the energy of the highest particle bound state.

the “absolute” separation energy for the chain of odd-mass nuclei (Z, N-1). Therefore for odd-mass nuclei the pattern of the “absolute” separation energy is staggered above a flat pattern of ground states.

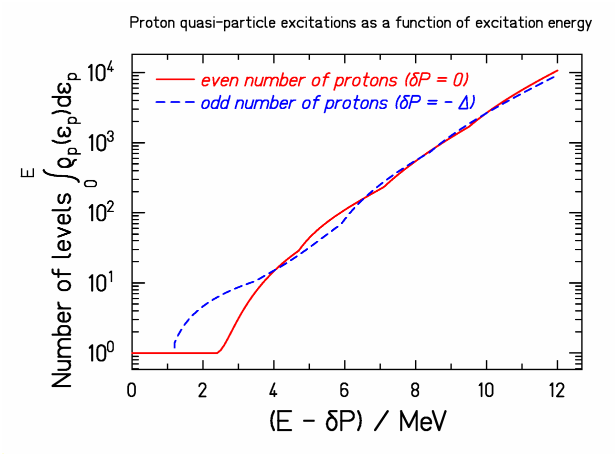

Figure 7.7: Number of proton quasiparticle excitations of two nuclei, ^{100}Zr and ^{100}Nb, one with an even and one with an odd number of protons, calculated with equation 7.3. The energy scale (E-δP) accounts for the even-odd staggering of the binding energies.

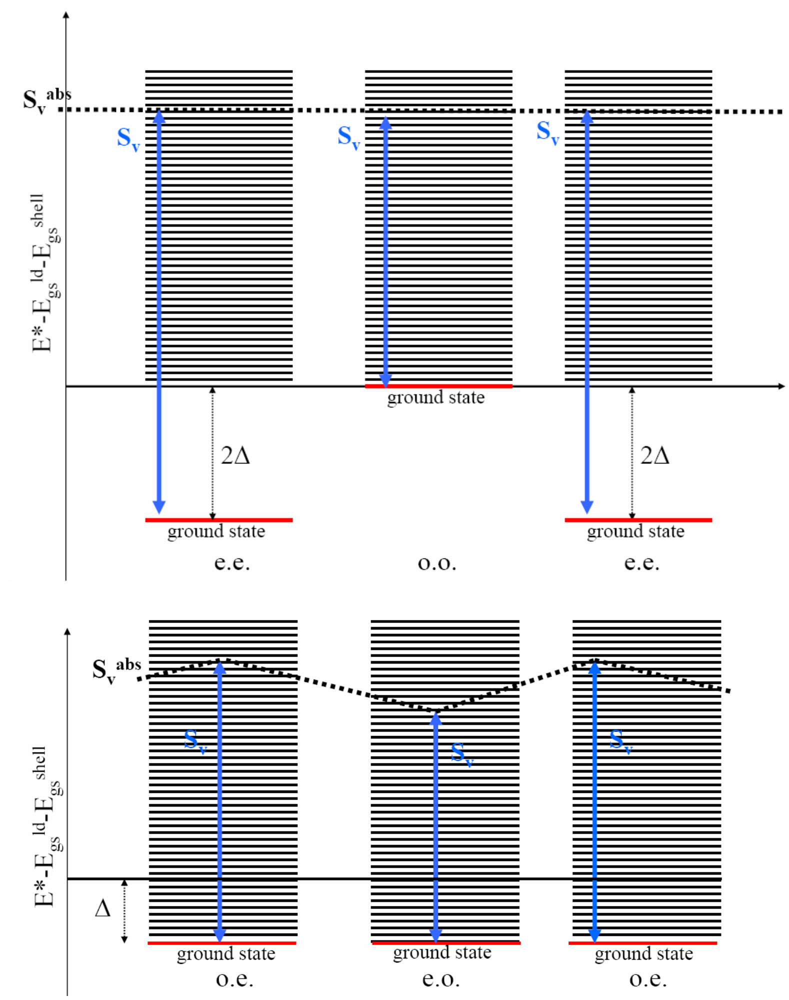

Figure 7.8: Schematic pattern (not to scale) of the levels of energy for three close nuclei (see text for explanation).

The number of final states, obtained with this method, is shown in figure 7.10. The analysis is aimed just to compare the local relative even-odd structure. The simple model that we used can only indicate whether structural effects can be restored at the end of the decay chain, in the last step of the de-excitation process, which is dominated by the available phase space of the final residue. The number of possible final states must not be compared with the global tendencies of the cross sections since other effects, connected to reaction mechanisms, affect the final result and have to be taken into account for a quantitative description.

The results show that the simple statistical model predicts a smooth pattern for the N-Z=even chains, and a staggering patter for the N-Z=odd chains. The reason for this can be intuitively understood analysing the schematic plots of figure 7.8, by counting the number of levels above the ground state and below the separation energy.

The prediction of Ericson (no staggering effects should be visible in the cross sections) is partially[1] confirmed by the calculations based on the simple statistical model.

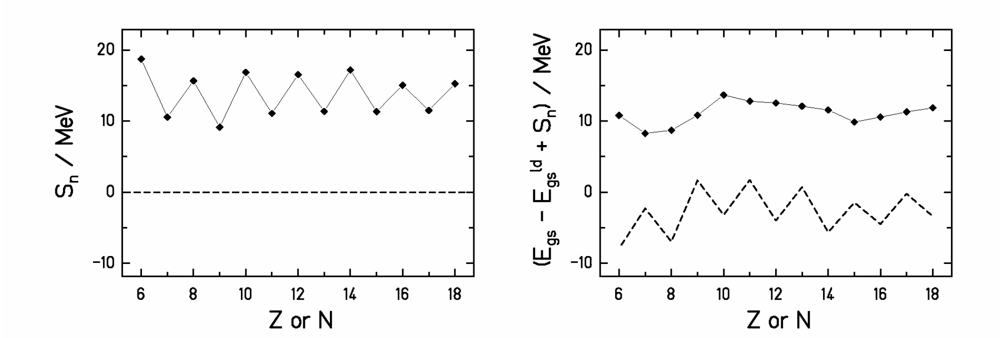

Figure 7.9: Left: experimental values of the neutron separation energies taken from ref. [BNL]. Right: experimental values of the neutron separation energies relative to the base $E_{gs} - E_{gs}^{ld}$. E_{gs}^{ld} *was calculated with the liquid-drop model of Myers and Swiatecki [Mye67] without shell and pairing terms. In both figures the dashed line represents the base above which the separation energies are plotted.*

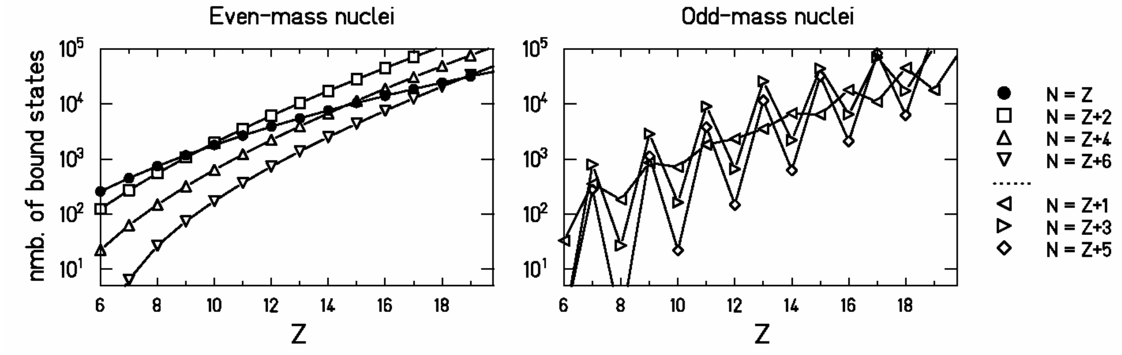

Figure 7.10: Number of bound states, representing the number of possible final states, determined by the number of energy levels available between the ground state and the lowest particle decay threshold.

---

[1] In his long article Ericson wrote [Eri60]: “The combined pairing effects in binding energies and level densities cancel in such a way that evaporation cross sections become approximately independent of pairing effects”. However he warned that “no systematic attempt at verifying this rule has been made”.

It is interesting to point out that for the odd-mass nuclei, the statistical model reproduces the observed structural effects in all their complexity. In particular, the reversed even-odd effect is reproduced and it even increases for nuclei with larger *N*-*Z* values. It turns into a standard even-odd effect at a certain Z_T value. The Z_T value increases as *N*-*Z* increases. For *N*-*Z*=1 nuclei, the model predicts Z_T=13, a value rather close to the one found in the experimental data of 1 A GeV ^{238}U on Ti. Finally, the effects vanish out as the mass of the fragment increases. We will offer our explanation of these behaviours at the end of section 7.6.

In this section, we tested the idea that structural effects are restored at the end of the evaporation cascade due to the influence of nuclear structure on the number of bound states. The good reproduction of the staggering of the experimental data for odd-mass residues encourages us to believe that the available phase space offered to the residual nucleus plays an important role. However, it is not the only quantity that plays a role in an evaporation cascade. In the following section we will study how the result changes when one follows the whole evaporation cascade.

7.6 Analysis with the abrasion-ablation statistical model

The analysis that will be presented in this section was done following the entire evaporation cascade. Again, we made use of a statistical model where the manifestation of pairing was taken into account in a simple but consistent way both in the masses and in the level densities.

In figure 7.11 the results obtained with the statistical abrasion-evaporation model, ABRABLA [Gai91], are presented for the reaction ^{238}U on Ti at 1 A GeV. In ABRABLA, after the nucleus-nucleus interaction, the pre-fragment at every step of its evolution has two possible decay channels: evaporation and fission. Evaporation is treated as described in ref. [Jun98] and fission as described in ref. [Ben98]. The physical content of the abrasion-evaporation mechanism was discussed in section 5.1.

In the evaporation part the masses are calculated with the liquid-drop model of Myers and Swiatecki [Mye67], this time with shell and pairing terms. The level densities, calculated as described in ref. [Ign95], take into account shell and pairing terms. The probability that a compound nucleus (Z, N) with excitation energy E, emits the particle ν is given by:

$$P_\nu = \frac{\Gamma_\nu(Z,N,E)}{\sum_i \Gamma_i(Z,N,E)} \qquad (7.4)$$

where *i* denotes all the possible decays channels (specifically: neutron emission, proton emission, alpha emission, fission). The particle emission width Γ_ν is [Mor74]:

$$\Gamma_\nu = \frac{1}{2\pi\rho_c(E)} \frac{4m_\nu R^2}{\hbar^2} T_\nu^2 \rho_\nu(E - S_\nu - B_\nu) \qquad (7.5)$$

where m_ν denotes the particle mass, S_ν the separation energy, B_ν the effective Coulomb barrier [Gai91]. *R* is the radius of the nucleus, T_ν is the temperature of the residual nucleus after particle emission, ρ_c and ρ_ν are the level densities of the compound nucleus and the exit channel, respectively.

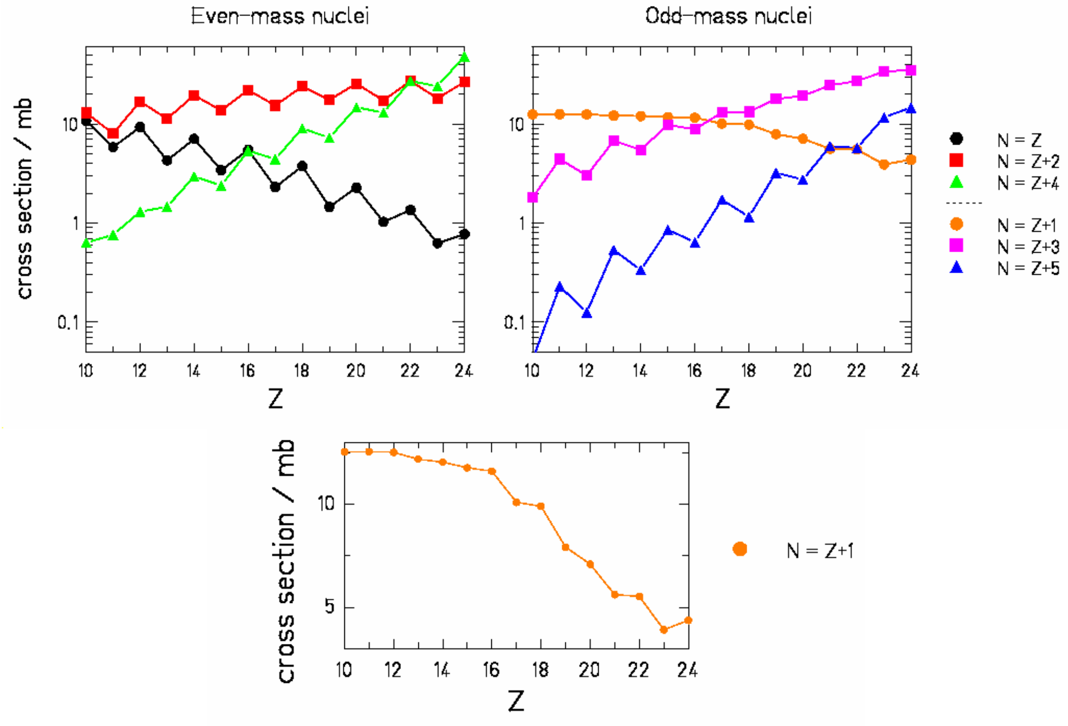

Figure 7.11: Production cross sections of fragmentation residues from the reaction ^{238}U +Ti at 1 A GeV, calculated with the statistical code ABRABLA

The most surprising result is the fact that the even-odd effect for the N-Z=even chains is quite well reproduced by the statistical abrasion-ablation code, contrary to the results of the simple calculation with the statistical model described in section 7.5. The main difference between ABRABLA and the simple statistical model is that in each step the probability of a certain decay channel is not only determined by the number of possible final bound states, but also by the number of possible excited levels in which the mother nucleus can sit before entering the decay channel. It is exactly for this reason that structural effects due to pairing are restored also for even-mass nuclei. This can be better understood with the help of figure 7.12. Let us consider an odd-even (Z=odd, N=even) mother nucleus that decays by neutron emission into an odd-odd daughter nucleus (figure 7.12, left). Both nuclei have at least one nucleon unpaired, so the levels of energy start immediately from the ground state. The ground state of the daughter nucleus is defined by the neutron separation energy of the mother nucleus, S_v^{mother}. For any excitation energy above S_v^{mother}, the mother nucleus can decay into an energy level of the daughter nucleus. So the numbers of energy levels of the daughter nucleus between the ground state and the separation energy $S_v^{daughter}$ determine the probability to create that nucleus. This is the same as what was calculated by the simple statistical model. Now let us consider an even-odd mother nucleus that decays by neutron emission into an even-even daughter nucleus (figure 7.12, right). The mother nucleus has one nucleon unpaired, so the levels of energy start immediately from the ground state, but in the daughter nucleus the ground state is separated from the 1st excited state because there are no nucleons unpaired. In the simple statistical model, the number of energy levels of the daughter nucleus between the ground state and the separation energy $S_v^{daughter}$ determine the

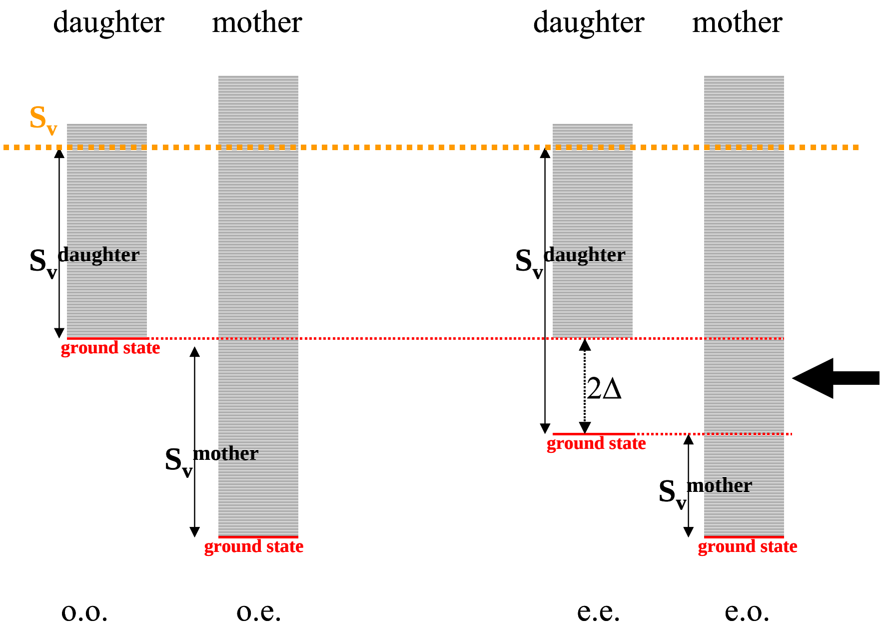

Figure 7.12: Schematic pattern (not to scale) of the levels of energy for two different cases of mother-daughter nuclei. When the even-odd mother nucleus occupies one of the levels indicated by the black arrow, it can decay to the ground state of the even-even daughter nucleus.

probability to create that nucleus. The number of levels available practically coincides with the number of levels between the 1st excited state and the separation energy $S_v^{daughter}$. As a consequence, according to the simple statistical model, there is no difference in the population of the odd-odd and of the even-even neighbouring nuclei. However, the mother nucleus can occupy levels of energy above S_v^{mother} and below the 1st excited state of the daughter. In these cases, the mother nucleus can decay onto the ground state of the daughter nucleus. Therefore the probability to decay into the daughter nucleus is determined not only by the number of energy levels of the daughter, but also by the number of levels occupied by the mother nucleus which are above the ground state of the daughter. This number is larger for an even-odd mother nucleus that decays into an even-even daughter nucleus than for an odd-even mother nucleus that decays into an odd-odd daughter nucleus. This is the reason why in the full evaporation code the staggering is reproduced also in the chains N-Z=even.

The results of the ABRABLA calculations give a quite satisfactory reproduction of the staggering effects observed in the experimental data. Specifically:

- The chains of odd-mass nuclei show a remarkable staggering effect. The reason for this is the staggering of the separation energies above the smooth chain of ground states (figure 7.8).
- The odd-even effect turns into an even-odd effect for the chain N = Z + 1 at Z = 11. This is due to the fact that, moving along a given N-Z=odd chain, the nucleus passes from being neutron-rich to proton-rich and, consequently, the lower particle separation energy

passes from neutron separation energy, S_n, to proton separation energy, S_p, as the charge of the fragment increases, as shown in figure 7.13-left. For the odd-mass chains, the production cross section is mostly determined by the number of particle bound states (i.e. number of energy levels) between the ground state and the lowest separation energy. The staggering of the separation energy is what determines the staggering in the cross sections (figure 7.8-down). The combination of the lowest value among S_n and S_p has the consequence that when S_n crosses S_p the staggering of the lowest separation energy turns from odd-even to even-odd. Please note that the proton separation energy is affected by the Coulomb barrier. This value affects the location of the turning point between odd-even and even-odd effect. This explains the differencies between the results of the simple statistical model and of ABRABLA.

- For similar reasons, the strength of the odd-even effect in the chains of odd-mass nuclei increases going from the chain N=Z+1 to N=Z+5. The explanation of this effect lies again in the interplay between neutron and proton separation energies. The combination of the lowest value among S_n and S_p is such that the staggering of the lowest separation energy is larger for the chains where only one of the two separation energies (S_n or S_p) dominates. In figure 7.13-left is clear how for the light neutron-rich nuclei S_n dominates.
- The chains of even-mass nuclei present an even-odd staggering. The reason for this is that there are many more possible energy levels for an even-odd mother nucleus that decays into an even-even daughter nucleus can occupy than for odd-even mother nucleus that decays into an odd-odd daughter nucleus (figure 7.12).
- The strength of the even-odd effect in the even-mass nuclei is constant for all the chains of even-mass nuclei. The reason for this is that the number of levels of energy above S_ν^{mother} and below the 1st excited state of the daughter (i.e. the integral of the level density between S_ν^{mother} and $S_\nu^{mother} + 2\Delta$) is more or less the same for nuclei that differ of few mass units (see equation 7.2).

There are only two remarkable differences between the ABRABRA predictions and the experimental results. The first one is that in the experimental data the staggering effects vanishes away when the fragment mass increases, while in ABRABRA it remains also for

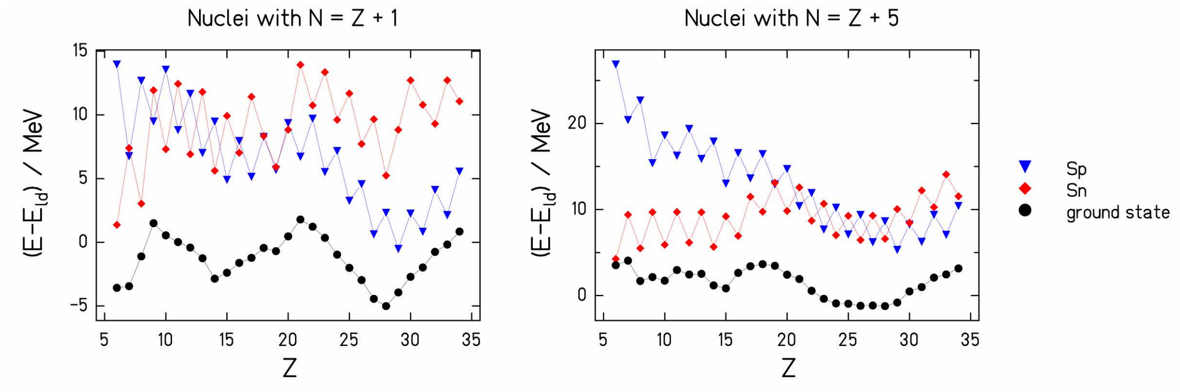

Figure 7.13: Ground state and separation energies, for N=Z+1 and N=Z+5 nuclei, above the energy of the corresponding liquid-drop ground state. The liquid-drop model does not contain any even-odd effect. The production cross-sections are approximately proportional to the number of energy levels between the ground state and the lowest separation energy.

heavier residues. The second one is that according to the calculations the strength of the even-odd effect in the even-mass nuclei is constant for all the chains, while in the experimental data the N=Z chains shows a particularly strong staggering. We will discuss these two discrepancies in the next two sections.

7.7 The disappearance of the even-odd effect for heavy residues

The experimental results show that the staggering effect in the cross sections rapidly vanishes away as the mass of the fragment increases. Furthermore, there are a lot of experimental results in literature that show that the fragmentation yields of heavy residues present a smooth behaviour.

There are, in our opinion, two main reasons why this occurs. The first one is that the pairing gap Δ diminishes with the mass of the nucleus: $\Delta \approx 12/\sqrt{A}$ MeV. The second reason is that gamma emission becomes competitive to particle decay for heavy compound nuclei. This latter aspect can be better understood again with the help of figure 7.12. When the even-odd mother nucleus occupies one of the levels indicated by the black arrow, it can decay to the ground state of the even-even daughter nucleus. This fact enhances the production of even-even nuclei with respect to the odd-odd ones. On the other hand, there is only one possible particle-decay channel: the ground state. In principle when the even-odd mother nucleus occupies one of the levels indicated by the black arrow, it can also de-excite by emitting a gamma and falling into a lower energy level. The emission of a gamma is much less probable than the particle decay (about 10^5 times less favourable). However the number of final levels available after the gamma emission (the levels between the mother ground-state and S_v^{mother}) can be extremely large for a heavy nucleus (maybe more than 10^5 levels). In that case gamma emission and particle decay into the ground state can be two competitive channels. If the number of final levels available after the gamma emission is very large, than the γ-radiation rate is dominant and the mother nucleus survives, washing out the enhancement of the production of even-even nuclei. Since the level density depends on the mass (heavier nuclei have denser energy levels) the number of levels available after the gamma emission increases rapidly with increasing mass of the fragment (see equation 7.2).

In several evaporation codes γ-radiation is not included as a possible channel, because the particle decay channels dominate above the particle emission threshold. In order to verify the effects of γ-radiation on the final cross-section distribution the γ-decay channel was introduced in the ABRABLA code [Kel03]. As the emission of statistical γ-rays occurs predominantly via the giant dipole resonance, the γ-radiation rate was calculated according to ref. [Ign00]:

$$\Gamma_\gamma(E) = \sum_{I=|J-1|}^{J+1} \int_0^E \varepsilon_\gamma^3 \cdot k(\varepsilon_\gamma) \cdot \frac{\rho(E-\varepsilon_y, I)}{\rho(E,I)} d\varepsilon_\gamma \tag{7.6}$$

where E is the excitation energy of the mother nucleus and k(εγ) is the radiative strength function for a dipole electric transition. As already said, for high excitation energy the γ emission is negligible compared to the particle emission and it becomes important only at the energies around and below the particle separation energies. As indicated in reference [Ign00], taking E = S_n, and using the power approximations for the radiative strength function [Axe62] and the constant temperature model [Eri60], equation 7.6 can be parameterised as:

$$\Gamma_{\gamma}(S_n) = 0.624 \cdot 10^{-9} \cdot A^{1.60} \cdot T^5 \,\mathrm{MeV} \qquad \text{with} \qquad T = \frac{17.6}{A^{0.699}}\,\mathrm{MeV} \tag{7.7}$$

In the above equation, A is the mass of a mother nucleus and T is the nuclear-temperature parameter of the constant-temperature model [Ign00]. As an example of the results of these calculations, the production cross sections of different isotopes of $_{71}$Lu in the reaction ^{208}Pb (1A GeV) + ^{1}H are shown in figure 7.14. The experimental data from [Enq01] are shown as full dots and compared with two sets of calculation: without including γ emission (open squares) and with including it (open triangles). One can observe that the γ competition tends to reduce the even-odd structure in the isotope cross sections to a great extent.

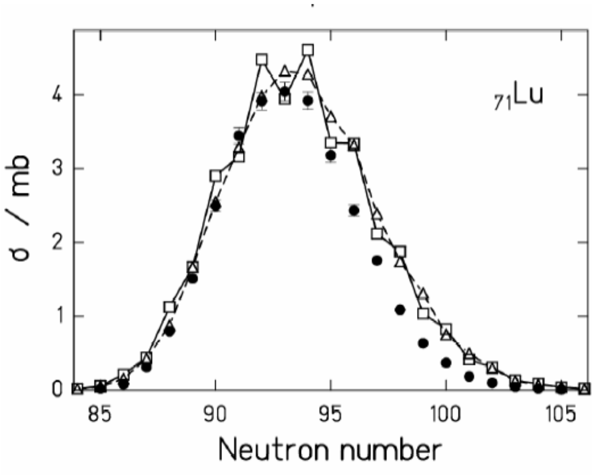

Figure 7.14: Production cross sections of the isotopes of lutetium produced in the reaction ^{208}Pb+H at 1 A GeV, calculated with the statistical code ABRABLA with (Δ) and without (□) the inclusion of the γ-radiation decay channel, and compared to the experimental data (●) from ref. [Enq01]. The errors on the experimental data are shown only if the error bars are larger than the symbol size.

7.8 The N=Z chain

Despite of this success obtained applying the picture of the statistical abrasion-ablation model, the enhancement in the production yields of N=Z nuclei could not be reproduced. In this section we discuss indications from binding energies and from spectroscopy of phenomena that go beyond the statistical evaporation model, which could offer an explanation for the peculiarity of the N=Z chain.

<u>Binding energies</u>

It is known that the nuclear binding energies are modulated by an even-odd staggering defined by the pairing gap $\Delta \approx 12/\sqrt{A}$ MeV. However, this is only an average value. A detailed analysis of the absolute even-odd fluctuations in the binding energies of light nuclei is shown in figure 7.15 using the following description, which is equivalent to the Tracy's formula (equation 7.1) expect that is not based on a Gaussian-like distribution, but on a parabolic distribution:

$$\delta_{abs}(Z+3/2)=\frac{1}{8}(-1)^{Z+1}\left[B(Z+3)-B(Z)-3(B(Z+2)-B(Z+1))\right] \tag{7.8}$$

where $B(Z)$ is the value of the experimental binding energy, taken from reference [Aud95], for the nucleus with charge Z and with given N-Z number. The values δ_{abs} give an absolute measure of the strength of the staggering. Most nuclei behave as expected. Chains along odd-mass nuclei, which are either even-odd or odd-even, hardly show any even-odd structure. In even-mass nuclei, except those with N=Z, the different binding energies of even-even and odd-odd nuclei lead to an even-odd effect around 2 MeV, which slightly decreases with mass, and coincides to good approximation with the pairing energy of $\Delta \approx 12/\sqrt{A}$ MeV. As a remarkable exception, the N=Z chain shows a considerably enhanced even-odd structure. This special behaviour of N=Z nuclei is caused by the Wigner term [Wig37] in nuclear binding, which is responsible for an additional deficit in the binding energy for N=Z odd-odd nuclei of about 30MeV/nucleon compared to N=Z even-even nuclei [Mye97, Jen84]. If we compare the even-odd structure in the production cross sections to the even-odd staggering in the binding energies we find a correspondence in the behaviour of the N=Z chain. Both in the cross sections and in the binding energies this even-odd structure is exceptionally strong. At the same time, these nuclei are particularly strongly produced. For that reason, the enhancement in mass for even-even nuclei has to be taken into account in the statistical model with a more reliable description. Figure 7.15 clearly demonstrates that the schematic assumption of an even-odd staggering of the binding energies by a pairing gap Δ, which only depends on mass, is not realistic: the even-odd staggering along the cut N=Z is about 1.5 times larger that the staggering along other cuts of even-A nuclei.

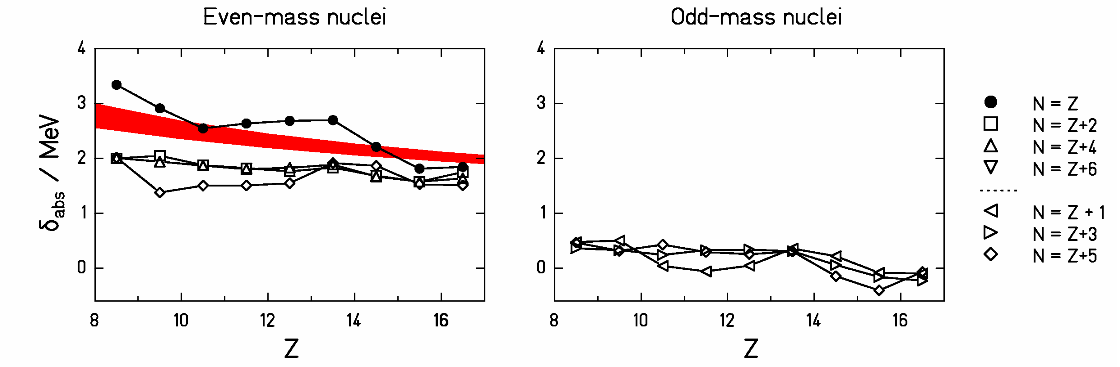

Figure 7.15: Local even-odd effect deduced from the experimental binding energies of ref. [Aud95] and calculated with equation (7.7). The values are given along specific cuts in N-Z. The values of the pairing gap Δ, calculated as $12/\sqrt{\mathrm{A}}$ *MeV, fall inside the grey band.*

Level densities

One may wonder if pairing correlations could affect the level density in a more complex way than what predicted by the standard description of the superfluid nucleus model. Motivated by this idea, we investigated the experimental level densities obtained with spectroscopic methods. Figure 7.16 shows the measured binding energies, the excitation energies of the 21st and the 60th state, and the particle separation energies with respect to the liquid-drop ground-state energy. The 60th and 21st experimental excited states were taken from the compilation of ENSDF [BNL]. As the most prominent features one observes a strong even-odd effect in the ground-state energies, which almost completely disappears in the excited levels. Thus, the expectation from the superfluid nucleus model is essentially confirmed. However, a tiny fraction of the even-odd staggering survives in the energies of excited levels. This effect goes beyond the behaviour of quasi-particle excitations depicted in figure 7.7 as expected from the superfuid nucleus model. While blocking effects are expected to destroy the even-odd staggering of the ground-state energies with the first quasi-particle excitations (see figure 7.7), the even-odd staggering in the *N*=*Z* nuclei obviously survives up to excitation energies in the order of 10 MeV above the ground state. For *N*=*Z*+2 nuclei, this effect seems to be smaller. Unfortunately, the available information from spectroscopy does not reach up to the separation energies. In addition, it is not sure that the experimental information from spectroscopy on the number of levels is complete, in particular at higher excitation energies.

The even-odd staggering of the energies of excited levels is an interesting phenomenon by itself. In addition, there is also a small even-odd staggering in the particle separation energies, which also influences the number of particle-bound states. These findings give an indication that, in contrast to the structure found in odd-mass nuclei, the even-odd effect in the production cross sections of even-mass nuclei goes beyond the superfluid nucleus model.

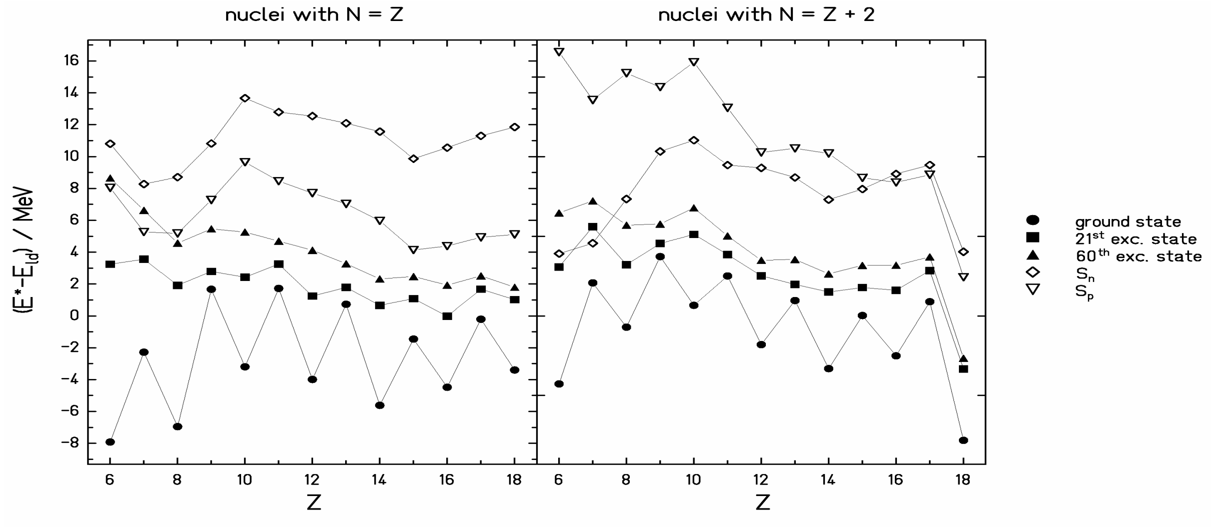

Figure 7.16: The energy of the ground state, of the 21st and 60th excited states and of separation energies, for N=Z and N=Z+2 nuclei, above the energy of the corresponding liquid-drop ground state. The liquid-drop model does not contain any even-odd effect. The figure demonstrates the gradual decrease of the even-odd structure with increasing excitation energy.

7.9 Possible effects beyond pairing

While the restoration of structural effects in the end-products of rather violent reactions is sufficiently well explained by the most prominent manifestation of pairing, the strength of the observed fine structure in *N*=*Z* nuclei needs a more elaborate discussion. There is no obvious first-order relation of this observation to pairing correlations. In this section, which has a rather speculative character, we would like to mention some complex phenomena, which have an additional influence on the fine structure observed in the even-mass end products of highly excited systems.

Wigner term

We have already mentioned that the particularly strong even–odd structure in the production cross sections of *N*=*Z* nuclei goes in line with an exceptionally strong fluctuation in the binding energies, which is caused by the Wigner energy [Wig37]. As the consequence of the Wigner energy, odd–odd nuclei with *N*=*Z* are bound by about 30/A MeV less than even–even *N*=*Z* nuclei in addition to the difference of 2Δ expected from pairing. For other nuclei with *N*≠*Z*, the Wigner energy is a smooth function proportional to |*N*−*Z*|, and, therefore, has no consequence on even–odd staggering. For a quantitative estimation of the influence of the Wigner energy on the production cross sections of *N*=*Z* nuclei, however, one needs to describe how the fluctuating Wigner energy in these nuclei behaves as the function of excitation energy.

Alpha clustering

On the other hand, as even–even *N*=*Z* nuclei are multiples of alpha particles it is tempting to relate their enhanced production to the alpha clusterisation in nuclei [Röp98,Hor02]. However, one should be careful with assigning the enhanced even–odd effects in the ground state masses for this class of nuclei to alpha clustering. Jensen et al. have analysed experimental ground-state masses using different filters and have not found any trace of alpha clustering [Jen84]. On the other hand, it could be possible that alpha clustering appears for excited states resulting in the enhanced production of even–even *N*=*Z* nuclei.

Neutron-proton pairing

Also neutron-proton pairing is discussed to play an important role in *N*=*Z* nuclei [Pal01]. An eventual influence of neutron-proton pairing on the energy of excited levels could be another explanation for the strong even-odd structure in the production yields of the *N*=*Z* nuclei.

Mean-field contributions to pairing effects

Recently, the interplay between pairing and mean-field effects has been discussed (e.g. [Dob01]). The even-odd mass differences are understood as the sum of the variation of pairing correlations in a given potential, the blocking effect, as discussed above, and the spontaneous breaking of spherical symmetry due to the presence of unpaired particles (Jahn-Teller effect [Jah37]). The second effect is derived to be particularly strong in light nuclei. It is to be expected that the mean-field contribution to the even-odd mass differences also influences excited levels in contrast to the blocking effect, which was schematically considered above. This would explain the general appearance of even-odd differences in the nuclear level densities, leading to an enhanced production of nuclei with even proton and neutron number. According to ref. [Dob01], this effect should decrease with increasing mass of the reaction products.

7.10 Final remarks

The striking point of the experimental results presented here is that nuclear structure manifests itself also in the end products of the decay of very hot nuclei. It seems that a systematic investigation of the fine structure in the production yields from highly excited nuclei is a rich source of information on nuclear-structure phenomena in slightly excited nuclei found at the end of their evaporation process. A statistical description of the evaporation cascade could reproduce most of the features of the experimental data, providing that the most prominent manifestation of pairing − its blocking effect − is taken into account in a consistent way both in the masses and in the level densities. Peculiar aspects of the $N=Z$ chain in the experimental production cross-sections, in the experimental masses and in the experimental level densities, require a deeper insight.

Apart from the interest for the study of nuclear-structure properties, the restoration of the structural properties of the nucleus while cooling down during the evaporation cascade has implication also in the study of the phases of nuclear matter. We can interpret our results as a manifestation of the transition from the normal Fermi liquid phase to the superfluid phase, which rules the nuclei at excitation energies below 10 MeV. When the nucleus cools down, in the very last steps of the deexcitation process, a phase transition occurs. Signatures of the phase transition from superfluid to normal liquid have been observed already several years ago. A beautiful example is represented by the sharp change in the moment of inertia with the increase of the temperature of low-energy fissioning polonium isotopes, shown in figure 7.17 [Ign82]. The results were obtained by the analysis of experimental data on the angular anisotropy of the fission fragments. The curve is the result of a superfluid-model calculation. At high temperatures the moments of inertia are high, indicating that the nucleus behaves almost like a rigid rotor. This is a condition of large viscosity. At very low temperatures the moments of inertia are low, indicating a behaviour similar to an irrotational flow. This is a condition of minimum viscosity, which is what characterizes a superfluid. The passage from high viscosity to low viscosity is not continuous, but it has a sharp change around the critical point, occurring at 10 MeV excitation energy. So, the even-odd structure in our data, as in many other yields of highly excited nuclear systems, can be considered a manifestation of the liquid-superfluid phase transition.

The restoration of the structural properties has also an important consequence for the measurement of the nuclear temperature by means of the isotope thermometer, and in general in every technique based on the ratio of the yields of specific isotopes produced in high-energy reactions, like for instance the “isoscaling” method [Tsa01]. This method relies on comparing complete isotopic sequences of products emerging from reactions with different reaction partners. In all these approaches, the data have to be corrected for the influence of sequential decay, i.e. the subsequent deexcitation of the reaction products by evaporation, which is considered as a disturbing effect. In this sense, light residues are more appropriate, because the influence of evaporation is less severe as for the heavy ones. However, our data showed the complexity of the structural effects on the yields of these light final products. A statistical evaporation code could reproduce most of the features of the staggering, but the exact quantitative description of the evaporation cascade is still not achieved, in particular for the light N=Z nuclei.

To conclude, we want to point out the importance of the restoration of the structural properties in astrophysics. The EOS of nuclear matter is relevant for the description of the interior of the neutron stars. Speculations about exotic phases of baryonic matter – including the existence of kaon condensates or quark matter – arose in the last years. However, not only the state of very high density is interesting, but also the crust of the neutron star, which is expected to be in the superfluid phase. The precise knowledge of the pairing gap is essential for the determination of the cooling rate of the neutron stars. The superfluidity of the crust influences the rotation frequency of the star. So, the investigation of the action of the pairing interaction in highly excited systems could turn to be a useful tool also in astrophysics.

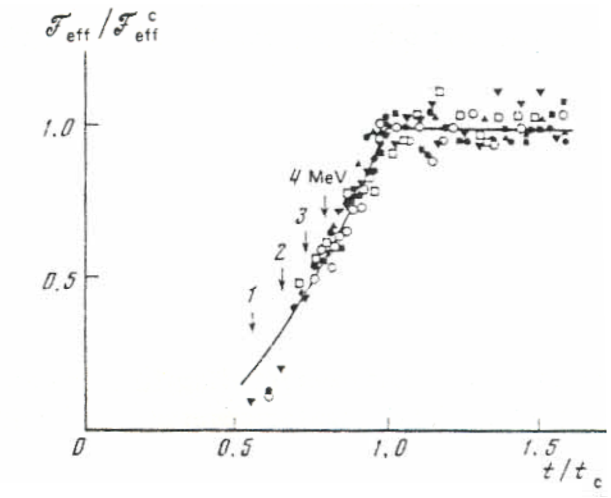

Figure 7.17: Temperature dependence of the moments of inertia of the nuclei ^{208}*Po (reversed triangles),* ^{210}*Po (circles),* ^{211}*Po (squares) and* ^{212}*Po (triangles). The arrows indicate the excitation energies of the fissioning nuclei at the saddle point. The figure is taken from ref. [Ign82].*

Conclusions

The experimental result of this work consists of the systematic measurement of formation cross-sections and velocity distributions of the light residual nuclei produced in the reactions ^{238}U on ^{1}H and ^{238}U on Ti at 1 GeV per nucleon. About 660 *formation cross-sections* of residual nuclides were measured for the first time. The cross sections of most of the isotopes, produced with more than 5 μb, were determined with an accuracy that is, in most of the cases, between 20% and 30%. Within this limit, the isotopes for the elements between charge 7 and 37 were identified in mass and atomic number, allowing to establish the isotopic distributions. The mean value of the N-over-Z-ratio of each isotopic chain is deduced with a relative uncertainty of ~ 1%. Thanks to a very accurate indirect measurement of the velocity, performed by determining the magnetic rigidity of the reaction products in the FRS with a relative uncertainty of about $5\cdot10^{-4}$, the *velocity distributions* for every produced nuclide were reconstructed and were presented, too.

According to our initial task, in the present work we explored the applicability of a high-resolution magnetic spectrometer to the investigation of the properties of nuclear matter. To do this, we profited from the specific experimental information achievable with our experimental apparatus, which is: the highly precise values of the longitudinal velocities and the fully resolved masses of the fragments.

The high-precision measurement of the velocity distributions of the remnants of the projectile spectator in the reaction ^{238}U + Ti at 1 A GeV revealed a surprising result: The velocities of the fragmentation products do not decrease any more if the mass loss becomes large, as expected from the systematics deduced for the products in peripheral collisions [Mor89]. The velocities of the very light fragments even tend to increase, until finally they are even faster than the projectiles. This finding sheds a new light on the systematics of previously measured data: The velocities of residues far from the projectile cannot simply be scaled by the mass loss. According to ref. [Shi01], the velocity of the spectator is modified by the expansion of the fireball, and other parameters like the mass of the target nucleus and the beam energy have a strong influence. This induces a large spreading in the systematics of previous data for light fragments, as observed in ref. [Mor89]. We interpreted these results as the re-acceleration of the spectator fragment by the participant blast, postulated by Shi, Danielewicz and Lacey [Shi01]. This result has an important consequence for the determination of the EOS of nuclear matter. The analysis of the data from 4π experiments has not yet reached a conclusion on the strength of the compressibility of the nuclear matter (i.e. on the *stiffness* of the EOS), because both the nuclear compressibility and the dependence of the interaction among nucleons on their momentum (i.e. the momentum dependent interaction - MDI) influence the flow pattern. Further progress requires observables that depend exclusively either on the EOS or on MDI. Since several years theoreticians predict that the transversal and the longitudinal momentum distributions of the residual fragments are influenced by the blast of nucleons and hadrons, occurring after the compression phase in the colliding zone, and thus the momentum distributions are sensitive to the nuclear force [Mol88]. More specifically for some favourable systems the expanding hadrons would cause an acceleration of the residual fragments. The theoretical work of Shi showed that this acceleration is almost exclusively sensitive to the MDI. However, the momentum distributions have to be measured with high precision in order to yield conclusive results. So, the limit in precision in the measurement of the residues velocity constituted an impasse up to now. The present work showed that this precision is achievable with the use of high-resolution spectrometers, and supports the feasibility of the method proposed by Shi. The precise measurement of the kinematical properties of the spectators represents a new tool to determine the in-medium nucleon-nucleon interactions. As stated in ref. [Shi01], the apparent re-acceleration of the projectile spectator – found in the present work – will represent a new tool to investigate the equation of state of nuclear matter. The results of the present work on this subject were published in Physical Review Letters [Ric03].

The precise identification in mass and charge of the light fragments of the reaction ^{238}U on Ti at 1 *A* GeV permitted to find an unexpected feature of the residual nuclide distributions: they do not occupy the well defined area in the neutron-deficient side of the chart of the nuclides (the so called "evaporation corridor"), as expected for the products in peripheral collisions, in the "limiting fragmentation" regime, to which the reaction ^{238}U on Ti at 1 *A* GeV was expected to belong. As the mass decreases, the neutron enrichment of the light products increases and even crosses the valley of stability to lie definitely on the neutron-rich side. We interpreted this fact as the evidence that the evaporation of neutrons and protons did not come to an equilibration, which is what characterises the products lying on the evaporation corridor, but preserved part of the neutron excess of the projectile. The loss of neutron excess was thus used as a measure of the excitation energy at the beginning of the evaporation stage. The *N*-over-*Z* ratio of the final fragments was used as an isospin thermometer: tracing back the evaporation cascade using the statistical multifragmentation model (SMM) we determined the mean temperature at break-up to T=5 MeV. This value was found to be independent of the size of the final fragment. The result represents new information on the break-up conditions which confirm previous results based on temperatures deduced from isotopic ratios and the population of excited states of small clusters. It is consistent with a kind of saturation of the nuclear temperature as a function of excitation energy introduced over that range of excitation energy where heavy clusters are formed. In the moment, it is not clear, whether this is a thermal or a dynamic phenomenon. In the first case, one might conclude that compound nuclei, equilibrated in both intrinsic and collective degrees of freedom, cannot exist above a limiting temperature of 5 MeV. This would have far-reaching consequences for many phenomena found in highly excited nuclear systems. The above presented results were published in Nuclear Physics A [Sch02].

The formation cross sections of the residues produced in the uranium fragmentation, fully resolved in mass and charge, provided interesting information on a nuclear-structure phenomenon, manifested as an even-odd effect. In the present work, a systematic investigation of the staggering structure over an extended area of the chart of the nuclides was performed for the first time. Specifically, the fine structure could be analysed in all its complexity by appropriately filtering the experimental data along different values of neutron excess *N*-*Z*. A complex behaviour was revealed. Odd-mass nuclei with positive *N*-*Z* values show an enhanced production of odd elements. For *N*=*Z*+5 nuclei, the enhancement is around 40%. Even-*Z* nuclei along *N*=*Z* show a particularly strong enhancement in the order of 50% in parallel with a particularly strong even-odd structure in the ground-state binding energies. The production of other even-mass nuclei fluctuates by about 10%: the production of even-even nuclei is slightly enhanced. The odd-even effect is a manifestation of the pairing residual interaction, which affects the structural properties of nuclei, such as the binding energy and the energy levels. This interaction is quite weak, and it is known to vanish for excitation energies above ~ 10 MeV [Ign73], when the nucleus leaves its superfluid phase to enter into its normal liquid state. It is therefore not expected that the structural effects survive in the residual fragments observed in our experiment, since the excitation energies introduced in the spectator nucleus are known to be well above 10 MeV. In the last years, in several experiments, in which different rather violent nuclear reactions were investigated, a fine structure in the nuclide production, manifested as an odd-even effect, was observed (see e.g. [Bla90, Web90, Bac93, Kno96, Zei97, Cav98, Yan99, Win01]). All these violent nuclear reactions, including the ^{238}U on Ti at 1 GeV per nucleon studied in the present work, have in common the last stage of the reaction: the sequential evaporation cascade of nucleons, leading to the slow deexcitation of the fragment. We tested the idea that structural effects are restored in the end products of hot decaying nuclei, where the nucleus cools down and passes from the liquid to the superfluid phase. To do this, an abrasion-evaporation statistical model was used. In the model, the blocking effect of pairing was included in a consistent way both in the masses and in the level densities. The model could reproduce almost all the features of the staggering of the experimental production yields for light odd-mass residues, with the remarkable exception of the N=Z nuclei, where an increased enhancement in the production is observed compared to other chains with *N*-*Z*=even. The peculiarity of the even-odd effect in the N=Z products goes beyond the blocking effect of pairing, and could be a possible indication for alpha clustering, for neutron-proton pairing, or for mean-field effects. The statistical-model calculation indicated that the structural effects are ruled by the available phase space in the last steps of the evaporation process, where the structure is restore. The results can be considered as an experimental manifestation of the passage from the normal liquid phase of the nucleus to its superfluid phase. These findings have interesting consequences for the determination of the nuclear temperature and for the cooling rate of the neutron stars. These results were published in Nuclear Physics A [Ric04].

Thanks to the high-precision measurement of the velocity distributions, the light fragments originating from the proton-induced reaction of ^{238}U at 1 *A* GeV, which populate far down the chart of the nuclides, could be qualified as binary-decay products. A detailed study of all the experimental observables – the mass and charge distributions, the isotopic distributions, the mean velocities, the width of the velocity distributions, the mean recoil velocities of the mean mother nuclei – showed that all the above-quoted signatures are consistent with the sequential binary decay of a fully equilibrated compound nucleus, while clear indications for fast break-up processes seem to be absent. As discussed in [Mor88], the binary decay of a compound nucleus includes fission and evaporation with a natural transition in-between, and it might be called fission in a generalized sense. Thus, very asymmetric fission of the system ^{238}U + ^{1}H at 1 A GeV seems to reach down to rather light nuclei, extending below Z = 7. In the spallation-fission reaction of ^{238}U this feature is unambiguously identified for the first time. The results presented here, along with those of refs. [Ber03, Ber04, Tai03], have been published in Physical Review Letters [Arm04]. A more detailed paper have been submitted to Nuclear Physics A [Ricc04].

Besides the interest for fundamental physics, the experimental results of the present work are of extreme importance for technical applications. In particular the design of accelerator-driven systems (ADS) and radioactive ion-beam facilities (RIB) relies strongly on the formation cross sections of residual nuclei produced in such reactions. This information is needed to calculate the short-term and long-term radioactivity, building up in these facilities, and thus for designing the shielding and estimating the residual activation of such devices. In ISOL-type radioactive ion-beam facilities, the formation cross sections are decisive to determine which nuclides far from stability can become accessible, and to estimate the attainable secondary-beam intensities, once appropriate extraction and ionisation procedures will be developed. Here, fission is of special interest, because it seems to be best suited for approaching the neutron drip line in the medium-mass range. The energy of 1 GeV per nucleon is estimated to be optimum for both applications [Rub95, Rid00]. Also the velocity of the fragments if of great importance for the design of RIB facilities and ADS, and in general for the new generation of accelerator at high intensities [GSI01], because the radiation damage of the structures depends on the kinetic energy of the fragments. Nuclear data of formation cross sections are also important for fundamental research. In astrophysics, for instance, they enter into the description of the processes that affect the composition of energetic nuclei during their transport through the Galaxy, from their source to the Earth where they are observed. The models for the propagation of cosmic rays rely heavily on the knowledge of the formation cross sections of light nuclei from the interactions of the heavy nuclei in the interstellar medium [Wie99, Geo01], which mostly consists of hydrogen.

All the results found in the present work rely on the unambiguous identification in N and Z of the reaction products and on the high-precision measurement of the longitudinal velocity, which allows, among other things, the discrimination between different reaction mechanisms. These are the special features of a high-resolution magnetic spectrometer, which was found to be a powerful tool for the measurement of production cross sections and for the investigation of fundamental properties of the nuclear matter. In particular, the original aim of this work was accomplished, demonstrating that high-resolution magnetic spectrometers can give important information which complements those of full-acceptance devices[1].

---

[1] The results of the present work have initiated an experimental research program dedicated to the investigation of the properties of nuclear matter with a high-resolution spectrometer in the course of which two experimental proposals were approved at GSI (S266: “Determination of the Freeze-out Temperature by the Isospin Thermometer”; S276: “Investigation of the nuclear mean field by precision measurements of the spectator response to the participants blast”).

Appendix A
Additional information on the data analysis

A.1 $B\rho$ and angle dependences of the flight path

In figure A.1 the results of an ion optic calculation are presented. The calculation reports the trajectories of the fragments for three magnetic rigidities and five angular bands. It is evident from the figure that the flight-path depends both on the angle, α, and on the magnetic rigidity, $B\rho$. The dependence on α and on the $B\rho$ (x_2-position) combine together and the flight-path, s, can be written as:

$$s = s_0(1 + ax_2 + bx_2^2)(1 + c\alpha) \tag{A.1}$$

The dependence on x_2 contains a linear and a quadratic term. The linear terms, ax_2 and $c\alpha$, are due to the curvature of the magnets, which is not visible in figure A.1. The piece of circle tracked by the fragments is proportional to the radius ρ of the trajectories, and therefore increases linearly with the angle and with the x_2 position. The quadratic term, bx_2^2, is due to the complex paths presented in figure A.1. The paths are completely symmetric with respect to the central trajectory, so we assume a quadratic dependence. Resolving equation A.1, neglecting the mixed terms, we obtain:

$$s = s_0(1 + c\alpha) + d_1x_2 + d_2x_2^2 \quad \text{with} \quad d_1 = as_0 \quad \text{and} \quad d_2 = bs_0 \tag{A.2}$$

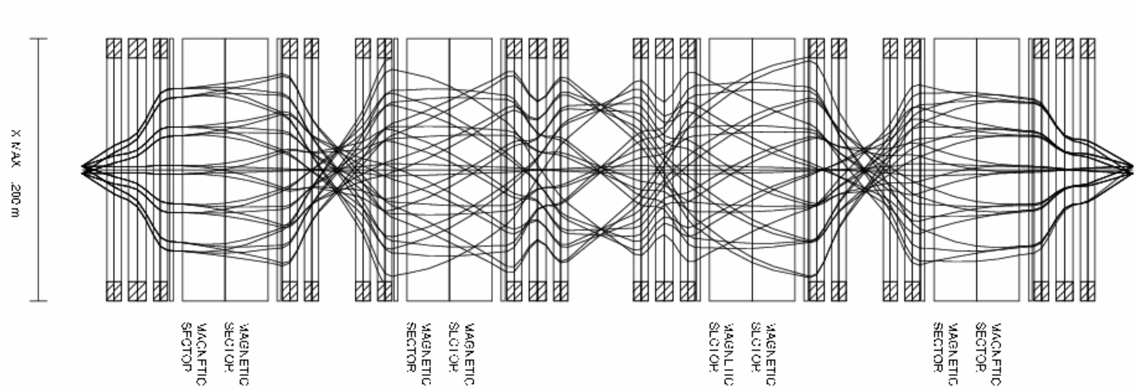

Figure A.1: Transversal x-positions of the trajectories of ions entering the FRS with three magnetic rigidities and five angular bands.

A.2 A new method for the precise determination of the calibration parameters

This section provides a detailed description of the method that was implemented to have the precise determination of the calibration parameters. The method exploits the totality of the recorded data that, due to integer numbers of the mass, *A*, and charge, *Z*, of the fragments, form a characteristic pattern. The precise determination of the calibration parameters is of extreme importance for an unambiguous identification of the fragments and, above all, for a correct measurement of the velocity.

The method is based on the fact that the correct parameters are such that:

1) the A/Z-ratio, determined according to equation 2.1, forms the characteristic pattern of figure 2.2-right,
2) the measured data must give values of the A/Z that must coincide with the expected values. This means, for instance, that the vertical line of the pattern of figure 2.2-right must be placed at A/Z=2,
3) for any given fragment, the A/Z-ratio must be a constant number, i.e. it must not show any dependence on the measured variables B_1, B_2, SCI_2, α_x, ToF_R^*, ToF_L^*.

Since the time-of-flight is measured between the intermediate and the final image planes, let us see how equation 2.1 is written when the second half of the FRS is considered. Inserting equations 2.3 and 2.5, and imposing $\Delta(B\rho)_{AB}=0$, we have[1]:

$$\frac{A}{Z} \propto \frac{(B\rho)_{A0}\left(1+\frac{x_2}{D_2}\right)\cdot\sqrt{1-\frac{\left(s_0\left(1+c_\alpha\alpha_x\right)+\Delta s\right)^2}{c^2\cdot\left(T_0-ToF*\right)^2}}}{\left(s_0\left(1+c_\alpha\alpha_x\right)+\Delta s\right)/\left(T_0-ToF*\right)} \tag{A.3}$$

with:

$$(B\rho)_{10}=\frac{B_1\rho_1+B_2\rho_2}{2} \qquad ToF*=\frac{ToF_L^*\cdot\alpha_L+ToF_R^*\cdot\alpha_R}{2}$$

$$\Delta s=d_1x_2+d_2x_2^2 \qquad x_2=b_2-a_2\cdot SCI_2$$

The parameters can be divided into two categories: those that mostly shift the numerical value of *A/Z*, but do not modify the mass resolution, and those that mostly spoil the mass resolution but do not modify the A/Z mean numerical value.

$(B\rho)_{A0}$, s_0 and T_0 belong to the first category. $(B\rho)_{A0}$ represents the magnetic rigidity of a fragment moving in the central trajectory (x_2=0). Fragments moving in not-central trajectories ($x_2\neq0$) can vary their magnetic rigidity by maximum 1.5% (considering x_{2max} ≈10 cm and D_2 = 6.81 cm/%). Thus a wrong value of x_2/D_2 does not change much the

---

[1] We recall that B_1, B_2, SCI_2, α_x, ToF_R^*, ToF_L^* are variables (measured quantities) and ρ_1, ρ_2, a_2, b_2, D_2, c_α, d_1, d_2, s_0, α_L, α_R, T_0 are parameters.

value of A/Z. Analogously, due to geometrical constrictions, the flight-path for not-central trajectories differs from s_0 by less then 15 cm, thus by few per mill. Concerning the time-of-flight, typical values are $T_0 \approx 170$ ns and $ToF^* \approx 24$ ns, so a variation of ToF^* of 20% produces a change in ToF of about 2%.

Among $(B\rho)_{A0}$, s_0 and T_0, the determination of $(B\rho)_{A0}$ is by far the safest one, since the relative error on the magnetic rigidity is about $3 \cdot 10^{-4}$. On the contrary s_0 and T_0 were determined with larger uncertainties[1] and their value could be wrong of 1-2%. Since what modifies the mean value of the A/Z is the ratio $(T_0 - ToF^*)/s_0 \approx T_0/s_0$, the value of s_0 was not changed and only T_0 was adjusted.

In conclusion, T_0 was the only parameter that had to be tuned in order to have the correct A/Z value for every nuclide.

To the second category belong x_2/D_2, $c_\alpha \alpha_x$, Δs and, in some sense also ToF^*. They bring a minor contribute to the values of the magnetic rigidity and of the velocity, but they contain the variables that can give a dependence of the A/Z on the measured quantities and therefore spoil the mass resolution. Among them, the parameters inside ToF^*, α_L and α_R, were determined with great precision (relative error ~ 10^{-3})[2], since both the pulse value, given by the pulse generator, and the ADC channel were well established. So the values of these parameters were not adjusted at all. The dispersion D_2 was calculated with accurate ion-optical programs. Its nominal value was not changed, since the correctness of the ratio x_2/D_2 could be established by tuning x_2. The calibration of x_2, on the other hand, was unstable and had to be controlled setting by setting. So a more rigorous criterion to establish the right values of a_2 and b_2 had to be found. A good tuning of x_2 is important also to have a good description of Δs, which gives the dependence of the flight-path on the $B\rho$. As well, also a good tuning of the flight-path required a determination of the parameter c_α, d_1, d_2, which at the beginning were set to zero.

In conclusion, the parameters that had to be tuned in order not to have any dependence of the A/Z on the measured signals were a_2, b_2, c_α, d_1, d_2.

The so-depicted role of every parameter can be better understood by the spectra reported in figure A.2. The spectra refer to one specific setting. Every row corresponds to different values of the calibration parameters. The 1st column contains the A/Z vs. Z spectra for the data of the file F216, cantered around ^{40}Ca, and the other columns report the two-dimensional plots with A/Z in the y-axis (calculated by equation A.3) and x_2, α_x or ToF in the x-axis, obtained for Z=15 (isotopes A=30, 31, 32, 33).

The spectra presented in the 1st row of figure A.2 were obtained with the optimised values of the parameters. The vertical line of the A/Z vs. Z spectrum is exactly at A/Z=2,

---

[1] The time-of-flight offset T_0, and the effective flight-path s_0, were determined by passing the beam through the FRS with different energies (i.e. with different velocities) and measuring the corresponding different ToF. A linear fit gave s_0 and T_0.

[2] To get a *real* value (in *ns*) of the time-of-flight it is necessary to calibrate the ADCs, to pass from *channels* to *ns*. This was done with a pulse generator with a know frequency. A TAC converted the known frequency in amplitude and the amplitude was the input of an ADC, which gave an output on a certain channel. In our experiment a generator with a pulse every 10 ns was used.

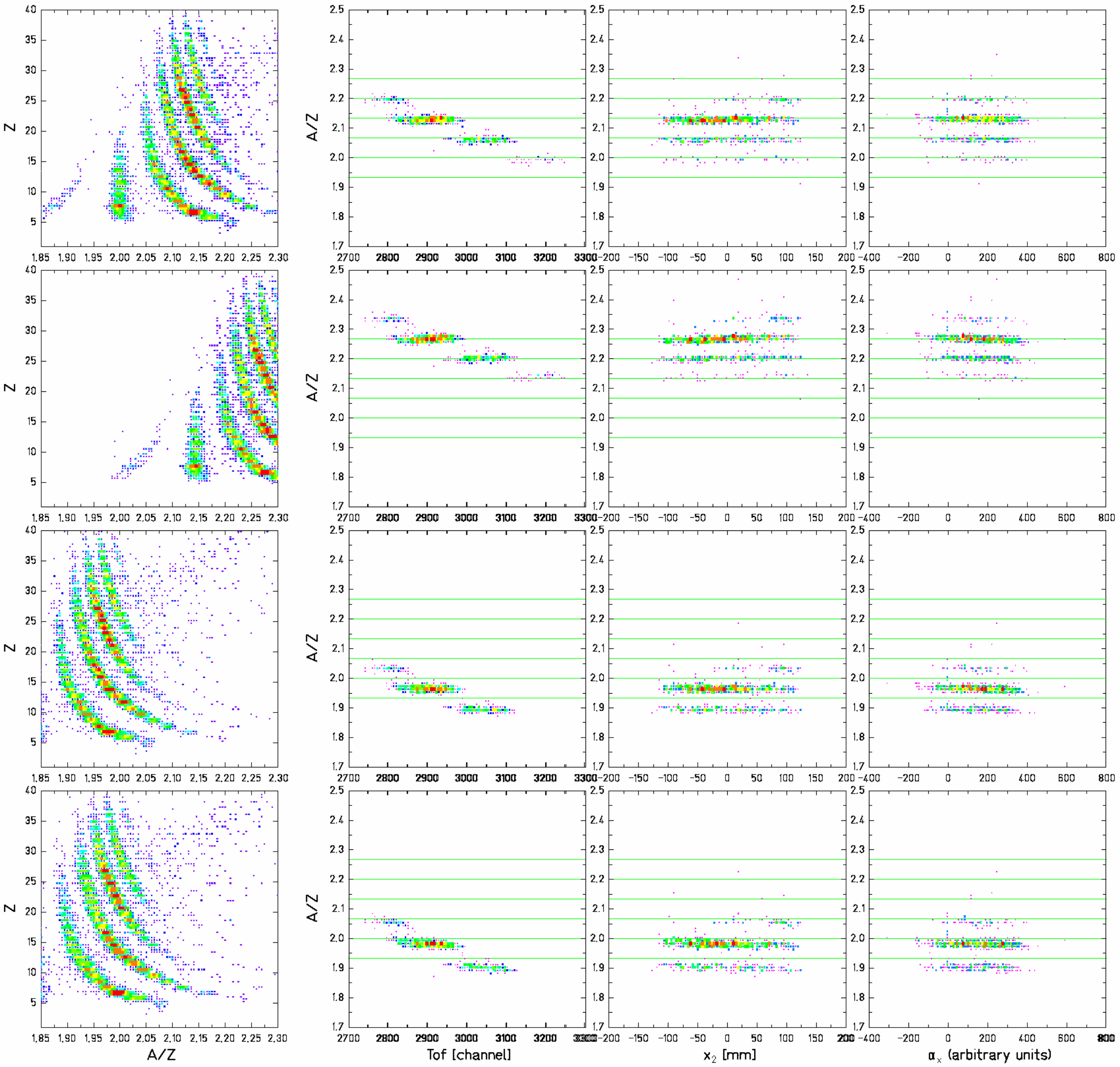

Figure A.2: A/Z vs. Z for setting F216 and plot of the A/Z for Z=15 resulting from eq. A.3 as a function of x_2, α_x and ToF. The horizontal lines are the expected values. The correct values of the parameters are used in the 1st row. Wrong values of T_0 (2nd row), of s_0 (3rd row), of α_R or α_L (4th row) lead to an incorrect value of the A/Z-ratio. Wrong values of D_2 (5th row), of a_2 (6th row), of b_2 (7th row) and of c_α (8th row) and of d_1 and d_2 (9th row) lead to a dependence of the A/Z on the measured signals and thus to a bad mass resolution.

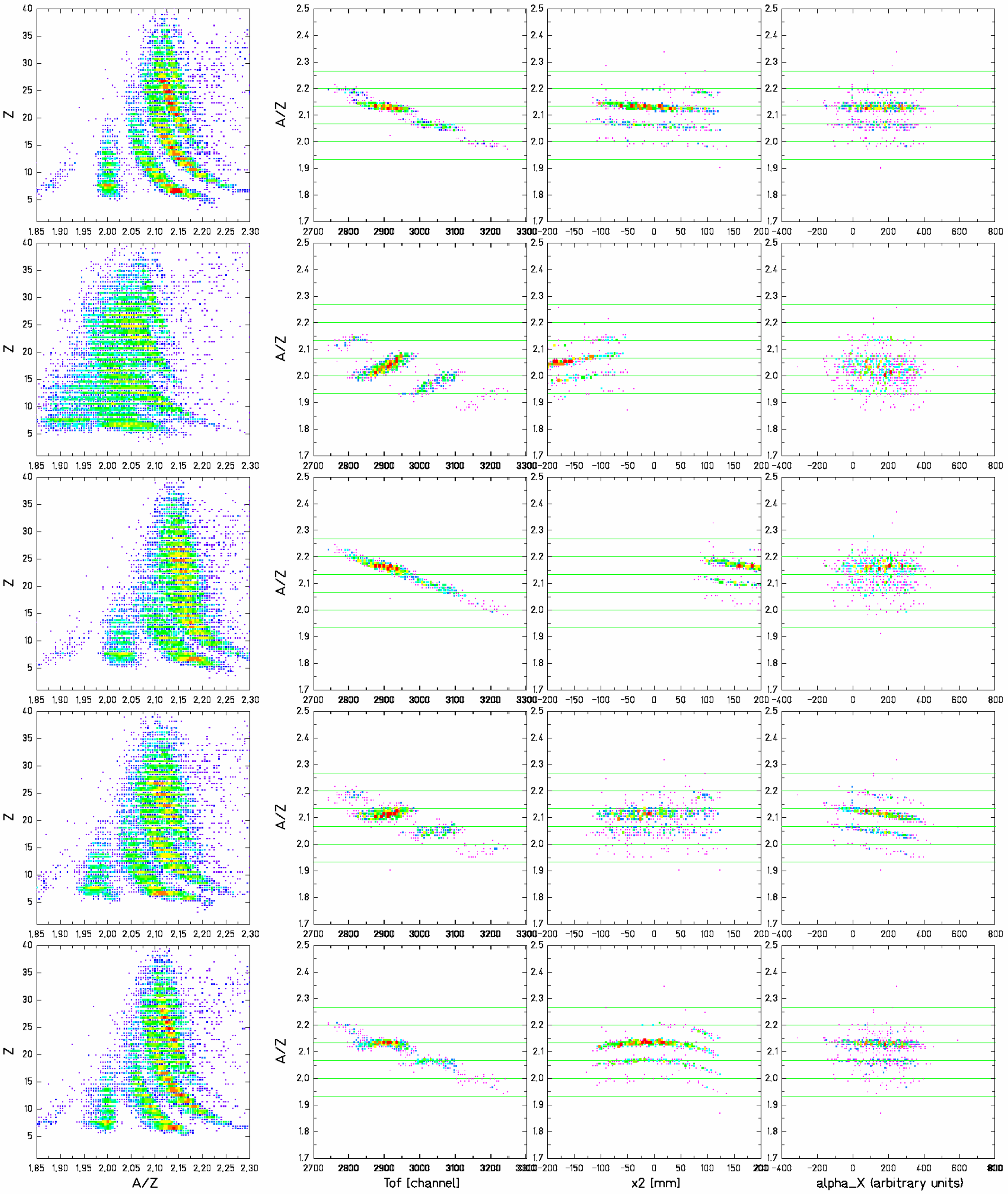

Z
A/Z
Tof [channel]
x2 [mm]
alpha_X (arbitrary units)
5
10
15
20
25
30
35
40
1.85
1.90
1.95
2.00
2.05
2.10
2.15
2.20
2.25
2.30
1.7
1.8
1.9
2.0
2.1
2.2
2.3
2.4
2.5
2700
2800
2900
3000
3100
3200
3300
-200
-150
-100
-50
0
50
100
150
200
-400
-200
0
200
400
600
800

and the other spectra (A/Z vs. x_2, α_x and ToF) show that A/Z does not depend on any of the measured variables.

In the 2nd and 3rd rows, T_0 and s_0 are 1.5% larger than their optimum values. As expected, the vertical line is now displaced from $A/Z=2$ and the values of the masses of the isotopes of $Z=15$ are off by 3 units. However the mass resolution is still good (actually a wrong T_0 affects also the mass resolution in the A/Z vs. ToF spectrum, but this is a minor effect).

When α_R or α_L are appreciably increased (10%) (4th row) the largest effect is that the A/Z values are wrong, but also the lines in the A/Z vs. ToF spectrum of the are not perfectly horizontal anymore.

As we pointed out, a wrong value of the dispersion D_2 does not change the mean value of the A/Z. In the 5th row the value of D_2 was doubled and still the vertical line is at $A/Z=2$, but the lines in the A/Z vs. ToF spectrum are now transversal. This would have the consequence that the width of the velocity distribution of every isotope would result much larger[1] than they are in reality. Of course, exactly the same result is obtained if, instead of doubling D_2, the values of a_2, b_2 would be reduced to the half.

If only a_2 or only b_2 is varied by 20%, the consequences are severe (rows 6th and 7th). The mean value of the A/Z is not so much changed (the vertical line is just a little displaced from $A/Z=2$) but the resolution is completely lost, and the width of the distributions would be strongly enlarged. In the equation 2.2 we would have:

$$1+\frac{(b_2-1.2\cdot a_2\cdot SCI_2)}{D_2}=1+\frac{(b_2-a_2\cdot SCI_2)}{D_2}-\frac{0.2\cdot a_2\cdot SCI_2}{D_2}=\left(1+\frac{x_2}{D_2}\right)-f(SCI_2)$$

$$1+\frac{(1.2\cdot b_2-a_2\cdot SCI_2)}{D_2}=1+\frac{(b_2-a_2\cdot SCI_2)}{D_2}+\frac{0.2\cdot b_2}{D_2}=\left(1+\frac{x_2}{D_2}\right)+constant$$

Similar effects are produced by a wrong calibration of the flight-path. If c_α is doubled we have the spectra shown in the 8th row. As well, when d_1 and d_2 are increased fivefold, the resolution is lost (9th row). Anyhow c_α, d_1, d_2 are much less sensitive parameters than a_2 and b_2.

Now that we have clarified the role of every parameter, the criterion according to which we had tuned the parameters is straightforward: the good combination of values of the parameters is that one which produces the correct A/Z vs. Z path and no dependence of the A/Z on the measured variables (i.e. the data of the A/Z vs. x_2, α_x, ToF spectra should form horizontal and well-separated lines). As we previously marked, it is enough to tune T_0, a_2, b_2, c_α, d_1 and d_2. The procedure to find the best value of these six parameters was simplified by the fact

---

[1] This can be deduced also by the equation 2.2, where to double the value of D_2 would give: $1+\frac{x_2}{2D_2}=1+\frac{x_2}{D_2}-\frac{x_2}{2D_2}=1+\frac{x_2}{D_2}-f(SCI_2)$

that they are practically independent (i.e. their values affect mostly the dependence of *A/Z* on the observable that they describe[1]). Nevertheless one iteration was needed.

While the values of a_2, b_2, and c_α are common to all the settings (as they should be, since they depend only on the electronic devices used) the parameter T_0 had to be adjusted for every setting. The difference among all the T_0 values was anyhow less then 2 per mill, so the identification and resolution were anyhow safe. This small variation from setting to setting was due to the fact that the operation conditions of the photo-multipliers depend on temperature and also on other effects, like the load of the scintillators (which is different for different measurements). In figure A.3 the combination of several setting is presented with the use of a unique value of T_0 (left) and with the adjustment of T_0 setting by setting (right).

It is important to stress that there is a biunique correspondence between "correct parameters" and "good plots", i.e. if the values of the parameters are correct, than the spectra are good, vice-versa if the spectra are good, than the parameters are for sure correct and the final result will be correct, too.

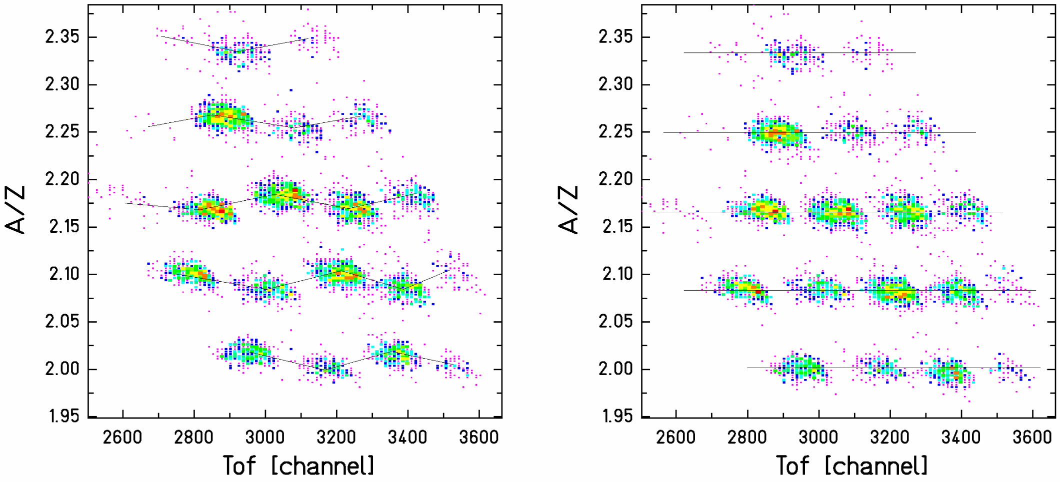

Figure A.3: A/Z vs. ToF for charge Z=12 for several settings. When the value of T_0 is not adjusted setting by setting (left) the data do not fall on the same horizontal line. A small tuning is needed to improve the mass resolution (right).

---

[1] This does not seem to be the case in the examples we showed in figure A.2. However, very exaggerate cases were presented there. In reality the parameters were varied of a few per cent, only.

Appendix B
Compilation of the results

In this appendix we list the numerical results for all the nuclides and depict the isotopic distributions of the elements from nitrogen to rubidium produced in fragmentation and fission reactions.

Fission of 1·A GeV ^{238}U on protons

Table B.1: Experimental cross sections for the fission products from the spallation of 1·A GeV ^{238}U on hydrogen. The last two columns represent the relative uncertainties, up and down. They include both the statistical and the systematic errors.

Z	N	σ/mb	$\Delta\sigma_{UP}$/%	$\Delta\sigma_{DOWN}$/%
7	8	1.8	23	22
7	9	0.44	22	21
7	10	0.14	67	44
8	8	0.52	33	29
8	9	0.80	28	28
8	10	0.95	55	23
8	11	0.29	27	25
9	10	0.46	28	26
9	11	0.68	57	28
9	12	0.49	57	28
10	10	0.14	28	28
10	11	0.52	28	28
10	12	0.73	28	28
10	13	0.36	56	24
10	14	0.15	29	26
11	12	0.45	25	24
11	13	0.53	23	23
11	14	0.50	55	22
11	15	0.26	56	24
12	12	0.17	54	28
12	13	0.34	25	24
12	14	0.62	22	22
12	15	0.52	55	23
12	16	0.16	73	31
13	14	0.22	37	31
13	15	0.50	21	21
13	16	0.57	55	23
13	17	==		
13	18	0.21	36	31
14	14	0.054	34	30
14	15	0.25	28	26
14	16	0.56	23	23
14	17	0.41	23	23
14	18	0.25	32	28
15	16	0.12	29	27
15	17	0.39	21	21
15	18	0.47	28	28
15	19	0.34	57	28
15	20	0.23	56	24
16	17	0.11	29	27
16	18	0.40	22	22
16	19	0.46	28	28
16	20	0.35	54	21
16	21	0.20	57	26
16	22	0.084	33	29
17	18	0.18	32	28
17	19	0.29	24	23
17	20	0.40	28	26
17	21	0.37	55	23
17	22	0.29	28	28
17	23	0.18	55	23
18	19	0.11	35	30
18	20	0.24	23	22
18	21	0.55	25	24
18	22	0.59	22	22
18	23	==		
18	24	0.27	55	22
18	25	0.096	61	58
18	26	0.047	44	35
19	20	0.041	38	32
19	21	0.15	24	23
19	22	0.33	27	25
19	23	0.57	22	22
19	24	0.58	56	23
19	25	0.62	57	26
19	26	0.23	57	25
19	27	0.13	43	34

Z	N	σ/mb	$\Delta\sigma_{UP}$/%	$\Delta\sigma_{DOWN}$/%
20	21	0.057	29	27
20	22	0.18	23	23
20	23	0.39	25	24
20	24	0.61	21	21
20	25	0.54	21	21
20	26	0.64	24	23
20	27	0.32	23	23
20	28	0.091	66	34
21	25	0.50	22	22
21	26	0.76	21	21
21	27	0.59	28	28
21	28	0.65	21	21
21	29	==		
21	30	0.070	59	28
21	22	0.040	36	30
21	23	0.15	26	25
21	24	0.38	23	23
22	24	0.11	23	22
22	25	0.39	24	23
22	26	==		
22	27	0.90	20	20
22	28	==		
22	29	0.71	21	21
22	30	0.29	57	26
22	31	0.13	58	27
22	32	0.030	60	52
23	25	0.086	28	28
23	26	0.36	22	22
23	27	==		
23	28	1.1	20	20
23	29	1.3	57	28
23	30	1.1	28	28
23	31	0.55	23	22
24	26	0.062	23	22
24	27	0.34	22	21
24	28	0.59	24	23
24	29	1.0	20	20
24	30	1.1	57	28
24	31	1.3	22	22
24	32	0.73	21	20
24	33	==		
24	34	0.18	24	23
25	27	0.047	25	24
25	28	0.28	22	22
25	29	==		
25	30	1.3	21	21
25	31	1.3	21	21
25	32	==		
25	33	0.95	20	20
25	34	0.53	24	23
25	35	==		
25	36	0.11	58	26
26	27	0.0082	28	28
26	28	0.045	24	23
26	29	0.26	22	22
26	30	0.59	24	23
26	31	1.3	21	21
26	32	1.6	57	28
26	33	1.4	28	28
26	34	1.6	20	20
26	35	1.0	28	28
26	36	==		
26	37	0.23	23	22
27	29	0.039	24	23
27	30	0.23	22	22
27	31	==		
27	32	1.2	21	21
27	33	1.6	20	20
27	34	1.7	28	28
27	35	2.2	20	20
27	36	1.8	28	28
27	37	==		
27	38	0.55	54	21
27	39	0.24	58	27
28	30	0.028	26	24
28	31	0.11	22	22
28	32	0.31	57	25
28	33	0.87	22	21
28	34	1.6	20	20
28	35	2.1	28	28
28	36	2.3	21	21
28	37	2.3	28	28
28	38	1.8	28	28
28	39	==		
28	40	==		
28	41	==		
28	42	==		
28	43	0.010	54	39
28	44	0.035	24	23
28	45	0.0058	50	37

Z	N	σ/mb	$\Delta\sigma_{UP}$/%	$\Delta\sigma_{DOWN}$/%
29	31	0.011	30	27
29	32	0.075	24	23
29	33	0.30	28	28
29	34	==		
29	35	1.5	20	20
29	36	2.2	28	28
29	37	2.7	21	21
29	38	2.8	20	20
29	39	2.3	28	28
29	40	1.4	24	23
29	41	==		
29	42	==		
29	43	==		
29	44	==		
29	45	0.084	24	23
29	46	0.030	26	25
29	47	0.0041	36	30
30	32	0.014	32	28
30	33	0.059	22	22
30	34	==		
30	35	0.61	28	28
30	36	1.1	21	21
30	37	2.4	57	28
30	38	2.9	28	28
30	39	3.6	20	20
30	40	3.7	28	28
30	41	2.8	28	28
30	42	==		
30	43	==		
30	44	==		
30	45	==		
30	46	==		
30	47	0.12	22	22
31	33	0.0039	38	31
31	34	0.047	24	23
31	35	==		
31	36	0.48	21	21
31	37	1.1	54	21
31	38	2.3	57	28
31	39	3.0	28	28
31	40	4.4	20	20
31	41	3.6	21	20
31	42	3.8	28	28
31	43	==		
31	44	==		
31	45	==		
31	46	==		
31	47	==		
31	48	0.19	21	21
31	49	0.16	22	22
31	50	0.025	31	23
32	35	0.034	23	23
32	36	==		
32	37	0.41	28	28
32	38	1.1	21	21
32	39	1.7	22	22
32	40	3.4	28	28
32	41	4.7	21	21
32	42	4.5	20	20
32	43	5.1	28	28
32	44	3.4	21	21
32	45	==		
32	46	==		
32	47	==		
32	48	==		
32	49	0.73	59	41
32	50	0.39	28	28
32	51	==		
32	52	0.060	28	28
33	36	0.013	26	25
33	37	==		
33	38	0.35	22	22
33	39	0.89	21	21
33	40	1.8	21	21
33	41	2.9	57	28
33	42	5.1	21	21
33	43	4.6	29	26
33	44	6.5	28	28
33	45	5.6	28	28
33	46	==		
33	47	==		
33	48	==		
33	49	==		
33	50	==		
33	51	==		
33	52	0.62	21	21
34	37	0.017	28	28
34	38	==		
34	39	0.26	22	22
34	40	0.82	22	21
34	41	1.2	21	21
34	42	3.1	28	28
34	43	4.7	28	28
34	44	5.7	20	20
34	45	8.6	28	28
34	46	7.2	28	28
34	47	5.4	21	21
34	48	==		
34	49	==		
34	50	==		
34	51	==		
34	52	0.89	65	43
34	53	1.2	21	21
34	54	0.77	24	23

Z	N	σ/mb	$\Delta\sigma_{UP}$/%	$\Delta\sigma_{DOWN}$/%
35	38	0.0098	31	28
35	39	0.030	57	28
35	40	0.13	25	24
35	41	0.16	22	21
35	42	1.1	21	21
35	43	2.2	57	28
35	44	4.6	28	28
35	45	6.3	20	20
35	46	6.9	32	28
35	47	7.8	28	28
35	48	8.8	28	28
35	49	==		
35	50	==		
35	51	==		
35	52	==		
35	53	==		
35	54	1.4	44	30
35	55	1.3	22	22
35	56	0.30	22	22
35	57	0.034	22	22
36	39	0.0065	62	42
36	40	0.015	28	28
36	41	0.058	33	29
36	42	0.49	21	21
36	43	0.79	21	21
36	44	2.2	26	25
36	45	4.1	57	28
36	46	6.7	21	21
36	47	8.2	55	56
36	48	11.	28	28
36	49	10.	28	28
36	50	==		
36	51	==		
36	52	==		
36	53	==		
36	54	==		
36	55	==		
36	56	2.0	21	21
36	57	1.5	21	21
36	58	0.25	28	28
36	59	0.083	23	22
37	41	0.017	28	28
37	42	==		
37	43	0.27	22	21
37	44	0.58	21	21
37	45	1.5	25	24
37	46	3.7	57	28
37	47	7.0	28	28
37	48	7.0	20	20
37	49	12.	28	28
37	50	11.	28	28
37	51	11.	21	21
37	52	==		
37	53	5.8	36	28
37	54	==		
37	55	==		
37	56	==		
37	57	==		
37	58	1.8	22	21
37	59	1.0	22	22
37	60	0.16	23	22
37	61	0.016	23	23

Table B.2: Experimental mean velocities and kinetic energies for the fission products from the spallation of 1·A GeV ^{238}*U on hydrogen.*

Z of fission fragment	Mean velocity in the mother-nucleus frame (cm/ns)	Mean recoil velocity of mother nuclei in the beam frame (cm/ns)	Mean kinetic energy in the mother-nucleus frame (MeV)
17	2.00 ± 0.03	-0.13 ± 0.02	77.9 ± 0.8
18	1.99 ± 0.03	-0.09 ± 0.02	82.4 ± 1.2
19	1.94 ± 0.02	-0.13 ± 0.01	83.4 ± 1.3
20	1.88 ± 0.01	-0.12 ± 0.01	82.0 ± 1.4
21	1.86 ± 0.02	-0.12 ± 0.01	84.8 ± 1.6
22	1.83 ± 0.02	-0.13 ± 0.01	86.1 ± 0.6
23	1.80 ± 0.01	-0.13 ± 0.01	87.2 ± 1.3
24	1.76 ± 0.01	-0.12 ± 0.01	86.8 ± 1.2
25	1.71 ± 0.03	-0.10 ± 0.01	85.9 ± 1.2
26	1.70 ± 0.01	-0.12 ± 0.01	87.9 ± 1.0
27	1.67 ± 0.01	-0.10 ± 0.01	88.8 ± 1.3
28	1.61 ± 0.01	-0.12 ± 0.01	86.9 ± 0.9
29	1.60 ± 0.01	-0.11 ± 0.01	89.3 ± 1.4
30	1.57 ± 0.01	-0.11 ± 0.01	88.8 ± 0.5
31	1.55 ± 0.01	-0.10 ± 0.01	90.6 ± 1.4
32	1.49 ± 0.02	-0.12 ± 0.01	86.2 ± 1.2
33	1.46 ± 0.02	-0.12 ± 0.01	86.3 ± 1.5
34	1.44 ± 0.02	-0.12 ± 0.01	86.3 ± 1.4
35	1.42 ± 0.01	-0.11 ± 0.01	86.9 ± 1.2
36	1.38 ± 0.02	-0.12 ± 0.01	84.9 ± 1.2
37	1.36 ± 0.01	-0.12 ± 0.01	84.4 ± 1.4
38	1.35 ± 0.02	-0.11 ± 0.01	77.9 ± 0.8
39	1.29 ± 0.01	-0.12 ± 0.01	82.4 ± 1.2

Figure B.1: Isotopic cross sections for the fission fragments between Z=7 and Z=37 produced in the spallation of ^{238}U on hydrogen at 1 GeV per nucleon. The dashed lines are set to guide the eye and do not necessarily represents the expected trend of the missing data. The error bars include both the statistical and systematic uncertainties. The pictures were done using the data listed in table B.1.

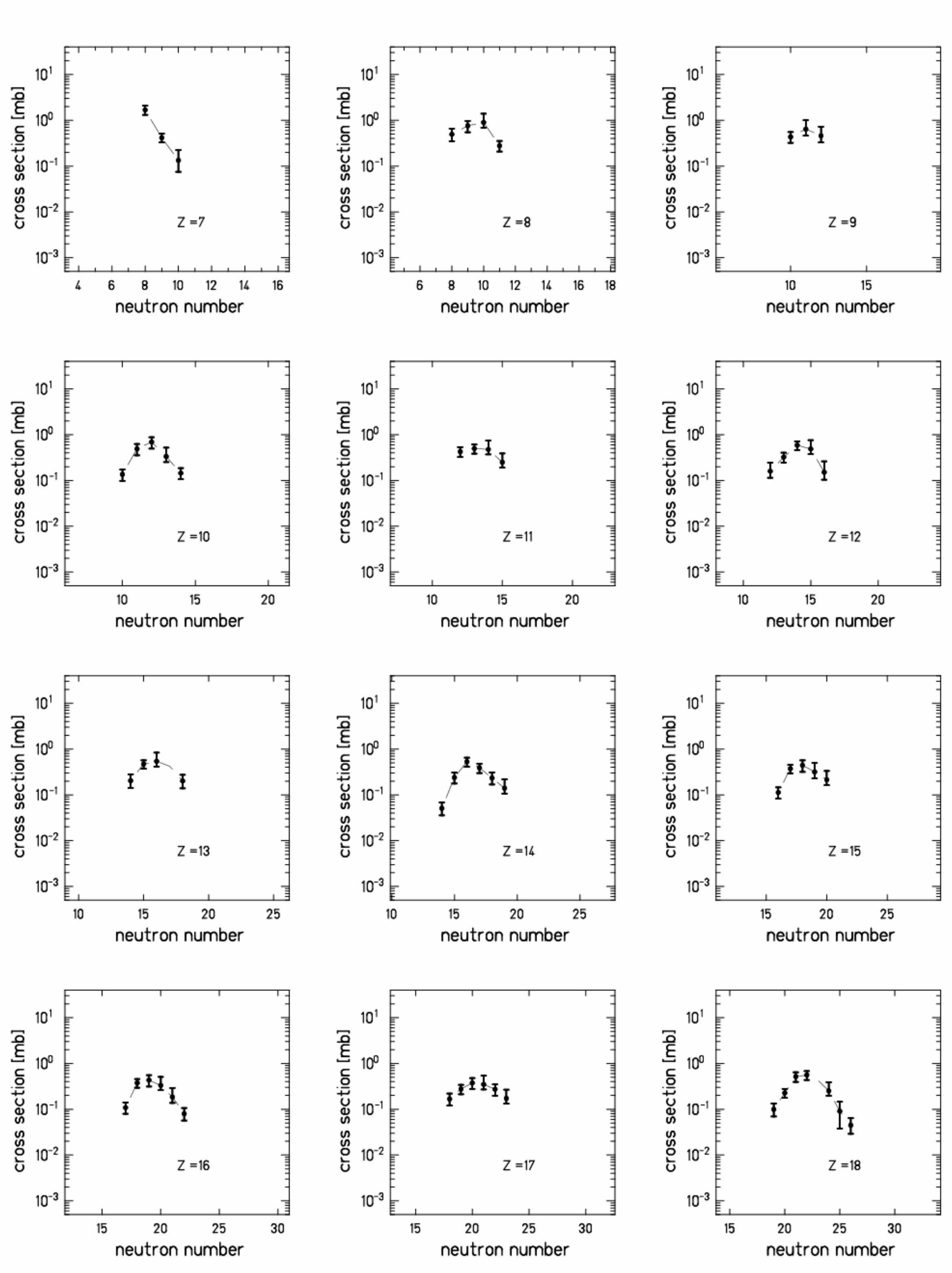

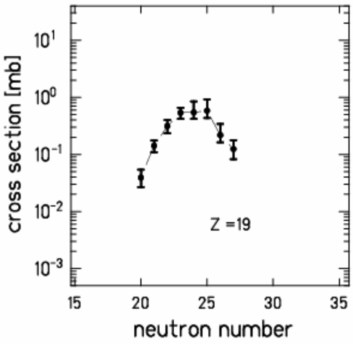

cross section [mb]
10^{1}
10^{0}
10^{-1}
10^{-2}
10^{-3}
Z =19
15
20
25
30
35
neutron number

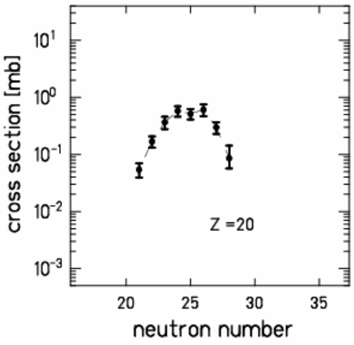

cross section [mb]
10^{1}
10^{0}
10^{-1}
10^{-2}
10^{-3}
Z =20
20
25
30
35
neutron number

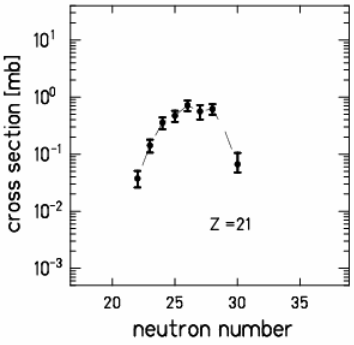

cross section [mb]
10^{1}
10^{0}
10^{-1}
10^{-2}
10^{-3}
Z =21
20
25
30
35
neutron number

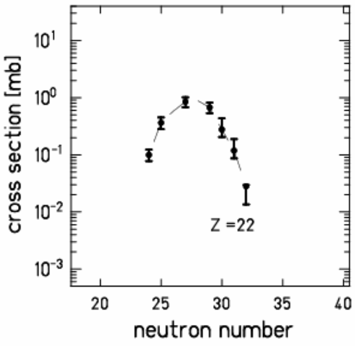

cross section [mb]
10^{1}
10^{0}
10^{-1}
10^{-2}
10^{-3}
Z =22
20
25
30
35
40
neutron number

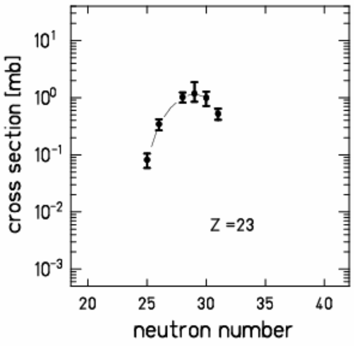

cross section [mb]
10^{1}
10^{0}
10^{-1}
10^{-2}
10^{-3}
Z =23
20
25
30
35
40
neutron number

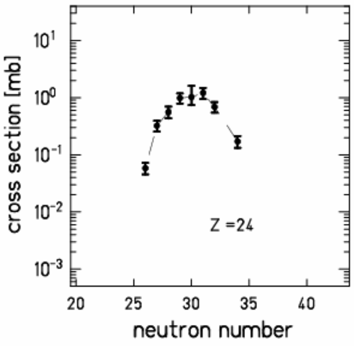

cross section [mb]
10^{1}
10^{0}
10^{-1}
10^{-2}
10^{-3}
Z =24
20
25
30
35
40
neutron number

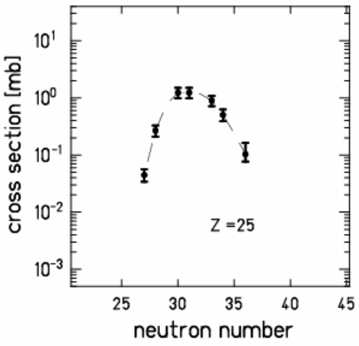

cross section [mb]
10^{1}
10^{0}
10^{-1}
10^{-2}
10^{-3}
Z =25
25
30
35
40
45
neutron number

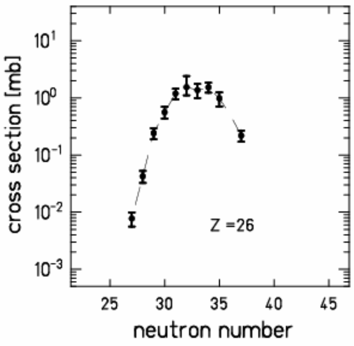

cross section [mb]
10^{1}
10^{0}
10^{-1}
10^{-2}
10^{-3}
Z =26
25
30
35
40
45
neutron number

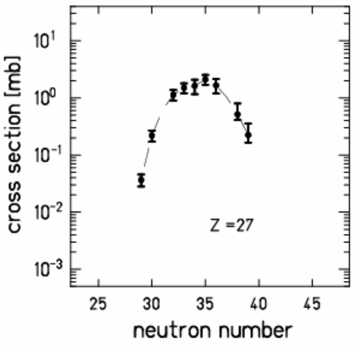

cross section [mb]
10^{1}
10^{0}
10^{-1}
10^{-2}
10^{-3}
Z =27
25
30
35
40
45
neutron number

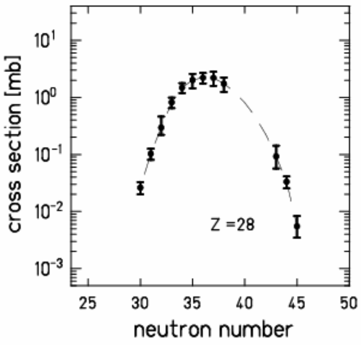

cross section [mb]
10^{1}
10^{0}
10^{-1}
10^{-2}
10^{-3}
Z =28
25
30
35
40
45
50
neutron number

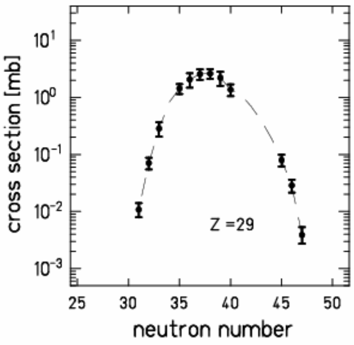

cross section [mb]
10^{1}
10^{0}
10^{-1}
10^{-2}
10^{-3}
Z =29
25
30
35
40
45
50
neutron number

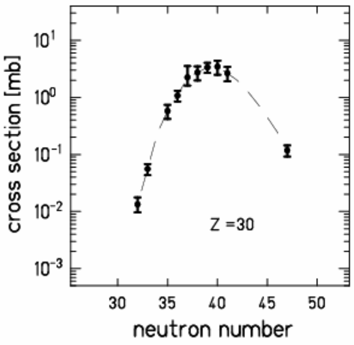

cross section [mb]
10^{1}
10^{0}
10^{-1}
10^{-2}
10^{-3}
Z =30
30
35
40
45
50
neutron number

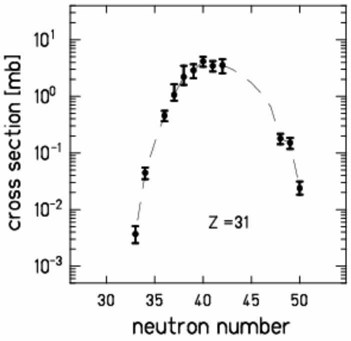

cross section [mb]
10^1
10^0
10^{-1}
10^{-2}
10^{-3}
Z =31
30
35
40
45
50
neutron number

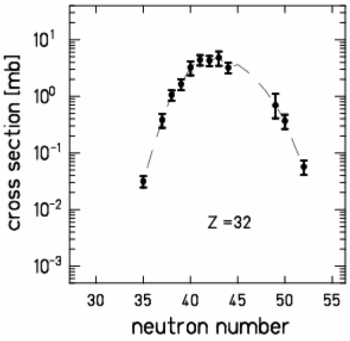

cross section [mb]
10^1
10^0
10^{-1}
10^{-2}
10^{-3}
Z =32
30
35
40
45
50
55
neutron number

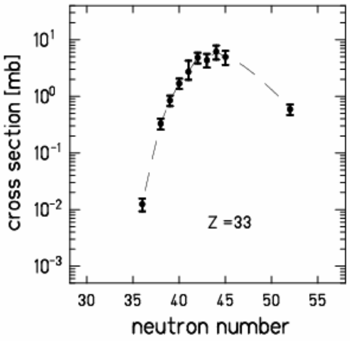

cross section [mb]
10^1
10^0
10^{-1}
10^{-2}
10^{-3}
Z =33
30
35
40
45
50
55
neutron number

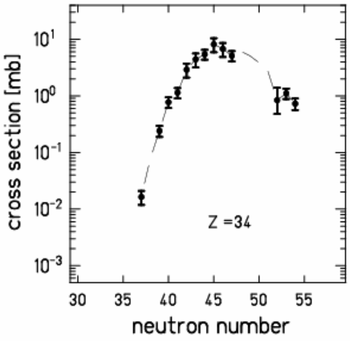

cross section [mb]
10^1
10^0
10^{-1}
10^{-2}
10^{-3}
Z =34
30
35
40
45
50
55
neutron number

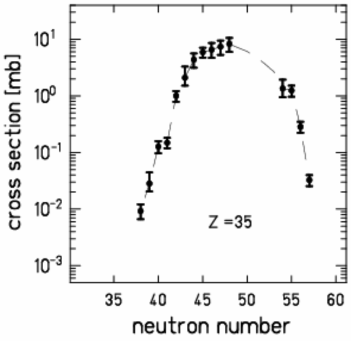

cross section [mb]
10^1
10^0
10^{-1}
10^{-2}
10^{-3}
Z =35
35
40
45
50
55
60
neutron number

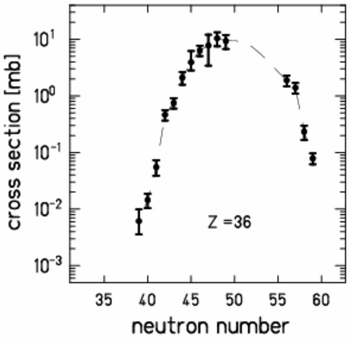

cross section [mb]
10^1
10^0
10^{-1}
10^{-2}
10^{-3}
Z =36
35
40
45
50
55
60
neutron number

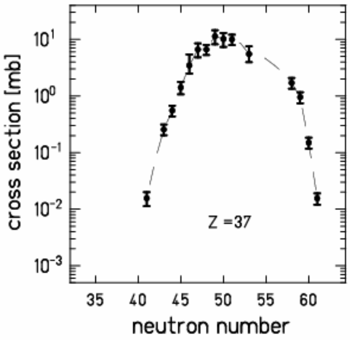

cross section [mb]
10^1
10^0
10^{-1}
10^{-2}
10^{-3}
Z =37
35
40
45
50
55
60
neutron number

Production from 1·A GeV ^{238}U on titanium

The production of the residues in the reaction 1·*A* GeV ^{238}U on titanium was attributed to two processes: fragmentation, with a Gaussian-like velocity distribution and a fission-like process populating a diffuse shell sphere in velocity space.

In table B.3 we present the integrated differential production cross-sections (both processes are considered) for the products in the *Z* range between 7 and 21. In tables B.4 and B.5 we present the cross sections for the fragmentation products obtained assuming angular isotropy. In the *Z* range between 7 and 21 the forward component of the fission-like process could not be observed directly, and specific assumptions were needed to deduce the fragmentation cross sections (see section 2.6.6).

Table B.3: Experimental differential production cross-sections integrated between 0 and 15 mrad, for the reaction 1·A GeV ^{238}U on titanium. The last two columns represent the relative uncertainties, up and down. They include both the statistical and the systematic errors.

Z	N	σ/mb	$\Delta\sigma_{UP}$/%	$\Delta\sigma_{DOWN}$/%
7	7	2.9	33	32
7	8	11.	30	30
7	9	3.2	31	30
7	10	2.6	32	31
7	11	0.57	41	37
7	12	0.17	34	33
8	7	0.30	62	47
8	8	7.6	31	31
8	9	5.7	30	30
8	10	8.8	30	30
8	11	3.4	30	30
8	12	1.4	35	34
8	13	0.26	52	43
8	14	0.12	57	44
9	8	0.082	56	43
9	9	1.4	39	36
9	10	5.7	30	30
9	11	7.6	33	32
9	12	5.2	30	30
9	13	1.4	40	37
9	14	0.64	40	36
9	15	0.067	92	64
10	10	1.9	39	36
10	11	5.9	29	29
10	12	8.3	32	31
10	13	3.4	31	31
10	14	2.0	33	33
10	15	0.29	64	50
10	16	0.072	71	48
11	10	0.085	60	45
11	11	1.2	51	41
11	12	6.7	30	29
11	13	5.5	32	31
11	14	5.8	32	30
11	15	1.8	33	33
11	16	==		
11	17	0.14	98	63
12	11	0.053	73	49
12	12	1.4	30	29
12	13	5.3	30	30
12	14	7.2	30	30
12	15	5.0	37	35
12	16	2.5	36	34
12	17	0.40	58	44
12	18	0.20	127	83
13	12	0.13	127	79
13	13	0.42	33	31
13	14	5.5	30	30
13	15	5.0	30	30
13	16	5.5	40	36
13	17	2.2	36	34
13	18	1.0	99	69
14	14	0.81	30	30
14	15	4.0	33	33
14	16	6.5	31	30
14	17	4.5	43	37
14	18	2.9	31	30
14	19	0.67	44	39
14	20	0.21	44	38

Z	N	σ/mb	$\Delta\sigma_{UP}$/%	$\Delta\sigma_{DOWN}$/%
15	15	0.14	41	36
15	16	3.0	33	32
15	17	4.5	30	30
15	18	4.2	45	39
15	19	2.8	36	34
15	20	1.4	33	33
15	21	0.30	97	81
16	16	0.16	47	39
16	17	2.0	36	33
16	18	4.9	30	30
16	19	3.7	43	37
16	20	3.7	38	35
16	21	1.5	33	32
16	22	0.54	62	46
16	23	0.19	63	46
17	17	0.061	92	62
17	18	1.2	61	46
17	19	3.6	31	30
17	20	4.0	37	34
17	21	2.7	30	30
17	22	2.2	36	34
17	23	0.67	51	42
17	24	0.11	58	44
18	18	0.087	85	53
18	19	0.85	55	44
18	20	3.3	31	31
18	21	3.2	38	35
18	22	2.3	30	30
18	23	2.6	32	32
18	24	1.2	34	33
18	25	0.23	33	31
19	20	0.54	56	46
19	21	2.5	33	32
19	22	3.2	38	35
19	23	2.6	30	30
19	24	2.9	37	34
19	25	1.36	33	33
19	26	0.49	83	53
20	21	0.42	56	46
20	22	2.3	32	31
20	23	3.1	37	34
20	24	2.2	31	30
20	25	3.31	41	37
20	26	1.5	33	32
20	27	0.52	46	40
20	28	0.089	51	41
21	22	0.20	45	38
21	23	1.6	38	35
21	24	3.3	34	32
21	25	2.5	29	29
21	26	2.6	30	30
21	27	1.9	34	33
21	28	0.61	36	34
21	29	0.10	30	30

Table B.4: Experimental cross sections for the fragmentation of 1·A GeV ^{238}*U on titanium. The last two columns represent the relative uncertainties, up and down. They include both the statistical and the systematic errors. Please note that the cross sections were determined under the assumptions listed in section 2.6.6.*

Z	N	σ/mb	$\Delta\sigma_{UP}$/%	$\Delta\sigma_{DOWN}$/%
7	7	7.7	65	65
7	8	37.	64	64
7	9	11.	64	64
7	10	8.5	65	65
7	11	1.6	68	67
7	12	0.86	67	66
8	7	0.97	50	49
8	8	24.	46	46
8	9	19.	46	46
8	10	31.	46	46
8	11	11.	46	46
8	12	4.8	47	47
8	13	0.64	54	51
8	14	0.58	67	57
9	8	0.33	63	53
9	9	4.0	43	43
9	10	18.	42	42
9	11	25.	42	42
9	12	17.	42	42
9	13	4.5	45	44
9	14	1.9	45	44
9	15	0.24	97	71
10	10	5.2	42	42
10	11	18.	41	41
10	12	25.	41	41
10	13	12.	41	41
10	14	6.2	42	42
10	15	0.71	61	51
10	16	0.26	77	57
11	10	0.28	66	51
11	11	2.8	40	39
11	12	20.	38	38
11	13	15.	39	39
11	14	17.	39	38
11	15	5.1	39	39
11	16	==		
11	17	0.22	89	59
12	11	0.17	74	50
12	12	4.7	32	31
12	13	15.	30	30
12	14	19.	31	31
12	15	14.	31	31
12	16	7.3	32	32
12	17	1.4	59	45
12	18	0.49	93	64
13	12	0.18	93	59
13	13	1.3	34	32
13	14	14.	30	30
13	15	12.	30	30
13	16	15.	30	30
13	17	5.6	31	31
13	18	2.9	93	64
14	14	2.4	30	29
14	15	10.	29	29
14	16	16.	29	29
14	17	11.	29	29
14	18	7.1	29	28
14	19	1.8	30	30
14	20	0.63	44	37
15	15	0.39	40	35
15	16	7.2	28	28
15	17	10.	28	28
15	18	9.6	28	28
15	19	6.4	28	28
15	20	3.4	28	28
15	21	0.64	41	36
16	16	0.42	46	38
16	17	4.4	27	27
16	18	11.	27	27
16	19	8.4	27	27
16	20	7.8	27	27
16	21	3.2	27	27
16	22	1.2	30	29
16	23	0.49	62	44

Z	N	σ/mb	$\Delta\sigma_{UP}$/%	$\Delta\sigma_{DOWN}$/%
17	17	0.13	91	61
17	18	2.4	31	29
17	19	7.4	26	26
17	20	8.3	26	26
17	21	6.5	28	27
17	22	4.6	26	26
17	23	1.5	28	27
17	24	0.25	56	42
18	18	0.17	84	50
18	19	1.7	27	26
18	20	6.7	24	24
18	21	6.5	24	24
18	22	5.1	26	25
18	23	5.0	24	24
18	24	2.3	24	24
18	25	0.53	29	27
19	20	0.92	34	31
19	21	4.7	25	25
19	22	6.0	25	25
19	23	5.6	26	26
19	24	5.3	25	25
19	25	2.4	25	25
19	26	0.91	27	27
20	21	0.59	38	33
20	22	4.1	26	26
20	23	5.7	26	26
20	24	4.4	28	27
20	25	5.6	26	26
20	26	2.8	26	26
20	27	0.82	27	27
20	28	0.16	49	39
21	22	0.39	40	32
21	23	2.8	22	21
21	24	5.8	20	20
21	25	4.8	21	21
21	26	5.0	23	22
21	27	3.2	21	21
21	28	0.99	22	22
21	29	0.18	22	22

Table B.5: Experimental cross sections for the fragmentation of 1·A GeV ^{238}U on titanium.
The last two columns represent the relative uncertainties, up and down. They include both the statistical and the systematic errors.

Z	N	σ/mb	$\Delta\sigma_{UP}$/%	$\Delta\sigma_{DOWN}$/%
22	24	2.9	23	23
22	25	4.6	21	21
22	26	5.3	21	21
22	27	3.3	23	22
22	28	3.9	22	22
22	29	1.2	22	22
22	30	0.30	27	25
23	24	0.20	68	44
23	25	1.7	22	22
23	26	4.7	21	21
23	27	4.4	21	21
23	28	3.5	23	23
23	29	2.4	31	28
23	30	1.7	22	22
23	31	0.42	23	23
23	32	0.14	40	33
24	25	0.14	88	50
24	26	1.3	31	28
24	27	3.9	21	21
24	28	4.5	21	20
24	29	3.2	22	21
24	30	2.7	24	23
24	31	1.7	28	26
24	32	0.83	23	22
24	33	0.17	33	29
25	26	0.11	90	73
25	27	1.0	28	26
25	28	3.2	21	21
25	29	4.1	20	20
25	30	3.1	22	22
25	32	1.9	26	25
25	33	0.92	24	23
25	34	0.38	24	23
25	35	0.10	43	34
26	28	0.75	29	26
26	29	2.5	22	21
26	30	4.1	21	21
26	31	3.1	22	22
26	32	2.3	23	23
26	33	1.8	33	29
26	34	1.1	26	25
26	35	0.47	24	23
26	36	0.12	65	43
27	29	0.24	90	64
27	30	2.0	22	21
27	31	3.4	21	21
27	32	3.4	21	21
27	35	1.5	26	25
27	36	0.59	25	24
27	37	0.19	28	26
28	31	1.3	26	25
28	32	3.2	21	21
28	33	3.5	21	21
28	34	2.6	22	22
28	35	1.9	27	25
28	36	1.3	27	25
28	37	0.93	23	22
28	38	0.22	27	25
29	32	0.76	25	24
29	33	2.2	21	21
29	34	2.9	21	21
29	35	2.6	21	21
29	38	0.92	25	24
29	39	0.49	25	24
29	40	0.11	37	31
30	33	0.73	29	26
30	34	1.9	23	22
30	35	3.1	21	21
30	36	2.5	24	23
30	39	1.6	27	25
30	40	0.59	26	24
30	41	0.17	36	30
30	42	0.10	38	32
31	35	1.4	22	22
31	36	2.6	21	21
31	37	2.7	21	21
31	38	2.2	24	23
31	41	1.3	23	22
31	42	0.30	26	24
31	43	0.091	47	36

Z	N	σ/mb	$\Delta\sigma_{UP}$/%	$\Delta\sigma_{DOWN}$/%	Z	N	σ/mb	$\Delta\sigma_{UP}$/%	$\Delta\sigma_{DOWN}$/%
32	35	0.23	51	38	35	39	0.25	47	36
32	36	1.2	24	23	35	40	1.3	21	21
32	37	2.4	21	21	35	41	2.5	21	21
32	38	2.8	21	21	35	42	2.7	21	21
32	39	1.6	27	25	35	43	2.0	24	23
32	41	1.7	28	26	35	46	1.6	24	23
32	42	1.2	23	22	35	47	0.52	24	23
32	43	0.49	26	24	35	48	0.18	31	28
32	44	0.13	30	27	35	49	0.066	63	42
33	36	0.075	90	64	36	40	0.28	35	30
33	37	0.69	28	26	36	41	0.99	22	22
33	38	2.0	21	21	36	42	2.5	21	21
33	39	2.9	21	21	36	43	2.6	21	21
33	40	2.4	27	22	36	44	1.9	22	22
33	41	2.1	31	25	36	47	1.8	28	26
33	44	0.82	23	22	36	48	0.74	23	23
33	45	0.26	26	25	36	49	0.32	27	25
33	47	0.078	90	57	36	50	0.077	58	40
34	37	0.069	90	73	37	42	0.88	22	22
34	38	0.61	26	25	37	43	2.0	21	21
34	39	1.9	21	21	37	44	2.44	21	21
34	40	2.6	21	21	37	45	1.9	21	21
34	41	2.5	21	21	37	46	1.7	26	24
34	45	0.89	24	23	37	49	1.1	23	23
34	46	0.34	24	23	37	50	0.27	29	27
34	47	0.11	37	31	37	51	0.15	34	29

Figure B.2: Isotopic distributions for elements produced in the fragmentation of 1·A GeV ^{238}U on titanium. The error bars include both the statistical and systematic uncertainties.
The pictures were done using the data listed in tables B.4 and B.5.

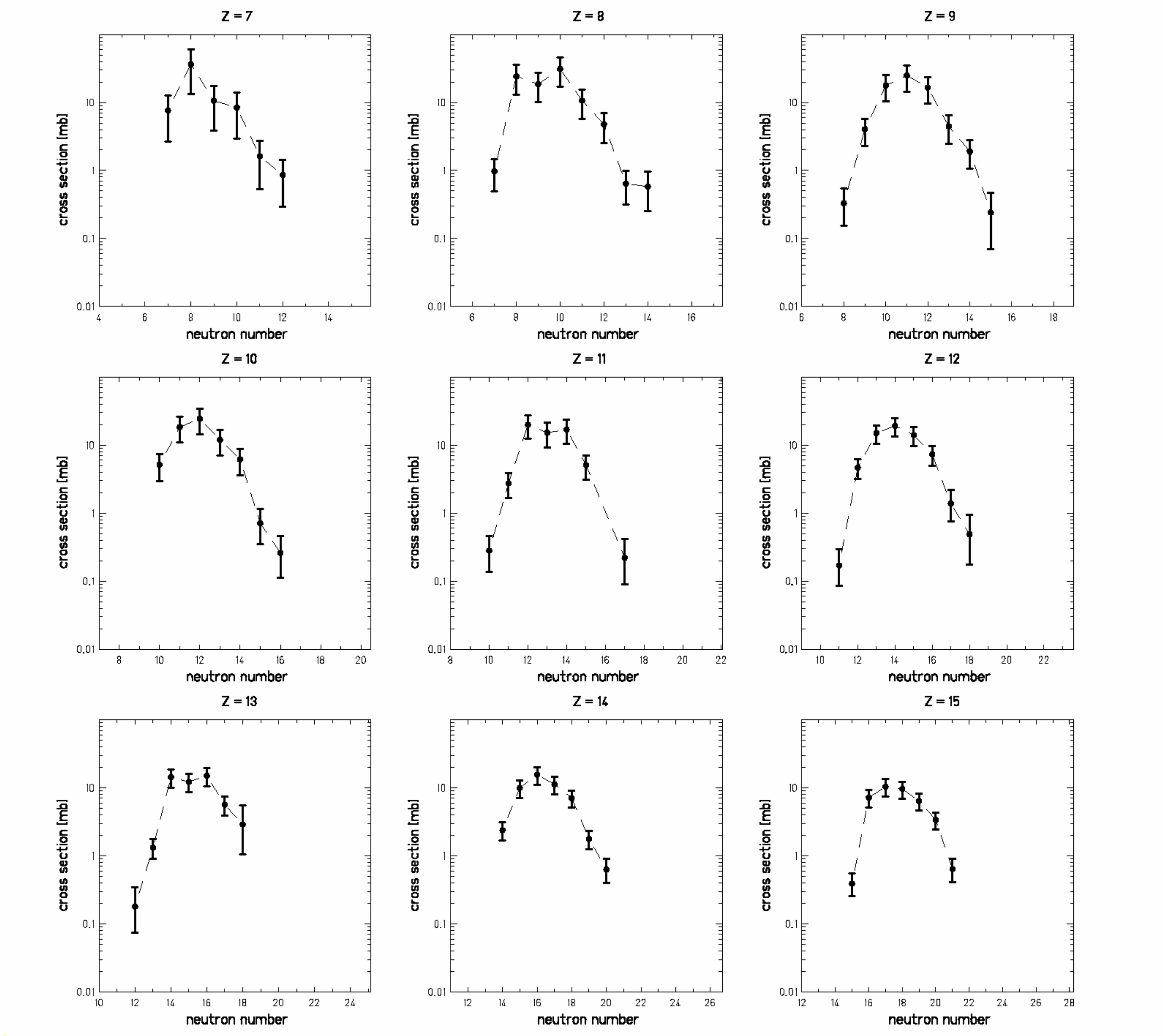

(continue on the next two pages)

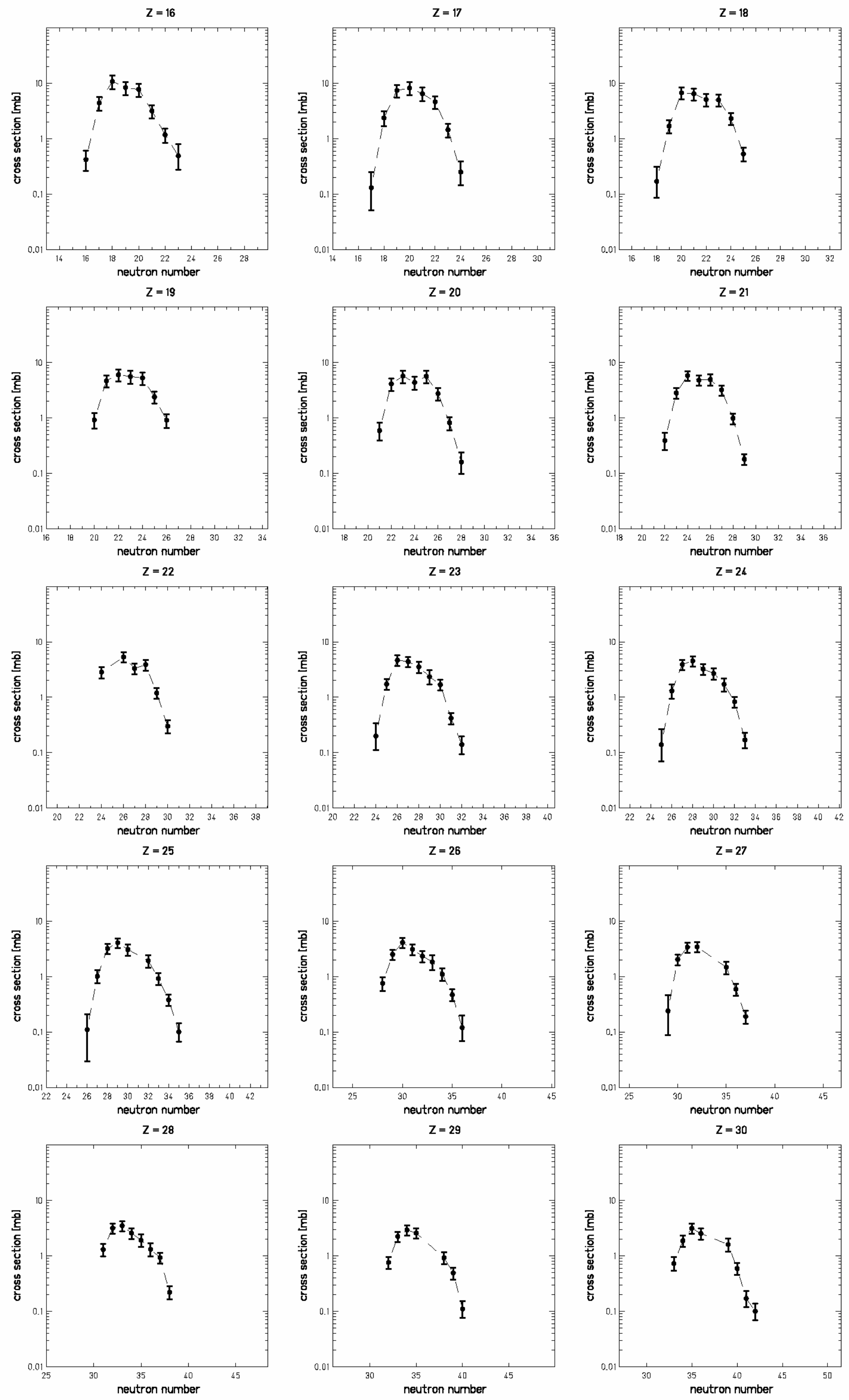
Z = 16
Z = 17
Z = 18
Z = 19
Z = 20
Z = 21
Z = 22
Z = 23
Z = 24
Z = 25
Z = 26
Z = 27
Z = 28
Z = 29
Z = 30
cross section [mb]
neutron number
0.01
0.1
1
10

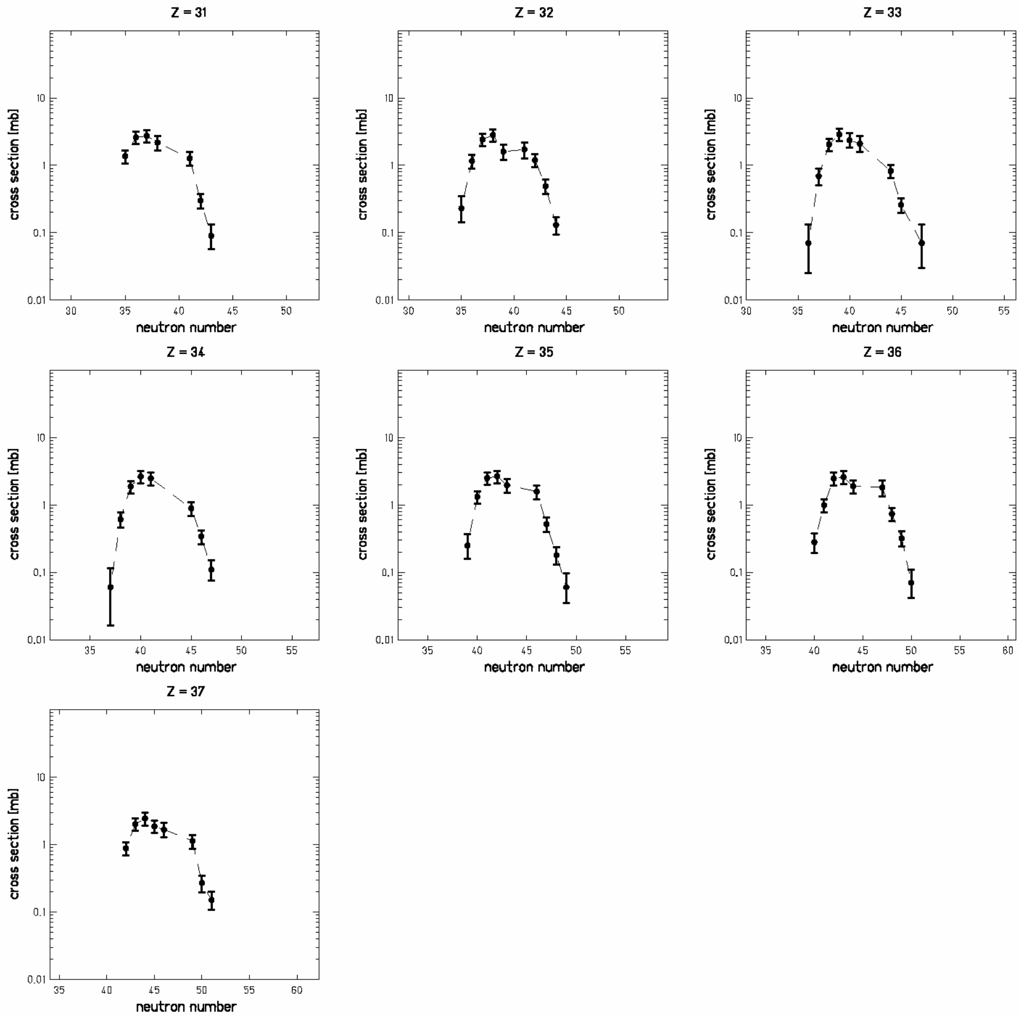
Z = 31
Z = 32
Z = 33
Z = 34
Z = 35
Z = 36
Z = 37
cross section [mb]
neutron number
0.01
0.1
1
10
30
35
40
45
50
55
60

Resumen

Motivación y objetivos

La ecuación de estado de la materia nuclear EOS (del inglés, “equation of state”) describe las propiedades macroscópicas fundamentales de dicha materia en función de las condiciones de presión, volumen o temperatura a los que está sometida. Además de aspectos básicos de la física nuclear, la ecuación de estado está relacionada con cuestiones fundamentales de astrofísica y cosmología como lo son la dinámica de las explosiones supernova, la estabilidad de las estrellas de neutrones frente a la presión gravitacional y la naturaleza de la materia durante los primeros instantes del Universo.

La investigación en física nuclear ha dedicado un esfuerzo muy importante durante las últimas décadas para formular correctamente la ecuación de estado. El objetivo final ha sido el describir correctamente propiedades fundamentales de la materia nuclear tales como su incompresibilidad o las transiciones entre diferentes estados de agregación, en particular la llamada transición líquido-gas. Las técnicas experimentales utilizadas en la investigación de la ecuación de estado se basan fundamentalmente en el estudio de colisiones entre iones pesados a energías relativistas. En estos experimentos se alcanzan condiciones óptimas para el desarrollo de estos estudios. Así, en la llamada zona del participante (en inglés, “fireball”), se pueden alcanzar valores extremos de densidad y presión, lo que permite estudiar la incompresibilidad nuclear. En los espectadores, los residuos de los núcleos blanco y proyectil adquieren energía interna o de excitación que puede dar lugar a la llamada transición de fase líquido-gas. En estos experimentos se obtiene información sobre la ecuación de estado utilizando dispositivos de gran aceptancia (ref. [ReiR97]) que permiten detectar las partículas ligeras emitidas en colisiones centrales o caracterizar el comportamiento estadístico de los espectadores. En ambos casos, el estudio de la incompresibilidad nuclear o la transición de fase líquido-gas, se utilizan multidetectores de partículas con una aceptancia 4π, o espectrómetros magnéticos de gran aceptancia. Aunque, estos dispositivos experimentales permiten registrar todas las partículas producidas en la colisión, proporcionando una imagen completa sobre la misma, su resolución no es suficiente para poder medir de forma precisa determinados observables que pueden proporcionar información sobre la ecuación de estado, como por ejemplo, las distribuciones de impulsión de los núcleos residuales de la colisión.

Teniendo en cuenta esta situación, el objetivo de este trabajo es el uso de un espectrómetro magnético de gran resolución (el “Fragment Separator” -FRS- del GSI) para estudiar determinadas propiedades de la materia nuclear. En particular se ha investigado la información que puede obtenerse a partir de la identificación completa (masa y carga), y la medida con precisión de las velocidades de los residuos del proyectil producidos en colisiones entre iones pesados relativistas. Estos dos tipos de medidas pueden realizarse gracias al gran poder de resolución del FRS.

Experimento

En este trabajo se han investigado dos reacciones: ^{238}U sobre ^{1}H y ^{238}U sobre Ti ambas a 1 *A* GeV. El experimento se realizó en cinemática inversa (el núcleo más pesado es el proyectil). La primera reacción se estudió utilizando un blanco de hidrógeno líquido situado en un contenedor de titanio. La segunda reacción se utilizó para corregir la contaminación debida al titanio.

El sincrotrón SIS18 del GSI, Darmstadt, se utilizó para producir un haz de ^{238}U acelerado a 1 A GeV, trabajando por tanto en el régimen relativista. Gracias a la energía cinética inicial, la mayor parte de los residuos de la reacción eran emitidos hacia delante pudiendo entrar en el separador de fragmentos, utilizado como espectrómetro de alta resolución. Estos residuos fueron completamente identificados en carga y masa a partir de la medida de su pérdida de energía en una cámara de ionización, y determinando el cociente masa sobre carga A/Z a partir de la medida de su rigidez magnética y tiempo de vuelo según la ecuación:

$$\frac{A}{Z} = \frac{e}{u}\frac{B\rho}{\beta\gamma c} \qquad (1)$$

donde *A* es el número másico, *Z* es el número atómico, *B* es el campo magnético dentro del imán, ρ es el radio de la trayectoria, *u* es la unidad atómica de masa, -*e* es la carga del electrón, $\gamma = (1 - \beta^2)^{-½}$ con $\beta = v/c$, donde *v* es la velocidad del ión y *c* es la velocidad de la luz. Este dispositivo experimental permite determinar la masa de los núcleos residuales con una resolución de $A/\Delta A \sim 400$. Por tanto, todos los núcleos producidos en la desintegración del uranio pudieron ser identificados.

En este trabajo nos centramos en la producción de núcleos residuales ligeros con número atómico comprendido entre 7 y 37. Considerando que la aceptancia del espectrómetro es 3% en momento y 15 mrad en ángulo, se tuvieron que combinar las medidas realizadas con diferentes valores de los campos magnéticos del espectrómetro con el fin de poder reconstruir completamente la distribución de momento de los núcleos residuales. Una vez que los núcleos residuales fueron identificados, la medida de su rigidez magnética, obtenida a partir de las posiciones horizontales de sus trayectorias en el plano imagen intermedio del separador, permitió determinar con gran precisión su momento longitudinal *p* y su velocidad *v* de acuerdo con la ecuación:

$$p = m_0 \cdot \gamma \cdot v = B \cdot \rho \cdot Z \cdot \mathrm{e} \qquad (2)$$

donde m_0 es la masa en reposo del residuo. Los campos magnéticos fueron medidos con sensores Hall con una precisión relativa de 10^{-4}. El radio de curvatura de las trayectorias ρ se dedujo a partir de las posiciones en el plano imagen intermedio con una precisión relativa estadística de $\pm 5\cdot10^{-4}$, basada en una resolución de la medida de la posición de ± 3 mm. Todo ello resulta en una precisión de $\pm 5\cdot10^{-4}$ en la determinación del momento individual de cada producto de la reacción.

Análisis de los datos

Un núcleo con una determinada masa y carga puede producirse por diferentes mecanismos de reacción, en particular por fragmentación o fisión. La información experimental que obtenemos con el FRS a parte de la identificación isotópica, es la componente longitudinal de la velocidad del residuo alrededor de cero grados. En la figura 1.c, representamos en un diagrama bidimensional, la correlación entre la velocidad y el número de neutrones de los isótopos de hierro producidos en la reacción ^{238}U sobre ^{1}H. La velocidad de los núcleos residuales de hierro producidos por fragmentación fluctua alrededor de la velocidad inicial del proyectil, por tanto su distribución está representada en el sistema de referencia del proyectil por una esfera difusa. Sin embargo, en el caso de residuos de hierro producidos por fisión, la fuerza Coulombiana que actua entre los dos residuos de fisión caracteriza la velocidad final de los mismos. La principal consecuencia es que los posibles valores de velocidad de los residuos de fisión cubren solo la capa externa de una esfera en el espacio de velocidades. Si tenemos en cuenta la limitación en aceptancia angular del FRS (15 mrad alrededor de 0º), representada por un cono en el sistema de referencia del laboratorio (ver figura 1.a), sólo se observa una parte de la producción real, la que entra dentro del cono. La proyección de la distribución de velocidad observada en el eje longitudinal, origina una distribución como la que se representa en la figura 1.b.

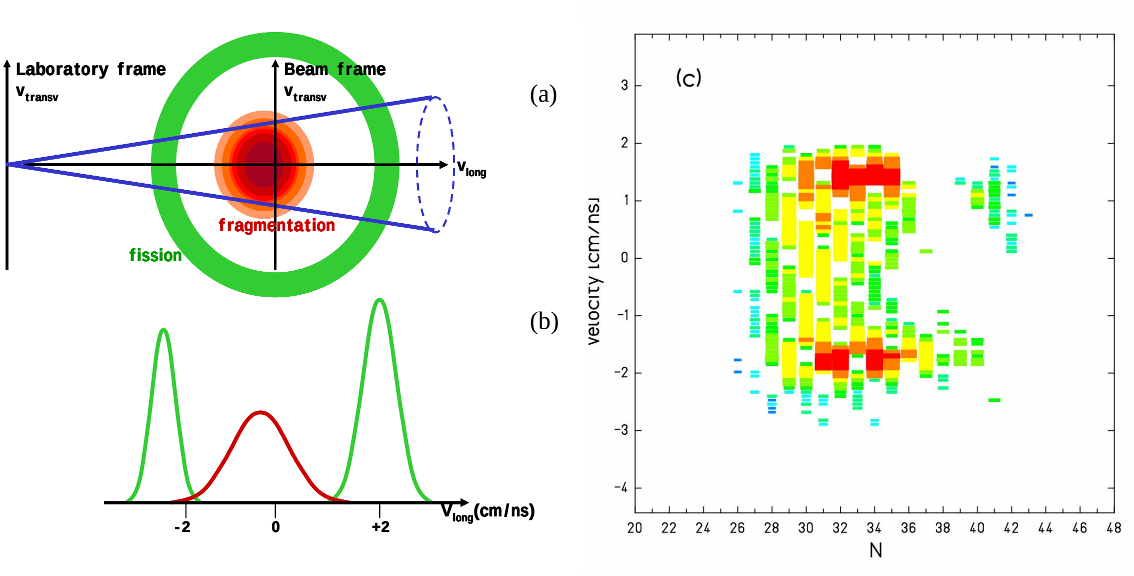

Figure 1: (a): representación esquemática de la distribución de velocidades transmitida por el FRS para un determinado núcleo producido por fisión (capa externa) o por fragmentación (esfera completa). Las velocidades están representadas en el sistema de referencia del proyectil (v_{238U} = 0 cm/ns). El cono representa la acceptancia angular del FRS. (b): proyección de las velocidades en el eje longitudinal. (c): diagrama bidimensional de la correlación existente entre la velocidad y el número de neutrones medido para los residuos de hierro producidos en la reacción ^{238}U sobre ^{1}H. La figura incluye tanto los fragmentos producidos por reacción con el hidrógeno como con el titanio de las ventanas del blanco.

Los isótopos más ricos en neutrones aparecen en dos rangos de velocidad relativamente estrechos que corresponden a la emisión hacia delante o hacia detrás de los fragmentos de fisión. Sin embargo, los isótopos más deficitarios en neutrones, producidos por fragmentación, aparecen distribuidos alrededor de la velocidad del proyectil. Esta observación permite separar la producción de núcleos residuales por fragmentación o fisión a partir de la correlación existente entre la velocidad longitudinal y el número de neutrones de los núcleos identificados por el FRS.

En el caso particular de la multifragmentación, las propiedades cinemáticas de los residuos producidos serán muy similares a las de la fragmentación. De forma análoga, todo proceso binario cuya cinemática esté caracterizada por la repulsión Coulombiana entre dos residuos finales, como es el caso de la evaporación de partículas cargadas o reacciones binarias de ruptura, las distribuciones de velocidad observadas serán similares a las de la fisión.

El análisis de los datos se basa en la reconstrucción de la distribución de velocidad de cada isótopo producido en la reacción. Como durante el experimento no pudo medirse la producción para determinados valores de los campos magnéticos de los dipolos del FRS, las distribuciones de velocidad reconstruídas no están completas. Por esta razón se desarrolló un método de ajuste de las distribuciones medidas utilizando tres funciones Gaussianas para cada uno de los isótopos. El resultado de estos ajustes proporcionó las tasas de producción así como el valor medio y la desviación típica de la distribución longitudinal de velocidad para cada una de las tres componentes (fragmentación, fisión hacia delante y fisión hacia detrás).

Las tasas de producción de cada uno de los isótopos producidos en la reacción ^{238}U+^{1}H se obtuvo sustrayendo las tasas de producción con el blanco de titanio. Tal y como se describe en la referencia [Ben02], la fracción de residuos transmitidos puede ser evaluada asumiendo una distribución isotópica de los mismos, pudiendo así determinar las producciones reales. A partir de estas producciones reales y normalizando a la intensidad de proyectiles y número de átomos del blanco se pudo determinar las secciones eficaces de producción de cada uno de los isótopos resultantes de la reacción para cada uno de los mecanismos de reacción (fisión y fragmentación) y sistemas estudiados (^{238}U+^{1}H y ^{238}U+Ti).

Resultados

Procesos binarios en colisiones inducidas por ^{238}U sobre hidrógeno a 1 *A* GeV

Al sustraer la producción correspondiente a las ventanas de titanio del blanco, sólo observamos las dos alas externas del la figura 1.c. Estas dos alas corresponden a las dos componentes externas que se observan en el figura 1.b, indicando que todos los productos ligeros ($7<Z<37$) medidos en la reacción ^{238}U+^{1}H son producidos en un mecanismo de reacción con las mismas propiedades cinemáticas que la fisión. Hasta ahora se han propuesto dos mecanismos compatibles con estas propiedades cinemáticas, la fisión [Mor88] o la ruptura binaria [Bar86].

Las distribuciones de carga y masa de los fragmentos observados en este trabajo son consistentes con las predicciones del modelo de los estados transitorios para la fisión (figura 2). En este modelo, la tasa de desintegración por fisión depende de las propiedades del núcleo fisionante en el estado transitorio, es decir, en el espacio de fases disponible en la configuración del punto de silla. En el modelo estadístico de la fisión [Mor75] la tasa de producción de un determinado fragmento de fisión, para una determinada energía de excitación, se calcula a partir del peso estadístico de estados transitorios sobre la barrera condicional del potencial. A su vez, este peso estadístico está relacionado con la densidad de estados nucleares. Si consideramos el núcleo como un gas de Fermi, la distribución de masa de los residuos producidos en la fisión de un núcleo pesado con un valor elevado de energía de excitación tiene la forma de una W, tal y como puede verse en la figura 2, cuya máximo corresponde a la partición simétrica del núcleo. En este modelo, la desintegración binaria de un núcleo termalizado incluye la fisión y la evaporación con una transición natural entre ambos mecanismos que de una forma general podrían denominarse fisión [Sto88]. Las velocidades de estos residuos binarios también son compatibles con un proceso de fisión/evaporación. Si consideramos la repulsión Coulombiana entre los dos fragmentos e imponiendo la conservación del momento, podemos determinar las velocidades de los fragmentos producidos en este proceso y compararlas con las velocidades medidas en este trabajo. El resultado de esta comparación muestra un buen acuerdo si se considera la variación del "cuello" del sistema fisionante.

Por el contrario, no se observan indicaciones de un posible canal de ruptura binaria. Por tanto se puede concluir que este experimento ha permitido establecer por la primera vez que la fisión asimétrica en la reacción ^{238}U + ^{1}H alcanza núcleos bastante ligeros por debajo de Z=7.

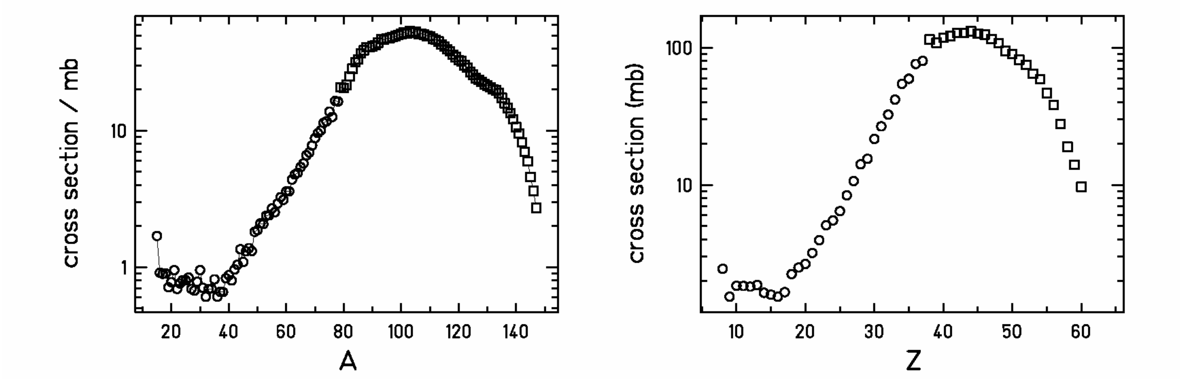

Figure 2: Distribuciones de masa y carga de los residuos producidos en procesos binarios medidos en la reacción ^{238}U+p a 1 A GeV. Puntos: este trabajo; cuadrados: ref. [Ber03].

Exceso medio de neutrones en los residuos de fragmentación producidos en la reacción ^{238}U con titanio a 1 *A* GeV

En la figura 3 representamos los valores medios del cociente *N/Z* de los residuos de fragmentación en función de su número atómico, *Z*. Los resultados experimentales se comparan con dos líneas de referencia, la posición del valle de estabilidad y las predicciones de EPAX [Süm00], un modelo semiempírico que describe la distribución isotópica de residuos de fragmentación en base a la idea de que los residuos de fragmentación son producidos como consecuencia de una larga cadena de evaporación. Para nuestra sorpresa, los residuos de fragmentación presentan valores de *N/Z* bastante grandes que incluso cruzan el valle de estabilidad por debajo de la carga 28. Aparentemente, los residuos de evaporación más ligeros son el resultado de una cadena de evaporación más corta que les impide evaporar el número suficiente de neutrones para alcanzar el valle de estabilidad. Por lo tanto *reacciones más violentas parecen introducir* *menos energía de excitación.* Este resultado aparentemente contradictorio puede explicarse suponiendo que estos residuos se han producido como consecuencia de un proceso de ruptura simultanea del núcleo. Este proceso tiene dos características esenciales. Primero, la mayor parte de la energía inducida en la colisión es consumida en el proceso de ruptura mientras que la energía restante es distribuida entre los fragmentos producidos. Segundo, se espera que el valor medio del cociente *N/Z* de estos fragmentos sea muy similar al del núcleo inicial que se desexcita. De hecho, los datos pueden explicarse suponiendo que la llamada temperatura de "freeze-out", o temperatura de los fragmentos producidos en la ruptura a partir de la cual se inicia el proceso de evaporación, tenga un valor bien definido, representando una temperatura límite por encima de la cual un núcleo excitado completamente equilibrado no puede existir.

Esta idea es la base del llamado *termómetro del isospín* [Sch93], un método específico para determinar la temperatura de un sistema nuclear a partir de la distribución isotópica de los residuos finales. El método consiste en utilizar un código de evaporación, cuyos ingredientes del modelo estadístico están bien establecidos, para deducir la temperatura al inicio del proceso de evaporación. Para ello hemos utilizado el modelo estadístico de multifragmentación SMM [Bot95]. Este modelo produce una muestra microcanónica de todos los posibles canales de ruptura formados por nucleones y fragmentos de diferente masa. Además, se supone que un núcleo excitado en equilibrio termodinámico definido por un determinado valor de la temperatura *T*, se expande hasta un cierto volumen y entonces se fragmenta en un conjunto de nucleones y fragmentos excitados. Después de la ruptura del sistema, los fragmentos resultantes se propagan independientemente según el campo Coulombiano que actua entre ellos, al mismo tiempo que experimentan un proceso de desexcitación que puede describirse como una evaporación estadística, fisión o mediante una ruptura de Fermi

En la figura 3 representamos el valor medio del cociente *N/Z* de los núcleos residuales obtenidos con este modelos de multifragmentación estadística considerando diferentes valores de la temperatura de "freeze-out", comparados con los valores experimentales.

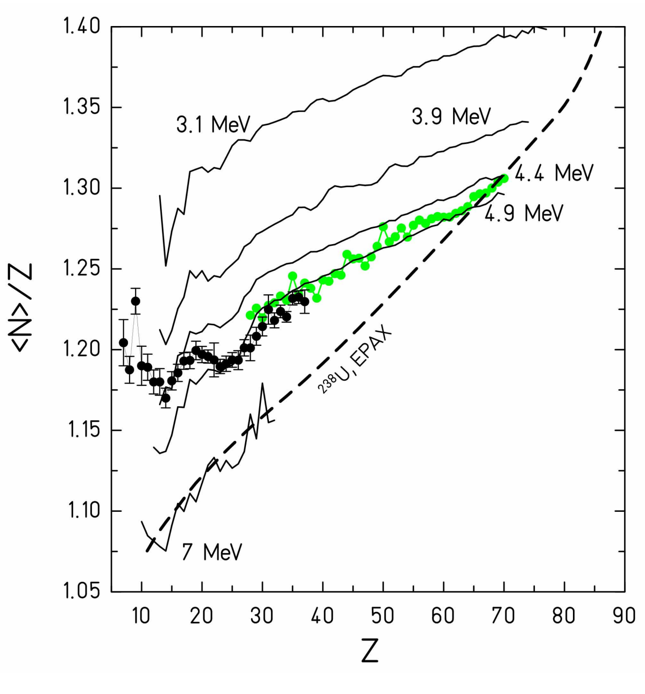

Figura 3: Valor medio experimental del cociente N/Z de los núcleos residuales producidos en reacciones de fragmentación ^{238}U + ^{208}Pb *(puntos grises, ref. [Enq99]) y* ^{238}U *+ Ti (puntos negros [este trabajo]) en función de su número atómico, comparados con la posición de valle de estabilidad y las predicciones del código EPAX. Los residuos de fisión no se han incluido en esta figura. Cálculos realizados con el código SMM con diferentes valores de la temperatura de "freeze-out" muestran que el valor medio del cociente N/Z puede describirse cuando se asume una temperatura de "freeze-out" de 5 MeV.*

Podemos observar que cuando aumenta la temperatura, el valor medio del exceso de neutrones se aproxima al pasillo de evaporación representado por el cálculo de EPAX. Además, obtenemos un acuerdo remarcable con los datos cuando la temperatura de “freeze-out” se aproxima a 5 MeV. Este valor coincide con el obtenido en experimentos de gran aceptancia. El proceso fundamental que está detrás de esta temperatura límite es la transición de fase líquido-gas de la materia nuclear.

Por tanto hemos demostrado que el uso de un espectrómetro magnético de gran resolución nos ha proporcionado una nueva evidencia experimental de las inestabilidades térmicas de los núcleos.

Aceleración de los residuos de fragmentación producidos en la reacción ^{238}U sobre titanio a 1 *A* GeV

En la figura 4 se muestra el valor medio de las distribuciones de velocidad de los fragmentos residuales producidos en la reacción ^{238}U + Ti en el sistema de referencia del proyectil ($v_{beam} = 0$). Por razones técnicas se realizaron dos tipos de análisis. Para $Z>22$ los resultados corresponden a los valores medios de la distribución central que aparece en los espectros de velocidades de los residuos. Para $Z<22$ los puntos abiertos representan el valor mínimo posible de la velocidad media, mientras que los puntos enteros indican el valor medio de la distribución central del espectro de velocidad. En todos los casos, los datos fueron corregidos de las limitaciones angulares del FRS.

En la figura se observa que la velocidad media de los residuos empieza disminuyendo con la pérdida de masa tal y como predicen las sistemáticas [Mor89], después satura y finalmente aumenta. Incluso para los fragmentos más ligeros, su velocidad media llega a ser mayor que la del proyectil. Esta observación parece contradecir el resultado esperado según el cual, los residuos más ligeros deberían experimentar una mayor pérdida de velocidad ya que éstos se producen en reacciones más violentas en las que la fricción es mayor [Abu76]. Como veremos a continuación esta nueva observación va a proporcionarnos información sobre las propiedades del campo medio nuclear y por tanto sobre la ecuación de estado.

Durante las últimas décadas se han dedicado muchos esfuerzos a investigar tanto la ecuación de estado como las propiedades de la interacción nucleón-nucleón en el medio nuclear. Para ello se han utilizado detectores de gran aceptancia para caracterizar las partículas ligeras producidas en colisiones centrales entre iones pesados relativistas. Los observables que más se han utilizado en estos experimentos son el llamado flujo colectivo de partículas y la producción de kaones provenientes de la región de interacción o “fireball”. Sin embargo, la interpretación de estos observables utilizando códigos de transporte todavía no ha permitido obtener conclusiones definitivas sobre la curvatura de la ecuación de estado. Ello se debe a que tanto la incompresibilidad de la materia nuclear como la dependencia en momento de la interacción nuclear influencian estos observables. Por esta razón, actualmente se requieren observables sensibles únicamente a la compresibilidad de la materia nuclear o la dependencia en momento de la interacción nuclear. En este sentido, recientemente se han definido nuevos observables relacionados con las propiedades cinemáticas de los residuos del espectador producidos en estas colisiones. Según estos cálculos [Shi00], las distribuciones de momento longitudinal y transversal del espectador están influenciadas por la explosión del participante que tiene lugar tras la fase de compresión, y por tanto proporcionan información sobre la naturaleza de la interacción nuclear. En concreto, para determinados sistemas, la expansión del participante induciría una aceleración de los residuos del espectador. Esta aceleración es un observable que es sensible principalmente a la dependencia en momento de la interacción nuclear. Sin embargo el efecto predicho es bastante pequeño y por tanto solo podría identificarse con medidas de mucha precisión de las distribuciones de impulsión de los espectadores.

De acuerdo con esta discusión, hemos interpretado la aceleración de los residuos del proyectil observada en nuestro experimento como la respuesta del espectador a la expansión del participante predicha por Shi, Danielewicz y Lacey [Shi00]. Según este trabajo, la medida de las propiedades cinemáticas de los espectadores constituye una nueva herramienta para estudiar la interacción nucleón-nucleón en el medio nuclear. En este sentido, nuestras medidas experimentales validan la viabilidad de este tipo de experimentos. Tal y como se indica en la referencia [Shi00], este nuevo observable proporcionará información sobre la ecuación de estado de la materia nuclear. En particular, la aceleración observada para parámetros de impacto pequeños es sensible de forma selectiva a la dependencia en momento de la interacción nuclear [Shi00].

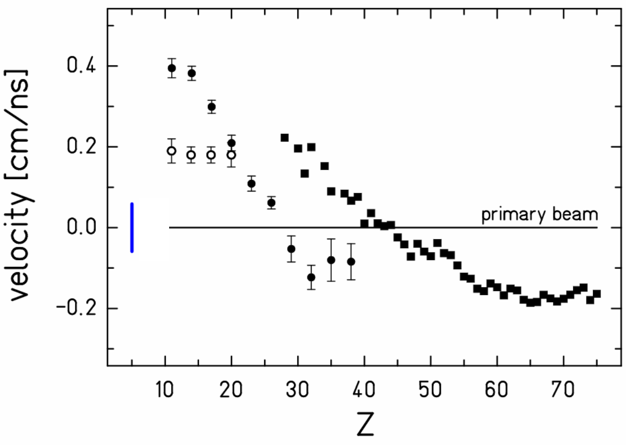

Figura 4: Valor medio de las distribuciones de velocidad de los residuos producidos en la fragmentación de ^{238}U sobre plomo (cuadrados) [Enq99] y sobre titanio (puntos) [este trabajo].

Estructura par-impar en las tasas de producción de residuos de fragmentación en la reacción ^{238}U sobre titanio a 1 A GeV

Un análisis detallado de las secciones eficaces de fragmentación revela la existencia de efectos de estructura interesantes. En la figura 5 se muestran las secciones eficaces de los residuos de fragmentación observados, agrupadas según el valor de N-Z de cada núcleo. Como puede verse, los datos muestran una estructura clara. Todos los núcleos con número másico par presentan un claro efecto par-impar que es particularmente pronunciado para los núcleos con N=Z. Por el contrario, los núcleos con número másico impar, presentan un efecto par-impar invertido que se acentúa a medida que el valor de N-Z aumenta. En el caso de núcleos con N-Z=1, este efecto par-impar invertido desaparece alrededor de Z=16, para pasar a observarse una mayor producción de isótopos pares a partir de este valor.

Estructuras similares ya han sido observadas en las distribuciones de carga de núcleos residuales producidos en reacciones de fragmentación, sin embargo, ésta es la primera vez en la que este efecto es observado en toda su complejidad. En principio se espera que éstas sean reacciones muy violentas dando lugar a núcleos altamente excitados que se enfrían mediante un proceso de evaporación de nucleones. De acuerdo con este escenario, se cree que los efectos observados son una consecuencia de la influencia de la estructura nuclear, en particular del apareamiento entre nucleones, en las propiedades de los niveles excitados y en las masas de los núcleos involucrados en las últimas etapas de la cadena de desexcitación. Para verificar esta hipótesis se ha utilizado un código estadístico de evaporación en el que los efectos de apareamiento entre nucleones se introducen de forma coherente tanto en la descripción de las masas como de las densidades de niveles. Los resultados obtenidos con este código han permitido describir todas las estructuras observadas en los datos, excepto para la cadena de núcleos con *N=Z*, cuya peculiaridad podría estar relacionada con otros fenómenos como podría ser la clusterización alpha. La desaparición de estas estructuras con la masa de los núcleos residuales también es descrita por el código como una consecuencia de la competición entre los canales de emisión de partículas y de gammas.

Hasta ahora, el efecto par-impar en las tasas de producción de núcleos residuales en reacciones nucleares a baja energía se había explicado mediante la teoría de la superfluídez nuclear. Según esta teoría, se espera que los núcleos abandonen la fase superfluída para entrar en la llamada fase líquida a partir de una energía de excitación de 10 MeV. Por encima de esta energía cualquier efecto de apareamiento debería desaparecer. En nuestro caso está claro que tales efectos de estructura no deberían manifestarse en los residuos del proyectil altamente excitados que producimos. Sin embargo, los cálculos con un modelo estadístico nos indican que estos efectos de estructura pueden ser restaurados durante las últimas etapas de la cadena de desexcitación cuando los núcleos involucrados se aproximan a energías de excitación en torno a 10 MeV. Por tanto interpretamos nuestros resultados como una manifestación de la transición de fase superfluidez-líquido de la materia nuclear.

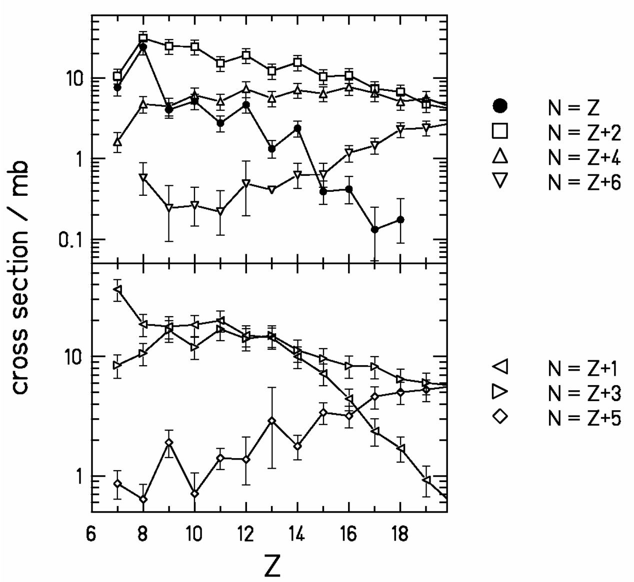

Figura 5: Secciones eficaces de producción de residuos del proyectil en la reacción ^{238}*U + Ti a 1 A GeV. Los datos se presentan en cadenas en función del valor del parámetro N-Z. La sección eficaz para el* ^{32}*Al (Z=13, N=Z+6) es un valor extrapolado. La cadena N=Z muestra un efecto par-impar más marcado, mientras que la cadena N-Z=5 muestra el efecto par-impar inverso más fuerte.*

Conclusiones

En este trabajo hemos estudiado y demostrado el papel que las medidas de gran precisión con espectrómetros magnéticos juegan en la caracterización de las propiedades de la materia nuclear. El uso de dos reacciones, ^{238}U sobre ^{1}H y ^{238}U sobre Ti ambas 1 *A* GeV, ha permitido obtener cuatro resultados muy interesantes que proporcionan información complementaria a la obtenida con dispositivos experimentales de gran aceptancia. De esta manera confirmamos el enorme potencial que este tipo de medidas de gran resolución puede tener en el futuro.

Bibliographie

[Abu76] A. Abul-Magd, J. Hüfner, B. Schürmann, Phys. Lett. **B 60** (1976) 327.

[Ahl80] S. P. Ahlen, Rev. Mod. Phys. **52** (1980) 121

[ALA] http://www-kp3.gsi.de/www/kp3/s114_data.html

[Alb85] S. Albergo et al., Nuovo Cimento Soc. Ital. Fis. **89A** (1985) 1

[Ale63] J. M. Alexander, C. Baltzinger and M. F. Gazdik, Phys Rev. **129** (1963) 1826.

[AMA] http://www-wnt.gsi.de/kschmidt/amadeus.htm

[Ama67] I. Amarel et al., Phys. Lett. **B 24** (1967) 402

[Ami75] S. Amiel, H. Feldstein, Phys. Rev. **C 11** (1975) 845

[And86] L. N. Andronenko et al., Phys. Lett. **B 174** (1986) 18

[And87] L. N. Andronenko et al., Sov. J. Part. Nucl. **18** (1987) 289

[Arm70] P. Armbruster, Nucl. PHys. **A 140** (1970) 385

[Arm96] P. Armbruster et al., Z. Phys. **A 355** (1996) 191

[Arm04] P. Armbruster et al., Phys. Rev. Lett. 93 (2004) 212701

[Atc80] F. Atchinson, “ Meeting on Targets for neutron beam spallation sources”, ed. G. Bauer, KFA Jülich Germany, Jül-conf-34 (1980)

[Aud95] G. Audi, A. H. Wapstra, Nucl. Phys. **A 595** (1995) 409.

[Avd01] Avdeyev et al., Phys. Lett. **B 503** (2001) 256

[Avi78] Y. Avishai, Z. Physik **A 286** (1978) 285

[Axe62] P. Axel, Phys. Rev. **126** (1962) 271

[Bac93] Ch. O. Bacri et al., Nucl. Phys. **A 555** (1993) 477.

[Bao97] Bao-An Li, C. M. Ko, Nucl. Phys. **A 618** (1997) 498

[Bal03] M. Balasubramaniam, R. Kumar, R.K. Gupta, C. Beck, W. Scheid, J. Phys. G: Nucl. Part. Phys. **29** (2003) 2703

[Bar86] H. W. Barz et all., Nucl. Phys. **A 460** (1986) 714.

[Bas79] R. Bass, Proceeding of the Symposium on Deep-Inelastic and Fusion Reactions with Heavy Ions, Berlin 1979, Springer Verlag, Berlin

[Beg71] K. Beg and T. Porile, Phys. Rev. **C 3** (1971) 1631.

[Bel80] B. N. Belyaevet al., Nucl. Phys. **A 348** (1980) 479

[Ben89] C. J. Benesh, B. C. Cook, and J. P. Vary, Phys. Rev **C 40** (1989) 1198

[Ben98] J. Benlliure et al., Nucl. Phys. **A 628** (1998) 458

[Ben01] J. Benlliure et al., Nucl. Phys. **A 683** (2001) 513

[Ben02] J. Benlliure, J. Pereire-Conca, K.-H. Schmidt., Nuc. Inst. Meth. **A 478** (2002) 493.

[Ber03] M. Bernas et al., Nucl. Phys. **A 725** (2003) 213-253

[Ber04] M. Bernas, IPN Orsay, France. Work in progress.

[Ber93] M. Bernas et al., Phys. Rev. Lett. 67 (1993) 3661

[Bin87] W. R. Binns et al., Phys. Rev. **C 36** (1987) 1870.

[Bla90] B. Blank et al., Nucl. Instr. Meth. **A 286** (1990) 160.

[BNL] http://www.nndc.bnl.gov/nndc/nudat/levform.html

[Böc97] C. Böckstiegel et al., Phys. Lett. **B 398** (1997) 259.
[Böc98] C. Böckstiegel, Diploma Thesis, Institut für Kernphysik, TH Darmstadt (1998).
[Boh39] N. Bohr, J. A. Wheeler, Phys. Rev. **56** (1939) 426.
[Boh48] N. Bohr, The penetration of atomic particles through matter, Einar Munnskgaard, 6 Noregade, Köbenhavn, Denmark, 1948.
[Bot01] A. S. Botvina, I. N. Mishustin, Phys. Rev. C 63 (2001) 061601.
[Bot85] A. S. Botvina, A. S. Iljinov, I. N. Mishustin, Sov. J. Nucl. Phys. **42** (1985) 712.
[Bot87] A. S. Botvina et al., Nucl. Phys. **A 475** (1987) 633.
[Bot90] A. S. Botvina, A. S. Iljinov, I. N. Mishustin, Nucl. Phys. **A 507** (1990) 649.
[Bot95] A. S. Botvina et al., Nucl. Phys. **A 584** (1995) 737.
[Bou02] A. Boudard, J. Cugnon, S. Leray, C. Volant, Phys. Rev. **C 66** (2002) 044615
[Bus57] U. L. Businaro, S. Gallone, Nuovo Cimento **5** (1957) 315-17
[Cam81] P X. Campi, J. Huefner, Phys. Rev. **C 24** (1981) 2199.
[Car58] A.A. Caretto, J. Hudis and G. Friedlander, Phys. Rev. **110** (1958) 1130.
[Cas03] E. Casarejos et al., Phys. At. Nuclei **66** (2003) 1413-1420
[Cav98] Sl. Cavallaro et al., Phys. Rev. **C 57** (1998) 731.
[Cha88] R. J. Charity et al., Nuc. Phys. **A 483** (1988) 371.
[Cha98] R. J. Charity, Phys. Rev. **C 58** (1998) 1073.
[Cha02] R. J. Charity, in "Isospin Physics in Heavy-Ion Collisions at Intermediate Energies", Bao-An Li, W. U. Schröder eds., Nova Science Publishers, Huntington, 2002, pp. 341
[Che96] P. Chesny et al., GSI annual report 97-1, 1996, page 190.
[Cre68] V. P. Crespo, J. B. Cumming and A. M. Poskanzer, Phys. Rev. **174** (1968) 1455.
[Cre70] V. P. Crespo, J. B. Cumming and J. A. M. Alexander, Phys. Rev. **C 2** (1970) 1777.
[Dan00] P. Danielewicz, Nucl. Phys. **A 673** (2000) 375
[Dan02] P. Danielewicz, R. Lacey, W. G. Lynch, Science **22** (2002) 1592
[DATA] http://www-w2k.gsi.de/kschmidt/data.htm
[DeJ98] M. de Jong et al., Nucl. Phys. **A 628** (1998) 479
[Dob01] J. Dobaczewski et al., Phys. Rev. **C 63** (2001) 024308
[Don98] C. Donzaud et al., Eur. Phys. Jour. **A 1** (1998) 407
[Dug02] T. Duguet et al., Phys. Rev. **C 65**, 014310 (2002)
[Dug02] T. Duguet et al., Phys. Rev. **C 65**, 014311 (2002)
[Duf82] J.-P. Dufour et al., Nucl. Phys. **A 387** (1982) 157c.
[Duf86] J.-P. Dufour et al., Nucl. Instr. Methods **A 248** (1986) 267
[Dur98] D. Durand, Nucl. Phys. **A 630** (1998) 52c
[Eng74] G. English, N. T. Porile, E. P. Steiberg, Phys. Rev. **C 10** (1974) 2268
[Eng98] C.O. Engelmann, PhD Thesis, Universität Tübingen, 1998, Report GSI DISS-98-15.
[Enq99] T. Enqvist et al., Nucl. Phys. **A 658** (1999) 47.
[Enq01] T. Enqvist et al., Nucl. Phys. **A 686** (2001) 481.
[Enq02] T. Enqvist et al., Nucl. Phys. **A 703** (2002) 435.
[Eri60] T. Ericson, Advances in Physics **IX** (1960) 425.
[Fon65] P. Fong, Phys. Rev. **102** (1965) 434
[FRS] http://www-wnt.gsi.de/frs/index.asp
[Gai91] J.-J. Gaimard, K.-H. Schmidt, Nucl. Phys. **A 531** (1991) 709.

[Gei92] H. Geissel et al., Nucl. Instr. Meth. **B 70** (1992) 286.

[Geo01] J. S. George et al., Proceedings of the 27th International Cosmic Ray Conference, Hamburg, Germany, Vol. 5 (2001) 1956-1959.

[Gol74] A.S. Goldhaber, Phys. Lett. **B 53** (1974) 306.

[Gön86] F. J. Gönnenwein, Radiation Effects **94** (1986) 205-226.

[Gön91] F. Gönnenwein, "Mass, Charge and Kinetic Energy of Fission Fragments" in "The Nuclear Fission Process", CRC Press, London, 1991, C. Wagemans ed., pp 409.

[Gro62] J. R. Grover, Phys. Rev. **126** (1962) 1540

[GSI01] "An International Accelerator Facility for Beams of Ions and Antiprotons", Conceptual Design Report, Pub. GSI, November 2001.

[Hof94] P. Hofmann et al., Phys. Rev. **C 49** (1994) 2555

[Hor02] H. Horiuchi, Eur. Phys. J. **A 13** (2002) 39.

[Hub91] J. Hubele et al., Z. Phys. **A 340** (1991) 263-270

[Hüf75] J. Hüfner, K. Schäfer, B. Schürmann, Phys. Rev. **C 12** (1975) 1888

[Hüf85] J. Hüfner, Heavy fragments produced in proton-nucleus and nucleus-nucleus collisions at relativistic energies, Phys. Rep. **125** (1985) 129-185

[Hui72] J. R. Huizenga, L. G. Moretto, Ann. Rev. Nucl. Sci **22** (1972) 427

[Ign73] A. V. Ignatyuk, Yu. V. Sokolov, Yad. Fiz. **17** (1973) 723-733 (Sov. J. Nucl. Phys. 17 (1973) 376-380

[Ign74] A. V. Ignatyuk, Yu. V. Sokolov, Yad. Fiz. **19** (1974) 1229-38 (Sov. J. Nucl. Phys. 19 (1974) 628-32)

[Ign79] A.V. Ignatyuk *et al.*, Sov. J. Nucl. Phys. **29** (1979) 450

[Ign82] A. V. Ignatyuk, K. K. Istekov, G. N. Smirenkin, Sov. J. Nuc. Phys. **36** (1982) 32

[Ign95] A.V. Ignatyuk *et al.*, Nucl. Phys. **A 593** (1995) 519

[Ign00] A.V. Ignatyuk, in: G.C. Bonsignori, M. Bruno, A. Ventura, D. Vretenar (Eds.), Proceedings on of the Conference Bologna 2000: Structure of the Nucleus at the Dawn of the Century, Bologna, Italy 29 May–3 June 2000, World Scientific, Singapore, 2001.

[Itk98] M. G. Itkis, A. Ya. Rusanov, Phys. Part. Nucl. 29 (1998) 160

[Jah37] H. A. Jahn, E. Teller, Proc. R. Soc. London, Ser. **A 161** (1937) 220.

[Jen84] A. S. Jensen, P. G. Hansen, B. Jonson, Nucl. Phys. **A 431** (1984) 393

[Jun96] A. Junghans et al., Nucl. Instr. Meth. . **A 370** (1996) 312.

[Jun98] A. R. Junghans et al., Nucl. Phys. **A 629** (1998) 635.

[Jur02] B. Jurado, K.-H. Schmidt, K.-H. Behr, Nucl. Instr. Meth. **A 483** (2002) 603.

[Kau80] S. B. Kaufman, E. P. Steinberg, Phys. Rev. **C 22** (1980) 167

[Kat68] S. Katcoff, H. R. Fickel, A. Wyttenbach, Phys. Rev. **166** (1968) 1147

[Kel03] Implementation in ABRABLA done by Aleksandra Kelić, GSI, November 2003.

[Klu86] H.-J. Kluge, ISOLDE user's guide, CERN 86-05 (1986)

[Kno96] C. N. Knott et al., Phys. Rev. **C 53** (1996) 347

[Kon96] J. Konopka and H. Stöcker, "Multifragment Break-up of Highly Excited Nuclear Clusters", Chap.3 of "Nuclear Decay Modes", D.N. Poenaru, Institut of Physics Publishing - Bristol and Philadelphia (1996)

[Kös01] U. Köster for the ISOLDE collaboration, Radiochim. Acta **89** (2001) 749

[Kot95] A. A. Kotov et all., Nucl. Phys. **A 583** (1995) 575.

[Lan80] W. Lang et al., Nucl. Phys. **A 345** (1980) 34

[Lin93] V. Lindenstruth, “Dynamik der Multifragmentation”, PhD Thesis, Universität Frankfurt, 1993, Report GSI-93-18.

[Lop01] O. Lopez, Nuc. Phys. **A 685** (2001) 246

[Lov88] W. Loveland et al., Phys. Rev. **C 37** (1988) 1311.

[Mar98] N. Marie et al., Phys. Rev. **C 58** (1998) 256.

[Mar69] P. Marmier, E. Sheldon, “Physics of Nuclei and Particles”, Academic Press, 1969, page 36.

[Mic97] R. Michel, P. Nagel, International Codes and Model Intercomparison for Intermediate Energy Activation Yields, NSC/DOC(97)-1, NEA/P&T No 14 (1997).

[Mol88] J. J. Molitoris et al., Phys. Rev. **C 37** (1988) 1020.

[Mon04] F. Montani, C. May, H. Muether, Phys. Rev. **C 69** (2004) 065801

[Mor72] L. G. Moretto et al., Nucl. Phys. **A 185** (1972) 145.

[Mor74] L.G. Moretto. In: Proc. third IAEA Symp. on the physics, chemistry of fission **vol. 1**, IAEA, Vienna (1974), p. 329 Rochester, NY, 13–17 August 1973 .

[Mor75] L. G. Moretto et al., Nucl. Phys. **A 247** (1975) 211.

[Mor88] L. G. Moretto, G. Wozniak, "The Categorial Space of Fission", LBL-25744 (1988)

[Mor89] D. J. Morrissey, Phys. Rev. **C 39** (1989) 460.

[Mül95] H. Müller, B. D. Serot, Phys. Rev. **C 52** (1995) 2072

[Mul98] S.I. Mulgin *et al.*, Nucl. Phys. **A 640** (1998) 375

[Mus99] B. Mustapha, PhD Thesis, Universite Paris-XI (1999), IPNO-T-99-05.

[Mye67] W. D. Myers, W. J. Swiatecki, Arkiv foer Fysik **36** (1967) 343.

[Mye97] W. D. Myers, W. J. Swiatecki, Nucl. Phys. **A 612** (1997) 249.

[Nap03] P. Napolitani, L. Tassan-Got, P. Armbruster, M. Bernas, Nucl. Phys. **A 727** (2003) 120

[Nap04] P. Napolitani et al., GSI preprint 2004-13 June.

[Ner55] W. E. Nervik and G. T. Seaborg, Phys. Rev. **97** (1955) 1092

[Ode00] T. Odeh et al., Phys. Rev. Lett. **84** (2000) 4557

[Ogi91] C. A. Ogilvie et al., Phys. Rev. Lett. **67** (1991) 1214

[Oli79] L. F. Oliveira, R. Donangelo, and J. O. Rasmussen, Phys. Rev. **C 19** (1979) 826.

[Pal01] Yu. V. Palchikov, J. Dobe, R. V. Jolos, Phys. Rev. **C 63** (2001) 034320.

[Pfu94] M. Pfützner et al., Nucl. Instr. Meth. **B 86** (1994) 213.

[Poc95] J. Pochodzalla et al., Phys. Rev. Lett. **75** (1995) 1040.

[Poc97] J. Pochodzalla., Prog. Part. Nucl. Phys. **39** (1997) 443.

[Pos71] A. M. Poskanzer et al., Phys. Rev. C **3** (1971) 882.

[Pro01] A. V. Prokofiev, Nucl. Instr. Meth. **A 463** (2001) 555

[Rei97] W. Reisdorf et al, Nucl. Phys. **A 612** (1997) 493-556

[ReiR97] W. Reisdorf, H. G. Ritter, Annu. Rev. Nuc. Part. Sci. **47** (1997) 663

[Rej00] F. Rejmund, A. V. Ignatyuk, A. R. Junghans, K.-H. Schmidt, Nucl. Phys. **A 678** (2000) 215.

[Rej01] F. Rejmund et al., Nucl. Phys. **A 683** (2001) 540.

[Ric03] M. V. Ricciardi et al., Phys. Rev. Lett. **90** (2003) 212302

[Ric04] M. V. Ricciardi et al., Nucl. Phys. **A 733** (2004) 299

[Ricc04] M. V. Ricciardi et al., submitted to Nucl. Phys. **A** (2004)

[Rid00] D. Ridikas, W. Mittig, N. Alamanos, Internal Report CEA France (2000), DAPNIA-SPHN-2000-59
[Rod02] Rodionov et al., Nucl. Phys. **A 700** (2002) 457
[Röp98] G. Röpke, A. Schnell, P. Schuck, P. Nozières, Phys. Rev. Lett. **80** (1998) 3177.
[Rub95] C. Rubbia et al., Internal Report CERN (1995), CERN-AT-95-44 ET.
[Sar87] D. G. Saranties et al., LBL preprint LBL-24495 (1987)
[SAT] http://www-wnt.gsi.de/kschmidt/SATAN/GHELP/satanhelp.htm
[San92] T. C. Sang et al., Phys. Rev. **C 46** (1992) 1404
[Sar89] D. G. Saranties et al., Phys. Lett. **B 218** (1989) 427
[Sat98] W. Satula, J. Dobaczewski, W. Nazarewicz, Phys. Rev. Lett**. 81** (1998) 3599
[Sch00] K.-H. Schmidt et al., Nucl. Phys. **A 665** (2000) 221
[Sch02] K.-H. Schmidt, M. V. Ricciardi, A. S. Botvina, T. Enqvist, Nucl. Phys. **A 710** (2002) 157
[Sch87] K.-H. Schmidt et al., Nucl. Instr. Meth. **A 260** (1987) 287-303
[Sch93] K.-H. Schmidt et al., Phys. Lett. **B 300** (1993) 313.
[Sch94] O. Schapiro, A. R. DeAngelis, D. H. E. Gross, Nucl. Phys. **A 568** (1994) 333.
[Sch96] A. Schüttauf et al., Nucl. Phys. **A 607** (1996) 457.
[Sch98] W. Schwab et al., Eur. Phys. J. **A 2** (1998) 179.
[Sche98] C. Scheidenberger et al., Nucl. Instr. Meth. **B 141** (1998) 441.
[Schwe98] C. Schweitzer, Thesis of the Stage DEA at the GSI, 1998.
[Shi01] L. Shi, P. Danielewicz, and R. Lacey, Phys. Rev. **C 64** (2001) 034601
[Sob84] L. G. Sobotka et al., Phys. Rev. Lett. **53** (1984) 2004
[Sou00] S. R. Souza et al., Phys. Rev. **C 62** (2000) 064607
[Ste91] M. Steiner, Diploma Thesis, Institut für Kernphysik, TH Darmstadt (1991).
[Stel91] H. Stelzer, Nucl. Instr. and Meth. **A 310** (1991) 103
[Ste92] M. Steiner et al., Nucl. Instr. Meth. **A 312** (1992) 420
[Ste98] S. Steinhaeuser et al., Nucl. Phys. **A 634** (1998) 89
[Sto88] R. G. Stokstad, Treatise on Heavy-Ion Science, Vol. 3, ed D. A. Bromley, Plenum Press, New York (1988) p. 83-197
[Str58] V. M. Strutinski, Int. Conf. on Nuclear Physics, Paris (1958) 617
[Stu01] C. Sturm et al., Phys. Rev. Lett. **86** (2001) 39
[Süm00] K. Sümmerer, B. Blank, Phys. Rev. **C 61** (2000) 034607
[Tai03] J. Taieb et al., Nucl. Phys. **A 724** (2003) 413-430
[Tra72] B. L. Tracy et al., Phys. Rev. **C 5** (1972) 222
[Tra97] W. Trautmann, in Correlations and Clustering Phenomena in Subatomic Physics, Edited by Harakeh et al., Plenum Press, New York, (1997) page 115.
[Tsa01] M. B. Tsang et al., Phys. Rev. **C 64** (2001) 041603.
[Tsa02] M. B. Tsang et al., Phys. Rev. **C 66** (2002) 044618
[Vio76] V. E. Viola, K. Kwiatkowski, M. Walker, Phys. Rev. **C 31** (1985) 1550.
[Vog00] P. Vogel, Nuc. Phys. **A 662** (2000) 148
[Vos95] B. Voss, Diploma Thesis, Institut für Kernphysik, TH Darmstadt (1995).
[Wag99] P. Wagner, J. Richert, V. A. Karnaukhov, H. Oeschler, Phys. Lett. **B 460** (1999) 31.
[Web90] W. R. Webber, J. C. Kish, D. A. Schrier, Phys. Rev. **C 41** (1990) 547.
[Web98] W. R. Webber et al., Astroph. Jour. **508** (1998) 949.
[Wei37] V. F. Weisskopf, "Statistics And Nuclear Reactions", Phys. Rev. **52** (1937) 295
[Wes78] G. D. Westfall et al., Phys. Rev. **C 17** (1978) 1368

[Wie99] M. E. Wiedenbeck et al., Astroph. Jour. **523** (1999) L61-L64.
[Wig33] E. Wigner and F. Seitz, Phys. Rev. 43, 804 (1933)
[Wig37] E. Wigner, Phys. Rev. **51** (1937) 947
[Wil76] B. D. Wilkins, E. P. Steinberg, R. R. Cashman, Phys. Rev. **C 14** (1976) 1832.
[Win01] E. M. Winchester et al., Phys. Rev. **C 63** (2001) 014601.
[Wol56] R. Wolfagang et al., Phys. Rev. **103** (1956) 394
[Yan99] L. B. Yang et al., Phys. Rev. **C 60** (1999) 041602(R).
[Zei97] C. Zeitlin et al, Phys. Rev. **C 56** (1997) 388
[Zie92] C. Ziegler, Diploma Thesis, Institut für Kernphysik, TH Darmstadt (1992)
[Zol74] A. M. Zolotov et al., Sov. J. Nucl. Phys. **18** (1974) 15

Acknowledgments

This thesis would have never been possible without the direct support of three people, towards whom I am deeply grateful.

Prof. Gottfried Münzenberg, who invited me to the GSI and set the basis for my permanence in Germany. He does not know, but he changed my life in a radical (and positive) way. I appreciate his naturalness, friendliness and intelligence, which create the nice atmosphere that everybody feels at the KPII division.

Dr. Karl-Heinz Schmidt, a true explorer of Nature's mysteries, and by far the best teacher I have ever had, my Virgilio who guided my through the Dantesque circles of physics. I like his intuition, his curiosity, his inquiring mind, and also his artistic indomitable spirit, which makes him so unpredictable. I really enjoyed the long discussions on physics I had with him, when we tried to recompose the beautiful mosaic of the nucleus, putting together the pieces of our puzzling results. It was a genuine pleasure to speak with him about physics and science, but also about music, children education, psychology, philosophy, religion, history, politics, and economy.

Prof. José Benlliure, who helped me in the most dark and hopeless moments of this troublesome journey. I appreciated the nice and friendly atmosphere in Santiago de Compostela. I thank him for his fruitful comments and discussions on physics, which improved the quality of the thesis, and his decisive contribution during the experiment.

I would like to thank also Prof. Peter Armbruster and Dr. Monique Bernas, for the regular contacts, discussions and exchange of information, but also for promoting always women in science. Last, but not least, I would like to thank all the colleagues and collaborators, in particular Dr. Fanny Rejmund, Dr. Timo Enqvist, and the technicians of the FRagment Separator whose contribution during the experiment was essential.

***

In un certo senso, devo ringraziare questa tesi: se non fosse per essa non avrei mai incontrato José. D'altro canto, senza José non avrei mai finito la tesi. I piu' grandi ringraziamenti vanno quindi a Josè, per l'amore, la pazienza e il conforto durante gli anni di questa problematica tesi, e al di la' della tesi, per tutto quello che di bello lui rappresenta per me. Grazie a Pablo, perchè anche nei giorni piu' grigi, un suo sorriso mi restituisce il buon umore e l'allegria.

Grazie alla mia famiglia, sempre presente anche se lontana; il punto di riferimento e "nucleo" primo, dove ho imparato l'amore per la cultura.

Grazie ad Antonella, a Marina, a Maria e a tutti gli amici "infimi" per il supporto durante questi anni in questa e nella altre fondamentali tappe della vita.

Muchas gracias a Beatriz, mi amiga, y fiel compañera de oficina y de casa, que ha compartido conmigo un buen trecho de este camino. Ella me ha abierto las puertas de los Pirineos, que según parece nunca se cerrarán más... Gracias también a Pepe, Lola, Pablo y toda la gente de Santiago por la cariñosa hospitalidad. Thanks to Kerttuli and Aleksandra, who brought friendship and good mood in the group.

Dedico questo lavoro ai miei genitori.